Title

Single-cell molecular profiling of experience-dependent cell type development in mouse retina and cortex

Author

Butrus, Salwan Younus

Publication Date

2024

Single-Cell Molecular Profiling of Experience-Dependent Cell Type Development in Mouse Retina and Cortex

By

Salwan Younus Butrus

A thesis submitted in partial satisfaction of the

requirements for the degree of

Doctor of Philosophy

in

Chemical Engineering

in the

Graduate Division

of the

University of California, Berkeley

Committee in charge:

Professor Karthik Shekhar, Chair
Professor Daniel Feldman
Professor Markita Landry

Fall 2024

Abstract

Single-Cell Molecular Profiling of Experience-Dependent Cell Type Development in Mouse Retina and Cortex

By

Salwan Younus Butrus

Doctor of Philosophy in Chemical Engineering with a
Designated Emphasis in Computational and Genomic Biology
University of California, Berkeley

Professor Karthik Shekhar, Chair

Sensory experience ("nurture") acts upon a genetically hardwired blueprint ("nature") to sculpt the brain during early developmental stages known as "critical periods" (CPs). In the process, immature neurons acquire diverse identities and assemble into circuits defined by specific synaptic connections. Disrupted organization of neural circuits during CPs underlies a myriad of neural disorders, making the study of experience-dependent neural development fundamentally and clinically important. Recent advances in single-cell transcriptomics have enabled the "bottom-up" characterization of neural diversity at molecular resolution. By applying unsupervised machine learning approaches to large-scale gene expression measurements, catalogs of cell types have been generated and used to study development, function, dysfunction, and evolution across the nervous system. However, the influence of sensory experience during CPs on the development and maturation of diverse neuronal types remains unknown. Furthermore, due to the destructive nature of single-cell transcriptomic assays, temporal changes cannot be directly observed. They must be inferred from high-dimensional gene expression "snapshots" in distinct samples of single cells spanning developmental stages, conditions, and animals. In this thesis, I present developmental transcriptomic cell type atlases in three regions of the mouse brain: the retina, the whisker somatosensory cortex, and the primary visual cortex. I then use these atlases to understand the role of sensory experience in the maturation of cell types within each system.

In the first part of this thesis, I investigate the role of vision in the development of 45 retinal ganglion cell (RGC) types, the retina's sole output neuron. The development and connectivity of RGCs are patterned by activity-independent transcriptional programs and activity-dependent remodeling. To inventory the molecular correlates of these influences, high-throughput single-cell RNA sequencing (scRNA-seq) was applied to mouse RGCs at six embryonic and postnatal ages. I identified temporally regulated modules of genes that correlate with, and likely regulate, multiple phases of RGC development, ranging from differentiation and axon guidance to synaptic recognition and refinement. Some of these genes are expressed broadly, while others, including key transcription factors and recognition molecules, are selectively expressed by one or a few of the 45 transcriptomically distinct types defined previously in adult mice. Next, I used these results as a foundation to analyze the transcriptomes of RGCs in mice lacking visual experience due to dark rearing from birth or due to mutations that ablate either bipolar or photoreceptor cells. 98.5% of visually deprived (VD) RGCs could be unequivocally assigned to a single RGC type based on their transcriptional profiles, demonstrating that visual activity is dispensable for acquisition and maintenance of RGC type identity. However, visual deprivation significantly reduced the transcriptomic distinctions among RGC types, implying that activity is required for complete RGC maturation or maintenance. Consistent with this notion, transcriptomic alterations in VD RGCs significantly overlapped with gene modules found in developing RGCs. These results provide a resource for mechanistic analyses of RGC differentiation and maturation and for investigating the role of activity in these processes.

In the second part of this thesis, I investigate the influence of vision on the development of cell types in the mouse primary visual cortex (V1), the area of the brain that processes visual information. By combining unsupervised and supervised machine learning approaches, single-nucleus RNA sequencing, visual deprivation, genetics, and functional imaging, my colleagues and I discovered that vision selectively drives the specification of glutamatergic neuronal types in upper layers (L) (L2/3/4), while deep-layer glutamatergic neuronal types, GABAergic neuronal types, and non-neuronal cell types are established before eye opening. Furthermore, I found that L2/3 neuronal types form an experience-dependent spatial continuum defined by the graded expression of ~200 genes, including regulators of cell adhesion and synapse formation. One of these genes, *Igsf9b*, a vision-dependent gene encoding an inhibitory synaptic cell adhesion molecule, is required for the normal development of binocular neurons in L2/3. These results raise the intriguing possibility that sensory experience acts differentially in regulating the plasticity of individual cell types and provide a blueprint for future studies into the experience-dependent development of other brain regions.

In the third part of this thesis, I investigate whether experience-dependent regulation of cell types exists in another cortical region known as the primary whisker somatosensory cortex (wS1). wS1 is a major model system to study the experience-dependent plasticity of cortical neuron physiology, morphology, and sensory coding. However, the role of sensory experience in regulating neuronal cell type development and gene expression in wS1 remains poorly understood. I assembled and annotated a transcriptomic atlas of wS1 during postnatal development comprising 45 molecularly distinct neuronal types that can be grouped into eight excitatory and four inhibitory neuron subclasses. Using this atlas, I examined the influence of whisker experience from postnatal day (P) 12, the onset of active whisking, to P22, on the maturation of molecularly distinct cell types. During this developmental period, when whisker experience was normal, ~250 genes were regulated in a neuronal subclass-specific fashion. At the resolution of neuronal types, I found that only the composition of layer (L) 2/3 glutamatergic neuronal types, but not other neuronal types, changed substantially between P12 and P22. These compositional changes resemble those observed previously in the primary visual cortex (V1), and the temporal gene expression changes were also highly conserved between the two regions. In contrast to V1, however, cell type maturation in wS1 is not substantially dependent on sensory experience, as 10-day full-face whisker deprivation did not influence the transcriptomic identity and composition of L2/3 neuronal types. A one-day competitive whisker deprivation protocol also did not affect cell type identity but induced moderate changes in plasticity-related gene expression. Thus, developmental maturation of cell types is similar in V1 and wS1, but sensory deprivation minimally affects cell type development in wS1.

Finally, I highlight the major conclusions of each chapter, discuss their historical context, and suggest future work on the experience-dependent development of neuronal cell types and circuits in the mammalian nervous system.

To my parents, نیران and یونس
The privilege I was afforded to perform this work is a product of their sacrifices

Table of Contents

Acknowledgements

"Endlessly one could thank, for one is nothing without those amongst whom one lived, from whom one learned, on whose knowledge one builds up. If only I, in my way, can someday be of use!"

Quest, by George Dibbern, 1941.

I have looked forward to writing this section of my thesis ever since I saw it in the first thesis I read seven years ago. It's always the first section I go to in a thesis because it's the only place where the person behind the work—and the village surrounding them—is revealed to the reader. I finally get to exercise the distinct privilege of thanking those who have tremendously enriched my personal and academic journeys.

First and foremost, I would like to express my utmost gratitude to my advisor, Prof. Karthik Shekhar. I joined Karthik's group with little experience in machine learning and neuroscience. He didn't care one bit. All he cared about was that I showed excitement for his work. At the beginning of my PhD, he spent countless hours answering my questions, and the enthusiasm he showed for educating others about his work instantly drew me to work with him. His ability to be at the cutting edge of several disciplines while explaining the most complex concepts in the simplest possible manner is awe-inspiring. During the five years I worked with him, I cannot recall a single time when he wasn't accessible to me as a mentor. I would sometimes go into a meeting with him stressed about certain aspects of a project, but I always left those meetings feeling refreshed and energized because of his helpful advice and supportive attitude. Karthik combines relentless curiosity with sharpness, kindness, and sincerity that I am confident will continue to enrich the academic journeys of Shekhar Lab members for decades to come.

In addition, I would like to thank the rest of my committee for their support throughout my PhD. I was fortunate to work closely with Prof. Dan Feldman during the second half of my PhD. He welcomed me into his lab to work on the wS1 project, and that work would not have been possible without his guidance at critical junctures in experimental design and computational analysis. I am forever grateful for his mentorship and support. Prof. Markita Landry has been a mentor of mine ever since she welcomed me into her lab as an Amgen Scholar in 2018. The summer I spent in her lab was the final deciding factor that convinced me to pursue a PhD. I owe a great deal of gratitude to Markita for her mentorship and support before and throughout my PhD.

Performing research at the intersection of multiple fields gave me the opportunity to collaborate with several incredible scientists. At the beginning of my PhD, Dr. Sarah Cheng and Profs. Larry Zipursky and Josh Trachtenberg introduced me to the field of experience-dependent visual cortex development and made me feel like another member of their labs (despite working together virtually for three years before meeting them in person!). It was a pleasure to work alongside them. I also had the privilege of working with Prof. Josh Sanes on a retinal development project that gave me a deeper appreciation of why exactly he is such a giant in his field. I was then fortunate enough to meet Drs. Juyoun Yoo and Prof. Saumya Jain from Larry's lab. The term "tour de force" can be overused in science, but the effort they undertook to collect multiomic visual cortex data across several developmental stages and rearing conditions was astonishing. The data they collected gave rise to a new collaboration that enabled us to pursue mechanisms for the results Dr. Sarah Cheng and I had previously reported. This project also introduced me to another incredible colleague, Dr. Fangming Xie, with whom I have had the privilege of working closely on multiple other projects. It's a joy working with Juyoun, Saumya, and Fangming because they are stellar scientists and human beings. I am thankful to call them lifelong colleagues.

Last, and certainly not least, is Dr. Hannah Monday. Without her willingness to mentor me in the lab, the wS1 project would never have happened. She helped refine my ideas for the project and played a major role in making them a reality. Her diligence, persistence in the face of obstacles, creativity, and ability to operate at the highest level in her field while caring for two children were a constant inspiration to me during the second half of my PhD. I am fortunate to call Hannah a lifelong friend and colleague.

I would like to think that I would have had the courage to be Karthik's sole first student. In all likelihood, if the recently minted Dr. Joshua Hahn had not been around, I would have chosen a different lab. Josh was the best possible person with whom to build a new lab. He is curious, collaborative, diligent, and capable of learning any topic and teaching it effectively to his colleagues. Most importantly, he is an easygoing and friendly person who could get along with anyone. I'm thankful for our time together in the lab and our friendship beyond. Moreover, it has been a joy to watch the lab grow over the last five years. Alhad, Josh F., Kushal, Hyeongjoo, Matthew, Dario, and Jafar each contributed their own personal and professional magic that made coming to the office worthwhile. Despite most of us working on disparate research projects spanning applied physics, machine learning, and neuroscience, each one of them has asked incredibly insightful questions that have changed the way I think about my work. I am thankful for the lifelong friendships I gained from being in Karthik's lab. I would also like to thank my undergraduate mentees Srikant, Jason, and Xiaoqi. They absorbed everything I told them and every resource I shared, constantly returning with insightful questions that demonstrated their deep curiosity, diligence, and immense potential for research. I am so proud to see them thriving in their post-Berkeley endeavors.

Beyond research, I've had the privilege of getting to know many people who enriched my time here at Berkeley. There are too many to name, but some include my initial housemates: Jordan, Nate, and Justin. They were the best possible group to live with after moving across the country and enduring the COVID-19 pandemic. I will miss our shenanigans and barbecue parties. Members of my cohort were, and continue to be, a source of joy during my time in Berkeley. Josh Hahn, Francis, Darby (and Mark), Ahmad, Morgan, Matt, Erika, Josh Hubbard, and Kimberly were the core Loud House crew. I will miss our weekly lunches and annual trips. Beyond the 2019 cohort, the CBE department introduced me to countless individuals who enriched my PhD experience, from our basketball, ultimate frisbee, and soccer teams to holiday celebrations, ski trips, and everything in between. I have met so many amazing people who made my PhD both memorable and enjoyable. A special shoutout goes to my friend Dr. Zach Konz. Our hikes, dinners, and soccer ball juggling sessions (we hit 600 once!) were some of the highlights of my PhD. I'm so fortunate to have made a lifelong friend in Zach during my time here. Finally, I'm thankful for picking up the sport of cycling over the last few years and for all the wonderful friends it introduced me to, especially through the Berkeley Bicycle Club.

I would also like to thank the many colleagues and mentors at the University of Michigan who inspired me to pursue a PhD and contributed immensely to preparing me for it. My freshman year UROP experience in Dr. Somnath Bhattacharjee's group, under the guidance of James Otis, was a great initial foray into research. It taught me foundational skills in a welcoming, low-pressure environment. Around the same time, I took Organic Chemistry II with Prof. John Montgomery, whose enthusiasm for the topic and genuine investment in students remain unmatched by any class I've taken since. After discussing my research interests with him, he encouraged me to explore opportunities in the Chemical Engineering department. There, I met the inimitable Dr. Susan Montgomery, who is the greatest academic advisor of all time. Shortly after committing to the ChemE major, I joined Prof. Joerg Lahann's lab and had the fortune of being mentored by Prof. Ramya Kumar and Dr. Ayse Muniz. Working with them taught me countless technical and soft research skills and convinced me that pursuing a PhD would be a great choice for me. This experience prepared me well for a summer internship in Prof. Paula Hammond's lab under the guidance of Dr. Brett Geiger. There, I had the opportunity to design and execute my own project to completion in a highly collaborative environment, cementing my desire to pursue a PhD.

The ChemE major also introduced me to several colleagues and friends who made my time at UM memorable and meaningful. To our core homework group—including Vinod, Andrew, Irina, Akira, Nolan, Rishabh, and Lucas—those countless hours we spent in the UGLi working on problem sets shaped the student and scientist I am today. I'd also like to acknowledge friends I met through ChemE and beyond, like Rebecca, Kevin, Jenna, Caleb, and Sarah. It was a once-in-a-lifetime experience to build and fund UM's first-ever undergraduate research symposium together. A special thanks goes to Prof. Steven Chavez and Dr. Eshita Khera, who in 2018 took a chance on a few undergraduates (myself, Kevin, Irina, and Akira) with a crazy idea and helped us start and operate the department's first undergraduate-led, research-focused course. Finally, beyond schoolwork and research, the community that had the greatest impact on me at UM was Camp Kesem. All of the wonderful volunteers I worked with and the amazing kids we served were the highlight of my time in Ann Arbor. The strength and resolve of those kids continue to inspire me to this day through any adversity I experience.

Last but not least, my loved ones. A special acknowledgment goes to my lovely fiancé, Elizabeth Voke. She is my best friend and the one person who can always get the best out of me with her kindness, wit, and spontaneity. This PhD would not have been possible without her support and love over the past several years. I am so fortunate to have a partner as accomplished, resilient, and caring as her in my life. I am thankful for what we have built together and thrilled for all the adventures that await us. Moreover, I would like to thank the individuals who made the largest possible sacrifices to help me reach this stage. My parents, Niran and Younus, did not have the means to pursue higher education in our home country, so they made it their life's mission to ensure their children would not meet the same fate. They sheltered us from the war, arranged for our escape to safety, and sacrificed their happiness and comfort at every turn to maintain the smoothness of our journeys. There are no two people in the world who work harder or dedicate their lives to their children as much as my parents. None of my accomplishments would have been possible without their love and support. And to my brothers—my best friends from far away—they keep me grounded and remind me what's important. I am incredibly proud of their achievements and the wonderful men they have become. We don't get to choose our families, but I know that I won the lottery with mine.

Chapter 1: Introduction

Critical periods of experience-dependent plasticity in mouse cortex

For more than two centuries, we have known that sensory experience refines a genetically hardwired “rough draft” of the brain during development (James, 1890; Rosenzweig, 1996; Zanatta et al., 2018). However, the influence of sensory experience on the organization of neurons in the brain was not elucidated until the work of Hubel and Wiesel in the primary visual cortex (V1). Through studies in cats and monkeys, they discovered that V1 is organized into stripes containing neurons that respond to stimulation from either the left or the right eye (**Figure 1.1A**) (Hubel and Wiesel, 1969; LeVay et al., 1975; Wiesel and Hubel, 1963). They became immediately interested in how this macroscopic organization of V1 into “ocular dominance columns” (ODCs) arises during development and whether sensory experience is necessary for its establishment. They found that depriving the animals of vision in one eye (i.e., monocular deprivation) during early development led to a reduction in the size of columns connected to the closed eye and enlargement of those receiving input from the open eye (**Figure 1.1A**) (Hubel et al., 1977; Wiesel and Hubel, 1963). Three key observations contextualize these results. First, while a columnar organization of V1 is evident by birth, the mature pattern is not achieved until several weeks after birth. Second, the effects of monocular deprivation could be reversed by reopening the closed eye, but this was only true during a specific time period early in development. Third, monocular deprivation of adult animals beyond this time period had no effect on ODCs. Together, these findings established that nurture (vision) acts upon nature’s genetically hardwired blueprint to sculpt organization within V1 during a critical period (CP) of early development. The malleability of V1 circuitry during the CP became known as “ocular dominance plasticity.”

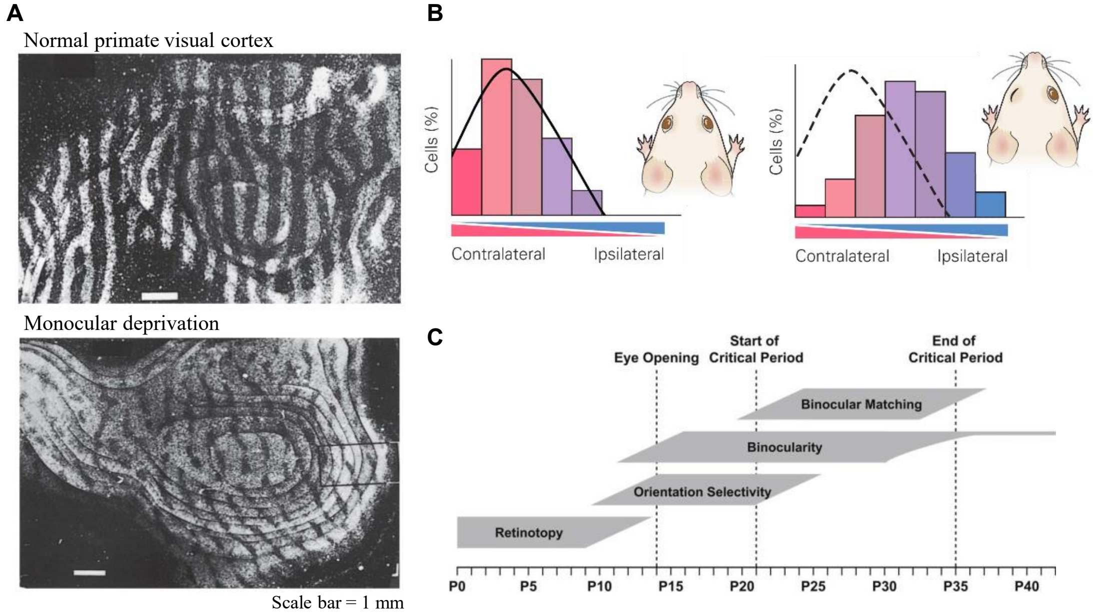

Figure 1.1. Experience-dependent plasticity in V1. (**A**) Visual deprivation of one eye during a critical period of development reduces the width of the ocular dominance columns for that eye (adapted from Levay et al., 1977). (**B**) A critical period for ocular dominance plasticity is evident in mice (adapted from Hensch, 2005). (**C**) Major milestones in mouse V1 development (adapted from Espinosa and Stryker, 2012).

In subsequent decades, the influence of experience on cortical circuitry in V1 was dissected at a molecular, genetic, and functional level in mice because mice are more amenable to mechanistic studies than cats and monkeys (Hooks and Chen, 2020). Unlike cats and monkeys, most of the mouse V1 receives only contralateral input and its binocular zone is not divided into ODCs. Despite the binocular zone comprising only 20% of mouse V1 and containing a mixture of monocularly and binocularly driven neurons (Tan et al., 2021, 2020), closure of the contralateral eye markedly shifts the preference of binocular neurons to inputs from the ipsilateral eye (**Figure 1.1B**) (Gordon and Stryker, 1996). This only occurs during a critical period for ocular dominance plasticity between P21 and P35 (**Figure 1.1C**) (Espinosa and Stryker, 2012; Gordon and Stryker, 1996). Visual experience during this period is necessary for the development and maintenance of the neural circuitry underlying binocular vision (Espinosa and Stryker, 2012; Gordon and Stryker, 1996; Ko et al., 2014, 2013).

Another cortical region that is highly amenable to investigating the role of sensory experience in regulating the development and plasticity of neural circuits is the mouse whisker primary somatosensory cortex (wS1) (Fox and Wong, 2005). wS1 processes tactile (touch) information from the facial whiskers and contains a somatotopic map of the whisker pad. Sensory manipulation (plucking or activation) of specific whiskers drives plasticity in the cortical columns corresponding to those whiskers (**Figure 1.2A**). This provides strong technical advantages in studying plasticity and has made wS1 a workhorse for studying morphological and physiological experience-dependent plasticity (Erzurumlu and Gaspar, 2012; Feldman and Brecht, 2005; Fox and Wong, 2005). Cortical circuit development and critical periods are also well described in wS1 (**Figure 1.2B**). Thalamocortical axons arrive in L4 at postnatal day (P) 1-2, segregate into whisker-specific clusters at P3, and drive patterning of postsynaptic L4 neurons into cylindrical modules (termed barrels) in L4. Barrel pattern development is partly driven by neural activity during this early period (P0-3). After this age, the anatomical barrel pattern remains stable, but alterations in whisker use drive physiological plasticity in wS1 that is maximal during two overlapping critical periods (CP1 and CP2). CP1 and CP2 initiate at the onset of active whisking (at P12) and coincide with peak synaptogenesis in wS1. From P12-14, whisker deprivation (WD) disrupts receptive field structure (Maravall et al., 2004; Stern et al., 2001) and spine motility (Lendvai et al., 2000) in L2/3 pyramidal (PYR) cells (CP1). From P12-16, removal of all but one whisker strengthens L4-L2/3 and L2/3-L2/3 synapses to enhance the representation of the spared whisker (CP2) (Wen and Barth, 2011). Brief 1-day whisker deprivation (WD) also drives physiological plasticity in

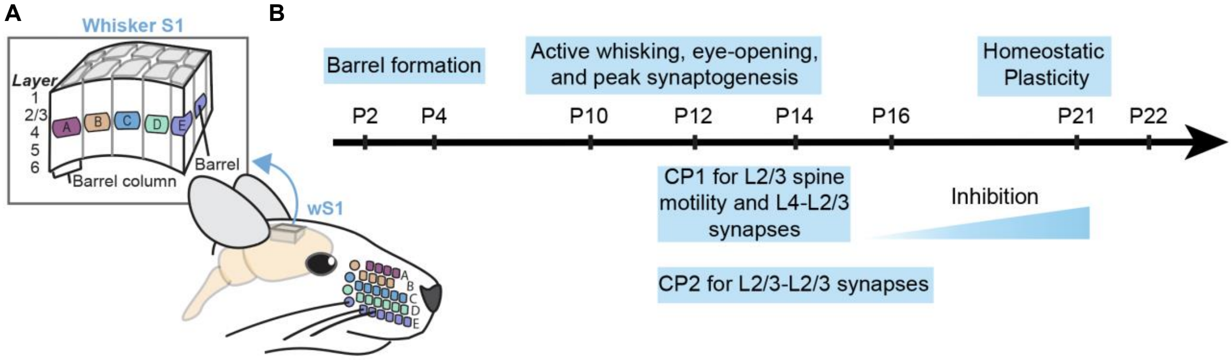

Figure 1.2. Mouse whisker somatosensory cortex (wS1). (**A**) Schematic of the mouse wS1, which contains a somatotopic map of the mouse's whisker pad in which individual whiskers are represented by neural activity within barrel columns of the cortex. (**B**) Timeline of key milestones in wS1 development.

parvalbumin-positive (PV) interneurons in L2/3, which acts to homeostatically preserve whisker-evoked firing rates in PYR cells, a form of plasticity that is robust at P21 (Gainey et al., 2018).

Beyond their macroscopic organization into binocular/monocular zones and whisker-specific barrels, V1 and wS1 contain a staggering level of diversity in the form of hundreds of neuron types. Since the work of Santiago Ramón y Cajal over a century ago, neurons in cortex have been classified into discrete types based on morphological and anatomical features (Ramón y Cajal and Ramón y Cajal, 1909; y Cajal, Santiago Ramon, 1899), functional properties (Gouwens et al., 2019; Hubel and Wiesel, 1962; Wiesel and Hubel, 1963), connectivity patterns (Chiang et al., 2011; Swanson and Lichtman, 2016; Varshney et al., 2011), and more recently, transcriptomic features (Hrvatin et al., 2018; Sarropoulos et al., 2021; Tasic et al., 2018; Tran et al., 2019). What remain less well known are the underlying mechanisms of experience-dependent plasticity at the level of cortical cell types. Experience-dependent plasticity has been extensively investigated at the level of morphological and physiological diversity (Antonini and Stryker, 1993; Oray et al., 2004). At the molecular level, previous investigations of experience-dependent changes in gene expression during the critical period have compared bulk transcriptomic profiles of V1 and S1 between normally reared (NR) and sensory-deprived animals (Kole et al., 2017; Majdan and Shatz, 2006; Mardinly et al., 2016; Tropea et al., 2006) or within NR animals at different points during the critical period (Lyckman et al., 2008). However, the influence of vision on individual neuron types in V1 cannot be gleaned from "bulk" gene expression changes. To study plasticity during the CP in the context of the extensive molecular diversity of neuron types in V1 (Tasic et al., 2018), we need approaches that can resolve gene expression changes in single cells. This level of detail is essential for understanding how activity regulates the structure and function of cortical circuitry.

Cell type classification and assessment using single-cell transcriptomics

Droplet-based single-nucleus RNA-sequencing

Since Santiago Ramón y Cajal first observed the neuron under a microscope over a century ago, neuroscientists have classified neurons based on their morphological features and electrophysiological characteristics (**Figure 1.3A**) (Fishell and Heintz, 2013; Franke et al., 2017; Markram et al., 2015; Migliore and Shepherd, 2005; Tyner, 1975). While these cell identity properties are important for studying any neuroscience problem, data acquisition (mostly involving light microscopy or cell attached recordings) tends to be laborious and low-throughput (**Figure 1.3B**) (Zeng and Sanes, 2017). Tools for robustly classifying neurons into types are highly desirable because they would facilitate reproducible studies across laboratories and experimental conditions. Indeed, classification would enable genetic access for functional studies and analyses of development, evolution, and disease (Zeng, 2022).

The advent of single-cell RNA-sequencing (scRNA-seq) marked a watershed moment in the field of cell type classification (Macosko et al., 2015; Svensson et al., 2018; Zheng et al., 2017). First, it enabled the measurement of >20,000 features (genes) simultaneously in 10,000 cells per experiment (**Figure 1.3C**). Second, a variant was later developed using nuclei instead of cells (Habib et al., 2017), which was compatible with frozen tissue. With single-nucleus RNA-seq (snRNA-seq), tissues can be dissected, frozen, preserved for long periods, and transported across facilities before processing. More importantly for cortical tissue and this thesis in particular, snRNA-seq circumvents the challenges associated with dissociating cells from brain tissue without damaging them, as dissociating nuclei from brain tissue is a more time-efficient and reproducible process. In this thesis, the scRNA-seq technology from 10X Genomics was used in Chapter 2, and the snRNA-seq technology in Chapters 3-4.

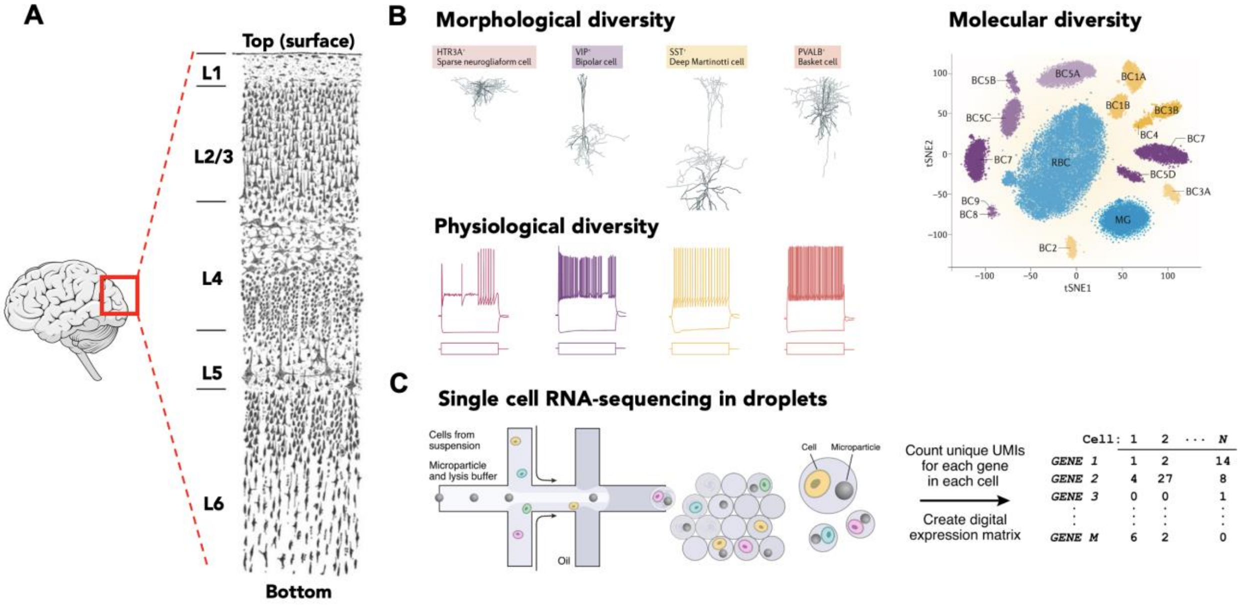

Cell:	1	2	···	*N*
GENE 1	1	2		14
GENE 2	4	27		8
GENE 3	0	0		1
⋮	⋮	⋮		⋮
GENE M	6	2		0

Figure 1.3. Multi-scale neuronal cell type classification. (**A**) Drawing by Santiago Ramón y Cajal illustrating the layered structure of the human cerebral cortex (Cajal, 1899). (**B**) Neurons can be classified by multiple criteria (Zeng and Sanes, 2017). (**C**) Single-cell RNA-sequencing experiment generates a gene expression matrix (Macosko et al., 2015).

Read alignment and data preprocessing

Identifying and characterizing cell types using snRNA-seq involves a series of computational steps. These include read alignment, data engineering and filtering, transformation, unsupervised learning, statistical differential expression tests, and supervised learning (Brüning et al., 2022; Hie et al., 2020). In this and the following section, we provide a high-level overview of the methods used in this thesis. First, the raw output of a snRNA-seq experiment involves millions of sequencing reads that have been barcoded to retain their single-cell origin (Zheng et al., 2017). These sequencing reads are mapped to a reference genome to quantify gene expression in each cell. High-quality reference genomes annotated with known protein-coding and non-coding genes are available for tens of species (Yates et al., 2020). The read alignment and quantification is often conducted using 10X Genomics' cellranger suite of tools. The result of this alignment is a $N \ x\, D$ gene expression matrix (GEM), where N is the number of cells obtained, and D is the number of genes detected in the experiment, with each entry reflecting the expression of each gene within each cell. N is typically no more than 10,000, and D ranges from 20,000 to 30,000 depending on the species profiled.

Basic quality control seeks to remove low-quality observations (cells) and features (genes) from the GEM. Cells and genes with extremely low or high counts relative to the parent distributions, cells with a high mitochondrial count fraction, and cells statistically inferred to be multiplets

(Wolock et al., 2019). The thresholds for each of the filtering criteria are determined on a dataset-by-dataset basis (Heumos et al., 2023). Next, we attempt to address sequencing biases across cells by normalizing each cell's counts such that it sums to its median counts or a base number such as 10,000. We then apply a natural log transformation X ← log(X+1) to reduce the data's dispersion and make it more amenable to downstream dimensionality reduction analyses (Ahlmann-Eltze and Huber, 2022).

Dimensionality reduction

The preprocessing steps typically leave us with 10,000-20,000 genes. Only a fraction of these are useful for finding patterns in the data that relate cells to each other and ultimately allow us to cluster them based on their transcriptional similarity (Brennecke et al., 2013). To identify this set of features, known as highly variable genes (HVGs), methods range from ranking genes by their dispersion (standard deviation divided by mean) to estimating the underlying mean-variance distribution of the data and ranking genes by their deviation from this null model (Sarkar and Stephens, 2021; Satija et al., 2015). This step typically reduces the number of features from 20,000-30,000 to 2000-5000 genes. The non-HVGs are not completely removed from the analysis, as their expression differences across experimental conditions may be of interest. Instead, they are simply held out during the process of cell type identification because their expression patterns within the dataset of interest are highly correlated and redundant.

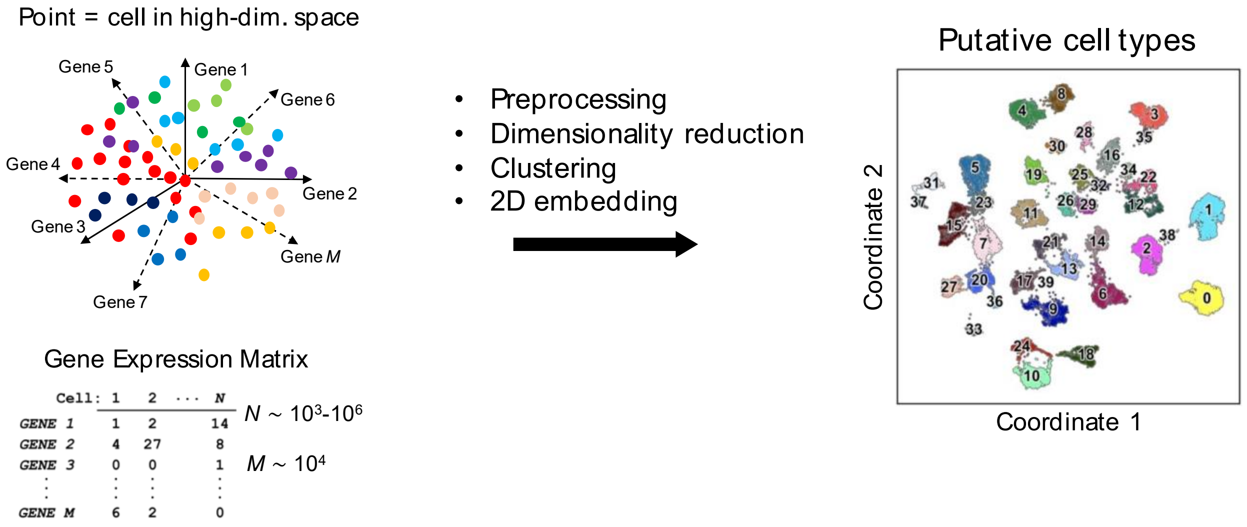

Figure 1.4. Using machine learning to uncover patterns in scRNA-seq data. Common analysis steps are highlighted.

Recall that the major goal of our analysis is to infer cellular diversity in the form of communities ("clusters", "types") of cells that share unique transcriptional profiles and to then study the influence of experimental variables such as time, dark rearing, whisker deprivation, and genetic manipulation on these clusters. Consider that each cell is a vector $x \in R^D$, where R^D represents the 2000-5000-dimensional gene expression space. Each dataset $D = \{x_1, x_2, \ldots, x_N\}$ represents discrete samples drawn from an unknown distribution P(x). The high dimensionality and sparse nature of the data makes it difficult to learn P(x) from D. Therefore, we resort to unsupervised learning approaches to uncover patterns in the data (**Figure 1.4**).

Each gene does not individually define the identity of a cell. Rather, groups of genes contribute collectively to transcriptomic distinctions between cells. To identify these collections of genes, we compute a reduced dimensional representation of the data using principal component analysis (PCA). After PCA, each cell exists in a 30- to 50-dimensional space of principal components (PCs), each a unique linear combination of the input genes. Since the PCs inferred represent the axes of maximum variance in the data, the percent variance contributed by each PC can be used to select the top PCs using an "elbow" plot. If the GEM being analyzed comprises cells sampled from multiple biological replicates collected on different days, from different labs, or using different technologies, we may perform batch correction to reduce systematic differences between replicates (Luecken et al., 2022). Throughout this thesis, the method we used learns the shared biological states across datasets by transforming the input PCs to batch-corrected PCs *via* an iterative process of clustering similar cells from different batches while maximizing the diversity of batches within each cluster (Korsunsky et al., 2019).

Clustering and visualization

To cluster cells based on transcriptomic similarity and infer putative cell types, we can apply clustering algorithms to the low-dimensional representation of the data. The clustering algorithms most commonly applied to snRNA-seq data are community detection algorithms such as Leiden (Traag et al., 2019; Yu et al., 2022). First, a k nearest-neighbor graph is computed in PC space. The Leiden algorithm then iteratively partitions this graph into highly interconnected communities under the control of an objective function seeking to maximize the difference between the actual number of edges in a community and the expected number of such edges (Traag et al., 2019). We can then project the neighborhood graph from the PC space to 2D using Uniform Manifold Approximation and Projection (UMAP) to visualize these communities and the expression of particular genes across them (**Figure 1.4**) (Becht et al., 2019). The distances from a UMAP embedding are not meant to be interpreted literally, as they emanate from a non-linear optimization problem that distorts the gene expression space to reduce it from 30-50 PCs to a 2D UMAP plot (McInnes et al., 2020). Throughout this thesis, UMAP coordinates are not used to perform any quantitative analyses or draw any scientific inferences. Any downstream quantitative analyses of cell types are always performed in either the ambient gene expression space or the PC space. We use the 2D embeddings only to visualize gene expression patterns, where cells can be colored based on their type identity to create a graph summarizing the diversity of the dataset. Indeed, recent work has dissected the limitations and advantages of UMAP and other embedding methods, determining that they manifest differently based on input data and warning users of over-interpreting the 2D coordinates (Chari and Pachter, 2023; Gorin et al., 2022; Lause et al., 2024). In addition to UMAP, 2D-3D plots of selected PCs can provide adequate visualization with directly interpretable axes and distances. Finally, we perform differential expression testing between each cluster and the rest to identify marker genes for each putative type, which facilitates the targeting of specific cell types in imaging and genetic gain- or loss-of-function experiments.

Comparing datasets across experimental conditions using supervised classification

To understand the influence of experimental variables such as time, dark rearing, and whisker deprivation on transcriptomic cell types, we would ideally measure x(t) from P(x, t) or x(c) from P(x, c), where t and c represent time and rearing condition, respectively. However, a cell must be lysed for its transcriptomic contents to be measured. In the case of developmental changes for example, we only have access to discrete snapshots D_{t0} , D_{t1} , · · · , D_{tT} . Consequently, we cannot directly observe the influence of time or rearing conditions on the molecular organization of neurons. We must infer it from snapshot measurements across developmental stages and rearing conditions. To do so, we can use transcriptomic similarity as a proxy for relationships between cell types as a function of experimental variables. Across a range of tissues and variables, it has been demonstrated that supervised classification is a suitable tool for inferring these relationships (Butrus et al., 2023; Cheng et al., 2022; Kölsch et al., 2021; Peng et al., 2019; Shekhar et al., 2016; Tran et al., 2019).

Supervised classification has been used for decades to train a model using labeled ground truth data and then to use that model for categorizing new, unseen data (Bishop, 2006). The model is trained on a dataset that includes both the input features and the corresponding output labels for each observation. In the context of scRNA-seq data, given a set of cells with type labels and their gene expression information, the model can learn the data structure and predict labels for new, unlabeled cells. This can be used to relate cell types across experimental variables. By training a model on one time point, for example, the classifier can be used to transfer those labels onto a different time point. These results can be used to relate cell types across time and to predict how cell types develop and mature.

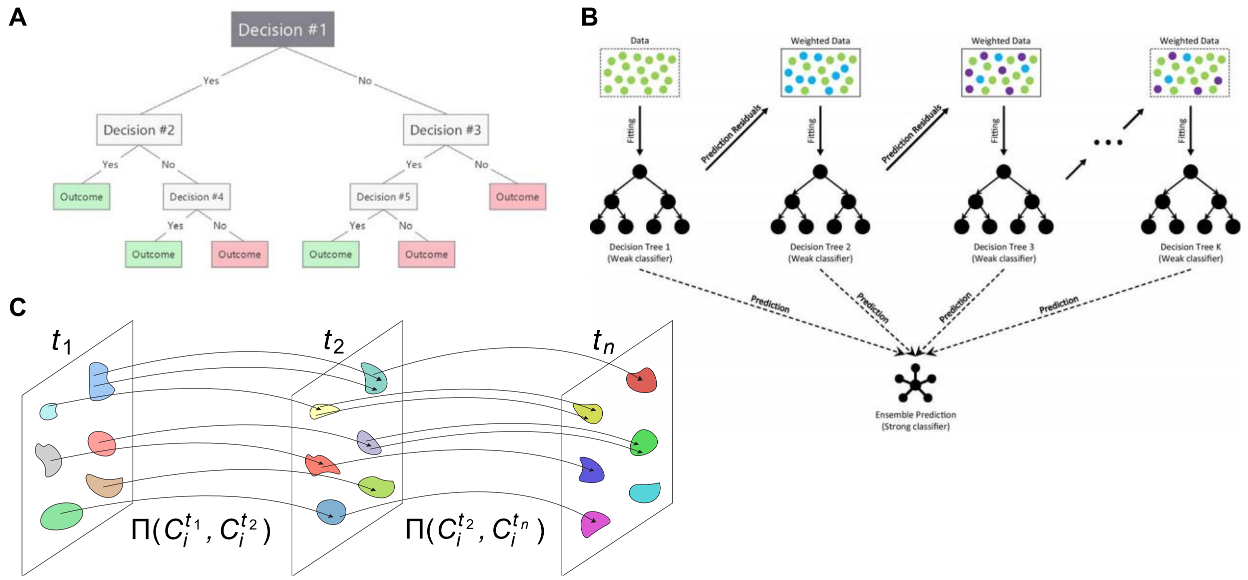

Figure 1.5. Comparing cell types across experimental conditions using supervised classification. (**A**) Decision tree example. (**B**) Ensemble learning with decision trees using boosting (Deng et al., 2021). (**C**) Inference of couplings between cell types across experimental conditions (here, time) using supervised classification.

Many machine learning methods have been used to train supervised classification models, including logistic regression, support vector machines, *k* nearest neighbor graphs, neural networks, and decision trees. Decision trees are especially popular for supervised classification owing to their interpretability and scalability for large datasets (Breiman et al., 1984; Wu et al., 2008). Decision trees model decisions and their possible consequences as a tree-like structure of nodes, branches, and leaves (**Figure 1.5A**). The optimal training of a decision tree is an NP-hard problem (Pitt and Valiant, 1988). Therefore, training is performed using a greedy, top-down learning heuristic—an accessible learning algorithm that yields a theoretically non-optimal decision tree, but close to optimal for practical purposes. At each node, the algorithm selects a feature (gene) and a threshold that best splits the data into pure nodes based on their class (cell type) label. The data is then divided into subsets based on the selected feature and threshold–typically using metrics such as Gini impurity or information gain (Hastie et al., 2009). This process is recursively repeated at each node, creating branches of the tree until a stopping criterion is met. Stopping criteria for decision trees include setting maximum depth, minimum samples per node or split, halting when nodes are pure or further splits offer no improvement, limiting the number of nodes/leaves, and applying post-pruning to decrease tree complexity and minimize overfitting.

Decision trees became especially ubiquitous with the advent of ensemble learning, which leverages the predictions of many models to improve overall performance (Freund and Schapire, 1997; Schapire, 1990). By leveraging the strengths and compensating for the weaknesses of many simple models that would perform poorly individually, ensemble methods can reduce errors and generalize better to unseen data than a single highly complex classifier. The key is that even if the individual models are weak, they should bring complementary information or have diverse error patterns, which the ensemble can exploit to improve overall performance. This diversity helps the ensemble generalize better to unseen data. Rather than take a single model's prediction, the individual models' predictions are combined to create an aggregate vote (Deng et al., 2021). Methods that train many models in parallel and take a majority vote fall under a category known as “bagging” (Breiman, 1996). We utilize a method that leverages the concept of “boosting”, wherein models are trained in series with each model focusing on the errors of the previous models (**Figure 1.5B**).

In each step, boosting adjusts weights associated with each observation. Data points misclassified by previous models are given more weight, forcing the updated model to focus more on these difficult-to-classify points. By focusing on the errors of previous models, the process iteratively yields models that increase in accuracy and generalizability (Freund and Schapire, 1997). In particular, we use a method called extreme gradient boosting (XGBoost), which is a gradient-boosted decision tree-based classification algorithm (Chen and Guestrin, 2016). In a typical workflow, we trained a classifier to learn cluster labels within a “reference” dataset and used it to classify cells from another “test” dataset (**Figure 1.5C**). If the experimental variable is time, for example, this generates a mapping $\Pi\left(C_i^{t_1}, C_i^{t_{n+1}}\right)$ between different time points that enables us to infer cell type maturation.

Spatial and functional characterization of transcriptomic cell types

The application of data analysis and machine learning tools to scRNA-seq data enables i) the identification of transcriptomically distinct putative cell types and ii) the assessment of how experimental variables such as time and rearing conditions affect their gene expression patterns. These analyses generate hypotheses that must be further investigated with independent tools to connect them to the animal's biology. Crucially, the analysis yields marker genes for labeling cell types and enables their characterization. One might be interested in determining if the putative cell types inferred in the computational analysis are distinct cell subpopulations in tissue or if their clustering is an artifact of the scRNA-seq data analysis. To test this, cells in the tissue can be labeled with their markers using fluorescence in situ hybridization (FISH) (Liao et al., 2021; Young et al., 2020). This technique can be used to study how transcriptomically defined cell types are arranged relative to each other and to further assay their morphological properties. Morphological properties include a type's spatial distribution across the cortex, downstream projection areas, and dendritic and axonal synaptic arrangements. These properties can be recorded using techniques such as fluorescence microscopy and electron microscopy, which provides a higher magnification view of a cell's morphology (**Figure 1.6A**). FISH also enables the validation of the influence of certain experimental variables on gene expression as predicted by scRNA-seq. FISH enables the assessment of several genes simultaneously and gives access to the spatial arrangement of expression lacking from bulk profiling methods such as quantitative polymerase chain reaction (qPCR) (Schwarzkopf et al., 2021).

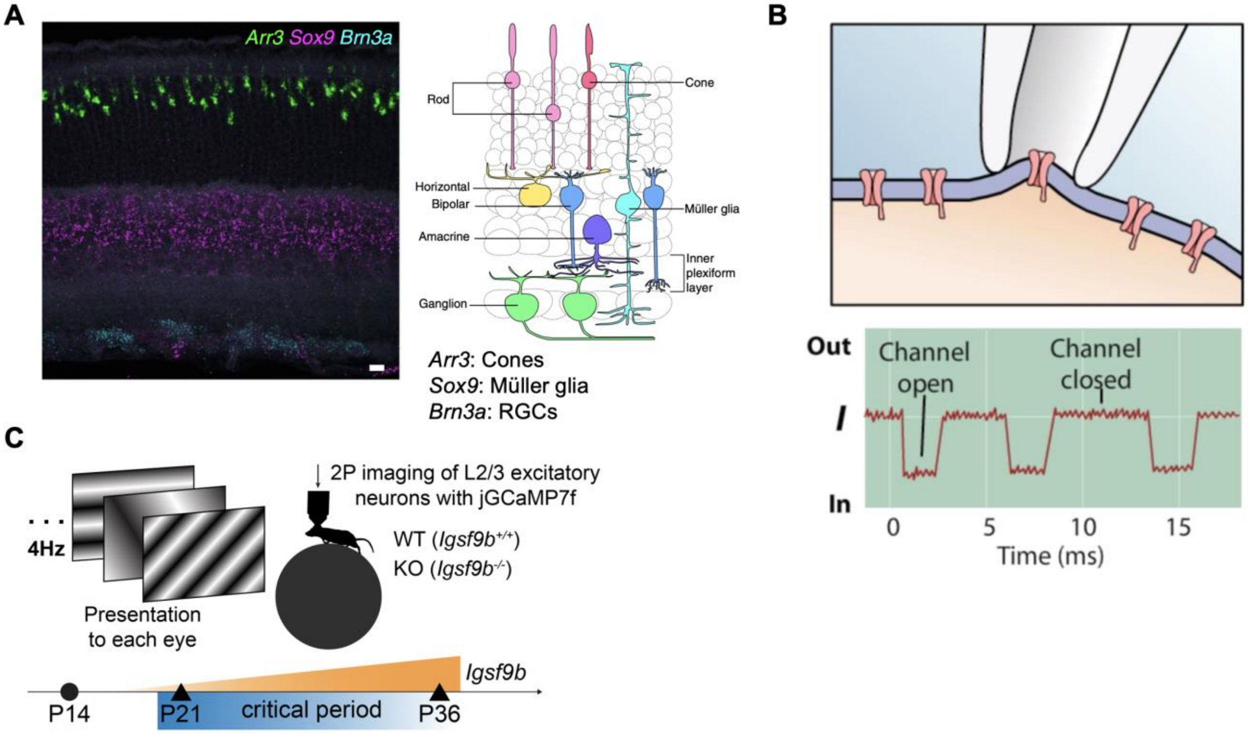

Figure 1.6. Spatial and functional characterization of cell types. (**A**) Example FISH image from the retina (Kishi et al., Nature Methods 2019). **B**) Cell-attached recordings of neuron electrophysiology (Biorender). (**C**) Two-photon imaging of L2/3 neurons in an awake behaving mouse (Cheng et al., 2022).

Cell type markers from scRNA-seq can also be leveraged to generate transgenic mouse lines using genome editing approaches (Navabpour et al., 2020). These techniques allow for targeted genetic access to transcriptomically defined types to further assess their functional properties, including their roles in development, cortical circuits, and animal behavior. After labeling a cell type using its markers, the synaptic physiology of its neurons can be studied using cell-attached recordings from acute tissue slices (**Figure 1.6B)**. Cell-attached recordings preserve the intracellular environment, allowing for the precise measurement of action potentials and synaptic currents without perturbing the cell's internal milieu. This technique involves gently sealing a glass pipette onto the membrane of the labeled cell, allowing for high-resolution recording of spontaneous or evoked activity while maintaining the integrity of the cellular environment. The data generated from these recordings primarily capture capacitive currents associated with action potential generation, offering insights into the timing and frequency of spiking activity. While this method does not measure synaptic currents, which require techniques like whole-cell or perforated patch recording, it can still reveal key aspects of a cell's excitability. If applied across multiple cell types labeled by FISH, these physiological properties can be linked to the transcriptomic profiles of the recorded cells.

Finally, we can interrogate the function of transcriptomically defined cells in awake, behaving animals. This enables chronic measurements of neuron activity to study the influence of variables such as development and rearing conditions on function. Calcium imaging is frequently used to record a neuron's functional properties. When a neuron is active and firing an action potential, voltage-gated calcium channels open in response to the depolarization of its membrane, allowing calcium ions to enter from the extracellular space. The neuron's intracellular calcium concentration rapidly increases. Several calcium indicators have been developed that optically record this calcium influx to track neuron activity (Grienberger et al., 2022; Grienberger and Konnerth, 2012). By expressing these calcium indicators in cell types of interest, calcium transients can be recorded in response to a battery of sensory stimuli (**Figure 1.6C**) (Ayaz et al., 2019; Condylis et al., 2022; Mineault et al., 2016; Ohki et al., 2005; Tan et al., 2020). In the visual cortex, for example, drifting sinusoidal gratings of varying orientations, spatial frequencies, and speeds are used to study orientation selectivity, motion sensitivity, and spatial tuning Flickering checkerboards and complex plaid patterns assess contrast sensitivity and feature integration, while naturalistic scenes and movies mimic real-world visual inputs to explore responses to ecologically relevant stimuli. Sparse noise patterns and white noise are employed for receptive field mapping. For the somatosensory (whisker) cortex, controlled whisker deflections using piezoelectric actuators allow for studying neural tuning to direction, amplitude, and velocity of whisker movements. Textured stimuli test tactile discrimination and air puffs directed at specific whiskers help map receptive fields and assess barrel cortex sensitivity. Thus by combining calcium imaging with genetic access informed by scRNA-seq data, molecular cell type properties can be linked to functional responses and animal behavior.

Molecular maturation of mouse retinal ganglion cell types

The mouse retina was a prominent experimental system for testing the experimental and computational methods outlined above (Macosko et al., 2015). By far the most accessible part of the mammalian brain, the retina is a thin neural tissue that lines the back of the eye and transmits visual input to the rest of the brain to enable vision (**Figure 1.7A-B**) (Dowling, 1987). Because decades of work had generated molecular information about many retinal cell types (Masland, 2012), researchers could confidently compare scRNA-seq data to prior ground truth classification of retinal heterogeneity. Neurons in the vertebrate retina reside in three layers and can be divided into five distinct classes (**Figure 1.7C**). Photoreceptors detect light and convert it into electrical signals. Horizontal cells integrate and regulate input from multiple photoreceptors, enhancing contrast and edge detection. Bipolar cells relay visual signals from photoreceptors to retinal ganglion cells (RGCs) while modulating contrast sensitivity. Amacrine cells mediate lateral interactions in the inner retina, influencing motion detection and the temporal aspects of vision. Finally, RGCs transmit visual information from the retina to the brain *via* the optic nerve. Each class can be further subdivided into morphologically, functionally, and molecularly distinct cell types for a total of 60-140 distinct retinal cell types, depending on species (Baden, 2024; Bae et al., 2018; Shekhar and Sanes, 2021).

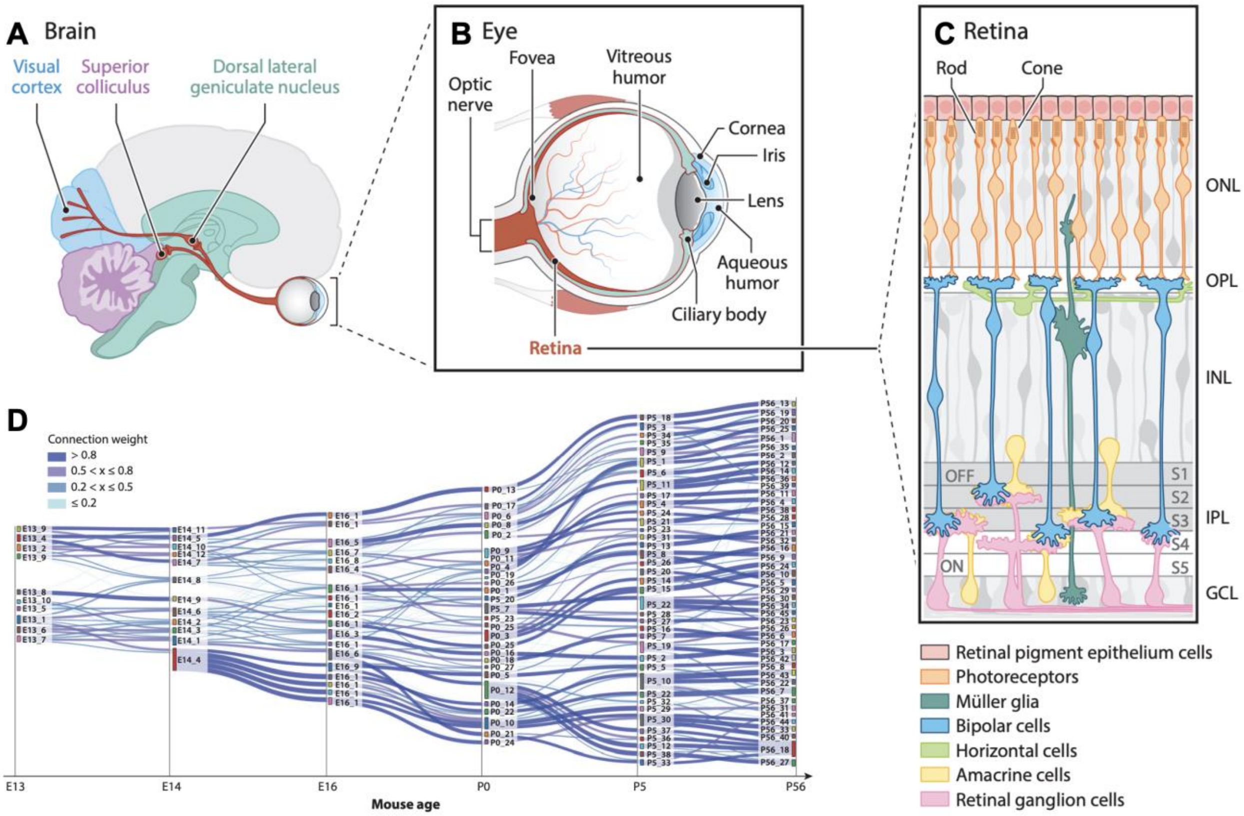

Figure 1.7. Retinal development. (**A**) The components of the visual system. (**B**) The anatomy of the eye, with major tissues highlighted. (**C**) Cross-section of the vertebrate retina showing its major cell classes: photoreceptors (i.e., rods and cones), horizontal cells, bipolar cells, amacrine cells, retinal ganglion cells, and Müller glia. (**D**) Temporal associations among immature retinal ganglion cell clusters (y-axis) between consecutive ages (x-axis) illustrated as a Sankey diagram. Adapted from (Shekhar and Sanes, 2021).

After several studies dissected transcriptomic cell type heterogeneity in each of these classes in adult mammals (Hahn et al., 2023; Peng et al., 2019; Shekhar et al., 2016; Tran et al., 2019; Yan et al., 2020), focus naturally shifted towards understanding how retinal neurons develop from embryonic to postnatal stages using scRNA-seq. Prior to scRNA-seq, retinal cell class development had been the focus of many studies (Bassett and Wallace, 2012; Cepko, 2014). First, lineage tracing in rodents and frogs showed that single retinal progenitor cells (RPCs) are multipotential because they can give rise to any retinal neuron (Holt et al., 1988; Turner et al., 1990; Turner and Cepko, 1987; Wetts and Fraser, 1988). Second, RPC competence to generate neurons of particular classes varies over time, accounting for their sequentially overlapping birth windows (Cepko, 2014; Livesey and Cepko, 2001). Third, studies suggested that competence may be partly probabilistic, with stochastic factors accounting for variations in the distribution of cell classes generated by individual RPCs (Boije et al., 2015; Gomes et al., 2011; Johnston and Desplan, 2010). Early scRNA-seq studies of retinal cell class development revealed differential temporal regulation of gene expression in transcriptomically distinct populations of RPCs (Clark et al., 2019; Lo Giudice et al., 2019). This is consistent with the segregation of birth windows observed in retinal cell classes. In contrast to these well-established dogmas of neuronal class development, far less is known about how immature postmitotic neurons (henceforth "neuronal precursors") committed to a specific retinal class diversify into distinct types. The reason for this lack of resolution was that approximately 80% of retinal cells are rod PRs (Jeon et al., 1998), leaving too few of the less abundant but more diverse neuronal classes to recover rare types or distinguish similar types from each other. In particular, RGCs, the class chiefly responsible for enabling vision, comprise <1% of retinal neurons (Jeon et al., 1998), making it impossible to assay RGC cell type diversification using standard whole-retina scRNA-seq.

To profile them in sufficient numbers, our colleagues enriched RGCs using VGlut2 (glutamate transporter) and Thy1 (CD90), which are broadly expressed in the brain but selectively expressed by RGCs in the retina (Tran et al., 2019). This protocol enabled a detailed characterization of RGC diversity in adult mice. RGC cell type classification using morphology and function had previously identified 30 cell types (Masland, 2012). scRNA-seq applied to enriched RGCs revealed 46 molecular distinct cell types that were then verified using function and morphology (Goetz et al., 2022). We then profiled RGCs at multiple times–from when they first become postmitotic through adulthood (Shekhar et al., 2022). We found no evidence that 46 types of specified progenitors give rise to 46 RGC types. Instead, RGC type identity was acquired gradually, with progressive but incompletely deterministic restriction of fate (**Figure 1.7D**). What remained unknown was the role of postnatal visual experience in diversifying multipotential postmitotic RGCs into discrete types. Would it be largely independent of synaptic input, suggesting primary roles for cell-intrinsic factors and nonsynaptic cell–cell interactions, or dependent on activity-derived signaling pathways that are influenced by visual input? Elucidating the mechanisms that regulate RGC development and underlie the interaction of activity-independent and -dependent influences would be greatly aided by comprehensive characterization of gene expression in developing RGCs in the presence and absence of vision.

Scope of the dissertation

This dissertation will focus on three projects that aim to understand how genetically hardwired developmental mechanisms interact with sensory experience to sculpt molecular cell type identity in three mouse sensory systems. Chapter 2 analyzes the transcriptomic response of RGCs to three distinct visual deprivation paradigms towards disentangling vision-dependent and -independent molecular maturation of 46 RGC types. Chapter 3 profiles the mouse primary visual cortex as a function of normal postnatal development and visual deprivation to determine how early sensory experience influences cell type development. Chapter 4 builds on the findings of the previous two chapters to profile experience-dependent cell type development in primary somatosensory cortex (S1) to gauge if the findings established in V1 can be generalized to other cortical regions corresponding to different sensory organs. Finally, in chapter 5, I discuss the findings of the preceding chapters in a broader neuroscience context while highlighting exciting avenues for future work.

References

Ahlmann-Eltze, C., Huber, W., 2022. Comparison of Transformations for Single-Cell RNA-Seq Data. https://doi.org/10.1101/2021.06.24.449781

Antonini, A., Stryker, M.P., 1993. Rapid remodeling of axonal arbors in the visual cortex. Science 260, 1819–1821. https://doi.org/10.1126/science.8511592

Ayaz, A., Stäuble, A., Hamada, M., Wulf, M.-A., Saleem, A.B., Helmchen, F., 2019. Layer-specific integration of locomotion and sensory information in mouse barrel cortex. Nat Commun 10, 2585. https://doi.org/10.1038/s41467-019-10564-8

Baden, T., 2024. The vertebrate retina: a window into the evolution of computation in the brain. Current Opinion in Behavioral Sciences 57, 101391. https://doi.org/10.1016/j.cobeha.2024.101391

Badia-i-Mompel, P., Wessels, L., Müller-Dott, S., Trimbour, R., Ramirez Flores, R.O., Argelaguet, R., Saez-Rodriguez, J., 2023. Gene regulatory network inference in the era of single-cell multi-omics. Nat Rev Genet 24, 739–754. https://doi.org/10.1038/s41576-023-00618-5

Bae, J.A., Mu, S., Kim, J.S., Turner, N.L., Tartavull, I., Kemnitz, N., Jordan, C.S., Norton, A.D., Silversmith, W.M., Prentki, R., Sorek, M., David, C., Jones, D.L., Bland, D., Sterling, A.L.R., Park, J., Briggman, K.L., Seung, H.S., Eyewirers, 2018. Digital Museum of Retinal Ganglion Cells with Dense Anatomy and Physiology. Cell 173, 1293-1306.e19. https://doi.org/10.1016/j.cell.2018.04.040

Bassett, E.A., Wallace, V.A., 2012. Cell fate determination in the vertebrate retina. Trends Neurosci 35, 565–573. https://doi.org/10.1016/j.tins.2012.05.004

Becht, E., McInnes, L., Healy, J., Dutertre, C.-A., Kwok, I.W.H., Ng, L.G., Ginhoux, F., Newell, E.W., 2019. Dimensionality reduction for visualizing single-cell data using UMAP. Nat Biotechnol 37, 38–44. https://doi.org/10.1038/nbt.4314

Boije, H., Rulands, S., Dudczig, S., Simons, B.D., Harris, W.A., 2015. The Independent Probabilistic Firing of Transcription Factors: A Paradigm for Clonal Variability in the Zebrafish Retina. Dev Cell 34, 532–543. https://doi.org/10.1016/j.devcel.2015.08.011

Bravo González-Blas, C., De Winter, S., Hulselmans, G., Hecker, N., Matetovici, I., Christiaens, V., Poovathingal, S., Wouters, J., Aibar, S., Aerts, S., 2023. SCENIC+: single-cell multiomic inference of enhancers and gene regulatory networks. Nat Methods 1–13. https://doi.org/10.1038/s41592-023-01938-4

Breiman, L., 1996. Bagging predictors. Mach Learn 24, 123–140. https://doi.org/10.1007/BF00058655

Breiman, L., Friedman, J.H., Olshen, R.A., Stone, C.J., 1984. Regression Trees, in: Classification and Regression Trees. Chapman and Hall/CRC.

Brennecke, P., Anders, S., Kim, J.K., Kołodziejczyk, A.A., Zhang, X., Proserpio, V., Baying, B., Benes, V., Teichmann, S.A., Marioni, J.C., Heisler, M.G., 2013. Accounting for technical noise in single-cell RNA-seq experiments. Nat Methods 10, 1093–1095. https://doi.org/10.1038/nmeth.2645

Brüning, R.S., Tombor, L., Schulz, M.H., Dimmeler, S., John, D., 2022. Comparative analysis of common alignment tools for single-cell RNA sequencing. GigaScience 11, giac001. https://doi.org/10.1093/gigascience/giac001

Buenrostro, J.D., Wu, B., Litzenburger, U.M., Ruff, D., Gonzales, M.L., Snyder, M.P., Chang, H.Y., Greenleaf, W.J., 2015. Single-cell chromatin accessibility reveals principles of regulatory variation. Nature 523, 486–490. https://doi.org/10.1038/nature14590

Butrus, S., Sagireddy, S., Yan, W., Shekhar, K., 2023. Defining Selective Neuronal Resilience and Identifying Targets of Neuroprotection and Axon Regeneration Using Single-Cell RNA Sequencing: Computational Approaches, in: Udvadia, A.J., Antczak, J.B. (Eds.), Axon Regeneration: Methods and Protocols. Springer US, New York, NY, pp. 19–41. https://doi.org/10.1007/978-1-0716-3012-9_2

Cepko, C., 2014. Intrinsically different retinal progenitor cells produce specific types of progeny. Nat Rev Neurosci 15, 615–627. https://doi.org/10.1038/nrn3767

Chari, T., Pachter, L., 2023. The specious art of single-cell genomics. PLOS Computational Biology 19, e1011288. https://doi.org/10.1371/journal.pcbi.1011288

Chen, T., Guestrin, C., 2016. XGBoost: A Scalable Tree Boosting System. Proceedings of the 22nd ACM SIGKDD International Conference on Knowledge Discovery and Data Mining 785–794. https://doi.org/10.1145/2939672.2939785

Cheng, S., Butrus, S., Tan, L., Xu, R., Sagireddy, S., Trachtenberg, J.T., Shekhar, K., Zipursky, S.L., 2022. Vision-dependent specification of cell types and function in the developing cortex. Cell 185, 311-327.e24. https://doi.org/10.1016/j.cell.2021.12.022

Chiang, A.-S., Lin, Chih-Yung, Chuang, C.-C., Chang, H.-M., Hsieh, C.-H., Yeh, C.-W., Shih, C.-T., Wu, J.-J., Wang, G.-T., Chen, Y.-C., Wu, Cheng-Chi, Chen, G.-Y., Ching, Y.-T., Lee, P.-C., Lin, Chih-Yang, Lin, H.-H., Wu, Chia-Chou, Hsu, H.-W., Huang, Y.-A., Chen, J.-Y., Chiang, H.-J., Lu, C.-F., Ni, R.-F., Yeh, C.-Y., Hwang, J.-K., 2011. Three-dimensional reconstruction of brain-wide wiring networks in Drosophila at single-cell resolution. Curr Biol 21, 1–11. https://doi.org/10.1016/j.cub.2010.11.056

Christopher M. Bishop, 2006. Pattern Recognition and Machine Learning, 1st ed. Springer New York, NY.

Clark, B.S., Stein-O'Brien, G.L., Shiau, F., Cannon, G.H., Davis-Marcisak, E., Sherman, T., Santiago, C.P., Hoang, T.V., Rajaii, F., James-Esposito, R.E., Gronostajski, R.M., Fertig, E.J., Goff, L.A., Blackshaw, S., 2019. Single-Cell RNA-Seq Analysis of Retinal Development Identifies NFI Factors as Regulating Mitotic Exit and Late-Born Cell Specification. Neuron 102, 1111-1126.e5. https://doi.org/10.1016/j.neuron.2019.04.010

Condylis, C., Ghanbari, A., Manjrekar, N., Bistrong, K., Yao, S., Yao, Z., Nguyen, T.N., Zeng, H., Tasic, B., Chen, J.L., 2022. Dense functional and molecular readout of a circuit hub in sensory cortex. Science 375, eabl5981. https://doi.org/10.1126/science.abl5981

Costa, I.G., 2023. Dissecting gene regulation with multimodal sequencing. Nat Methods 1–3. https://doi.org/10.1038/s41592-023-01957-1

Deng, H., Zhou, Y., Wang, L., Zhang, C., 2021. Ensemble learning for the early prediction of neonatal jaundice with genetic features. BMC Medical Informatics and Decision Making 21, 338. https://doi.org/10.1186/s12911-021-01701-9

Dowling, J.E., 1987. The Retina: An Approachable Part of the Brain. Harvard University Press.

Erzurumlu, R.S., Gaspar, P., 2012. Development and critical period plasticity of the barrel cortex. European Journal of Neuroscience 35, 1540–1553. https://doi.org/10.1111/j.1460-9568.2012.08075.x

Espinosa, J.S., Stryker, M.P., 2012. Development and Plasticity of the Primary Visual Cortex. Neuron 75, 230–249. https://doi.org/10.1016/j.neuron.2012.06.009

Feldman, D.E., Brecht, M., 2005. Map plasticity in somatosensory cortex. Science 310, 810–815. https://doi.org/10.1126/science.1115807

Fishell, G., Heintz, N., 2013. The neuron identity problem: form meets function. Neuron 80, 602–612. https://doi.org/10.1016/j.neuron.2013.10.035

Fox, K., Wong, R.O.L., 2005. A Comparison of Experience-Dependent Plasticity in the Visual and Somatosensory Systems. Neuron 48, 465–477. https://doi.org/10.1016/j.neuron.2005.10.013

Franke, K., Berens, P., Schubert, T., Bethge, M., Euler, T., Baden, T., 2017. Inhibition decorrelates visual feature representations in the inner retina. Nature 542, 439–444. https://doi.org/10.1038/nature21394

Freund, Y., Schapire, R.E., 1997. A Decision-Theoretic Generalization of On-Line Learning and an Application to Boosting. Journal of Computer and System Sciences 55, 119–139. https://doi.org/10.1006/jcss.1997.1504

Gainey, M.A., Aman, J.W., Feldman, D.E., 2018. Rapid Disinhibition by Adjustment of PV Intrinsic Excitability during Whisker Map Plasticity in Mouse S1. J. Neurosci. 38, 4749–4761. https://doi.org/10.1523/JNEUROSCI.3628-17.2018

Goetz, J., Jessen, Z.F., Jacobi, A., Mani, A., Cooler, S., Greer, D., Kadri, S., Segal, J., Shekhar, K., Sanes, J.R., Schwartz, G.W., 2022. Unified classification of mouse retinal ganglion cells using function, morphology, and gene expression. Cell Rep 40, 111040. https://doi.org/10.1016/j.celrep.2022.111040

Gomes, F.L.A.F., Zhang, G., Carbonell, F., Correa, J.A., Harris, W.A., Simons, B.D., Cayouette, M., 2011. Reconstruction of rat retinal progenitor cell lineages in vitro reveals a surprising degree of stochasticity in cell fate decisions. Development 138, 227–235. https://doi.org/10.1242/dev.059683

Gordon, J.A., Stryker, M.P., 1996. Experience-dependent plasticity of binocular responses in the primary visual cortex of the mouse. J Neurosci 16, 3274–3286. https://doi.org/10.1523/JNEUROSCI.16-10-03274.1996

Gorin, G., Fang, M., Chari, T., Pachter, L., 2022. RNA velocity unraveled. PLOS Computational Biology 18, e1010492. https://doi.org/10.1371/journal.pcbi.1010492

Gouwens, N.W., Sorensen, S.A., Berg, J., Lee, C., Jarsky, T., Ting, J., Sunkin, S.M., Feng, D., Anastassiou, C.A., Barkan, E., Bickley, K., Blesie, N., Braun, T., Brouner, K., Budzillo, A., Caldejon, S., Casper, T., Castelli, D., Chong, P., Crichton, K., Cuhaciyan, C., Daigle, T.L., Dalley, R., Dee, N., Desta, T., Ding, S.-L., Dingman, S., Doperalski, A., Dotson, N., Egdorf, T., Fisher, M., de Frates, R.A., Garren, E., Garwood, M., Gary, A., Gaudreault, N., Godfrey, K., Gorham, M., Gu, H., Habel, C., Hadley, K., Harrington, J., Harris, J.A., Henry, A., Hill, D., Josephsen, S., Kebede, S., Kim, L., Kroll, M., Lee, B., Lemon, T., Link, K.E., Liu, X., Long, B., Mann, R., McGraw, M., Mihalas, S., Mukora, A., Murphy, G.J., Ng, Lindsay, Ngo, K., Nguyen, T.N., Nicovich, P.R., Oldre, A., Park, D., Parry, S., Perkins, J., Potekhina, L., Reid, D., Robertson, M., Sandman, D., Schroedter, M., Slaughterbeck, C., Soler-Llavina, G., Sulc, J., Szafer, A., Tasic, B., Taskin, N., Teeter, C., Thatra, N., Tung, H., Wakeman, W., Williams, G., Young, R., Zhou, Z., Farrell, C., Peng, H., Hawrylycz, M.J., Lein, E., Ng, Lydia, Arkhipov, A., Bernard, A., Phillips, J.W., Zeng, H., Koch, C., 2019. Classification of electrophysiological and morphological neuron types in the mouse visual cortex. Nat Neurosci 22, 1182–1195. https://doi.org/10.1038/s41593-019-0417-0

Grienberger, C., Giovannucci, A., Zeiger, W., Portera-Cailliau, C., 2022. Two-photon calcium imaging of neuronal activity. Nat Rev Methods Primers 2, 67. https://doi.org/10.1038/s43586-022-00147-1

Grienberger, C., Konnerth, A., 2012. Imaging Calcium in Neurons. Neuron 73, 862–885. https://doi.org/10.1016/j.neuron.2012.02.011

Habib, N., Avraham-Davidi, I., Basu, A., Burks, T., Shekhar, K., Hofree, M., Choudhury, S.R., Aguet, F., Gelfand, E., Ardlie, K., Weitz, D.A., Rozenblatt-Rosen, O., Zhang, F., Regev, A., 2017. Massively parallel single-nucleus RNA-seq with DroNc-seq. Nat Methods 14, 955–958. https://doi.org/10.1038/nmeth.4407

Hahn, J., Monavarfeshani, A., Qiao, M., Kao, A.H., Kölsch, Y., Kumar, A., Kunze, V.P., Rasys, A.M., Richardson, R., Wekselblatt, J.B., Baier, H., Lucas, R.J., Li, W., Meister, M., Trachtenberg, J.T., Yan, W., Peng, Y.-R., Sanes, J.R., Shekhar, K., 2023. Evolution of neuronal cell classes and types in the vertebrate retina. Nature 624, 415–424. https://doi.org/10.1038/s41586-023-06638-9

Hastie, T., Tibshirani, R., Friedman, J., 2009. Boosting and Additive Trees, in: Hastie, T., Tibshirani, R., Friedman, J. (Eds.), The Elements of Statistical Learning: Data Mining, Inference, and Prediction. Springer, New York, NY, pp. 337–387. https://doi.org/10.1007/978-0-387-84858-7_10

Herring, C.A., Simmons, R.K., Freytag, S., Poppe, D., Moffet, J.J.D., Pflueger, J., Buckberry, S., Vargas-Landin, D.B., Clément, O., Echeverría, E.G., Sutton, G.J., Alvarez-Franco, A., Hou, R., Pflueger, C., McDonald, K., Polo, J.M., Forrest, A.R.R., Nowak, A.K., Voineagu, I., Martelotto, L., Lister, R., 2022. Human prefrontal cortex gene regulatory dynamics from gestation to adulthood at single-cell resolution. Cell 185, 4428-4447.e28. https://doi.org/10.1016/j.cell.2022.09.039

Heumos, L., Schaar, A.C., Lance, C., Litinetskaya, A., Drost, F., Zappia, L., Lücken, M.D., Strobl, D.C., Henao, J., Curion, F., Schiller, H.B., Theis, F.J., 2023. Best practices for single-cell analysis across modalities. Nat Rev Genet 1–23. https://doi.org/10.1038/s41576-023-00586-w

Hie, B., Peters, J., Nyquist, S.K., Shalek, A.K., Berger, B., Bryson, B.D., 2020. Computational Methods for Single-Cell RNA Sequencing. Annu. Rev. Biomed. Data Sci. 3, 339–364. https://doi.org/10.1146/annurev-biodatasci-012220-100601

Holt, C.E., Bertsch, T.W., Ellis, H.M., Harris, W.A., 1988. Cellular determination in the Xenopus retina is independent of lineage and birth date. Neuron 1, 15–26. https://doi.org/10.1016/0896-6273(88)90205-x

Hooks, B.M., Chen, C., 2020. Circuitry Underlying Experience-Dependent Plasticity in the Mouse Visual System. Neuron 106, 21–36. https://doi.org/10.1016/j.neuron.2020.01.031

Hrvatin, S., Hochbaum, D.R., Nagy, M.A., Cicconet, M., Robertson, K., Cheadle, L., Zilionis, R., Ratner, A., Borges-Monroy, R., Klein, A.M., Sabatini, B.L., Greenberg, M.E., 2018. Single-cell analysis of experience-dependent transcriptomic states in the mouse visual cortex. Nat Neurosci 21, 120–129. https://doi.org/10.1038/s41593-017-0029-5

Hubel, D.H., Wiesel, T.N., 1969. Anatomical demonstration of columns in the monkey striate cortex. Nature 221, 747–750. https://doi.org/10.1038/221747a0

Hubel, D.H., Wiesel, T.N., 1962. Receptive fields, binocular interaction and functional architecture in the cat's visual cortex. J Physiol 160, 106–154. https://doi.org/10.1113/jphysiol.1962.sp006837

Hubel, D.H., Wiesel, T.N., LeVay, S., 1977. Plasticity of ocular dominance columns in monkey striate cortex. Philos Trans R Soc Lond B Biol Sci 278, 377–409. https://doi.org/10.1098/rstb.1977.0050

James, W., 1890. The Principles of Psychology. H. Holt.

Jeon, C.J., Strettoi, E., Masland, R.H., 1998. The major cell populations of the mouse retina. J Neurosci 18, 8936–8946. https://doi.org/10.1523/JNEUROSCI.18-21-08936.1998

Johnston, R.J., Desplan, C., 2010. Stochastic mechanisms of cell fate specification that yield random or robust outcomes. Annu Rev Cell Dev Biol 26, 689–719. https://doi.org/10.1146/annurev-cellbio-100109-104113

Kartha, V.K., Duarte, F.M., Hu, Y., Ma, S., Chew, J.G., Lareau, C.A., Earl, A., Burkett, Z.D., Kohlway, A.S., Lebofsky, R., Buenrostro, J.D., 2022. Functional inference of gene regulation using single-cell multi-omics. Cell Genomics 2. https://doi.org/10.1016/j.xgen.2022.100166

Klemm, S.L., Shipony, Z., Greenleaf, W.J., 2019. Chromatin accessibility and the regulatory epigenome. Nat Rev Genet 20, 207–220. https://doi.org/10.1038/s41576-018-0089-8

Ko, H., Cossell, L., Baragli, C., Antolik, J., Clopath, C., Hofer, S.B., Mrsic-Flogel, T.D., 2013. The emergence of functional microcircuits in visual cortex. Nature 496, 96–100. https://doi.org/10.1038/nature12015

Ko, H., Mrsic-Flogel, T.D., Hofer, S.B., 2014. Emergence of feature-specific connectivity in cortical microcircuits in the absence of visual experience. J Neurosci 34, 9812–9816. https://doi.org/10.1523/JNEUROSCI.0875-14.2014

Kole, K., Komuro, Y., Provaznik, J., Pistolic, J., Benes, V., Tiesinga, P., Celikel, T., 2017. Transcriptional mapping of the primary somatosensory cortex upon sensory deprivation. GigaScience 6, gix081. https://doi.org/10.1093/gigascience/gix081

Kölsch, Y., Hahn, J., Sappington, A., Stemmer, M., Fernandes, A.M., Helmbrecht, T.O., Lele, S., Butrus, S., Laurell, E., Arnold-Ammer, I., Shekhar, K., Sanes, J.R., Baier, H., 2021. Molecular classification of zebrafish retinal ganglion cells links genes to cell types to behavior. Neuron 109, 645-662.e9. https://doi.org/10.1016/j.neuron.2020.12.003

Korsunsky, I., Millard, N., Fan, J., Slowikowski, K., Zhang, F., Wei, K., Baglaenko, Y., Brenner, M., Loh, P., Raychaudhuri, S., 2019. Fast, sensitive and accurate integration of single-cell data with Harmony. Nat Methods 16, 1289–1296. https://doi.org/10.1038/s41592-019-0619-0

Lause, J., Kobak, D., Berens, P., 2024. The art of seeing the elephant in the room: 2D embeddings of single-cell data do make sense. bioRxiv 2024.03.26.586728. https://doi.org/10.1101/2024.03.26.586728

Lendvai, B., Stern, E.A., Chen, B., Svoboda, K., 2000. Experience-dependent plasticity of dendritic spines in the developing rat barrel cortex in vivo. Nature 404, 876–881. https://doi.org/10.1038/35009107

LeVay, S., Hubel, D.H., Wiesel, T.N., 1975. The pattern of ocular dominance columns in macaque visual cortex revealed by a reduced silver stain. J Comp Neurol 159, 559–576. https://doi.org/10.1002/cne.901590408

Liao, J., Lu, X., Shao, X., Zhu, L., Fan, X., 2021. Uncovering an Organ’s Molecular Architecture at Single-Cell Resolution by Spatially Resolved Transcriptomics. Trends in Biotechnology 39, 43–58. https://doi.org/10.1016/j.tibtech.2020.05.006

Livesey, F.J., Cepko, C.L., 2001. Vertebrate neural cell-fate determination: lessons from the retina. Nat Rev Neurosci 2, 109–118. https://doi.org/10.1038/35053522

Lo Giudice, Q., Leleu, M., La Manno, G., Fabre, P.J., 2019. Single-cell transcriptional logic of cell-fate specification and axon guidance in early-born retinal neurons. Development 146, dev178103. https://doi.org/10.1242/dev.178103

Luecken, M.D., Büttner, M., Chaichoompu, K., Danese, A., Interlandi, M., Mueller, M.F., Strobl, D.C., Zappia, L., Dugas, M., Colomé-Tatché, M., Theis, F.J., 2022. Benchmarking atlas-level data integration in single-cell genomics. Nat Methods 19, 41–50. https://doi.org/10.1038/s41592-021-01336-8

Lyckman, A.W., Horng, S., Leamey, C.A., Tropea, D., Watakabe, A., Van Wart, A., McCurry, C., Yamamori, T., Sur, M., 2008. Gene expression patterns in visual cortex during the critical period: synaptic stabilization and reversal by visual deprivation. Proc Natl Acad Sci U S A 105, 9409–9414. https://doi.org/10.1073/pnas.0710172105

Macosko, E.Z., Basu, A., Satija, R., Nemesh, J., Shekhar, K., Goldman, M., Tirosh, I., Bialas, A.R., Kamitaki, N., Martersteck, E.M., Trombetta, J.J., Weitz, D.A., Sanes, J.R., Shalek, A.K., Regev, A., McCarroll, S.A., 2015. Highly Parallel Genome-wide Expression Profiling of Individual Cells Using Nanoliter Droplets. Cell 161, 1202–1214. https://doi.org/10.1016/j.cell.2015.05.002

Majdan, M., Shatz, C.J., 2006. Effects of visual experience on activity-dependent gene regulation in cortex. Nat Neurosci 9, 650–659. https://doi.org/10.1038/nn1674

Maravall, M., Koh, I.Y.Y., Lindquist, W.B., Svoboda, K., 2004. Experience-dependent Changes in Basal Dendritic Branching of Layer 2/3 Pyramidal Neurons During a Critical Period for Developmental Plasticity in Rat Barrel Cortex. Cerebral Cortex 14, 655–664. https://doi.org/10.1093/cercor/bhh026

Mardinly, A.R., Spiegel, I., Patrizi, A., Centofante, E., Bazinet, J.E., Tzeng, C.P., Mandel-Brehm, C., Harmin, D.A., Adesnik, H., Fagiolini, M., Greenberg, M.E., 2016. Sensory experience regulates cortical inhibition by inducing IGF1 in VIP neurons. Nature 531, 371–375. https://doi.org/10.1038/nature17187

Markram, H., Muller, E., Ramaswamy, S., Reimann, M.W., Abdellah, M., Sanchez, C.A., Ailamaki, A., Alonso-Nanclares, L., Antille, N., Arsever, S., Kahou, G.A.A., Berger, T.K., Bilgili, A., Buncic, N., Chalimourda, A., Chindemi, G., Courcol, J.-D., Delalondre, F., Delattre, V., Druckmann, S., Dumusc, R., Dynes, J., Eilemann, S., Gal, E., Gevaert, M.E., Ghobril, J.-P., Gidon, A., Graham, J.W., Gupta, A., Haenel, V., Hay, E., Heinis, T., Hernando, J.B., Hines, M., Kanari, L., Keller, D., Kenyon, J., Khazen, G., Kim, Y., King, J.G., Kisvarday, Z., Kumbhar, P., Lasserre, S., Le Bé, J.-V., Magalhães, B.R.C., Merchán-Pérez, A., Meystre, J., Morrice, B.R., Muller, J., Muñoz-Céspedes, A., Muralidhar, S., Muthurasa, K., Nachbaur, D., Newton, T.H., Nolte, M., Ovcharenko, A., Palacios, J., Pastor, L., Perin, R., Ranjan, R., Riachi, I., Rodríguez, J.-R., Riquelme, J.L., Rössert, C., Sfyrakis, K., Shi, Y., Shillcock, J.C., Silberberg, G., Silva, R., Tauheed, F., Telefont, M., Toledo-Rodriguez, M., Tränkler, T., Van Geit, W., Díaz, J.V., Walker, R., Wang, Y., Zaninetta, S.M., DeFelipe, J., Hill, S.L., Segev, I., Schürmann, F., 2015. Reconstruction and Simulation of Neocortical Microcircuitry. Cell 163, 456–492. https://doi.org/10.1016/j.cell.2015.09.029

Masland, R.H., 2012. The neuronal organization of the retina. Neuron 76, 266–280. https://doi.org/10.1016/j.neuron.2012.10.002

McInnes, L., Healy, J., Melville, J., 2020. UMAP: Uniform Manifold Approximation and Projection for Dimension Reduction. arXiv:1802.03426 [cs, stat].

Migliore, M., Shepherd, G.M., 2005. Opinion: an integrated approach to classifying neuronal phenotypes. Nat Rev Neurosci 6, 810–818. https://doi.org/10.1038/nrn1769

Mineault, P.J., Tring, E., Trachtenberg, J.T., Ringach, D.L., 2016. Enhanced Spatial Resolution During Locomotion and Heightened Attention in Mouse Primary Visual Cortex. J. Neurosci. 36, 6382–6392. https://doi.org/10.1523/JNEUROSCI.0430-16.2016

Navabpour, S., Kwapis, J.L., Jarome, T.J., 2020. A neuroscientist's guide to transgenic mice and other genetic tools. Neuroscience & Biobehavioral Reviews 108, 732–748. https://doi.org/10.1016/j.neubiorev.2019.12.013

Ohki, K., Chung, S., Ch'ng, Y.H., Kara, P., Reid, R.C., 2005. Functional imaging with cellular resolution reveals precise micro-architecture in visual cortex. Nature 433, 597–603. https://doi.org/10.1038/nature03274

Oray, S., Majewska, A., Sur, M., 2004. Dendritic spine dynamics are regulated by monocular deprivation and extracellular matrix degradation. Neuron 44, 1021–1030. https://doi.org/10.1016/j.neuron.2004.12.001

Peng, Y.-R., Shekhar, K., Yan, W., Herrmann, D., Sappington, A., Bryman, G.S., van Zyl, T., Do, M.T.H., Regev, A., Sanes, J.R., 2019. Molecular Classification and Comparative Taxonomics of Foveal and Peripheral Cells in Primate Retina. Cell 176, 1222-1237.e22. https://doi.org/10.1016/j.cell.2019.01.004

Pitt, L., Valiant, L.G., 1988. Computational limitations on learning from examples. J. ACM 35, 965–984. https://doi.org/10.1145/48014.63140

Ramón y Cajal, S., Ramón y Cajal, S., 1909. Histologie du système nerveux de l'homme & des vertébrés, Ed. française rev. & mise à jour par l'auteur, tr. de l'espagnol par L. Azoulay. ed. Maloine, Paris. https://doi.org/10.5962/bhl.title.48637

Rosenzweig, M.R., 1996. Aspects of the search for neural mechanisms of memory. Annu Rev Psychol 47, 1–32. https://doi.org/10.1146/annurev.psych.47.1.1

Sarkar, A., Stephens, M., 2021. Separating measurement and expression models clarifies confusion in single-cell RNA sequencing analysis. Nat Genet 53, 770–777. https://doi.org/10.1038/s41588-021-00873-4

Sarropoulos, I., Sepp, M., Frömel, R., Leiss, K., Trost, N., Leushkin, E., Okonechnikov, K., Joshi, P., Giere, P., Kutscher, L.M., Cardoso-Moreira, M., Pfister, S.M., Kaessmann, H., 2021. Developmental and evolutionary dynamics of cis-regulatory elements in mouse cerebellar cells. Science 373, eabg4696. https://doi.org/10.1126/science.abg4696

Satija, R., Farrell, J.A., Gennert, D., Schier, A.F., Regev, A., 2015. Spatial reconstruction of single-cell gene expression data. Nat Biotechnol 33, 495–502. https://doi.org/10.1038/nbt.3192

Schapire, R.E., 1990. The strength of weak learnability. Mach Learn 5, 197–227. https://doi.org/10.1007/BF00116037

Schwarzkopf, M., Liu, M.C., Schulte, S.J., Ives, R., Husain, N., Choi, H.M.T., Pierce, N.A., 2021. Hybridization chain reaction enables a unified approach to multiplexed, quantitative, high-resolution immunohistochemistry and in situ hybridization. Development 148, dev199847. https://doi.org/10.1242/dev.199847

Shekhar, K., Lapan, S.W., Whitney, I.E., Tran, N.M., Macosko, E.Z., Kowalczyk, M., Adiconis, X., Levin, J.Z., Nemesh, J., Goldman, M., McCarroll, S.A., Cepko, C.L., Regev, A., Sanes, J.R., 2016. Comprehensive Classification of Retinal Bipolar Neurons by Single-Cell Transcriptomics. Cell 166, 1308-1323.e30. https://doi.org/10.1016/j.cell.2016.07.054

Shekhar, K., Sanes, J.R., 2021. Generating and Using Transcriptomically Based Retinal Cell Atlases. Annual Review of Vision Science 7, 43–72. https://doi.org/10.1146/annurev-vision-032621-075200

Shekhar, K., Whitney, I.E., Butrus, S., Peng, Y.-R., Sanes, J.R., 2022. Diversification of multipotential postmitotic mouse retinal ganglion cell precursors into discrete types. eLife 11, e73809. https://doi.org/10.7554/eLife.73809

Stern, E.A., Maravall, M., Svoboda, K., 2001. Rapid Development and Plasticity of Layer 2/3 Maps in Rat Barrel Cortex In Vivo. Neuron 31, 305–315. https://doi.org/10.1016/S0896-6273(01)00360-9

Svensson, V., Vento-Tormo, R., Teichmann, S.A., 2018. Exponential scaling of single-cell RNA-seq in the past decade. Nat Protoc 13, 599–604. https://doi.org/10.1038/nprot.2017.149

Swanson, L.W., Lichtman, J.W., 2016. From Cajal to Connectome and Beyond. Annu Rev Neurosci 39, 197–216. https://doi.org/10.1146/annurev-neuro-071714-033954

Tan, L., Ringach, D.L., Zipursky, S.L., Trachtenberg, J.T., 2021. Vision is required for the formation of binocular neurons prior to the classical critical period. Curr Biol 31, 4305-4313.e5. https://doi.org/10.1016/j.cub.2021.07.053

Tan, L., Tring, E., Ringach, D.L., Zipursky, S.L., Trachtenberg, J.T., 2020. Vision Changes the Cellular Composition of Binocular Circuitry during the Critical Period. Neuron 108, 735-747.e6. https://doi.org/10.1016/j.neuron.2020.09.022

Tasic, B., Yao, Z., Graybuck, L.T., Smith, K.A., Nguyen, T.N., Bertagnolli, D., Goldy, J., Garren, E., Economo, M.N., Viswanathan, S., Penn, O., Bakken, T., Menon, V., Miller, J., Fong, O., Hirokawa, K.E., Lathia, K., Rimorin, C., Tieu, M., Larsen, R., Casper, T., Barkan, E., Kroll, M., Parry, S., Shapovalova, N.V., Hirschstein, D., Pendergraft, J., Sullivan, H.A., Kim, T.K., Szafer, A., Dee, N., Groblewski, P., Wickersham, I., Cetin, A., Harris, J.A., Levi, B.P., Sunkin, S.M., Madisen, L., Daigle, T.L., Looger, L., Bernard, A., Phillips, J., Lein, E., Hawrylycz, M., Svoboda, K., Jones, A.R., Koch, C., Zeng, H., 2018. Shared and distinct transcriptomic cell types across neocortical areas. Nature 563, 72–78. https://doi.org/10.1038/s41586-018-0654-5

Traag, V.A., Waltman, L., van Eck, N.J., 2019. From Louvain to Leiden: guaranteeing well-connected communities. Sci Rep 9, 5233. https://doi.org/10.1038/s41598-019-41695-z

Tran, N.M., Shekhar, K., Whitney, I.E., Jacobi, A., Benhar, I., Hong, G., Yan, W., Adiconis, X., Arnold, M.E., Lee, J.M., Levin, J.Z., Lin, D., Wang, C., Lieber, C.M., Regev, A., He, Z., Sanes, J.R., 2019. Single-Cell Profiles of Retinal Ganglion Cells Differing in Resilience to Injury Reveal Neuroprotective Genes. Neuron 104, 1039-1055.e12. https://doi.org/10.1016/j.neuron.2019.11.006

Tropea, D., Kreiman, G., Lyckman, A., Mukherjee, S., Yu, H., Horng, S., Sur, M., 2006. Gene expression changes and molecular pathways mediating activity-dependent plasticity in visual cortex. Nat Neurosci 9, 660–668. https://doi.org/10.1038/nn1689

Turner, D.L., Cepko, C.L., 1987. A common progenitor for neurons and glia persists in rat retina late in development. Nature 328, 131–136. https://doi.org/10.1038/328131a0

Turner, D.L., Snyder, E.Y., Cepko, C.L., 1990. Lineage-independent determination of cell type in the embryonic mouse retina. Neuron 4, 833–845. https://doi.org/10.1016/0896-6273(90)90136-4

Tyner, C.F., 1975. The naming of neurons: applications of taxonomic theory to the study of cellular populations. Brain Behav Evol 12, 75–96. https://doi.org/10.1159/000124141

Varshney, L.R., Chen, B.L., Paniagua, E., Hall, D.H., Chklovskii, D.B., 2011. Structural properties of the Caenorhabditis elegans neuronal network. PLoS Comput Biol 7, e1001066. https://doi.org/10.1371/journal.pcbi.1001066

Vu, H., n.d. Unsupervised contrastive peak caller for ATAC-seq [WWW Document]. URL https://genome.cshlp.org/content/33/7/1133 (accessed 10.13.24).

Wen, J.A., Barth, A.L., 2011. Input-specific critical periods for experience-dependent plasticity in layer 2/3 pyramidal neurons. J Neurosci 31, 4456–4465. https://doi.org/10.1523/JNEUROSCI.6042-10.2011

Wetts, R., Fraser, S.E., 1988. Multipotent precursors can give rise to all major cell types of the frog retina. Science 239, 1142–1145. https://doi.org/10.1126/science.2449732

Wiesel, T.N., Hubel, D.H., 1963. SINGLE-CELL RESPONSES IN STRIATE CORTEX OF KITTENS DEPRIVED OF VISION IN ONE EYE. J Neurophysiol 26, 1003–1017. https://doi.org/10.1152/jn.1963.26.6.1003

Wolock, S.L., Lopez, R., Klein, A.M., 2019. Scrublet: Computational Identification of Cell Doublets in Single-Cell Transcriptomic Data. Cell Syst 8, 281-291.e9. https://doi.org/10.1016/j.cels.2018.11.005

Wu, X., Kumar, V., Ross Quinlan, J., Ghosh, J., Yang, Q., Motoda, H., McLachlan, G.J., Ng, A., Liu, B., Yu, P.S., Zhou, Z.-H., Steinbach, M., Hand, D.J., Steinberg, D., 2008. Top 10 algorithms in data mining. Knowl Inf Syst 14, 1–37. https://doi.org/10.1007/s10115-007-0114-2

y Cajal, Santiago Ramon, 1899. Comparative study of the sensory areas of the human cortex. Clark University.

Yan, F., Powell, D.R., Curtis, D.J., Wong, N.C., 2020. From reads to insight: a hitchhiker’s guide to ATAC-seq data analysis. Genome Biology 21, 22. https://doi.org/10.1186/s13059-020-1929-3

Yan, W., Laboulaye, M.A., Tran, N.M., Whitney, I.E., Benhar, I., Sanes, J.R., 2020. Mouse Retinal Cell Atlas: Molecular Identification of over Sixty Amacrine Cell Types. J Neurosci 40, 5177–5195. https://doi.org/10.1523/JNEUROSCI.0471-20.2020

Yates, A.D., Achuthan, P., Akanni, W., Allen, James, Allen, Jamie, Alvarez-Jarreta, J., Amode, M.R., Armean, I.M., Azov, A.G., Bennett, R., Bhai, J., Billis, K., Boddu, S., Marugán, J.C., Cummins, C., Davidson, C., Dodiya, K., Fatima, R., Gall, A., Giron, C.G., Gil, L., Grego, T., Haggerty, L., Haskell, E., Hourlier, T., Izuogu, O.G., Janacek, S.H., Juettemann, T., Kay, M., Lavidas, I., Le, T., Lemos, D., Martinez, J.G., Maurel, T., McDowall, M., McMahon, A., Mohanan, S., Moore, B., Nuhn, M., Oheh, D.N., Parker, A., Parton, A., Patricio, M., Sakthivel, M.P., Abdul Salam, A.I., Schmitt, B.M., Schuilenburg, H., Sheppard, D., Sycheva, M., Szuba, M., Taylor, K., Thormann, A., Threadgold, G., Vullo, A., Walts, B., Winterbottom, A., Zadissa, A., Chakiachvili, M., Flint, B., Frankish, A., Hunt, S.E., IIsley, G., Kostadima, M., Langridge, N., Loveland, J.E., Martin, F.J., Morales, J., Mudge, J.M., Muffato, M., Perry, E., Ruffier, M., Trevanion, S.J., Cunningham, F., Howe, K.L., Zerbino, D.R., Flicek, P., 2020. Ensembl 2020. Nucleic Acids Research 48, D682–D688. https://doi.org/10.1093/nar/gkz966

Young, A.P., Jackson, D.J., Wyeth, R.C., 2020. A technical review and guide to RNA fluorescence in situ hybridization. PeerJ 8, e8806. https://doi.org/10.7717/peerj.8806

Yu, L., Cao, Y., Yang, J.Y.H., Yang, P., 2022. Benchmarking clustering algorithms on estimating the number of cell types from single-cell RNA-sequencing data. Genome Biology 23, 49. https://doi.org/10.1186/s13059-022-02622-0

Zanatta, A., Cherici, C., Bargoni, A., Buzzi, S., Cani, V., Mazzarello, P., Zampieri, F., 2018. Vincenzo Malacarne (1744–1816) and the First Description of the Human Cerebellum. Cerebellum 17, 461–464. https://doi.org/10.1007/s12311-018-0932-7

Zeng, H., 2022. What is a cell type and how to define it? Cell 185, 2739–2755. https://doi.org/10.1016/j.cell.2022.06.031

Zeng, H., Sanes, J.R., 2017. Neuronal cell-type classification: challenges, opportunities and the path forward. Nat Rev Neurosci 18, 530–546. https://doi.org/10.1038/nrn.2017.85

Zheng, G.X.Y., Terry, J.M., Belgrader, P., Ryvkin, P., Bent, Z.W., Wilson, R., Ziraldo, S.B., Wheeler, T.D., McDermott, G.P., Zhu, J., Gregory, M.T., Shuga, J., Montesclaros, L., Underwood, J.G., Masquelier, D.A., Nishimura, S.Y., Schnall-Levin, M., Wyatt, P.W., Hindson, C.M., Bharadwaj, R., Wong, A., Ness, K.D., Beppu, L.W., Deeg, H.J., McFarland, C., Loeb, K.R., Valente, W.J., Ericson, N.G., Stevens, E.A., Radich, J.P., Mikkelsen, T.S., Hindson, B.J., Bielas, J.H., 2017. Massively parallel digital transcriptional profiling of single cells. Nat Commun 8, 14049. https://doi.org/10.1038/ncomms14049

Chapter 2: Vision-dependent and-independent molecular maturation of mouse retinal ganglion cells

This chapter is adapted from the following published work:

Irene E. Whitney*, **Salwan Butrus***, Michael A. Dyer, Fred Rieke, Joshua R. Sanes#, Karthik Shekhar#. Vision-dependent and -independent molecular maturation of mouse retinal ganglion cells. *Neuroscience*, **508**, 153-173 (2023).

* Equal contribution
\# Corresponding authors

I.W. performed all scRNA-seq experiments and F.R. performed all recordings. S.B. and K.S. performed all computational analyses.

Abstract

The development and connectivity of retinal ganglion cells (RGCs), the retina's sole output neurons, are patterned by activity-independent transcriptional programs and activity-dependent remodeling. To inventory the molecular correlates of these influences, we applied high-throughput single-cell RNA sequencing (scRNA-seq) to mouse RGCs at six embryonic and postnatal ages. We identified temporally regulated modules of genes that correlate with, and likely regulate, multiple phases of RGC development, ranging from differentiation and axon guidance to synaptic recognition and refinement. Some of these genes are expressed broadly while others, including key transcription factors and recognition molecules, are selectively expressed by one or a few of the 45 transcriptomically distinct types defined previously in adult mice. Next, we used these results as a foundation to analyze the transcriptomes of RGCs in mice lacking visual experience due to dark rearing from birth or to mutations that ablate either bipolar or photoreceptor cells. 98.5% of visually deprived (VD) RGCs could be unequivocally assigned to a single RGC type based on their transcriptional profiles, demonstrating that visual activity is dispensable for acquisition and maintenance of RGC type identity. However, visual deprivation significantly reduced the transcriptomic distinctions among RGC types, implying that activity is required for complete RGC maturation or maintenance. Consistent with this notion, transcriptomic alternations in VD RGCs significantly overlapped with gene modules found in developing RGCs. Our results provide a resource for mechanistic analyses of RGC differentiation and maturation, and for investigating the role of activity in these processes.

Introduction

Retinal ganglion cells (RGCs) are the sole output neurons of the retina (**Figure 2.1A**). They receive and integrate visual information from photoreceptors via interneurons and project axons to the rest of the brain. In mice, RGCs can be divided into ~45 discrete types that are distinguishable by their morphological, physiological and molecular properties (Baden et al., 2016; Bae et al., 2018; Goetz et al., 2021; Rheaume et al., 2018; Tran et al., 2019). Many of these types respond selectively to particular visual features such as motion or edges, thereby parcellating visual information into parallel channels that are transmitted to numerous central brain targets (Dhande et al., 2015; Martersteck et al., 2017). The structure, function and development of RGCs have been extensively studied, making them among the best-characterized of vertebrate central neuronal classes (Sanes and Masland, 2015). Consequently, studying the genesis, specification and differentiation of RGCs can not only help elucidate principles that govern the development of the visual system, but also inform our understanding of neural development generally.

The development of RGCs and their integration into circuits are orchestrated by a combination of activity-independent and -dependent influences. Nowhere is this more evident than in the retinotectal projection (retinocollicular in mammals). Sperry hypothesized that RGCs and their tectal targets bear graded "chemoaffinity" labels that lead to the orderly retinotopic mapping of the dorso-ventral and anterior-posterior axes of the retina onto those of the tectum (Sperry, 1963). In a long series of experiments, Bonhoeffer and colleagues devised *ex vivo* assays that recapitulated essential features of retinotopic matching (Bonhoeffer and Huf, 1985; Walter et al., 1987a; Walter et al., 1987b), leading eventually to the demonstration that opposing gradients of Eph kinases and their ligands, the ephrins, underlie the establishment of this mapping (Cheng et al., 1995; Drescher et al., 1995; Feldheim and O'Leary, 2010; Stahl et al., 1990a; Stahl et al., 1990b). On the other hand, the "hard-wired" retinotopic map is somewhat imprecise, and is extensively refined by activity-dependent mechanisms, leading to the more accurate topography seen in adulthood (Cang et al., 2005; Feldheim and O'Leary, 2010; McLaughlin et al., 2003; Schmidt and Buzzard, 1993).

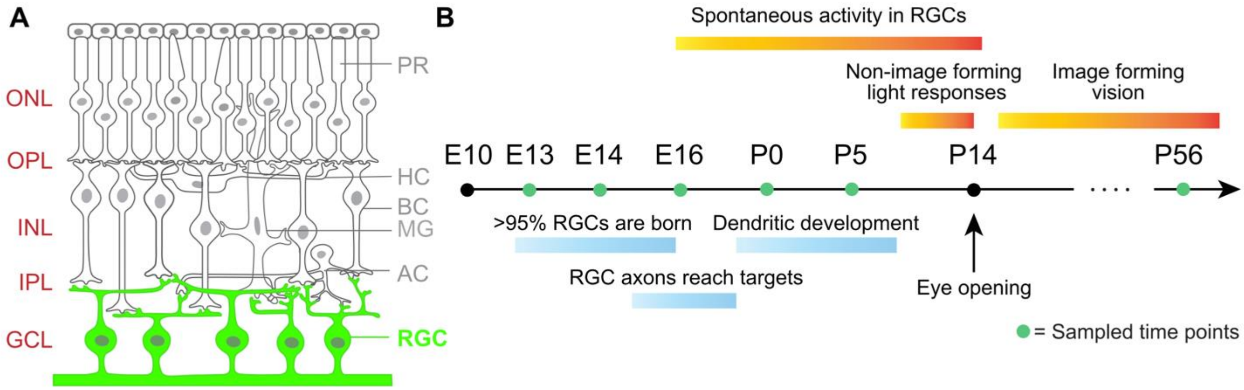

Figure 2.1. Retinal ganglion cell (RGC) development in mice. (**A**) Sketch of a cross-section of the retina, highlighting retinal ganglion cells (RGCs) located in the ganglion cell layer (GCL). PR, photoreceptors; HC, horizontal cells; BC, bipolar cells; MG, Müller glia; AC, amacrine cells; ONL, outer nuclear layer; OPL, outer plexiform layer; INL, inner nuclear layer; IPL, inner plexiform layer, (**B**) Timeline of RGC development in mice highlighting key developmental milestones. Green dots indicate ages considered in this study.

Other features of RGCs are also shaped by an interplay of activity-dependent and -independent influences. For example, the segregation of RGC axons into discrete laminae in the lateral geniculate nucleus requires initial molecular recognition followed by activity-dependent refinement. In this case, however, little is known about the molecular basis of the initial phases (Hooks and Chen, 2007; 2008; Katz and Shatz, 1996). Within the retina, the dendritic arbors of specific RGC types appear to be shaped predominantly by intrinsic transcriptional programs (Liu et al., 2018; Peng et al., 2017) that also specify the interneuron types from which they receive synapses (Duan et al., 2014; Krishnaswamy et al., 2015; Sanes and Zipursky, 2020). However, visual deprivation and/or decreased activity affect both dendritic morphology (Bodnarenko et al., 1995; Chalupa and Gunhan, 2004; El-Quessny et al., 2020; Tian and Copenhagen, 2003) and patterns of synaptic input (Arroyo and Feller, 2016; Kerschensteiner et al., 2009; Morgan et al., 2011; Okawa et al., 2014).

Interactions of activity-independent and -dependent influences occur dynamically and over a protracted period. The transcriptomes of RGCs change dramatically as they diversify, develop and mature (see **Results**). Likewise, activity arises from multiple sources that change during development. In late embryonic and early postnatal life in rodents, RGC activity is "spontaneous", arising from intrinsic biophysical properties of neighboring interneurons and their connections to each other and to RGCs (Arroyo and Feller, 2016; Wong, 1999). Later, but prior to eye-opening, light-dependent activity affects development by non-image forming activation of rod and cone photoreceptors (Tiriac et al., 2018). Later still, conventional visual input affects maturation of RGC dendritic and axonal arbors as well as their maintenance (see above). Finally, both pre- and postnatally, activation of melanopsin-containing intrinsically photosensitive RGCs (ipRGCs) affects development of retinal vasculature and patterns of spontaneous activity (Kirkby and Feller, 2013).

Elucidating the mechanisms that regulate RGC development and the ways in which activity-independent and -dependent influences interact would be greatly aided by comprehensive characterization of gene expression in developing RGCs. Our aim in this study is to provide a resource that can be used for these purposes. The paper is divided into two parts. First, we analyzed the transcriptomes of 110,814 single RGCs at six ages from embryonic day (E)13, when RGCs are newly postmitotic, to adulthood (postnatal day [P]56; mice are sexually mature by around P40). We previously used these datasets to define 45 mouse RGC types (Tran *et al.*, 2019), and analyze their diversification from a limited repertoire of postmitotic precursors (Shekhar et al., 2022). Here, we surveyed shared and type-specific gene expression changes to identify candidate regulators of RGC development. We identify genes whose temporal regulation overlaps with different phases of RGC development such as differentiation, axonal and dendritic elaboration, synaptic recognition and signaling.

In the second part, we used three models of visual deprivation to assess the effects of light-driven activity on RGC maturation. They were: (1) dark-rearing from birth to adulthood; (2) a well-characterized mutant line (*rd1*) in which visual signals are undetectable shortly after eye-opening (at P14) due to photoreceptor dysfunction and death (Farber et al., 1994; Gibson et al., 2013); and (3) a mutant that lacks bipolar interneurons, which convey photoreceptor input to RGCs (*Vsx2*-SE$^{-/-}$) (Norrie et al., 2019). For each of these three models, we used high-throughput single cell RNA-seq (scRNA-seq) to characterize the transcriptomic diversity of RGCs at P56 and compare their gene expression with that of RGCs from age-matched normally reared mice. We find that all 45 RGC types are present in all models, indicating that visual activity (or lack thereof) does not alter the core transcriptional signatures that specify type-identity. However, visual deprivation attenuates the gene expression differences among RGC types, indicating an impact on transcriptomic maturation or maintenance. We then surveyed the gene groups impacted by visual deprivation and found that they share a significant overlap with the temporally regulated programs underlying normal RGC development. Together, these results indicate that while RGC diversification may be largely governed by vision-independent factors, visual activity plays a role in the final stages of cell type maturation.

Results

Mouse RGCs are the first-born neuronal class in the retina, with >95% of RGCs arising between embryonic days (E) 12 and 17 (Drager, 1985; Farah and Easter, 2005; Marcucci et al., 2019; Voinescu et al., 2009). RGC axons begin reaching retinorecipient targets by E15 and are refined in an activity-dependent manner postnatally as noted above (Godement et al., 1984; Osterhout et al., 2011). Dendritic development, however, only commences during early postnatal life, when RGCs receive synapses in the inner plexiform layer (IPL) from amacrine cells by P4 and from bipolar cells soon thereafter (Kim et al., 2010; Lefebvre et al., 2015; Sernagor et al., 2001). Beginning around E16, RGCs exhibit spontaneous and synchronized activity that propagates in a wave-like fashion (Feller and Kerschensteiner, 2020). Initially, activity is light-independent but starting around P10, light penetrating the eyelids generates responses in the photoreceptors that are transmitted to RGCs (Tiriac *et al.*, 2018). Image-forming vision begins after P14, when the eyes open (Hooks and Chen, 2007) (**Figure 2.1B**). By the time of eye-opening, RGCs exhibit diverse type-specific axonal and dendritic arborization patterns (Kim *et al.*, 2010), and feature-selective responses can be recorded *ex vivo* (Tiriac et al., 2022), indicating that RGC types and their basic circuitry are established without image-forming visual experience.

RGC diversification

To study RGC diversification we recently used scRNA-seq to profile RGCs at E13, E14, E16, P0, P5, and P56 (Shekhar *et al.*, 2022; Tran *et al.*, 2019). We briefly summarize the main conclusions of that study before proceeding to describe changes in gene expression during this period.

First, the number of molecularly distinct groups of RGCs as well as their transcriptomic distinctiveness increases with age. Groups of RGCs at the earliest stages studied exhibit graded gene expression differences spanning a transcriptomic continuum, but they become increasingly discrete as development proceeds. Second, using a computational method called Waddington optimal transport (WOT; (Schiebinger et al., 2019); described below), we found that RGC types are not specified at the progenitor level but rather that multipotentiality persists in postmitotic precursor RGCs. Third, these precursor RGCs become gradually and asynchronously restricted to specific types with developmental age. Finally, diversification may in many cases occur in two steps, with precursors initially committing to subclasses, each defined by the selective expression of TFs in the adult. Subsequently, precursors within a subclass become restricted to single types by a process we named “fate-decoupling” (Shekhar *et al.*, 2022).

Gene expression changes as RGCs develop

To analyze gene expression patterns during RGC development, we first combined all single cell transcriptomes at each age to identify changes broadly shared among types. We visualized the developmental progression at single-RGC resolution using a force-directed layout embedding (FLE; **Figure 2.2A**). FLE arranges cells on a 2D map based on mutually attractive/repulsive “forces” that depend on transcriptional similarity (Fruchterman and Reingold, 1991; Jacomy *et al.*, 2014). We then identified 1,707 global temporally-regulated DE genes and used *k*-means clustering to group them into modules with distinct temporal dynamics, choosing k=6 based on the gap-statistic method (see **Methods**; **Figure 2.2B**; **Table S2.1**). **Figure 2.2C** shows the FLE plot with each cell colored based on the average expression levels of genes in each of the six modules, verifying that the expression of these modules varied systematically with age and were broadly shared among RGCs.

We analyzed the modules (Mod1-6) in two ways. First, we examined the enrichment of nine functional groups of genes chosen because of their well-documented importance in the development and function of RGCs: cell surface molecules (CSMs), G-protein coupled receptors (GPCRs), ion channels, neuropeptides, nuclear hormone receptors (NHRs), neurotransmitter receptors (NTRs), ribosomal genes (Ribo), transcription factors (TFs) and transporters (**Figure 2.2D**). Second, we used conventional gene ontology (GO) enrichment analysis to highlight distinct biological processes, molecular functional units and cellular components that were enriched in each of these modules (**Figure 2.3**)(The Gene Ontology, 2019).

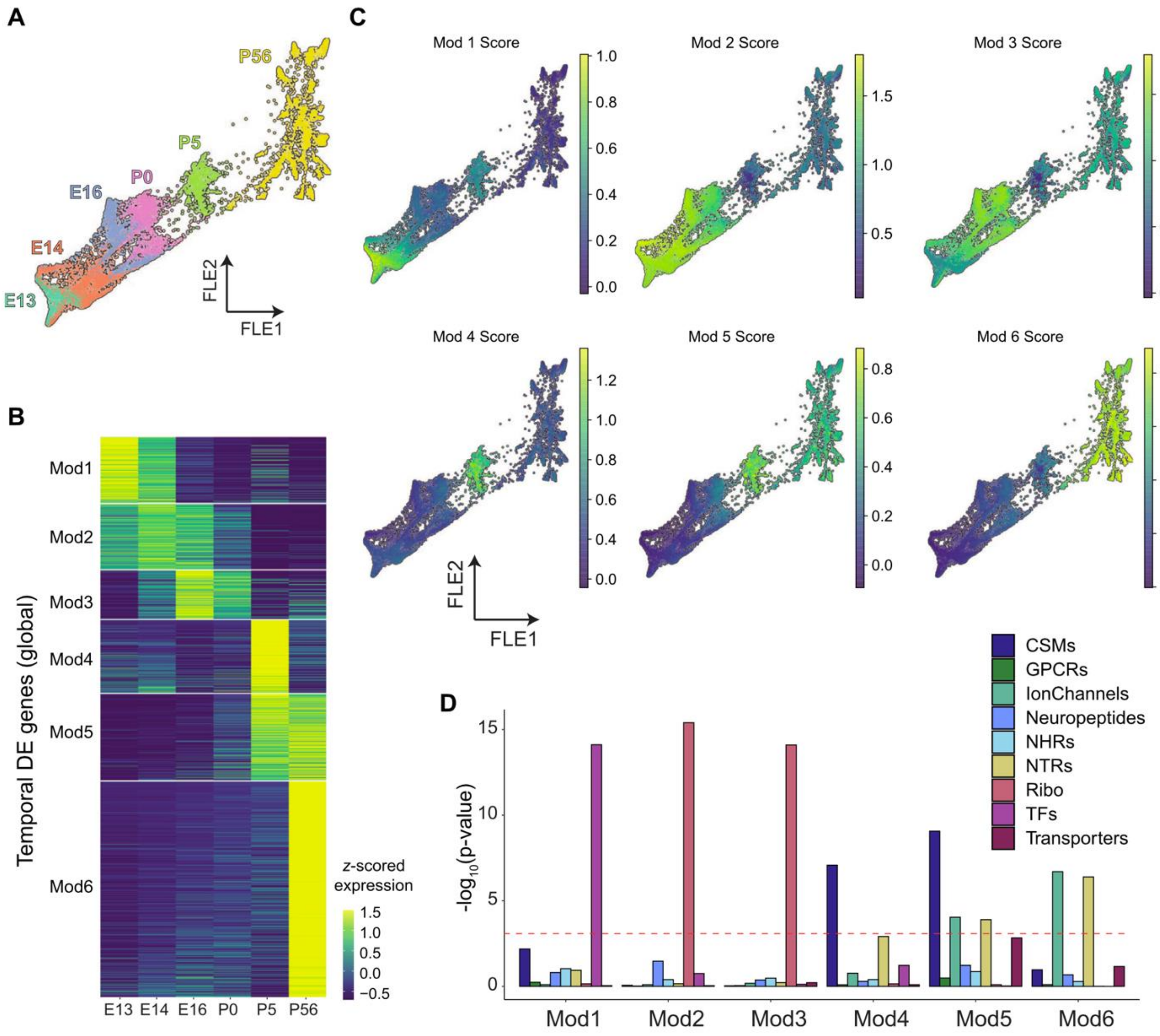

Figure 2.2. Global gene expression changes during RGC development. (**A**) 2D representation of progressive transcriptomic development of RGCs using a Force-directed layout (FLE) embedding (Weinreb et al., 2018). Individual points represent single RGCs colored by their age. (**B**) Heatmap of temporally regulated genes broadly shared among developing RGCs. Expression values of each gene (row) are averaged across all RGCs at a given age (columns) and z-scored across ages. White horizontal bars separate genes into six modules (Mod1-6) identified by k-means clustering. (**C**) 2D representation as in panel A with individual RGCs colored based on average expression of genes enriched in Mods1-6 (Table S2.1). (**D**) Barplot showing enrichment of cell surface molecules (CSMs), G-protein coupled receptors (GPCRs), ion channels, neuropeptides, nuclear hormone receptors (NHRs), neurotransmitter receptors (NTRs), ribosomal genes (Ribo), transcription factors (TFs) and transporters among Mod1- 6. Note that our list of CSMs excludes GPCRs, ion channels, NHRs and NTRs, which are captured in other groups. Each group of bars represents a module, and bar color indicates gene group. y-axis shows statistical enrichment in _log10(p-value) units. Bonferroni corrected p-values were calculated according to the hypergeometric test (see Experimental procedures).

Mod1, consisting of 202 genes, was most active at E13. It included genes associated with retinoic acid signaling (*Crabp1, Crabp2, Nr2f2*) as well as axon guidance (*Robo1, Nrp1, Sema3a, Slit1*), coinciding with the initial period of axon growth (Zhang et al., 2017) (**Figures 2.3A,B**). Mod1 was also the only module significantly enriched for TFs (**Figure 2.2D**). TFs included several previously shown to influence RGC differentiation, such as SoxC class TFs *Sox11/12* (Jiang et al., 2013; Kuwajima et al., 2017), *Onecut2/3 (*Sapkota et al., 2014*), Nhlh2*, *Ebf3* and *Irx3,5* (Jin et al., 2010; Lu et al., 2020; Lyu and Mu, 2021). We also found many TFs that have not, to our knowledge, been previously described in this context, including *Baz2b, Hmx1, Tbx2* and *Zeb2*.

Expression of genes in Mod2 and Mod3 was highest at later prenatal ages - E14 for Mod2 and E16 for Mod3. Genes enriched in these modules included those associated with ribosome biogenesis and assembly (Rps-genes and Rpl-genes), translation, and mitochondrial function (*Ndufa1-3, Ndufb2,4, Ndufv3*), all consistent with requirements for neuronal growth and maturation during this period (**Figures 2.2D** and **2.3C**).

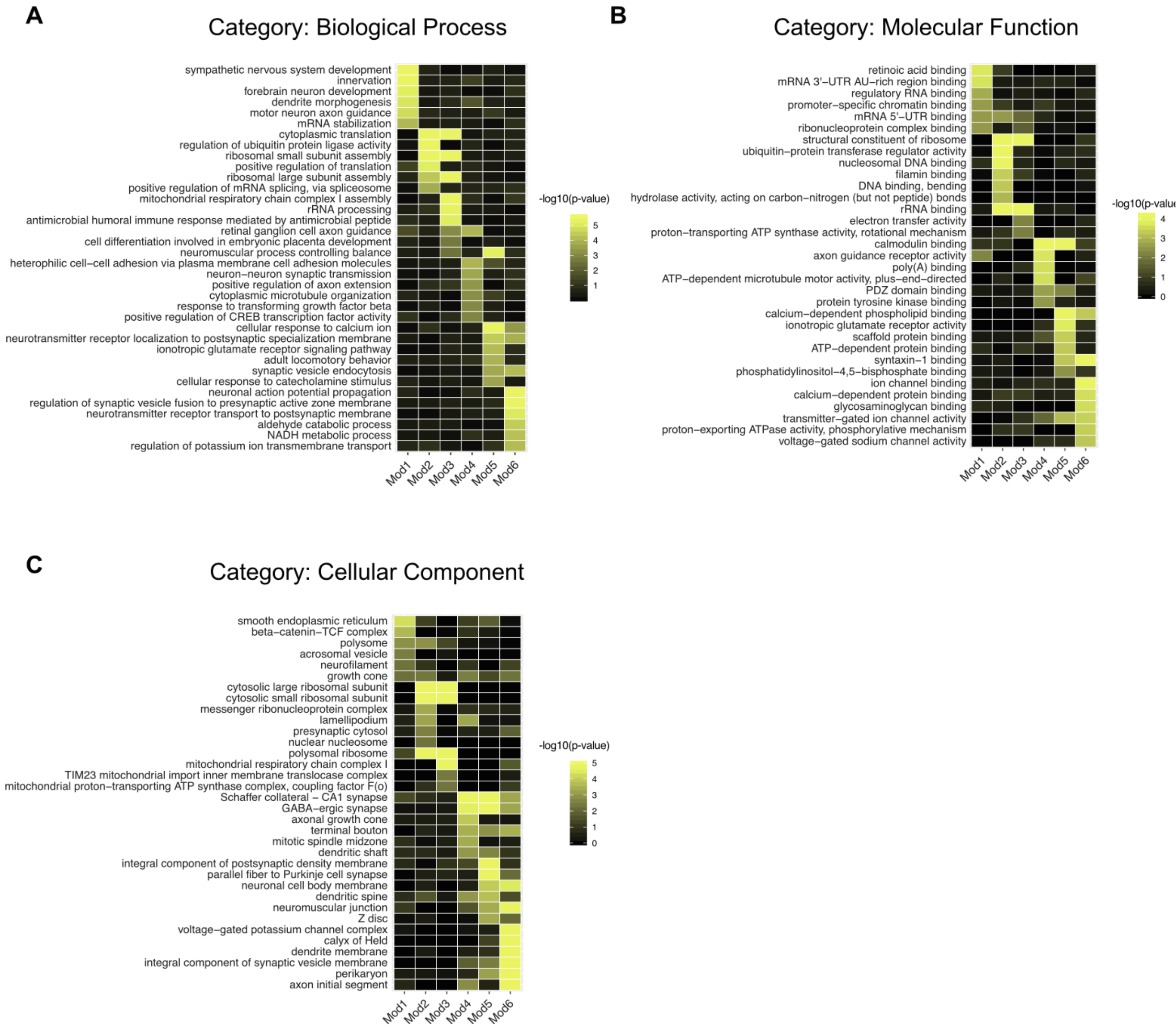

Figure 2.3. Gene Ontology (GO) analysis of temporally regulated gene modules Mod1-6. (**A**) Examples of significantly enriched Gene Ontology (GO) category ‘‘Biological Process (BP)” terms (rows) in Mod1-6 (columns). Colors correspond to enrichment corrected p-values (-log10 units). GO analysis was performed using the R package topGO (Alexa and Rahnenfu¨hrer, 2009). (**B**) Same as A, for GO category ‘‘Molecular Function (MF)”. (**C**) Same as A, for GO category ‘‘Cellular Component (CC)”.

Mod4-Mod6 were most active at the postnatal ages: P5 for Mod4, P56 for Mod6, and both ages for Mod5. Mod4 and Mod5 contained many genes encoding cell surface molecules (**Figure 2.2D**). Among them were genes implicated in formation of retinal neural circuits, including members of the three superfamilies most prominently implicated in synaptic specificity: the cadherin (e.g., *Cdh4, Cdh11, Pcdh17/19, Pcdha2, Pcdhga9*), immunoglobulin (e.g., *Dscam, Ncam2*, and *Nrcam*) and leucine-rich repeat super-families (*Lrrn3, Lrrtm2, Lrrc4c*) as well as teneurins (*Tenm1, Tenm2, Tenm4*), which are counter-receptors for leucine-rich repeat proteins (Sanes and Zipursky, 2020). Mod5 was enriched for transporters (e.g. *Slc6a1, Slc6a11, Slc24a3, Atp1a1, Atp1a3*). All three postnatal modules were enriched for genes required for synaptic transmission, such as GABA receptors (*Gabra3, Gabrbr3, Gabbr2*), ionotropic glutamate receptors (*Gria1-4* and *Grin1/2b*), and synaptotagmins (*Syt1,2,6*). Mod5 and Mod6 were especially enriched for genes encoding ion channels including many associated with action potential propagation (*Scn1a, Scn1b, Cacnb4*, *Kcna1, Kcnc2, Kcnip4, Kcnab2;* **see Figure 2.3B,C**).

Taken together, these data provide a comprehensive catalogue of molecular changes associated with RGC maturation, including genes implicated in neuronal differentiation and growth, axon guidance and synaptogenesis, and acquisition of electrical and synaptic capabilities.

Type-specific gene expression changes during RGC maturation

We next leveraged the single-cell resolution of our dataset to identify genes selectively expressed in small subsets of RGC precursors. Such genes may contain factors that instruct specific fates (fate determinants), or RGC type-specific properties. To this end, we identified genes that were specific to transcriptomic clusters at each age as defined in our previous studies: they were expressed in at least 30% of the cells in fewer than 10% of the clusters and in no more than 5% of the cells in any remaining cluster (Shekhar *et al.*, 2022; Tran *et al.*, 2019). The number of specific genes increased steadily with age, from 2 at E13 (*Lect1* and *Pou4f3*) to 200 at P56 (**Table S2.2**). The increase was striking even when taking the increasing number of clusters into account (10 at E13 and 45 at P56; **Figure 2.4A**; (Shekhar *et al.*, 2022). The gene categories introduced in **Figure 2.2D** accounted for 45-55% of genes at each age. The two most prominent categories were TFs and CSMs, accounting for 12-50% and 8-18% of all genes, respectively (**Figure 2.4B**). All the other categories were represented at lower proportions. There was substantial turnover of specific genes with age: only ~23% of specific genes at E14 and E16 and ~50% of specific genes at P0 and P5 remained specific at P56, reflecting the dramatic transcriptomic changes that occur during RGC diversification and maturation.

To visualize the temporal evolution of these genes as RGC diversification progressed, we linked cell types across time with Waddington optimal transport (WOT)(Schiebinger *et al.*, 2019). Briefly, WOT uses transcriptomic similarity as a proxy to directly compute fate associations at the level of individual cells without requiring clustering as a prior step, identifying putative precursors of each of the 45 adult RGC types at each of the early time points. This, in turn, enables us to visualize gene expression changes along the inferred developmental history of each type (see (Shekhar *et al.*, 2022) for further discussion and validation).

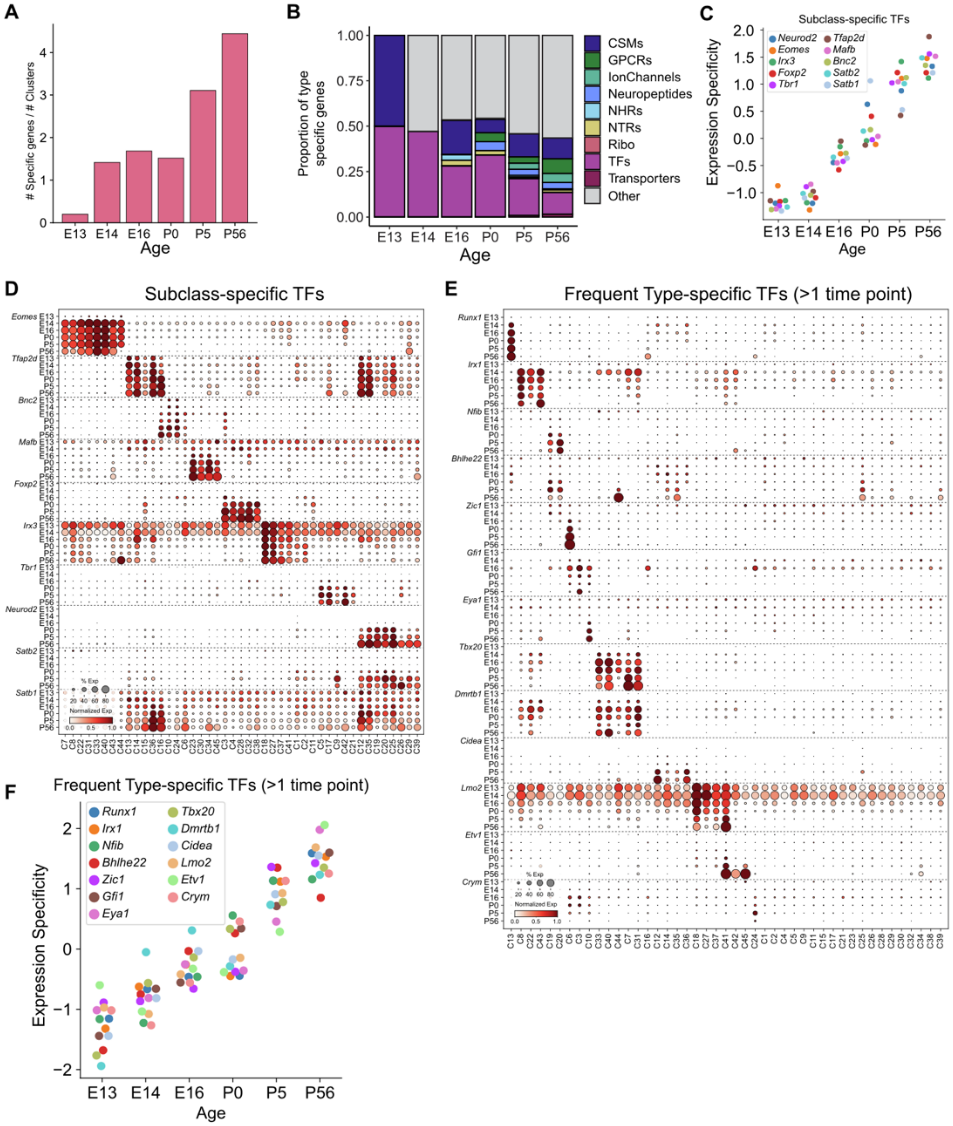

Figure 2.4. Subclass- and type-specific gene expression changes during RGC development. (**A**) The number of specific genes per cluster increases with age. y-axis plots the number of type-specific genes divided by the number of clusters at each age, as defined in Shekhar et al., 2022 (10 clusters at E13, 12 clusters at E14, 19 clusters at E16, 27 clusters at P0, 38 clusters at P5, and 45 clusters at P56). (**B**) Relative proportion of each of the 10 gene groups in **Figure 2.2D** among the specific genes in panel A. Abbreviations as in **Figure 2.2D**. The ‘‘other” category includes all expressed genes that were not present in any of the 10 gene groups. Note that E13 contains only two specific genes: one CSM and one TF. (**C**) Expression of eight RGC subclass-specific TFs (as in Shekhar et al., 2022) becomes increasingly specific with age. Expression specificity is defined as the z-scored dispersion of expression levels across cell types. At ages earlier than P56, putative precursors were inferred using WOT (see Experimental procedures). (**D**) Dot plot showing expression patterns of subclass-specific TFs with age among putative type-specific precursors. Each row displays the expression levels of a TF at a particular age among type-specific precursors (columns) identified using WOT. The size of a dot corresponds to the fraction of cells with non-zero transcripts, and color indicates normalized expression levels. Row blocks corresponding to different TF are demarcated by dotted horizontal lines. In addition to the eight subclass-specific TFs in C, we also plot the expression patterns two RGC selective TFs, *Satb1* and *Satb2* (Peng et al., 2017; Dhande et al., 2019). (**E**) Same as (D), showing the expression of TFs identified as type- specific among WOT-inferred precursors at least two ages via DE analysis. (**F**) Same as C, showing increasing specificity of type-specific TFs plotted in E.

We used this framework to examine three sets of genes. First, we queried expression of a set of TFs that are expressed in transcriptomically proximate types of adult RGCs that we nominated as subclasses defined by shared-fate association (Shekhar *et al.*, 2022). Many of these transcription factors have been noted in previous analyses as selectively expressed among RGC types (Kiyama et al., 2019; Liu *et al.*, 2018; Mao et al., 2020; Rheaume *et al.*, 2018; Rousso et al., 2016; Tran *et al.*, 2019). Analysis of their expression revealed a gradual increase in specificity (**Figure 2.4C-D**). This coincides with gradual specification of RGC subclasses observed by Shekhar et al. (2022), with the *Eomes* and *Neurod2* subclasses emerging earliest and latest, respectively. For the few that have been studied functionally, expression patterns were consistent with their roles (see **Discussion**).

Second, we sought TFs that were selectively expressed in just 1-3 inferred types at one or more of the six ages, reasoning that they might include type-specific fate determinants. TFs in this category included *Zic1* in type C6 (nomenclature of (Tran *et al.*, 2019)), *Gfi1* in C3, *Eya1* in C10, *Runx1* in C13, *Msc* in C31 and *Esrrb* in C41 (**Figures 2.4E**, **S2.1A**). Several of these types have been characterized morphologically and/or physiologically (see **Discussion**) but roles of the TFs remain to be explored. The majority of the selectively expressed TFs exhibited increasingly restricted expression with age, consistent with the overall transcriptomic divergence of RGCs (**Figure 2.4F**). However, this trend was not universal: for example, *Esrrg* and *Fgf1* became less specific with age (**Figure S2.1C**).

Third, we analyzed expression of recognition molecules that we and others have shown to play roles in synaptic choices of RGCs (**Figure S2.1B**) (Duan *et al.*, 2014; Duan et al., 2018; Krishnaswamy *et al.*, 2015; Liu *et al.*, 2018; Liu and Sanes, 2017; Matsuoka et al., 2011; Osterhout *et al.*, 2011; Osterhout et al., 2015; Peng *et al.*, 2017; Yamagata and Sanes, 2018). Most of the genes queried become specific only during postnatal ages (**Figure S2.1D**), consistent with the known timing of dendritic elaboration and synaptogenesis, but nonetheless exhibit variability in timing. These data provide a rich resource for identifying candidate molecules that may, likely in combination, regulate selective aspects of RGC type identity.

Visual deprivation models

To assess the effects of visual experience on RGC maturation we analyzed three groups of adult mice that had been visually deprived (VD) postnatally. The first model, dark-rearing (DR) from birth to analysis in adulthood (P56), deprives the retina of all postnatal visual input. Standard histology, including immunostaining with antibodies to the RGC-specific marker Rbpms showed that dark-rearing had no obvious effect on retinal structure, and that RGCs were normal in number and position (**Figure 2.5A**).

The second model is the well-characterized and widely used *rd1* line, which carries a nonsense mutation in the gene encoding the rod-specific cGMP phosphodiesterase 6-beta subunit (*Pde6b*), a key component of the phototransduction cascade in rods. Loss of *Pde6b* results in dysfunction of rod photoreceptors, which is followed, for reasons that remain unknown, by death of rods and, subsequently, loss of cone photoreceptors (Farber *et al.*, 1994; Keeler, 1924; Punzo and Cepko, 2007). Although rods are not completely lost until one month of age and cones later still, their function is disrupted earlier, and visual signals are undetectable by P21 (Gibson *et al.*, 2013). Since eye-opening does not occur until P14, RGCs in *rd1* mice experience conventional visual input only for a brief period. The outer nuclear layer, which contains rods and cones, was nearly absent from *rd1* retina by P56, but the number of RGCs in the ganglion cell layer was not detectably affected (**Figure 2.5A**).

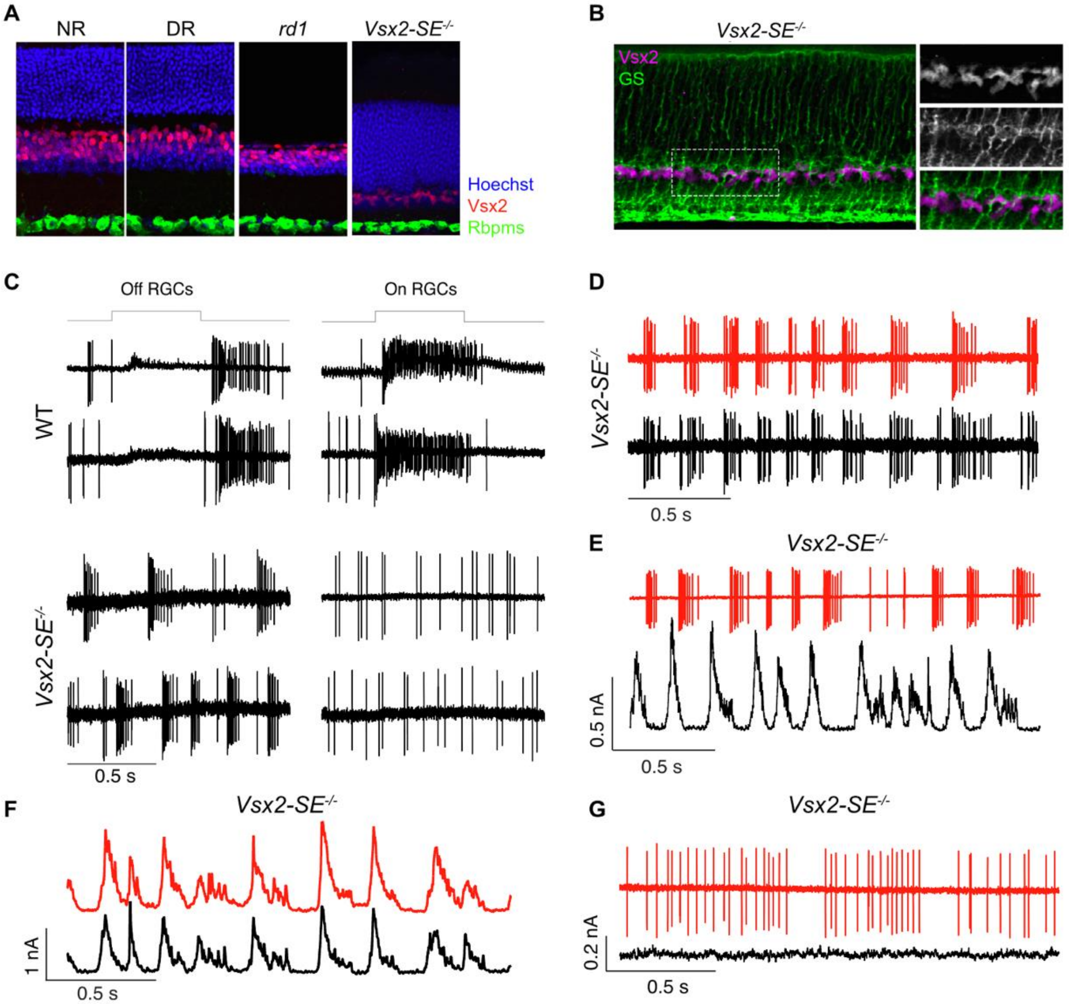

Figure 2.5. Three visual deprivation models. (**A**) Sections from adult (P56) retinas of normally reared (NR), dark-reared, *rd1* and *Vsx2*-SE$^{-/-}$ mice stained for Vsx2 (a pan-BC and Müller glia marker), Rbpms (pan-RGC marker), and Hoechst (nuclear marker). (**B**) Section from *Vsx2*-SE$^{-/-}$ retina co-stained for glutamine synthetase (GS), a marker of Müller glia, and Vsx2. All Vsx2 immunoreactivity in the mutant retina is associated with Müller glia. (**C**) *Vsx2*-SE$^{-/-}$ RGCs fail to respond to light. Cell-attached recordings of responses to a light step from four wild-type (WT) RGCs (two OFF-sustained and two ON-sustained) and lack of response from four *Vsx2*-SE$^{-/-}$ RGCs. Light step for WT RGCs was adjusted to 10 R*/rod/s. Light step for *Vsx2*-SE$^{-/-}$ RGCs was to 1000 R*/rod/s. Note that the pattern of spontaneous activity is very different between OFF and ON *Vsx2*-SE$^{-/-}$ RGCs. R*/rod/s is the photoisomerization rate. (**D**) Strong synchrony between two nearby *Vsx2*-SE$^{-/-}$ OFF RGCs. Simultaneously-recorded OFF RGCs produce highly correlated spontaneous bursts of activity. Colors indicate two different RGCs. (**E**) Increase in inhibitory input produces gaps in spontaneous firing. Panels show simultaneous recordings of spikes in one OFF RGC and inhibitory input in another nearly OFF RGC. Increases in inhibitory input are correlated with a decrease in spontaneous firing in the neighboring cell. (**F**) Inhibitory input to OFF RGCs is strongly correlated. Simultaneous recordings of spontaneous inhibitory input to two nearby OFF RGCs. The correlation coefficient for this pair was 0.8. (**G**) Blocking of GABA (gabazine and TPMPA) and glycine (strychnine) receptors eliminates synchrony and patterned spontaneous activity.

The third model is a mutant (*Vsx2*-SE$^{-/-}$) lacking the bipolar interneurons that convey signals from rod and cone photoreceptors to RGCs ((Gamlin et al., 2020; Norrie *et al.*, 2019); see **Figure 2.1A**). *Vsx2* is expressed in retinal progenitor cells and its expression is maintained in differentiated bipolar neurons and Müller glia. It is required for early progenitor divisions and also for formation of bipolar cells (Burmeister et al., 1996; Liu et al., 1994). An enhancer essential for *Vsx2* expression in bipolar cells is deleted in the *Vsx2*-SE$^{-/-}$ line, resulting in failure of bipolar cells to form. As other regulatory elements required for *Vsx2* expression are intact, other retinal cell classes form normally. Thus, RGCs receive no visual input in *Vsx2*-SE$^{-/-}$ mice, although it is likely that ipRGCs, which express the photosensitive pigment melanopsin, retain visual responsiveness. As expected, the inner nuclear layer was thin is this mutant, but there was no significant effect on the thickness of the outer nuclear layer, which contains photoreceptors, or the ganglion cell layer in which RGCs reside (**Figure 2.5A).** We noted some residual staining with anti-Vsx2 but determined that this reflected the retention of Müller glial cells (glutamine synthetase-positive), which express Vsx2 and are unaffected by deletion of the bipolar-specific enhancer (**Figure 2.5B**).

The physiology of RGCs in the *rd1* line has been characterized previously (Choi et al., 2014; Goo et al., 2015; Stasheff, 2008), but those in the *Vsx2*-SE$^{-/-}$ line have not. We therefore recorded from RGCs in isolated *Vsx2*-SE$^{-/-}$ retinas. RGCs were labeled by inclusion of a fluorescent dye in the recording pipette. We targeted cells with the largest somata, which in wild-type retinas are ON-sustained, OFF-sustained and OFF-transient RGCs. ON or OFF RGCs were identified based on confocal imaging following recording; dendrites of likely ON cells (n=5) arborized near the ganglion cell layer, while dendrites of likely OFF cells (n=10) arborized near the inner nuclear layer.

As expected, none of the recorded RGCs generated measurable changes in firing rate in response to light steps; identical steps elicited large responses in WT RGCs (**Figure 2.5C**). *Vsx2*-SE$^{-/-}$ OFF RGCs generated spontaneous rhythmic activity consisting of high-frequency bursts of spikes separated by periods of silence (**Figure 2.5C**). Firing rates during the bursts often exceeded 100 Hz. ON RGCs lacked this rhythmic activity, instead generating occasional spontaneous spikes that were not organized into bursts. Dual recordings demonstrated that spontaneous activity was strongly correlated between nearby OFF RGCs (**Figure 2.5D**). Similar spontaneous activity in *rd1* mice appears to originate in AII amacrine cells, which provide direct inhibitory input to OFF but not ON RGCs in wild-type mouse retina. Consistent with this mechanism, inhibitory input to an OFF RGC coincided with pauses in firing in a nearby OFF RGC (**Figure 2.5E**) and inhibitory input to nearby RGCs was very strongly synchronized (**Figure 2.5F**; peak correlation in three pairs was 0.7, 0.8 and 0.9, compared to 0.2-0.3 for pairs of WT RGCs). Moreover, pharmacological blockade of inhibitory synaptic transmission abolished the rhythmicity of activity in OFF RGCs (**Figure 2.5G**). RGCs did not show evidence for direct synaptic interactions: depolarizing one cell in a paired recording did not elicit a measurable response in the other (data not shown). These observations support a picture in which synchronized activity in the AII amacrine network produces strongly synchronized inhibitory input to OFF RGCs and produces coordinated pauses in their spontaneous firing.

Effects of visual deprivation on RGC type identity

To study the influence of visual input on RGC type identity, we obtained scRNA-seq profiles of 19,232 RGCs from DR mice, 14,864 RGCs from *rd1* mice, and 22,083 RGCs from *Vsx2*-SE$^{-/-}$ mice, all at P56 (**Methods**; **Figure S2.2A**). We separately clustered each dataset in an unsupervised fashion to identify molecularly distinct RGC clusters (**Figure S2.2B-E**). We then used a classification framework (Chen and Guestrin, 2016; Tran *et al.*, 2019) to map each VD RGC to P56 NR RGC types (Chen and Guestrin, 2016; Tran *et al.*, 2019) (**Methods**; **Figures 2.6A-D** and **S2.2F-H**). This framework employs an ensemble of gradient boosted decision trees, with each decision tree assigning any given VD RGC to one of the 45 adult types in NR mice. A VD RGC was assigned to the NR type that received the majority vote. Cells were considered unequivocally mapped if their voting margin was ≥12.5%, or 5-fold higher than 2.2% (1/45), the margin of a classifier that votes randomly. All 45 types were recovered in all three models, and mapping was highly specific in that 98.5% of the 56,179 VD RGCs mapped to a single type based on this criterion (**Figure 2.6E**). Indeed, the average voting margin for a VD RGC was >90% for all three conditions, or 40-fold higher than chance, and the distribution was similar among conditions. Moreover, TFs and adhesion molecules that were type-specific in NR retina retained their type-specificity in all three VD models (**Figure S2.3**).

Although nearly all VD RGCs could be assigned to NR types, two observations led us to examine the influence of visual deprivation on the specification of RGC types: First, VD RGCs were less transcriptomically separated in UMAP projections than their NR counterparts (**Figure 2.6A-D**). Second, when we assessed the correspondence of VD clusters to NR RGC types there were several cases in which not all RGCs within a single VD cluster mapped to the same NR type; instead, RGCs mapping to 2 or 3 different types co-clustered in the VD dataset (**Figure S2.2F-H**). To evaluate decreased transcriptomic separation as an explanation for multimapping, we calculated for each RGC in each condition, the silhouette score, a measure of the tightness of clustering in principal component space (Rousseeuw, 1987). The silhouette score for an RGC is a measure of how similar it is transcriptomically to other RGCs of the same type compared to RGCs of other types (**Methods**). VD RGCs exhibited consistently lower silhouette scores than their NR counterparts (**Figure 2.6F**) and nearly all types exhibited lower average silhouette scores compared to their NR counterparts (**Figure 2.6G**). Subsampling analyses verified that these differences were not driven by the larger sample size of NR RGCs. Moreover, RGCs in "multi-mapped" clusters generally belonged to the most transcriptomically similar types in the NR retina (Tran *et al.*, 2019). Consistent with the failure to fully acquire or maintain type-specific distinctions, >90% of RGC types in the VD conditions exhibited fewer DE genes than their NR counterparts (**Figure 2.6H**). Taken together, these results indicate that RGCs acquire their type identity in a vision-independent manner but require visual input for complete transcriptomic maturation or maintenance.

We also compared the relative frequencies of each RGC type in NR and VD models. 40/45 types exhibited less than 2-fold change in relative frequency compared to the atlas across the full range of observed frequencies (0.1% to 8%). Such changes were comparable to those observed between normally reared P56 biological replicates (**Figure 2.6I**), suggesting that they likely represent sampling variation rather than true biological changes. Further the frequency distributions of types between VD and NR RGCs were very similar, as quantified by near zero values of the Jensen-Shannon divergence (JSD), a measure of divergence between two frequency distributions (Bishop and Nasrabadi, 2006). Although we cannot rule out the possibility that larger samples and more replicates would reveal modest changes in type frequency, we conclude that VD has no significant differential effect on the generation or maintenance of specific RGC types.

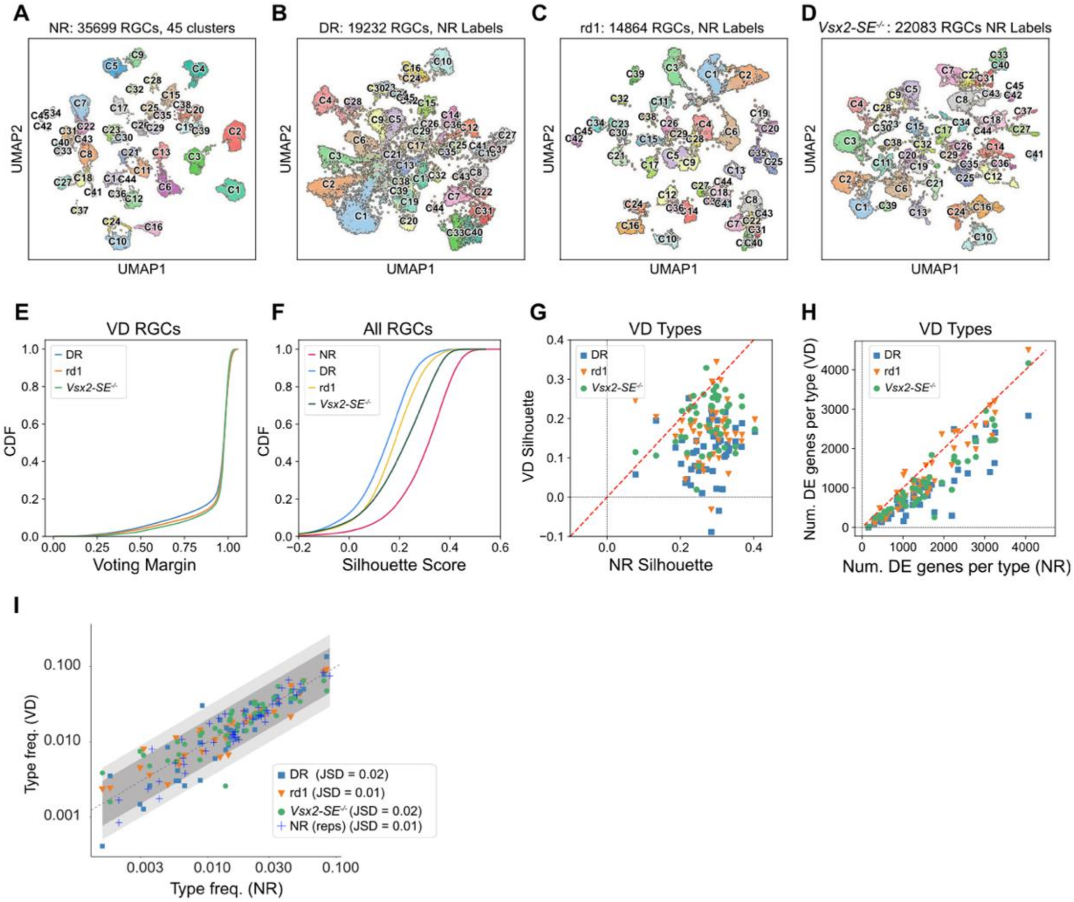

Figure 2.6. Transcriptomic classification of RGCs from visually deprived mice. (**A**) 2D visualization of the transcriptomic diversity in normally reared (NR) P56 RGCs using Uniform Manifold Approximation (UMAP; (Becht et al., 2019)). Individual cells (points) represent single RGCs, and are colored by type identity as in Tran et al. (2019). (**B**). UMAP visualization DR RGC transcriptomes profiled in this study. Individual RGCs are colored based on NR type-identity as determined using a supervised classification framework (**Methods**). (**C**) Same as B, for *rd1* RGCs. (**D**) Same as B, for *Vsx2*-SE$^{-/-}$ RGCs. (**E**) Cumulative distribution functions (CDFs) showing voting margins for VD RGCs by condition (colors). The voting margin is defined as the fraction of decision trees casting the majority vote. A VD RGC is assigned to the type receiving the majority vote as long as the margin is ≥5X greater than chance, corresponding to a margin of 0.022 (see **Methods**). (**F**) CDFs for silhouette coefficients for NR, DR, *rd1* and *Vsx2*-SE$^{-/-}$ RGCs (colors). Details of calculating the silhouette coefficients are described in the **Methods**. CDFs for VD RGCs were significantly different from the CDF for NR RGCs based on the two-sample Kolmogorov-Smirnov test (p-values are 10^{-106}, 10^{-88}, and 10^{-50} for DR vs. NR, *rd1* vs. NR, and *Vsx2*$^{-/-}$-SE vs. NR comparison, respectively). (**G**) Comparison of the average silhouette coefficient for each of the 45 RGC types under NR (x-axis) and VD conditions (y-axis). Each point corresponds to a type (45*3=135 total points), and colors and symbols (legend) indicate VD condition. (**H**) Scatter plot showing that there are fewer DE genes per type among VD RGCs (y-axis) than normally reared RGCs (x-axis). Colors and symbols as in G. (**I**) Scatter plot comparing relative frequencies of RGC types in NR (x-axis) vs. VD (y-axis). Colors and symbols of VD as in G. Blue crosses represent frequencies observed in replicates of NR RGCs. Dashed line shows y=x. Shaded ribbons are used to represent a frequency-fold change difference of 2 (dark gray) and 3 (light gray), respectively. JSD - Jensen Shannon Divergence, a measure of distance between the frequency distributions (0 – identical distributions, 1 – maximally disparate distributions). Difference between VD and control are in most cases comparable to those observed between NR replicates.

Effects of visual deprivation on gene expression

Finally, we compared RGCs from each VD condition to NR RGCs to identify visual-experience dependent DE (vDE) genes (**Methods**). We began by identifying transcriptomic alterations that were broadly shared among RGCs (global vDE) (**Figure S2.2I**). We found a total of 477 genes that exhibited a >1.5-fold change between NR and at least one VD condition (MAST DE test; adjusted p-value $< 10^{-4}$) and were detected in at least 70% of RGCs in either condition. At the bulk level, the transcriptomic profiles of RGCs from all three VD conditions were more similar to NR RGCs at P56 and to each other than they were to NR RGCs at P5 (**Figure 2.7A**). The number of global DE genes between P5 and P56 control RGCs, defined using identical metrics, is several-fold larger than the number of global vDE genes at P56 between NR RGCs and any of the VD conditions. This difference is easily appreciated from the elliptical rather than circular profiles when gene expression changes between P5 NR and P56 NR RGCs are compared to those between P56 NR and P56 VD RGCs (**Figures 2.7A-C)**. As an example, 217 genes are down-regulated and 759 up-regulated in NR RGCs between P5 and P56, whereas only 23 (11% as many) are down-regulated and 161 (21% as many) up-regulated in dark-reared compared to NR mice at P56 (**Figure 2.7B**). This difference is insensitive to the choice of DE threshold in the range 1.2-fold to 1.8-fold, and very few genes exhibit higher fold changes in VD. Based on these results, we conclude that the majority of gene expression changes that occur during the maturational period between P5 and P56 do not rely on visual experience-driven activity.

In addition to global vDE genes, we also sought genes that were selectively upregulated or downregulated in each of the 45 types (type-specific vDE genes). We identified 3637 type-specific vDE genes that exhibited a >1.5-fold change (MAST DE test; adjusted p-value $< 10^{-4}$), between at least one of the VD and the NR dataset in 5 or fewer types at a detection rate of ≥30% for either condition. We performed GO analysis on the combined set of global and type-specific vDE genes to assess pathways affected by VD (**Figure S2.4A,B**). We observed multiple instances of common GO terms enriched among vDE genes and those enriched in developmental modules. For example, most of the GO terms enriched in upregulated vDE genes in all three models were also enriched in developmental Mod2 and 3. However, it was challenging to interpret these similarities because of the redundancies among GO terms, a well-known problem (Jantzen et al., 2011). We therefore adopted the more direct approach of computing the statistical overlap between vDE genes and each of the six modules of temporally regulated genes identified in **Figure 2**. Upregulated genes in VD were significantly enriched for Mod 1-3, which are expressed in embryonic RGCs, while downregulated global vDE genes were enriched in Modules 4-6, which are postnatally active ($p < 10^{-4}$, Hypergeometric test; **Figures 2.7F,G**). Similar trends were evident for type-specific vDE genes (**Figures 2.7I,J**). Together, these results suggest that visual deprivation directly impacts biological pathways involved in RGC development.

Remarkably, both global and type-specific vDE genes, were highly condition specific (**Figures 2.7E,H**). Some of these differences may result from the different ways in which the three models affected visual input, but it is also likely that some genes that are vDE in single models are false positives, resulting from inadequate sampling or technical variations among samples. Lacking additional replicates or an independent validation method, we therefore focused on groups of related genes. We highlight three interesting trends.

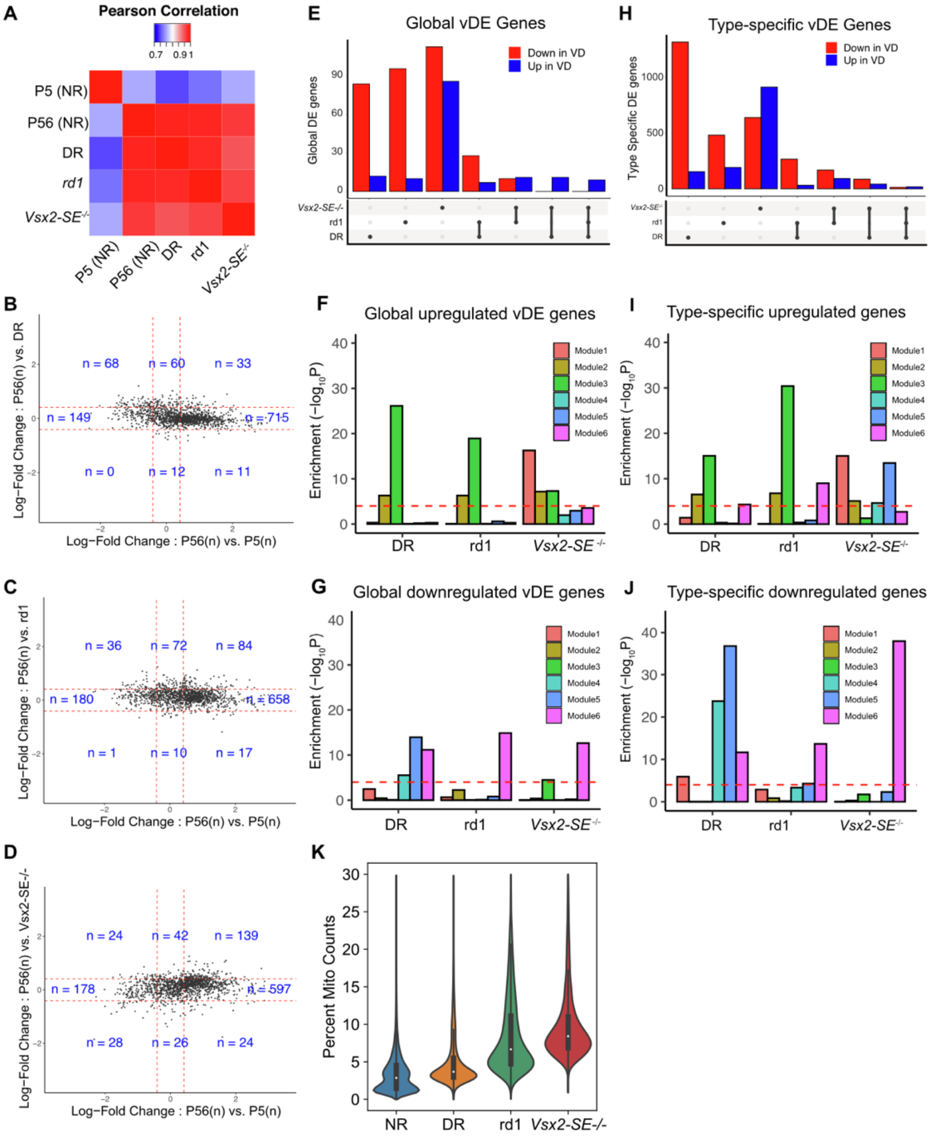

Figure 2.7. Global and type-specific gene expression changes in VD RGCs. (**A**) Pairwise correlation heatmap showing that the average transcriptional profiles of VD RGCs are more similar to the NR RGCs at P56 than they are to NR RGCs at P5. Colors represent Pearson correlation coefficients. (**B**) Scatter plot comparing average log2-fold changes in the expression of genes (points) between NR RGCs at P56 and NR RGCs at P5 (x-axis) versus between NR and DR RGCs at P56 (y-axis). Dashed red lines denote fold changes of 1.5 along each axis, and the number of genes in each region is indicated. The relative preponderance of dots with |log-fold| > 1.5 along the x-axis compared to the y-axis reflect the fact that maturation-related genes are not substantially impacted during VD. (**C**) Same as B, for *rd1* RGCs. (**D**) Same as B, for *Vsx2*-SE$^{-/-}$ RGCs. (**E**) Bar-plot showing the number of global vDE genes that are downregulated (red) or upregulated (blue) in a single VD condition compared to controls or shared among conditions. The combination of VD conditions corresponding to each pair of bars is indicated below. (**F**) Statistical enrichment of maturation modules Mod1-6 (as in **Figure 2.2A**) among globally upregulated vDE genes in each VD condition. (**G**) Same as F for globally downregulated vDE genes in each VD condition. (**H**) Same as E but for type-specific vDE genes. (**I**) Same as F but for type-specific upregulated vDE genes. (**J**) Same as F but for type-specific downregulated vDE genes. (**K**)Violin plot showing that the proportion of counts associated with mitochondrial transcripts is higher in the VD conditions compared to NR. Note that NR contains both control RGCs used in this study (Tran *et al.*, 2019) and RGCs from (Jacobi et al., 2022) (see **Figure S2.5A**).

First, enrichment patterns of the modules were different among VD conditions: only in *Vsx2*-SE$^{-/-}$ RGCs was Mod1 upregulated; only in DR mice were all three postnatal developmental modules downregulated; and only in *Vsx2*-SE$^{-/-}$ were large numbers of genes upregulated (**Figure 2.7F,G,I,J**). Likewise, few GO enrichment terms were shared among conditions (**Figure S2.4A,B).** Second, upregulated genes in *Vsx2*-SE$^{-/-}$ RGCs included many implicated in the formation and function of excitatory postsynaptic specializations. GO terms included G-protein coupled receptor activity, regulation of postsynaptic density organization, postsynaptic density assembly, PDZ domain binding, and dendritic membrane (**Figure S2.4**). Upregulated genes included several encoding glutamate receptor subunits (*Gria1, Gria3, Grik3, Grik5*) as well as other components of excitatory postsynaptic densities (*Dlg1, Dlg4, Dlgap3, Lrrtm2, Lrrc4b, Ntrk3, Shank1*)(Holt et al., 2019). By preventing formation of bipolar cells, this mutant deprives RGCs of their main source of glutamatergic excitatory activation. The upregulation observed is reminiscent of "denervation supersensitivity" in which postsynaptic receptors and proteins associated with them are dramatically upregulated when skeletal muscle is denervated (Tintignac et al., 2015); similar phenomena have been observed in neurons (e.g.,(Kong et al., 2011; Kuffler et al., 1971)).

Third, mitochondrially-encoded genes were upregulated in all three VD models (**Figure 2.7K** and **S5A**). The upregulation was broadly shared among RGC types, being evident in all 45 types in rd1 and *Vsx2*-SE$^{-/-}$ and in 36/45 types in DR (**Figure S2.5B**). Upregulated genes included *mt-Nd2*, *mt-Nd3*, *mt-Nd4*, *mt-Nd4l*, and *mt-Co3*, all of which have been found to bear missense (hypomorphic) mutations in Leber's Hereditary Optic Neuropathy (LHON). Although these genes are ubiquitously expressed, the disease selectively affects RGCs (Yu-Wai-Man et al., 2011).
Our results suggest the possibility that the decrease in mitochondrial gene expression caused by visual activity could further amplify respiratory chain dysfunction caused by the mutations, rendering RGCs particularly vulnerable to oxidative stress.

Discussion

The development of neurons, their differentiation into distinct types, and their integration into information processing circuits all result from hard-wired genetically encoded programs that are modified by neural activity. Both genetic and activity-dependent modes of development rely on molecular mediators, but our knowledge of their identities is incomplete for the former and rudimentary at best for the latter. Mouse RGCs are well suited for addressing these open questions for several reasons: (a) their structure, function and development have been studied in detail; (b) they comprise a neuronal class that has been divided into several subclasses and numerous (~45) types, enabling analysis at multiple levels; and (c) methods are available for manipulating the sensory input they receive and thereby the patterns of activity they experience.

Our method was scRNA-seq, which enables comprehensive classification of neuronal cell types, and their mapping across developmental stages and experimental conditions. An additional advantage is that we were able to identify cells that were not RGCs and remove them from the dataset, ensuring that changes observed over time or after VD were attributable to RGCs and not to contaminating populations. By profiling RGCs at multiple developmental ages, we were able to map the changing transcriptional landscape of RGCs as they develop from embryonic stages to adulthood. By profiling adult RGCs that had been visually deprived in three different ways, we showed that vision is not required for full diversification of RGCs into subclasses and types but does affect patterns of gene expression in both global and type-specific ways. Our results can serve as a starting point for screening and assessing key molecular mediators of activity-independent and -dependent patterning of RGC development.

RGC development

We first identified temporal gene expression changes broadly shared among developing RGC types. Both gene ontology and enrichment analysis of key gene classes (e.g., cell surface molecules, transcription factors, ion channels, neurotransmitter receptors) showed a systematic progression of expression patterns as RGCs differentiate, form synapses, and mature. DE genes expressed at E13 were enriched in TFs and regulators of neuronal differentiation and axon guidance. At later embryonic ages (E14 and E16), enriched genes included ones required for robust neuronal and axonal growth – for example, genes associated with ribosomal biogenesis and mitochondrial function. Perinatally (P0 and P5), genes required for synaptogenesis and synaptic choices – for example recognition molecules – are prominent, followed by genes encoding the machinery for axonal and synaptic signaling at P5 and P56 – for example, ion channels, neurotransmitter release components, and neurotransmitter receptors.

We next catalogued DE genes restricted to one or a few clusters at each age. TFs and CSMs were particularly prominent in this group. This is unsurprising in that genes involved in neuronal growth and function are shared among many neuronal types and classes. However, because the diversification into distinct RGC types occurs gradually, the relationship of embryonic clusters to adult types is not straightforward. We therefore used WOT, a statistical inference approach, to identify the likely precursors of each of the 45 types at each developmental stage. We used these assignments to trace the expression of two sets of TFs among these precursors: ones expressed in few precursor groups, which might be type-specific fate determinants, and ones previously suggested to be markers of RGC subclasses. Some potential type-specific TFs were expressed by characterized types for which reagents are available to test their roles – for example *Zic1* in W3B RGCs (C6), *Etv1* in alpha RGCs (C41, 42, 45; see also (Martersteck *et al.*, 2017)), and *Msc* in M2-ipRGCs (C31). Others are present in uncharacterized types and could be used to mark and manipulate them – for example *Eya1* in C10, *Runx1* in C13, and *Nfib* in C19 and 20. Of the TFs that defined subclasses, a few are expressed selectively at early times and might serve as fate determinants – for example, *Eomes/Tbr2*, *Mafb*, *Bnc2* and *Tfap2d*. Others are expressed selectively only peri- and postnatally – for example *Neurod2* and *Tbr1*. For those few that have been studied in retina, expression patters are consistent with mutant phenotypes: in *Eomes/Tbr2* mutants, most ipRGCs (a prominent set of *Eomes/Tbr2*-positive types) fail to develop, while in *Tbr1* mutants, T-RGCs develop but exhibit defects in dendritic morphogenesis (Kiyama *et al.*, 2019; Liu *et al.*, 2018; Sweeney et al., 2019).

Importantly, broader expression of other genes does not exclude the possibility that their functional roles may be type-specific. Specificity may arise due to combinatorial action of multiple genes, varying expression levels, or coupling with other molecular features. This may be particularly true for the broadly expressed TFs in Mod1 or the CSMs in Mod4 and Mod5 (**Figure 2.2D; Table S2.1**). Indeed, previous studies have found clear examples of redundancy among recognition molecules and TFs that regulate RGC development (e.g.(Duan *et al.*, 2018; Jiang *et al.*, 2013; Sajgo et al., 2017)).

Visual deprivation

We used three methods to deprive mice of visual experience so we could ask how vision affects RGC diversification and maturation. Two methods relied on genetic manipulations – *rd1* mice in which photoreceptors degenerate beginning in the second postnatal week, and *Vsx2*-SE$^{-/-}$ mice, in which no bipolar cells form, preventing communication from photoreceptors to RGCs. A third model, dark rearing from birth, prevents non-image forming vision noninvasively.

Importantly, although these perturbations prevent vision, they do not lead to complete inactivity of RGCs (Hooks and Chen, 2007); they therefore enabled us to assess roles of visually-evoked activity but not all electrical activity on RGC development. We observed that OFF RGCs in *Vsx2*-SE$^{-/-}$ mice exhibited spontaneous bursty activity that was correlated between neighboring cells and was driven by inhibitory input likely arising from AII amacrine neurons. ON RGCs did not exhibit such spontaneous activity. This pattern resembles that previously described for RGCs in in *rd1* mice (Stasheff, 2008). Whether different patterns of spontaneous activity have a role in instructing type specific maturation is unclear. Unfortunately, although there are methods for disrupting the coherence of spontaneous activity among RGCs (Kirkby et al., 2013), it is currently not feasible to inhibit all action potentials in RGCs over a prolonged period. However, visual input has been shown to have clear effects on dendritic morphology of RGCs and refinement and maintenance of RGC axonal arbors in the superior colliculus (see **Introduction**), and transcriptomic analyses have documented significant alterations in gene expression in the lateral geniculate nucleus and visual cortex following visual deprivation (Cheadle et al., 2018; Cheng et al., 2022; Hrvatin et al., 2018; Tropea et al., 2006).

The observation of fewer RGC clusters in VD retina than in NR retina initially suggested that late steps in diversification of types might require visual input. However, when assessed at a cell-by-cell level, over 98% of RGCs mapped with high confidence to a single adult type, even in clusters that contained RGCs of two or three types. Further, in terms of transcriptomic similarity, VD RGCs unequivocally resembled aged matched normally reared counterparts, rather than immature RGCs at P5. Previously, we have shown that RGC diversification is incomplete at P5 (Shekhar *et al.*, 2022). The present results suggest that non-image forming visual-activity during the early postnatal period is not required for the establishment of RGC diversity, and image-forming light-driven activity following eye opening is not required for its maintenance. However, we cannot rule out the possibility that light-independent activity, which begins by E16, influences RGC diversification.

VD had clear effects on gene expression in RGC generally as well as in specific RGC types. In aggregate, they suggested maturational defects. First, VD RGC types exhibited fewer DE genes than their NR counterparts. Second, the genes that were altered were enriched for those that are temporally regulated during normal development. Genes expressed at embryonic stages of RGC development and subsequently downregulated (Mods1-3) were expressed at higher levels in VD RGCs than normal RGCs, while genes upregulated in postnatal RGCs (Mods4-6) were expressed at lower levels in VD RGCs. We speculate that these subtle but systematic changes may be associated with previous studies showing that dark rearing perturbs both dendritic and axonal refinement (see above), without leading to a complete dedifferentiation of RGCs.

In all three VD models, we profiled adult RGCs. A remaining question is whether vision affects maturation per se, maintenance of mature characteristics, or both. Physiological studies have provided evidence for both possibilities (e.g., (Carrasco et al., 2005; Feldheim and O'Leary, 2010; Hooks and Chen, 2006; Hooks and Chen, 2007). Profiling of RGCs at earlier times could settle this issue.

Materials and methods

Data and code availability

The gene expression matrices and analysis scripts are available on our lab's Github repository at https://github.com/shekharlab/RGC_VD.

Experimental Methods

Mice

All animal experiments were approved by the Institutional Animal Care and Use Committees (IACUC) at Harvard University. Mice were maintained in pathogen-free facilities under standard housing conditions with continuous access to food and water. Mouse strains used for both scRNA-seq and histology, were: C57Bl/6J (JAX #000664), *rd1* mice with a mutation in the beta subunit of cGMP phosphodiesterase (*Pde6b*) gene, and *Vsx2*-SE$^{-/-}$ mice lacking bipolar cells (Norrie *et al.*, 2019). The *rd1* mutant had been backcrossed onto a C57Bl/6J background (a kind gift from Prof. Constance Cepko) and the *Vsx2*-SE$^{-/-}$ mice were maintained on a C57Bl/6J background. Embryonic and early post-natal C57Bl/6J mice were acquired either from Jackson Laboratories (JAX) from time-mated female mice or time-mated in-house. For timed-matings, a male was placed with a female overnight and removed the following morning, this being E0.5. The day of birth is denoted P0. For dark-rearing (DR) experiments, animals were kept in light-tight housing in a dark room from the day of birth.

Droplet-based single-cell RNA-sequencing of adult RGCs (scRNA-seq)

For each VD condition, RGCs from two separate groups of mice were profiled. Identical protocols were used to isolate RGCs from dark-reared (DR), *rd1* and *Vsx2*-SE$^{-/-}$ mice at P56 and profiled using the same methods described previously for normally reared mice (Shekhar *et al.*, 2022; Tran *et al.*, 2019), with one exception. Retinas from DR mice were dissected in a dark room using a microscope fitted with night-vision binocular goggles (Tactical Series G1, Night Owl), and an external infrared light source, with dissociation and staining steps conducted in LiteSafe tubes (Argos Technologies) to protect from light exposure.

For RGC collection, all solutions were prepared using Ames' Medium with L-glutamine and sodium bicarbonate, and subsequently oxygenated with 95% O2 / 5% CO2. Retinas were dissected out in their entirety immediately after enucleation and digested in ~80U of papain at 37°C, followed by gentle manual trituration in L-ovomucoid solution. We used a 70µm cell filter to remove clumps, and following this, the cell suspension was spun down and resuspended in Ames + 4% Bovine Serum Albumin (BSA) solution at a concentration of 10^6 per 100µl. All spin steps were conducted at 450g for 8 minutes in a refrigerated centrifuge. 0.5µl of 2µg/µl anti-CD90 conjugated to various fluorophores (Thermo Fisher Scientific) was added per 100µl of cells. After a 15 min incubation, the cells were washed with an excess of media, spun down and resuspended in Ames + 4% BSA at 7 x 10^6 cells per 1 ml concentration. Calcein blue was then added to cells. During fluorescent activated cell sorting (FACS), forward and side-scatter values were used to exclude cellular debris and doublets, calcein blue was used to select viable cells, and RGCs were collected based on high CD90 expression.

Following collection, RGCs were spun down and resuspended in PBS + 0.1% non-acetylated BSA at a concentration range of 2000 cells/µl for scRNA-seq processing per manufacturer's instructions (10X Genomics, Pleasanton, CA). The single-cell libraries for normally reared, *rd1* and DR mice were prepared using the single-cell gene expression 3' v2 kit on the 10X Chromium platform, while the Vsx2-SE$^{-/-}$ libraries were prepared using the v3 kit. scRNA-seq library processing was done using the manufacturer's instructions. Libraries were sequenced on the Illumina HiSeq 2500 platforms (paired end: read 1, 26 bases; read 2, 98 bases).

Histology and Imaging

Eyes were collected from animals intracardially perfused with 15-50ml of 4% paraformaldehyde (PFA), and post-fixed for an additional 15 min. Dissected eyes and lenses were visually inspected for signs of damage before proceeding further. Healthy eyes were transferred to PBS until retinal dissection, following which retinas were sunk in 30% sucrose, embedded in tissue freezing media and stored at -80°C. Later, retinas were sectioned at 20-25µm in a cryostat and mounted on slides (Tran *et al.*, 2019). Staining solutions were made up in PBS plus 0.3% Triton-X and all incubation steps were carried out in a humidified chamber. Following a 1hour protein block in 5% Normal Donkey Serum at room temperature, slides were incubated overnight at 4°C with primary antibodies, washed 2 times 5 minutes in PBS, and incubated for 2 hours at room temperature with secondary antibodies conjugated to various fluorophores (1:1,000, Jackson Immunological Research), and Hoechst (1:10,000, Life Technologies). Following this incubation, slides were washed again 2 times 5 minutes in PBS and coverslipped with Fluoro-Gel (#17985, Electron Microscopy Sciences).

Antibodies used in this study were guinea pig anti-RBPMS (1:1,000, #1832-RBPMS, PhosphoSolutions), goat anti-VSX2 (1:200, #sc-21690, Santa Cruz Biotechnology), mouse anti-Glutamine synthase (1:1,000, BD Bioscience, # 610517). All images were acquired using an Olympus Fluoview 1000 scanning laser confocal microscope, with a 20x oil immersion objective and 2x optical zoom. Optical slices were taken at 1µm steps. Fiji (Schindelin et al., 2012) was used to pseudocolor each channel and generate a maximum projection from image stacks. Brightness and contrast were adjusted in Adobe Photoshop.

Physiology

Mice (C57/Bl6 and *Vsx2*-SE$^{-/-}$) were dark adapted overnight and sacrificed according to protocols approved by the Administrative Panel on Laboratory Animal Care at the University of Washington. After hemisecting each eye, we removed the vitreous mechanically and stored the eyecup in a light-tight container in warm (~32°C), bicarbonate-buffered Ames Solution (Sigma-Aldrich, St. Louis) equilibrated with 5% CO_2 / 95% O_2. All procedures were carried out under infrared light (>900 nm) to keep the retina dark adapted. All experiments were performed in a flat mount preparation of the retina. We placed a piece of isolated retina ganglion cell-side up on a polylysine coated cover slip within a recording chamber. The retina was secured by nylon wires stretched across a platinum ring and perfused with warm (30-34°C) equilibrated Ames solution flowing at 6-8 mL/min. Light from a light-emitting diode (LED; peak output = 470 nm; spot diameter 0.5 mm) was focused on the retina through the microscope condenser.

RGC spike responses were recorded in the cell-attached configuration. RGC inhibitory synaptic inputs were recorded in the voltage-clamp configuration with a holding potential near +10 mV (determined empirically for each cell to eliminate spontaneous inward currents). We used an internal solution containing 105 mM $CsCH_3SO_3$, 10 mM TEA-Cl, 20 mM HEPES, 10 mM EGTA, 5 mM Mg-ATP, 0.5 mM Tris-GTP, and 2 mM QX-314 (pH ~7.3, ~280 mOsm); 0.1 mM alexa-488 or alexa-555 was included so that we could image RGC dendrites after recording and identify On and Off cells based on the level of stratification in the inner plexiform layer.

Computational Methods

Normally-reared RGC datasets

Gene Expression Matrices (GEMs) for normally reared (NR) RGCs for E13, E14, E16, P0, P5 and P56 were downloaded from our previous studies (Shekhar *et al.*, 2022; Tran *et al.*, 2019), Entries of raw GEMs reflect the number of unique molecular identifiers (nUMIs) detected per gene per cell, which is a proxy for transcript copy numbers. Raw GEMs were filtered, normalized and log-transformed following standard procedures described before (Shekhar *et al.*, 2022). For each RGC in this dataset, we retained metadata corresponding to cluster/type IDs and also fate associations computed using WOT in (Shekhar *et al.*, 2022), which allowed us to identify putative type-specific precursors at each age. These data can be downloaded from our Github repository: https://github.com/shekharlab/RGC_VD.

Force-directed layout embedding of developing RGCs

We visualized the developmental heterogeneity and progression of RGCs on a 2D force-directed layout embedding (FLE) using SPRING (Weinreb et al., 2018) (https://github.com/AllonKleinLab/SPRING_dev) (**Figure 2**). To keep the run time manageable, we downsampled our normally reared RGC dataset to 30,000 cells chosen randomly (E13:1661, E14: 4743, E16: 3753, P0: 4968, P5: 4837, P56:10038). The input to SPRING was a matrix of cells by principal component (PC) coordinates computed from the filtered GEMs as follows. To ameliorate within-age batch-effects, we tested RGCs within each age for genes that were globally differentially expressed (fold-difference > 2) within any of the biological replicates. We then computed highly-variable genes (HVGs) in the reduced dataset using a Poisson-Gamma model (Pandey et al., 2018), which resulted in 845 HVGs. The raw GEMs of 845 HVGs by 30,000 cells was once again median normalized and log-transformed. Using PCA, we reduced the dimensionality of this matrix to 41 statistically significant PCs. The 30,000 cells by 41 PCs matrix was supplied to SPRING, which constructed a *k*-nearest neighbor graph (*k*=30) on the data, and used the ForceAtlas2 algorithm (Jacomy et al., 2014) to compute the FLE coordinates over 500 iterations.

The aggregate expression levels for each of the six gene modules were visualized in the 2D FLE as follows. For each cell and module pair, we computed:

$$S_{j_k} = \frac{1}{N_{G_k}} \sum_{i \in G_k}^{N_{G_k}} x_{ij} - \frac{1}{N_G} \sum_{i \in G}^{N_G} x_{ij}$$

where S_{j_k} is a cell j's score for module k, N_{G_k} is the number of genes in module *k*, G_k is the set of genes in module k, *G* is the set of all genes, N_G is the total number of genes, and x_{ij} is cell *j's* normalized and log-transformed expression of gene *i.* The first term in the expression reflects the average expression of the module genes in the cell. The second term in the equation subtracts cell *j's* mean expression across all genes from its module score corrects for baseline differences in library size across cells, a well-known source of variation in scRNA-seq. These scores were used to color cells in the FLE to visualize module activity (**Figure 2**).

Global temporal gene expression changes in developing RGCs

Genes expressed in fewer than 20% of the cells at all the six ages (E13, E14, E16, P0, P5, P56) were discarded. For each remaining gene, the average expression strength $S_{g,t}$ was computed at each of the six ages as,

$$S_{g,t} = P_{g,t} * E_{g,t}$$

where, $P_{g,t}$ is the fraction of RGCs at time *t* that express gene *g* (nUMIs > 0) and $E_{g,t}$ is the log-average expression counts of gene *g* in the expressing cells. We further removed genes that satisfied the criteria,

$$\frac{(S_{g,t}) \ - min(S_{g,t})}{min(S_{g,t})} < 0.3$$

to only consider genes that exhibited > 30% change in expression strength temporally. Next, we randomized the data by shuffling the age labels across RGCs, and used this to compute a "randomized" average expression strength of each gene $\widetilde{S_{g,t}}$. We then ranked genes based on values of the following quantity,

$$f_g = \frac{\sum_{t=1}^{6} \left(S_{g,t} - \widetilde{S_{g,t}}\right)^2}{\sqrt{\sum_{t=1}^{6} \left(S_{g,t} + \gamma\right)^2} \sqrt{\sum_{t=1}^{6} \left(\widetilde{S_{g,t}} + \gamma\right)^2}}$$

Genes with high values of f_g exhibit greater temporal variability. Here γ represents a pseudo-count, chosen to be 0.1 to avoid erroneous inflation of scores for lowly expressed genes. To assess the significance of f_g, we computed a null distribution of $\widetilde{f_g}$ using two different randomizations,

$$\widetilde{f_g} = \frac{\sum_{t=1}^{6}\left(\widetilde{S_{g,t}^{1}} - \widetilde{S_{g,t}^{2}}\right)^2}{\sqrt{\sum_{t=1}^{6}\left(\widetilde{S_{g,t}^{1}} + \gamma\right)^2}\sqrt{\sum_{t=1}^{6}\left(\widetilde{S_{g,t}^{2}} + \gamma\right)^2}}$$

We selected genes that satisfied $f_g > percentile(\widetilde{f_g}, 0.99)$. This led to the identification of 1,707 temporally regulated genes. We used k-means clustering to cluster the $S_{g,t}$ matrix comprised of these 1,707 genes, with the number of groups determined using the gap statistic (Tibshirani et al., 2001). This analysis identified six groups with distinct temporal expression patterns.

Gene Ontology (GO) enrichment analysis

We assessed the biological significance of the temporal gene expression modules by performing a Gene Ontology (GO) enrichment analysis. Using the R package topGO (Alexa and Rahnenführer, 2009), each module was evaluated for enrichment of GO terms associated with the three ontology categories: Biological Processes (BP), Molecular Function (MF) and Cellular Component (CC). GO terms with FDR adjusted p-values less than 10^{-3} were identified for each module, and differentially enriched modules were visualized as heatmaps.

Enrichment of function gene groups in modules

We assembled lists of mouse transcription factors (TFs), neuropeptides, neurotransmitter receptors (NTRs), and cell surface molecules (CSMs) from the panther database (pantherdb.org). Genes encoding G-protein coupled receptors (GPCRs), ion channels, nuclear hormone receptors (NHRs), and transporters were downloaded from https://www.guidetopharmacology.org/. The list of CSMs were pruned for duplicates by removing genes that were NTRs, GPCRs, NHRs and Ion channels. All genes starting with "Rps" or "Rpl" were tagged as ribosome-associated genes. Each of these gene groups were filtered to only contain genes detected in our dataset. To assess the statistical enrichment of a gene group *g* within a module m, we computed the hypergeometric p-value,

$$p(g,m) = \sum_{k \geq k_1} \frac{\binom{K}{k}\binom{N-K}{n-k}}{\binom{N}{n}}$$

Here *N* is the number of genes in the data, *K* is the number of genes in the group *g*, *n* is the number of genes in the module m, and k_1 is the number of genes common between the module m and group *g*. $p(g,m)$ represents the probability that k_1 or more genes from the group could be observed in the module purely by random sampling, the null hypothesis. Consequently, low values of $p(g,m)$ or high values of $-\log p(g,m)$ are suggestive of significant statistical enrichment.

Preprocessing and clustering analysis of single-cell RNA-seq data to recover RGCs

Fastq files corresponding to single-cell RNA-seq libraries from the three VD mice were aligned to the mm10 transcriptomic reference (*M. musculus*) and gene expression matrices (GEMs) were obtained using the Cell Ranger 3.1 pipeline (10X Genomics). GEMs from each of the 12 VD libraries were combined and filtered for cells containing at least 700 detected genes. This resulted in 75,422 cells of which 23,433 were from dark-reared mice, 23,989 were from rd1 mice, and 28,000 were from *Vsx2*-SE$^{-/-}$ mice.

Following standard procedures described previously, the GEMs were normalized and log-transformed, and highly variable genes (HVGs) in the data were identified (Pandey *et al.*, 2018; Shekhar *et al.*, 2022). Within the reduced subspace of HVGs, the data was subjected to dimensionality reduction using PCA and the PCs were batch-corrected across experimental replicated using Harmony (Korsunsky et al., 2019). Using the top 40 PCs, we performed graph clustering (Blondel et al., 2008) and annotated each of the clusters based on their expression patterns of canonical markers for retinal subpopulations described previously (Macosko et al., 2015). The predominant subpopulations included RGCs (82%), amacrine cells (ACs; 12.8%), photoreceptors (4.4%) and non-neuronal cells (0.8%). RGCs were isolated based on the expression of *Slc17a6, Rbpms*, *Thy1*, *Nefl*, *Pou4f1-3*. Overall, we obtained 19,232 RGCs from dark reared mice, 14,864 RGCs from *rd1* mice, and 22,083 RGCs from *Vsx2*-SE$^{-/-}$ mice. RGC yield varied among the three conditions, being 85% for dark rearing, 63.6% for rd1 and 79.3% for Vsx2-SE$^{-/-}$. Following the *in silico* purification of RGCs (**Figure S2.2A**), they were subjected to a second round of dimensionality reduction and clustering to define VD clusters (**Figures 2.6, S2.2**).

Quantification of transcriptomic separation among RGC types

We used the silhouette score to quantify the degree of separation among RGCs in PC space. Assuming the data has been clustered, let

$$a(i) = \frac{1}{|C_I| - 1} \sum_{j \in C_I, i \neq j} d(i, j)$$

be the mean distance between cell $i \in C_I$ (cell i in cluster C_I) and all other cells in the same cluster, where $|C_I|$ is the number of cells in cluster I and $d(i, j)$ is the distance between cells i and j in the cluster I. We can interpret $a(i)$ as the average distance of cell i is from other members of its cluster. Similarly, we can define the distance of cell i to a different cluster C_J as the mean of the distance from cell i to all cells in $C_{J \neq I}$. Next, define for each cell $i \in C_I$

$$b(i) = \min_{J \neq I} \frac{1}{|C_J|} \sum_{j \in C_J} d(i, j)$$

to be the smallest mean distance between cell i and the cells of any cluster $C_{J \neq I}$. Finally, the silhouette score for each cell i is defined as,

$$s(i) = \frac{b(i) - a(i)}{max[a(i), b(i)]}$$

and $-1 \leq s(i) \leq 1$. $s(i)$ is a measure of how tightly grouped cell i is with other members of the same cluster. The smaller the value of $s(i)$, the tighter the grouping. Values of $s(i)$ across the dataset quantify the overall tightness of the clusters. Values near 0 reflect poorly separated, overlapping clusters, while values near 1 indicate highly distinct and well-separated clusters.

Negative values indicate that a cell has been assigned to the wrong cluster, as it is similar to cells of a different cluster than to cells of its own cluster.

Clustering of VD RGCs and transcriptomic mapping of VD RGCs to control RGC types.

RGCs in each VD group were processed separately using the pipeline described above to identify transcriptomically distinct clusters. We then mapped each VD RGC to a normally-reared (NR) RGC type using a classification approach. We used gradient boosted decision trees as implemented in the Python package xgboost to learn transcriptional signatures corresponding to the 45 NR types and used this classifier to assign each VD RGC a NR type label. Three separate classifiers were trained on the NR types, each trained using common HVGs between the atlas and a VD condition as the features. For training, we randomly sampled 70% of the cells in each NR type up to a maximum of 1000 cells. The remaining NR cells were used as "held-out" data for validating the trained classifier to ensure a per-type misclassification rate of less than 5%. Jupyter Notebooks detailing the analysis can be found on https://github.com/shekharlab/RGC_VD.

The trained classifiers were then applied to each VD RGC. To avoid spurious assignments, we only assigned a VD RGC to a type if the classifier voting margin, defined as the proportion of trees accounting for the majority vote, was higher than 12.5%. This is quite stringent as for a multiclass classifier assigning each data point to each of 45 types, a simple majority could be achieved at a voting margin of $\frac{100}{45} \approx 2.2\%$. Encouragingly >98% of VD RGCs could be unequivocally assigned to a single RGC type by this criterion. The final mapping between VD clusters and control types were visualized as confusion matrices (**Figure S2.2**).

Identification of global and type-specific visual-experience mediated DE (vDE) genes

VD-related globally differentially expressed (vDE) genes were evaluated for each visual deprivation condition by VD RGCs as a group with normally reared (NR) P56 RGCs. We used the MAST test (Finak et al., 2015). A gene was considered globally vDE if it exhibited a fold-difference of at least 1.5 and was expressed in at least one condition in >70% all RGCs. We used the same procedure to identify globally DE genes between NR P5 RGCs and NR P56 RGCs. To identify type-specific vDE genes, we repeated the above procedure to each of the 45 RGC type between each of the 3 VD condition and NR - a total of 45*3 = 135 tests. A gene was considered type specific vDE if it was not globally vDE, exhibited a fold-difference of at least 1.5 in a type across conditions, and was expressed in at least 30% of cells of that type in either condition.

Supplementary Materials

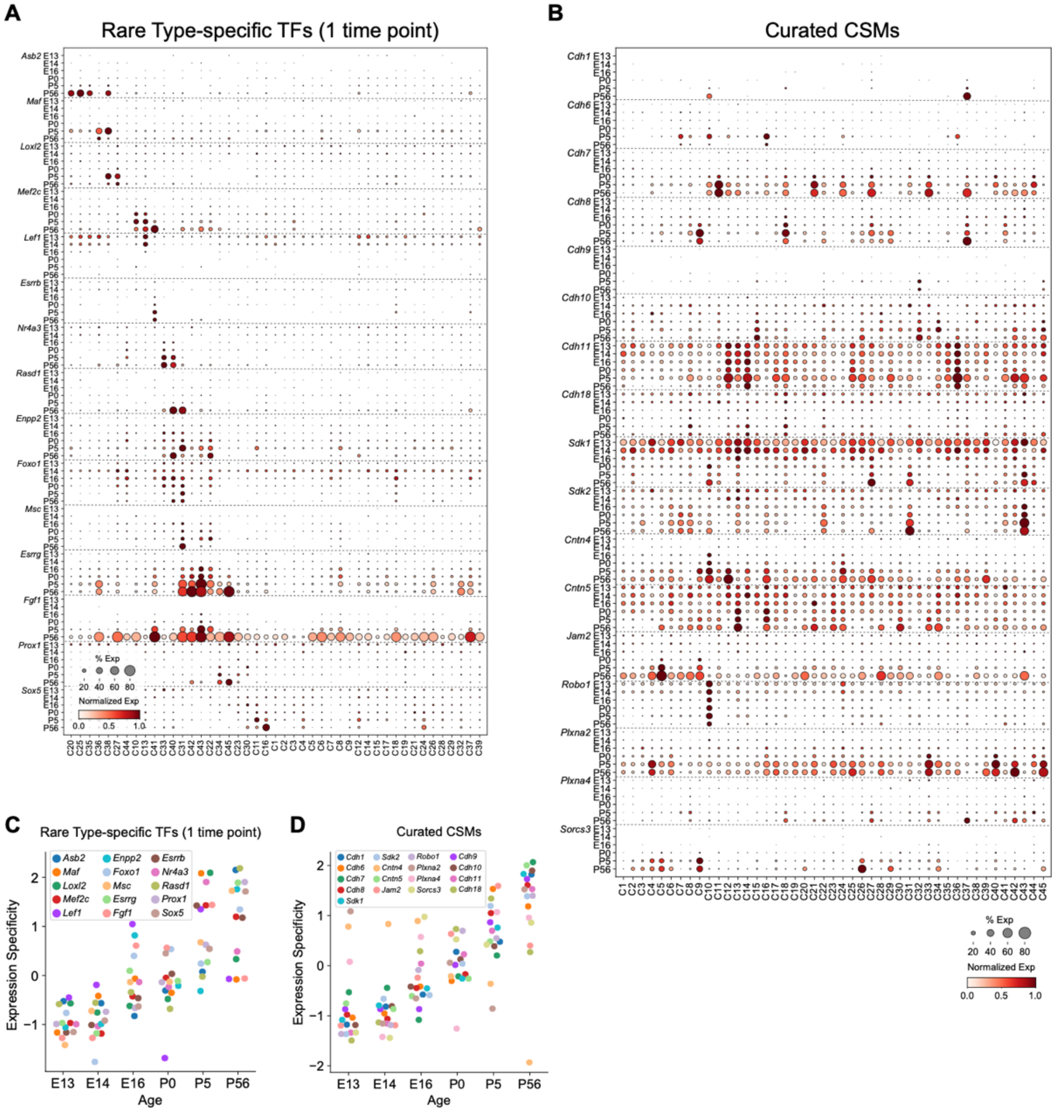

Figure S2.1. Rare type-specific TFs and assessment of CSM expression.

A. Dot plot showing expression patterns of type-specific TFs (rows) with age in putative type-specific precursors (columns). Representation as in **Figure 2.4D**. This panel only displays TFs that were identified as type-specific in at least one of the six ages.

B. Same as panel A, displaying expression patterns of a subset of CSMs known to play roles in synaptic choices of RGCs (see **Results**).

C. Expression specificity type-specific TFs shown in panel A with age. Unlike TFs in **Figure 2.4F**, here certain TFs become less specific with age.

D. Expression specificity with age for CSMs in panel B.

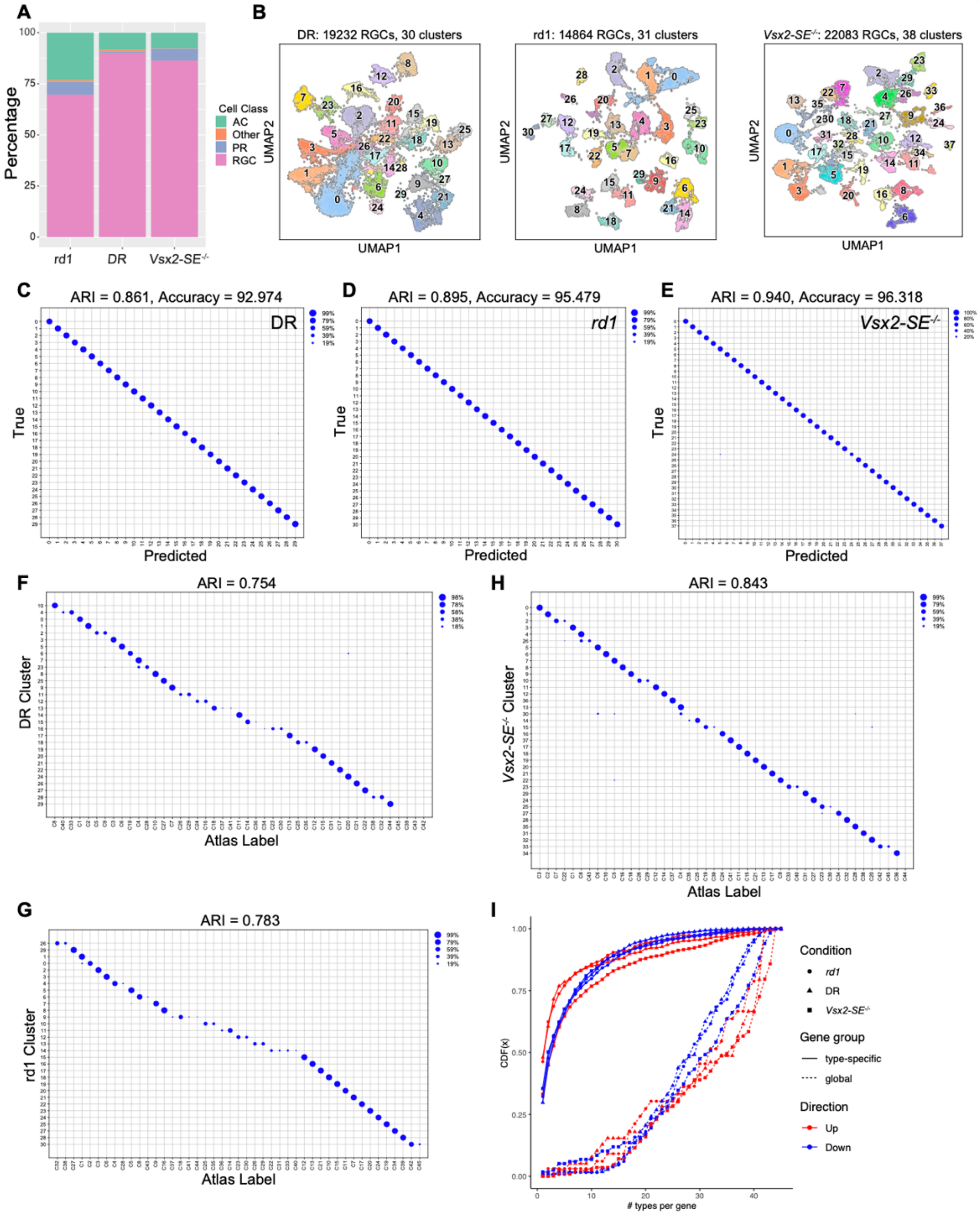

Figure S2.2. Analysis of scRNA-seq data from three visual deprivation conditions.

A. Composition (y-axis) of major cell classes in the scRNA-seq datasets collected from three visually deprived experiments (x-axis). RGCs comprised a majority (>70%) in all collections, while the main non-RGC classes included ACs and PRs. The minority category labeled as “other” predominantly comprised immune and endothelial cells.
B. Left to right: Panels showing UMAP visualization of DR RGCs, *rd1* RGCs and *Vsx2*-SE$^{-/-}$ RGCs colored by cluster identity. The coordinates are identical to Figures 2.6B-D. The number of single RGC transcriptomes analyzed in each VD model is indicated on the top of the corresponding panels.
C. Confusion matrix showing that all transcriptomically defined clusters in DR RGCs as in panel B are learnable by a classifier with >90% accuracy. ARI: adjusted Rand index, a measure (-1 to 1) of mapping specificity.
D. Same as C for *rd1* RGCs.
E. Same as C for *Vsx2*-SE$^{-/-}$ RGCs.

F. Confusion matrix showing mapping between DR clusters and NR types at P56 as in Tran et al., 2019.
G. Same as F, for *rd1* RGCs
H. Same as F, for *Vsx2*-SE$^{-/-}$ RGCs.
I. Post-hoc consistency check for global and type-specific vDE genes in each condition (shape). Each of the 12 curves corresponds to a set of vDE genes identified in a condition (*rd1*, DR, or Vsx2-SE$^{-/-}$), DE category (global or type-specific) and DE direction (up or down with respect to NR RGCs). Each vDE curve plots the cumulative distribution function or CDF (y-axis) corresponding to the number of types that show a significant change. CDF(x) denotes the fraction of genes in the vDE set that are DE in < x types. Thus, the "convex up" shape of the global vDE CDF suggests that these gene alterations are broadly shared. In contrast, the "concave up" shape of the type-specific CDFs suggests that these alterations are present only in a subset of types.

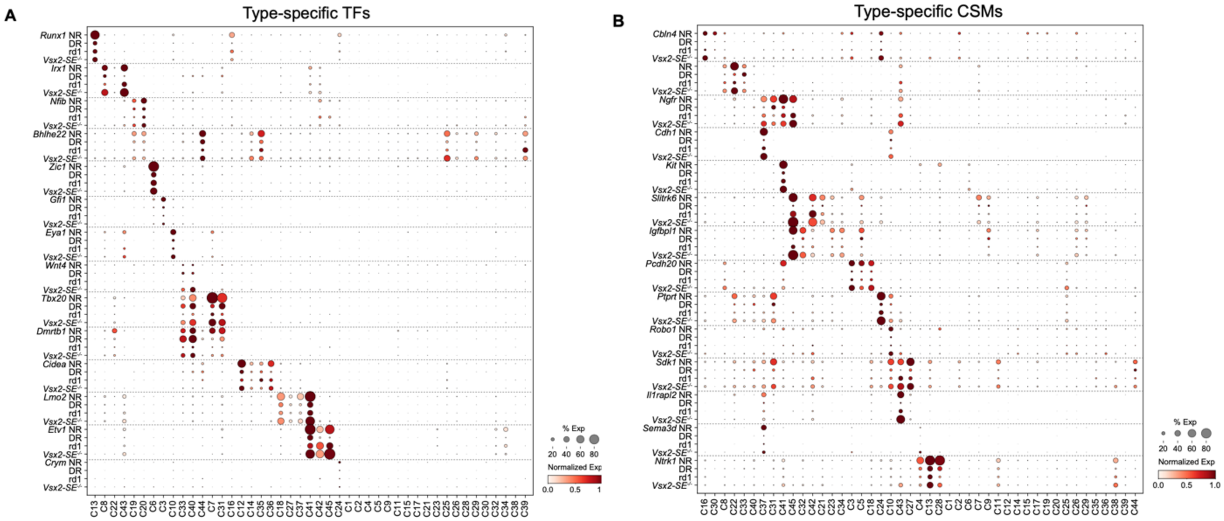

Figure S2.3. Type-specific gene expression of TFs and CSMs is maintained in VD.

A. Dot plot showing expression patterns of type-specific TFs in VD retina. Developmental profiles are shown in **Figure 2.4E**. The size of each dot corresponds to the fraction of cells with non-zero transcripts, and color indicates normalized expression levels. Row blocks corresponding to different TF are demarcated by dotted horizontal lines.
B. Same as A, but for a subset of the CSMs, including some shown in **Figure S2.1B**.

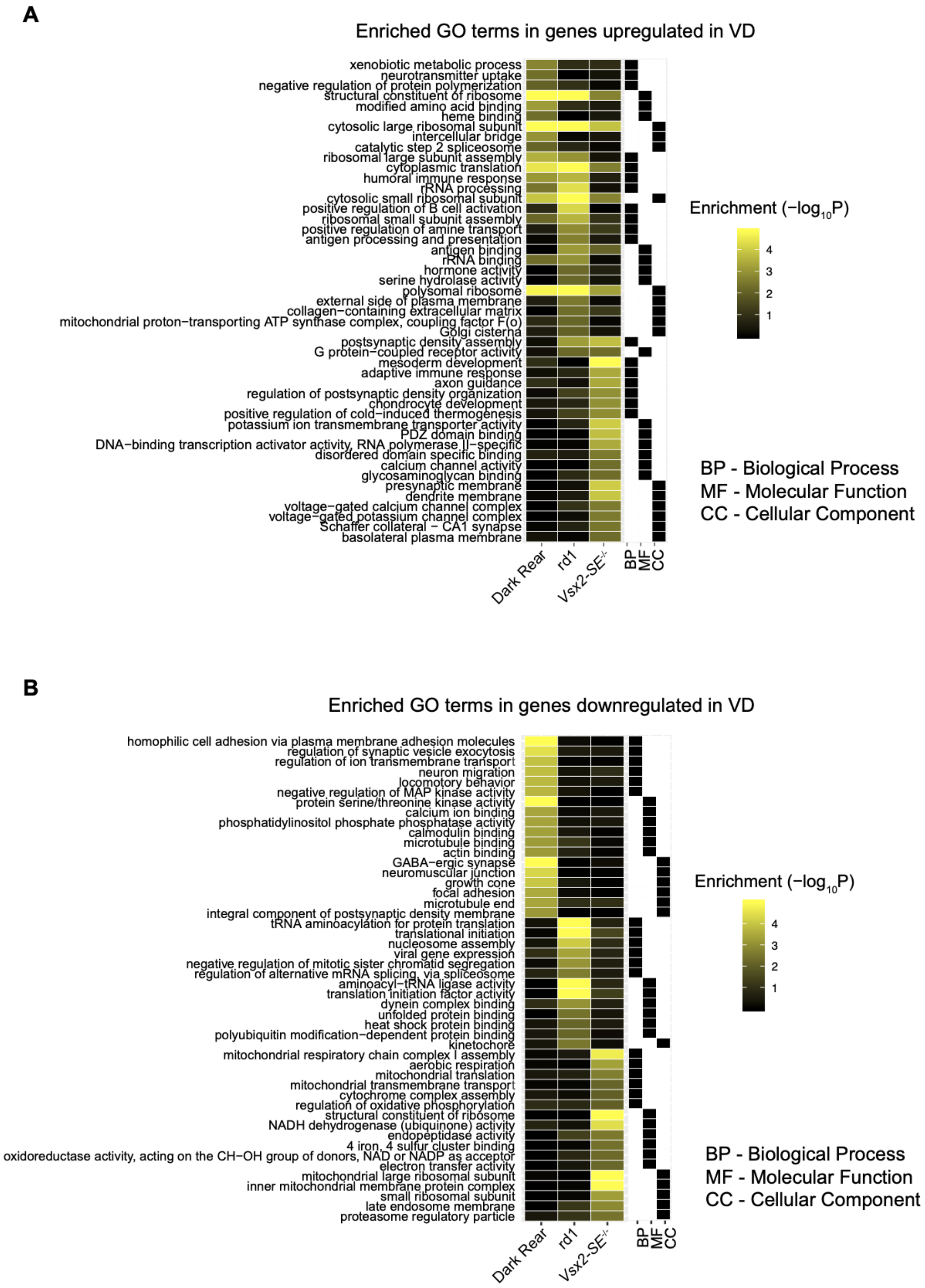

Figure S2.4. Analysis of vDE genes.

A. Heatmap displaying significant GO terms (rows) associated with genes (global and type-specific combined) that are upregulated in VD (columns) compared to NR RGCs. Values correspond to -log10(adjusted p-value). Black and white annotation bar on the right of the heatmap identifies the GO category corresponding to each row (BP, MF or CC).
B. Same as A, for downregulated genes in VD samples compared to control.

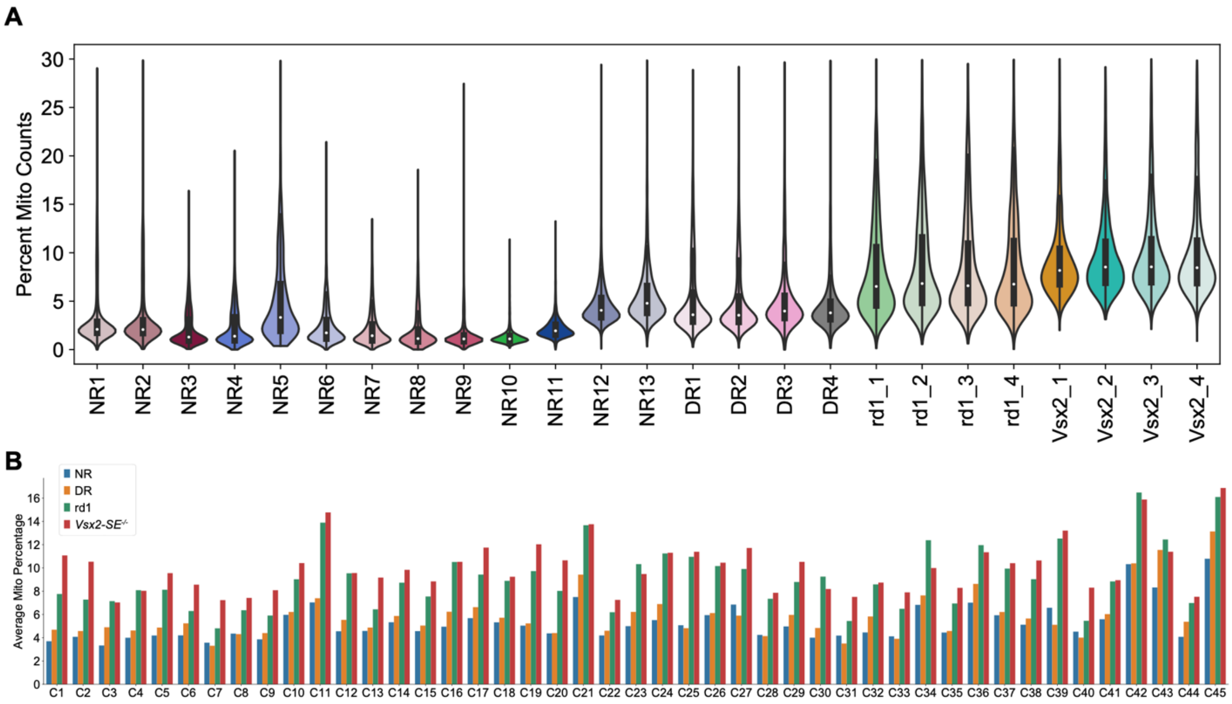

Figure S2.5. Expression of mitochondrially encoded genes in RGC types and conditions.

A. Violin plot showing that the percentage of counts associated with mitochondrial transcripts is higher in the VD biological replicates compared to NR. NR1-10 are from (Jacobi *et al.*, 2022) and constitute 36,620 RGCs not used in this study except in **Figure 2.7K**. NR11-13 are from (Tran *et al.*, 2019) and constitute the 35,699 NR RGCs used throughout this study in comparative analyses to VD RGCs. Batches were analyzed separately and the additional control data were included because apparent increases in mitochondrial gene expression are sometimes observed when cells are damaged during processing (Stegle et al., 2015). The consistent differences between NR and VD samples provides evidence that batch-to-batch variation does not account for the upregulation of mitochondrial gene expression we observed.
B. Bar plot showing the mean proportion of mitochondrial transcripts in each RGC type across all four conditions. The upregulation of mitochondrial genes in VD shows no apparent type specificity.

Supplementary Table Legends

Table S2.1. Global modules of temporally regulated genes during RGC development.

Table S2.2. Cluster-specific genes at each age during RGC development.

Table S2.3. Global vDE genes upregulated in two out of three VD conditions.

References

Alexa, A., and Rahnenführer, J. (2009). Gene set enrichment analysis with topGO. Bioconductor Improv *27*, 1-26.

Arroyo, D.A., and Feller, M.B. (2016). Spatiotemporal Features of Retinal Waves Instruct the Wiring of the Visual Circuitry. Front Neural Circuits *10*, 54. 10.3389/fncir.2016.00054.

Baden, T., Berens, P., Franke, K., Roman Roson, M., Bethge, M., and Euler, T. (2016). The functional diversity of retinal ganglion cells in the mouse. Nature *529*, 345-350. 10.1038/nature16468.

Bae, J.A., Mu, S., Kim, J.S., Turner, N.L., Tartavull, I., Kemnitz, N., Jordan, C.S., Norton, A.D., Silversmith, W.M., Prentki, R., et al. (2018). Digital Museum of Retinal Ganglion Cells with Dense Anatomy and Physiology. Cell *173*, 1293-1306 e1219. 10.1016/j.cell.2018.04.040.

Becht, E., McInnes, L., Healy, J., Dutertre, C.-A., Kwok, I.W., Ng, L.G., Ginhoux, F., and Newell, E.W. (2019). Dimensionality reduction for visualizing single-cell data using UMAP. Nature biotechnology *37*, 38-44.

Bishop, C.M., and Nasrabadi, N.M. (2006). Pattern recognition and machine learning (Springer).

Blondel, V.D., Guillaume, J.-L., Lambiotte, R., and Lefebvre, E. (2008). Fast unfolding of communities in large networks. Journal of statistical mechanics: theory and experiment *2008*, P10008.

Bodnarenko, S.R., Jeyarasasingam, G., and Chalupa, L.M. (1995). Development and regulation of dendritic stratification in retinal ganglion cells by glutamate-mediated afferent activity. J Neurosci *15*, 7037-7045.

Bonhoeffer, F., and Huf, J. (1985). Position-dependent properties of retinal axons and their growth cones. Nature *315*, 409-410. 10.1038/315409a0.

Burmeister, M., Novak, J., Liang, M.Y., Basu, S., Ploder, L., Hawes, N.L., Vidgen, D., Hoover, F., Goldman, D., Kalnins, V.I., et al. (1996). Ocular retardation mouse caused by Chx10 homeobox null allele: impaired retinal progenitor proliferation and bipolar cell differentiation. Nat Genet *12*, 376-384. 10.1038/ng0496-376.

Cang, J., Renteria, R.C., Kaneko, M., Liu, X., Copenhagen, D.R., and Stryker, M.P. (2005). Development of precise maps in visual cortex requires patterned spontaneous activity in the retina. Neuron *48*, 797-809. 10.1016/j.neuron.2005.09.015.

Carrasco, M.M., Razak, K.A., and Pallas, S.L. (2005). Visual experience is necessary for maintenance but not development of receptive fields in superior colliculus. Journal of neurophysiology *94*, 1962-1970.

Chalupa, L.M., and Gunhan, E. (2004). Development of On and Off retinal pathways and retinogeniculate projections. Prog Retin Eye Res *23*, 31-51. 10.1016/j.preteyeres.2003.10.001.

Cheadle, L., Tzeng, C.P., Kalish, B.T., Harmin, D.A., Rivera, S., Ling, E., Nagy, M.A., Hrvatin, S., Hu, L., Stroud, H., et al. (2018). Visual Experience-Dependent Expression of Fn14 Is Required for Retinogeniculate Refinement. Neuron *99*, 525-539 e510. 10.1016/j.neuron.2018.06.036.

Chen, T., and Guestrin, C. (2016). Xgboost: A scalable tree boosting system. pp. 785-794.

Cheng, H.J., Nakamoto, M., Bergemann, A.D., and Flanagan, J.G. (1995). Complementary gradients in expression and binding of ELF-1 and Mek4 in development of the topographic retinotectal projection map. Cell *82*, 371-381. 10.1016/0092-8674(95)90426-3.

Cheng, S., Butrus, S., Tan, L., Xu, R., Sagireddy, S., Trachtenberg, J.T., Shekhar, K., and Zipursky, S.L. (2022). Vision-dependent specification of cell types and function in the developing cortex. Cell *185*, 311-327 e324. 10.1016/j.cell.2021.12.022.

Choi, H., Zhang, L., Cembrowski, M.S., Sabottke, C.F., Markowitz, A.L., Butts, D.A., Kath, W.L., Singer, J.H., and Riecke, H. (2014). Intrinsic bursting of AII amacrine cells underlies oscillations in the rd1 mouse retina. J Neurophysiol *112*, 1491-1504. 10.1152/jn.00437.2014.

Dhande, O.S., Stafford, B.K., Franke, K., El-Danaf, R., Percival, K.A., Phan, A.H., Li, P., Hansen, B.J., Nguyen, P.L., Berens, P., et al. (2019). Molecular Fingerprinting of On-Off Direction-Selective Retinal Ganglion Cells Across Species and Relevance to Primate Visual Circuits. J Neurosci *39*, 78-95. 10.1523/JNEUROSCI.1784-18.2018.

Dhande, O.S., Stafford, B.K., Lim, J.A., and Huberman, A.D. (2015). Contributions of Retinal Ganglion Cells to Subcortical Visual Processing and Behaviors. Annu Rev Vis Sci *1*, 291-328. 10.1146/annurev-vision-082114-035502.

Drager, U.C. (1985). Birth dates of retinal ganglion cells giving rise to the crossed and uncrossed optic projections in the mouse. Proc R Soc Lond B Biol Sci *224*, 57-77. 10.1098/rspb.1985.0021.

Drescher, U., Kremoser, C., Handwerker, C., Loschinger, J., Noda, M., and Bonhoeffer, F. (1995). In vitro guidance of retinal ganglion cell axons by RAGS, a 25 kDa tectal protein related to ligands for Eph receptor tyrosine kinases. Cell *82*, 359-370. 10.1016/0092-8674(95)90425-5.

Duan, X., Krishnaswamy, A., De la Huerta, I., and Sanes, J.R. (2014). Type II cadherins guide assembly of a direction-selective retinal circuit. Cell *158*, 793-807. 10.1016/j.cell.2014.06.047.

Duan, X., Krishnaswamy, A., Laboulaye, M.A., Liu, J., Peng, Y.R., Yamagata, M., Toma, K., and Sanes, J.R. (2018). Cadherin Combinations Recruit Dendrites of Distinct Retinal Neurons to a Shared Interneuronal Scaffold. Neuron *99*, 1145-1154 e1146. 10.1016/j.neuron.2018.08.019.

El-Quessny, M., Maanum, K., and Feller, M.B. (2020). Visual Experience Influences Dendritic Orientation but Is Not Required for Asymmetric Wiring of the Retinal Direction Selective Circuit. Cell Rep *31*, 107844. 10.1016/j.celrep.2020.107844.

Farah, M.H., and Easter, S.S., Jr. (2005). Cell birth and death in the mouse retinal ganglion cell layer. J Comp Neurol *489*, 120-134. 10.1002/cne.20615.

Farber, D.B., Flannery, J.G., and Bowes-Rickman, C. (1994). The rd mouse story: seventy years of research on an animal model of inherited retinal degeneration. Progress in retinal and eye research *13*, 31-64.

Feldheim, D.A., and O'Leary, D.D. (2010). Visual map development: bidirectional signaling, bifunctional guidance molecules, and competition. Cold Spring Harb Perspect Biol *2*, a001768. 10.1101/cshperspect.a001768.

Feller, M., and Kerschensteiner, D. (2020). Retinal waves and their role in visual system development. In Synapse Development and Maturation, (Elsevier), pp. 367-382.

Finak, G., McDavid, A., Yajima, M., Deng, J., Gersuk, V., Shalek, A.K., Slichter, C.K., Miller, H.W., McElrath, M.J., Prlic, M., et al. (2015). MAST: a flexible statistical framework for assessing transcriptional changes and characterizing heterogeneity in single-cell RNA sequencing data. Genome Biol *16*, 278. 10.1186/s13059-015-0844-5.

Fruchterman, T.M., and Reingold, E.M. (1991). Graph drawing by force-directed placement. Software: Practice and experience *21*, 1129-1164.

Gamlin, C.R., Zhang, C., Dyer, M.A., and Wong, R.O.L. (2020). Distinct Developmental Mechanisms Act Independently to Shape Biased Synaptic Divergence from an Inhibitory Neuron. Curr Biol *30*, 1258-1268 e1252. 10.1016/j.cub.2020.01.080.

Gibson, R., Fletcher, E.L., Vingrys, A.J., Zhu, Y., Vessey, K.A., and Kalloniatis, M. (2013). Functional and neurochemical development in the normal and degenerating mouse retina. J Comp Neurol *521*, 1251-1267. 10.1002/cne.23284.

Godement, P., Salaun, J., and Imbert, M. (1984). Prenatal and postnatal development of retinogeniculate and retinocollicular projections in the mouse. J Comp Neurol *230*, 552-575. 10.1002/cne.902300406.

Goetz, J., Jessen, Z.F., Jacobi, A., Mani, A., Cooler, S., Greer, D., Kadri, S., Segal, J., Shekhar, K., and Sanes, J. (2021). Unified classification of mouse retinal ganglion cells using function, morphology, and gene expression. bioRxiv.

Goo, Y.S., Park, D.J., Ahn, J.R., and Senok, S.S. (2015). Spontaneous Oscillatory Rhythms in the Degenerating Mouse Retina Modulate Retinal Ganglion Cell Responses to Electrical Stimulation. Front Cell Neurosci *9*, 512. 10.3389/fncel.2015.00512.

Holt, C.E., Martin, K.C., and Schuman, E.M. (2019). Local translation in neurons: visualization and function. Nat Struct Mol Biol *26*, 557-566. 10.1038/s41594-019-0263-5.

Hooks, B.M., and Chen, C. (2006). Distinct roles for spontaneous and visual activity in remodeling of the retinogeniculate synapse. Neuron *52*, 281-291.

Hooks, B.M., and Chen, C. (2007). Critical periods in the visual system: changing views for a model of experience-dependent plasticity. Neuron *56*, 312-326. 10.1016/j.neuron.2007.10.003.

Hooks, B.M., and Chen, C. (2008). Vision triggers an experience-dependent sensitive period at the retinogeniculate synapse. J Neurosci *28*, 4807-4817. 10.1523/JNEUROSCI.4667-07.2008.

Hrvatin, S., Hochbaum, D.R., Nagy, M.A., Cicconet, M., Robertson, K., Cheadle, L., Zilionis, R., Ratner, A., Borges-Monroy, R., Klein, A.M., et al. (2018). Single-cell analysis of experience-dependent transcriptomic states in the mouse visual cortex. Nat Neurosci *21*, 120-129. 10.1038/s41593-017-0029-5.

Jacobi, A., Tran, N.M., Yan, W., Benhar, I., Tian, F., Schaffer, R., He, Z., and Sanes, J. (2022). Overlapping transcriptional programs promote survival and axonal regeneration of injured retinal ganglion cells. bioRxiv.

Jacomy, M., Venturini, T., Heymann, S., and Bastian, M. (2014). ForceAtlas2, a continuous graph layout algorithm for handy network visualization designed for the Gephi software. PLoS One *9*, e98679. 10.1371/journal.pone.0098679.

Jantzen, S.G., Sutherland, B.J., Minkley, D.R., and Koop, B.F. (2011). GO Trimming: Systematically reducing redundancy in large Gene Ontology datasets. BMC Res Notes *4*, 267. 10.1186/1756-0500-4-267.

Jiang, Y., Ding, Q., Xie, X., Libby, R.T., Lefebvre, V., and Gan, L. (2013). Transcription factors SOX4 and SOX11 function redundantly to regulate the development of mouse retinal ganglion cells. J Biol Chem *288*, 18429-18438. 10.1074/jbc.M113.478503.

Jin, K., Jiang, H., Mo, Z., and Xiang, M. (2010). Early B-cell factors are required for specifying multiple retinal cell types and subtypes from postmitotic precursors. J Neurosci *30*, 11902-11916. 10.1523/JNEUROSCI.2187-10.2010.

Katz, L.C., and Shatz, C.J. (1996). Synaptic activity and the construction of cortical circuits. Science *274*, 1133-1138. 10.1126/science.274.5290.1133.

Keeler, C.E. (1924). The Inheritance of a Retinal Abnormality in White Mice. Proc Natl Acad Sci U S A *10*, 329-333. 10.1073/pnas.10.7.329.

Kerschensteiner, D., Morgan, J.L., Parker, E.D., Lewis, R.M., and Wong, R.O. (2009). Neurotransmission selectively regulates synapse formation in parallel circuits in vivo. Nature *460*, 1016-1020. 10.1038/nature08236.

Kim, I.J., Zhang, Y., Meister, M., and Sanes, J.R. (2010). Laminar restriction of retinal ganglion cell dendrites and axons: subtype-specific developmental patterns revealed with transgenic markers. J Neurosci *30*, 1452-1462. 10.1523/JNEUROSCI.4779-09.2010.

Kirkby, L.A., and Feller, M.B. (2013). Intrinsically photosensitive ganglion cells contribute to plasticity in retinal wave circuits. Proc Natl Acad Sci U S A *110*, 12090-12095. 10.1073/pnas.1222150110.

Kirkby, L.A., Sack, G.S., Firl, A., and Feller, M.B. (2013). A role for correlated spontaneous activity in the assembly of neural circuits. Neuron *80*, 1129-1144. 10.1016/j.neuron.2013.10.030.

Kiyama, T., Long, Y., Chen, C.K., Whitaker, C.M., Shay, A., Wu, H., Badea, T.C., Mohsenin, A., Parker-Thornburg, J., Klein, W.H., et al. (2019). Essential Roles of Tbr1 in the Formation and Maintenance of the Orientation-Selective J-RGCs and a Group of OFF-Sustained RGCs in Mouse. Cell Rep *27*, 900-915 e905. 10.1016/j.celrep.2019.03.077.

Kong, X.Y., Wienecke, J., Chen, M., Hultborn, H., and Zhang, M. (2011). The time course of serotonin 2A receptor expression after spinal transection of rats: an immunohistochemical study. Neuroscience *177*, 114-126. 10.1016/j.neuroscience.2010.12.062.

Korsunsky, I., Millard, N., Fan, J., Slowikowski, K., Zhang, F., Wei, K., Baglaenko, Y., Brenner, M., Loh, P.R., and Raychaudhuri, S. (2019). Fast, sensitive and accurate integration of single-cell data with Harmony. Nat Methods *16*, 1289-1296. 10.1038/s41592-019-0619-0.

Krishnaswamy, A., Yamagata, M., Duan, X., Hong, Y.K., and Sanes, J.R. (2015). Sidekick 2 directs formation of a retinal circuit that detects differential motion. Nature *524*, 466-470. 10.1038/nature14682.

Kuffler, S.W., Dennis, M.J., and Harris, A.J. (1971). The development of chemosensitivity in extrasynaptic areas of the neuronal surface after denervation of parasympathetic ganglion cells in the heart of the frog. Proc R Soc Lond B Biol Sci *177*, 555-563. 10.1098/rspb.1971.0047.

Kuwajima, T., Soares, C.A., Sitko, A.A., Lefebvre, V., and Mason, C. (2017). SoxC Transcription Factors Promote Contralateral Retinal Ganglion Cell Differentiation and Axon Guidance in the Mouse Visual System. Neuron *93*, 1110-1125 e1115. 10.1016/j.neuron.2017.01.029.

Lefebvre, J.L., Sanes, J.R., and Kay, J.N. (2015). Development of dendritic form and function. Annu Rev Cell Dev Biol *31*, 741-777. 10.1146/annurev-cellbio-100913-013020.

Liu, I.S., Chen, J.D., Ploder, L., Vidgen, D., van der Kooy, D., Kalnins, V.I., and McInnes, R.R. (1994). Developmental expression of a novel murine homeobox gene (Chx10): evidence for roles in determination of the neuroretina and inner nuclear layer. Neuron *13*, 377-393. 10.1016/0896-6273(94)90354-9.

Liu, J., Reggiani, J.D.S., Laboulaye, M.A., Pandey, S., Chen, B., Rubenstein, J.L.R., Krishnaswamy, A., and Sanes, J.R. (2018). Tbr1 instructs laminar patterning of retinal ganglion cell dendrites. Nat Neurosci *21*, 659-670. 10.1038/s41593-018-0127-z.

Liu, J., and Sanes, J.R. (2017). Cellular and Molecular Analysis of Dendritic Morphogenesis in a Retinal Cell Type That Senses Color Contrast and Ventral Motion. J Neurosci *37*, 12247-12262. 10.1523/JNEUROSCI.2098-17.2017.

Lu, Y., Shiau, F., Yi, W., Lu, S., Wu, Q., Pearson, J.D., Kallman, A., Zhong, S., Hoang, T., Zuo, Z., et al. (2020). Single-Cell Analysis of Human Retina Identifies Evolutionarily Conserved and Species-Specific Mechanisms Controlling Development. Dev Cell *53*, 473-491 e479. 10.1016/j.devcel.2020.04.009.

Lyu, J., and Mu, X. (2021). Genetic control of retinal ganglion cell genesis. Cell Mol Life Sci *78*, 4417-4433. 10.1007/s00018-021-03814-w.

Macosko, E.Z., Basu, A., Satija, R., Nemesh, J., Shekhar, K., Goldman, M., Tirosh, I., Bialas, A.R., Kamitaki, N., Martersteck, E.M., et al. (2015). Highly Parallel Genome-wide Expression Profiling of Individual Cells Using Nanoliter Droplets. Cell *161*, 1202-1214. 10.1016/j.cell.2015.05.002.

Mao, C.-A., Chen, C.-K., Kiyama, T., Weber, N., Whitaker, C.M., Pan, P., Badea, T.C., and Massey, S.C. (2020). Tbr2-expressing retinal ganglion cells are ipRGCs. bioRxiv.

Marcucci, F., Soares, C.A., and Mason, C. (2019). Distinct timing of neurogenesis of ipsilateral and contralateral retinal ganglion cells. J Comp Neurol *527*, 212-224. 10.1002/cne.24467.

Martersteck, E.M., Hirokawa, K.E., Evarts, M., Bernard, A., Duan, X., Li, Y., Ng, L., Oh, S.W., Ouellette, B., Royall, J.J., et al. (2017). Diverse Central Projection Patterns of Retinal Ganglion Cells. Cell Rep *18*, 2058-2072. 10.1016/j.celrep.2017.01.075.

Matsuoka, R.L., Nguyen-Ba-Charvet, K.T., Parray, A., Badea, T.C., Chedotal, A., and Kolodkin, A.L. (2011). Transmembrane semaphorin signalling controls laminar stratification in the mammalian retina. Nature *470*, 259-263. 10.1038/nature09675.

McLaughlin, T., Torborg, C.L., Feller, M.B., and O'Leary, D.D. (2003). Retinotopic map refinement requires spontaneous retinal waves during a brief critical period of development. Neuron *40*, 1147-1160. 10.1016/s0896-6273(03)00790-6.

Morgan, J.L., Soto, F., Wong, R.O., and Kerschensteiner, D. (2011). Development of cell type-specific connectivity patterns of converging excitatory axons in the retina. Neuron *71*, 1014-1021. 10.1016/j.neuron.2011.08.025.

Norrie, J.L., Lupo, M.S., Xu, B., Al Diri, I., Valentine, M., Putnam, D., Griffiths, L., Zhang, J., Johnson, D., Easton, J., et al. (2019). Nucleome Dynamics during Retinal Development. Neuron *104*, 512-528 e511. 10.1016/j.neuron.2019.08.002.

Okawa, H., Della Santina, L., Schwartz, G.W., Rieke, F., and Wong, R.O. (2014). Interplay of cell-autonomous and nonautonomous mechanisms tailors synaptic connectivity of converging axons in vivo. Neuron *82*, 125-137. 10.1016/j.neuron.2014.02.016.

Osterhout, J.A., Josten, N., Yamada, J., Pan, F., Wu, S.W., Nguyen, P.L., Panagiotakos, G., Inoue, Y.U., Egusa, S.F., Volgyi, B., et al. (2011). Cadherin-6 mediates axon-target matching in a non-image-forming visual circuit. Neuron *71*, 632-639. 10.1016/j.neuron.2011.07.006.

Osterhout, J.A., Stafford, B.K., Nguyen, P.L., Yoshihara, Y., and Huberman, A.D. (2015). Contactin-4 mediates axon-target specificity and functional development of the accessory optic system. Neuron *86*, 985-999. 10.1016/j.neuron.2015.04.005.

Pandey, S., Shekhar, K., Regev, A., and Schier, A.F. (2018). Comprehensive Identification and Spatial Mapping of Habenular Neuronal Types Using Single-Cell RNA-Seq. Curr Biol *28*, 1052-1065 e1057. 10.1016/j.cub.2018.02.040.

Peng, Y.R., Tran, N.M., Krishnaswamy, A., Kostadinov, D., Martersteck, E.M., and Sanes, J.R. (2017). Satb1 Regulates Contactin 5 to Pattern Dendrites of a Mammalian Retinal Ganglion Cell. Neuron *95*, 869-883 e866. 10.1016/j.neuron.2017.07.019.

Punzo, C., and Cepko, C. (2007). Cellular responses to photoreceptor death in the rd1 mouse model of retinal degeneration. Invest Ophthalmol Vis Sci *48*, 849-857. 10.1167/iovs.05-1555.

Rheaume, B.A., Jereen, A., Bolisetty, M., Sajid, M.S., Yang, Y., Renna, K., Sun, L., Robson, P., and Trakhtenberg, E.F. (2018). Single cell transcriptome profiling of retinal ganglion cells identifies cellular subtypes. Nat Commun *9*, 2759. 10.1038/s41467-018-05134-3.

Rousseeuw, P.J. (1987). Silhouettes: a graphical aid to the interpretation and validation of cluster analysis. Journal of computational and applied mathematics *20*, 53-65.

Rousso, D.L., Qiao, M., Kagan, R.D., Yamagata, M., Palmiter, R.D., and Sanes, J.R. (2016). Two Pairs of ON and OFF Retinal Ganglion Cells Are Defined by Intersectional Patterns of Transcription Factor Expression. Cell Rep *15*, 1930-1944. 10.1016/j.celrep.2016.04.069.

Sajgo, S., Ghinia, M.G., Brooks, M., Kretschmer, F., Chuang, K., Hiriyanna, S., Wu, Z., Popescu, O., and Badea, T.C. (2017). Molecular codes for cell type specification in Brn3 retinal ganglion cells. Proc Natl Acad Sci U S A *114*, E3974-E3983. 10.1073/pnas.1618551114.

Sanes, J.R., and Masland, R.H. (2015). The types of retinal ganglion cells: current status and implications for neuronal classification. Annu Rev Neurosci *38*, 221-246. 10.1146/annurev-neuro-071714-034120.

Sanes, J.R., and Zipursky, S.L. (2020). Synaptic Specificity, Recognition Molecules, and Assembly of Neural Circuits. Cell *181*, 1434-1435. 10.1016/j.cell.2020.05.046.

Sapkota, D., Chintala, H., Wu, F., Fliesler, S.J., Hu, Z., and Mu, X. (2014). Onecut1 and Onecut2 redundantly regulate early retinal cell fates during development. Proc Natl Acad Sci U S A *111*, E4086-4095. 10.1073/pnas.1405354111.

Schiebinger, G., Shu, J., Tabaka, M., Cleary, B., Subramanian, V., Solomon, A., Gould, J., Liu, S., Lin, S., Berube, P., et al. (2019). Optimal-Transport Analysis of Single-Cell Gene Expression Identifies Developmental Trajectories in Reprogramming. Cell *176*, 1517. 10.1016/j.cell.2019.02.026.

Schindelin, J., Arganda-Carreras, I., Frise, E., Kaynig, V., Longair, M., Pietzsch, T., Preibisch, S., Rueden, C., Saalfeld, S., Schmid, B., et al. (2012). Fiji: an open-source platform for biological-image analysis. Nat Methods *9*, 676-682. 10.1038/nmeth.2019.

Schmidt, J.T., and Buzzard, M. (1993). Activity-driven sharpening of the retinotectal projection in goldfish: development under stroboscopic illumination prevents sharpening. J Neurobiol *24*, 384-399. 10.1002/neu.480240310.

Sernagor, E., Eglen, S.J., and Wong, R.O. (2001). Development of retinal ganglion cell structure and function. Prog Retin Eye Res *20*, 139-174. 10.1016/s1350-9462(00)00024-0.

Shekhar, K., Whitney, I.E., Butrus, S., Peng, Y.R., and Sanes, J.R. (2022). Diversification of multipotential postmitotic mouse retinal ganglion cell precursors into discrete types. Elife *11*. 10.7554/eLife.73809.

Sperry, R.W. (1963). Chemoaffinity in the Orderly Growth of Nerve Fiber Patterns and Connections. Proc Natl Acad Sci U S A *50*, 703-710. 10.1073/pnas.50.4.703.

Stahl, B., Muller, B., von Boxberg, Y., Cox, E.C., and Bonhoeffer, F. (1990a). Biochemical characterization of a putative axonal guidance molecule of the chick visual system. Neuron *5*, 735-743. 10.1016/0896-6273(90)90227-7.

Stahl, B., von Boxberg, Y., Muller, B., Walter, J., Schwarz, U., and Bonhoeffer, F. (1990b). Directional cues for retinal axons. Cold Spring Harb Symp Quant Biol *55*, 351-357. 10.1101/sqb.1990.055.01.036.

Stasheff, S.F. (2008). Emergence of sustained spontaneous hyperactivity and temporary preservation of OFF responses in ganglion cells of the retinal degeneration (rd1) mouse. J Neurophysiol *99*, 1408-1421. 10.1152/jn.00144.2007.

Stegle, O., Teichmann, S.A., and Marioni, J.C. (2015). Computational and analytical challenges in single-cell transcriptomics. Nat Rev Genet *16*, 133-145. 10.1038/nrg3833.

Sweeney, N.T., James, K.N., Nistorica, A., Lorig-Roach, R.M., and Feldheim, D.A. (2019). Expression of transcription factors divides retinal ganglion cells into distinct classes. J Comp Neurol *527*, 225-235. 10.1002/cne.24172.

The Gene Ontology, C. (2019). The Gene Ontology Resource: 20 years and still GOing strong. Nucleic Acids Res *47*, D330-D338. 10.1093/nar/gky1055.

Tian, N., and Copenhagen, D.R. (2003). Visual stimulation is required for refinement of ON and OFF pathways in postnatal retina. Neuron *39*, 85-96. 10.1016/s0896-6273(03)00389-1.

Tibshirani, R., Walther, G., and Hastie, T. (2001). Estimating the number of clusters in a data set via the gap statistic. Journal of the Royal Statistical Society: Series B (Statistical Methodology) *63*, 411-423.

Tintignac, L.A., Brenner, H.R., and Ruegg, M.A. (2015). Mechanisms Regulating Neuromuscular Junction Development and Function and Causes of Muscle Wasting. Physiol Rev *95*, 809-852. 10.1152/physrev.00033.2014.

Tiriac, A., Bistrong, K., Pitcher, M.N., Tworig, J.M., and Feller, M.B. (2022). The influence of spontaneous and visual activity on the development of direction selectivity maps in mouse retina. Cell Rep *38*, 110225. 10.1016/j.celrep.2021.110225.

Tiriac, A., Smith, B.E., and Feller, M.B. (2018). Light Prior to Eye Opening Promotes Retinal Waves and Eye-Specific Segregation. Neuron *100*, 1059-1065 e1054. 10.1016/j.neuron.2018.10.011.

Tran, N.M., Shekhar, K., Whitney, I.E., Jacobi, A., Benhar, I., Hong, G., Yan, W., Adiconis, X., Arnold, M.E., Lee, J.M., et al. (2019). Single-Cell Profiles of Retinal Ganglion Cells Differing in Resilience to Injury Reveal Neuroprotective Genes. Neuron *104*, 1039-1055 e1012. 10.1016/j.neuron.2019.11.006.

Tropea, D., Kreiman, G., Lyckman, A., Mukherjee, S., Yu, H., Horng, S., and Sur, M. (2006). Gene expression changes and molecular pathways mediating activity-dependent plasticity in visual cortex. Nat Neurosci *9*, 660-668. 10.1038/nn1689.

Voinescu, P.E., Kay, J.N., and Sanes, J.R. (2009). Birthdays of retinal amacrine cell subtypes are systematically related to their molecular identity and soma position. J Comp Neurol *517*, 737-750. 10.1002/cne.22200.

Walter, J., Henke-Fahle, S., and Bonhoeffer, F. (1987a). Avoidance of posterior tectal membranes by temporal retinal axons. Development *101*, 909-913. 10.1242/dev.101.4.909.

Walter, J., Kern-Veits, B., Huf, J., Stolze, B., and Bonhoeffer, F. (1987b). Recognition of position-specific properties of tectal cell membranes by retinal axons in vitro. Development *101*, 685-696. 10.1242/dev.101.4.685.

Weinreb, C., Wolock, S., and Klein, A.M. (2018). SPRING: a kinetic interface for visualizing high dimensional single-cell expression data. Bioinformatics *34*, 1246-1248. 10.1093/bioinformatics/btx792.

Wong, R.O. (1999). Retinal waves and visual system development. Annu Rev Neurosci *22*, 29-47. 10.1146/annurev.neuro.22.1.29.

Yamagata, M., and Sanes, J.R. (2018). Expression and Roles of the Immunoglobulin Superfamily Recognition Molecule Sidekick1 in Mouse Retina. Front Mol Neurosci *11*, 485. 10.3389/fnmol.2018.00485.

Yu-Wai-Man, P., Griffiths, P.G., and Chinnery, P.F. (2011). Mitochondrial optic neuropathies - disease mechanisms and therapeutic strategies. Prog Retin Eye Res *30*, 81-114. 10.1016/j.preteyeres.2010.11.002.

Zhang, C., Kolodkin, A.L., Wong, R.O., and James, R.E. (2017). Establishing Wiring Specificity in Visual System Circuits: From the Retina to the Brain. Annu Rev Neurosci *40*, 395-424. 10.1146/annurev-neuro-072116-031607.

Chapter 3: Vision-dependent specification of cell types and function in the developing cortex

This chapter is adapted from the following published work:

Sarah Cheng*, **Salwan Butrus***, Liming Tan*, Runzhe Xu, Srikant Sagireddy, Joshua T. Trachtenberg, Karthik Shekhar#, and S. Lawrence Zipursky#. *Cell*, **185**, 311-327 (2022).

* Equal contribution
\# Corresponding authors

S.C. and R.X. performed all scRNA-seq and FISH experiments. S.B. performed all computational analyses with assistance from S.S. L.T. performed all functional experiments.

Abstract

The role of postnatal experience in sculpting cortical circuitry, while long appreciated, is poorly understood at the level of cell types. We explore this in the mouse primary visual cortex (V1) using single-nucleus RNA-sequencing, visual deprivation, genetics, and functional imaging. We find that vision selectively drives the specification of glutamatergic cell types in upper layers (L) (L2/3/4), while deeper-layer glutamatergic, GABAergic, and non-neuronal cell types are established prior to eye opening. L2/3 cell types form an experience-dependent spatial continuum defined by the graded expression of ~200 genes, including regulators of cell adhesion and synapse formation. One of these, *Igsf9b*, a vision-dependent gene encoding an inhibitory synaptic cell adhesion molecule, is required for the normal development of binocular responses in L2/3. In summary, vision preferentially regulates the development of upper-layer glutamatergic cell types through the regulation of cell type-specific gene expression programs.

Introduction

The establishment of neural circuitry in the mammalian cortex relies on the interaction of the developing postnatal animal with its environment. Cortical circuits comprise diverse cell types interconnected by complex synaptic networks (Motta et al., 2019; Tasic et al., 2016). The formation of this circuitry relies on genetically hard-wired mechanisms mediated by cell recognition molecules and sensory-independent neural activity (Ackman et al., 2012; Katz and Shatz, 1996; Ko et al., 2013; Meister et al., 1991; Sanes and Zipursky, 2020; Xu et al., 2011). During postnatal development, experience-dependent processes are required for the maturation of this circuitry (Hensch, 2004, 2005; Hooks and Chen, 2020; Ko et al., 2013; Wiesel and Hubel, 1963). These periods of developmental plasticity, known as "critical periods", are observed in sensory cortical areas and regulate processes such as language development and cognition (Reh et al., 2020).

The influence of experience on cortical circuitry in the primary visual cortex (V1) is accessible to molecular, genetic, and functional analysis in the mouse and thus is well suited for mechanistic studies (Hooks and Chen, 2020). Neural circuitry is patterned by vision (Gordon and Stryker, 1996; Tan et al., 2020) and this process can be studied through longitudinal calcium imaging of neurons in V1 of awake behaving animals (Tan et al., 2021; Tan et al., 2020). Mice open their eyes around postnatal day (P)14. Binocular circuitry is sensitive to vision after eye opening, but its peak period of sensitivity, demonstrated and defined by the effects of monocular deprivation on cortical ocular dominance, begins about a week after eye opening (~P21) and continues through ~P35 (Espinosa and Stryker, 2012; Gordon and Stryker, 1996). Visual experience during this period is necessary for the development and maintenance of the neural circuitry underlying binocular vision (Espinosa and Stryker, 2012; Gordon and Stryker, 1996; Ko et al., 2013; Ko et al., 2014; Tan et al., 2021; Tan et al., 2020; Wang et al., 2010).

Recent advances in single-cell transcriptomics have uncovered a vast neuronal diversity in the adult mouse V1 (Hrvatin et al., 2018; Tasic et al., 2016; Tasic et al., 2018). Previous investigations of vision-dependent changes in gene expression during the critical period have relied on comparing bulk transcriptomic profiles of V1 between normally reared and visually deprived animals (Majdan and Shatz, 2006; Mardinly et al., 2016; Tropea et al., 2006), or within normally reared animals at different points during the critical period (Lyckman et al., 2008). Consequently, these studies did not investigate vision-dependent gene expression at the level of the diverse cell types in V1. This resolution is crucial to understanding the mechanisms by which experience regulates neural circuitry at the molecular, cellular, and functional levels.

Here, we studied the role of vision in the development of V1 cell types and their circuitry in mice by combining single-nucleus transcriptomics, statistical inference, sensory perturbations, genetics, and *in vivo* functional imaging. We assembled a developmental transcriptomic atlas of postnatal mouse V1. Using this as a foundation, we discovered that: 1) Vision is required for the establishment and maintenance of L2/3 glutamatergic types, but not other cell types in V1; 2) L2/3 glutamatergic cell types are organized as sublayers in V1 and form a transcriptomic continuum through the graded expression of ~200 genes; and 3) Among these genes, *Igsf9b*, a vision-regulated cell adhesion molecule, is required in a graded fashion for the functional maturation of L2/3 glutamatergic neurons. Together, our study establishes a framework for future investigations of how experience regulates cell type specification in the brain.

Results

Transcriptional profiling of mouse V1 development using single-nucleus RNA-seq

To survey the transcriptomic diversity and maturation of cells in V1, we used droplet-based single-nucleus (sn) RNA-seq to profile this region during postnatal development in normally reared mice (**Figures 3.1A** and **S3.1D**). We collected samples from six postnatal time points: P8, P14, P17, P21, P28 and P38 (**Figure 3.1B**). Three of these are prior to the classical critical period for ocular dominance plasticity, with synaptogenesis occurring between P8 and eye-opening (P14) (Hinojosa et al., 2018; Li et al., 2010) (**Figures S3.1A-C**), and the remaining three span the critical period of ocular dominance plasticity (Gordon and Stryker, 1996; Tan et al., 2020; Wang et al., 2010), including its start (P21), peak (P28), and closure (P38).

Data from each timepoint consisted of four single-nuclei library replicates, each derived from cells collected from multiple mice (**Methods**). The resulting gene expression matrices were filtered to remove low-quality cells and doublets (Wolock et al., 2019), as well as cells with a high proportion of mitochondrial transcripts (>1%). In total, we obtained 144,725 high-quality nuclear transcriptomes across the six time points (**Figures S3.1D-H**).

A postnatal developmental atlas of V1 cell classes, subclasses, and types

We used dimensionality reduction and clustering to derive a developmental taxonomy consisting of cell classes, subclasses, and types (Yao et al., 2021a; Yao et al., 2020; Yuste et al., 2020; Zeng and Sanes, 2017) at each of the six time points (**Figures 3.1C, D** and **S3.1D; Methods**). Cell classes consisted of glutamatergic neurons (n=92,856; 3176 genes/cell detected on average), GABAergic neurons (n=13,374; 2966 genes/cell), and non-neuronal cells (n=38,495; 1549 genes/cell) identified by canonical markers (**Figure S3.1I** and **Table S3.1**) (Hrvatin et al., 2018; Tasic et al., 2016; Tasic et al., 2018). The relative proportions of the three cell classes were consistent across biological replicates (data not shown).

Glutamatergic cells separated into eight subclasses within the four cortical layers - L2/3, L4, L5IT, L5NP, L5PT, L6CT, L6IT, and L6b (**Figures 3.2A, B**). We also identified six GABAergic subclasses, which included the four well-known groups defined by the selective expression of *Pvalb*, *Sst*, *Vip*, and *Lamp5* (Zeng and Sanes, 2017) and two smaller subclasses that selectively expressed the genes *Stac* and *Frem1*. Non-neuronal cells included oligodendrocytes, oligodendrocyte precursor cells, astrocytes, vascular and leptomeningeal cells, endothelial cells, and microglia (**Figure 3.1D**). Similar results were obtained using an alternative computational pipeline (**Figure S3.1K**). We found a tight correspondence between the transcriptome-wide gene signatures that defined developing subclasses in our dataset and the subclasses identified in a recent survey of the adult mouse cortex (Tasic et al., 2018) (**Figure S3.1J**).

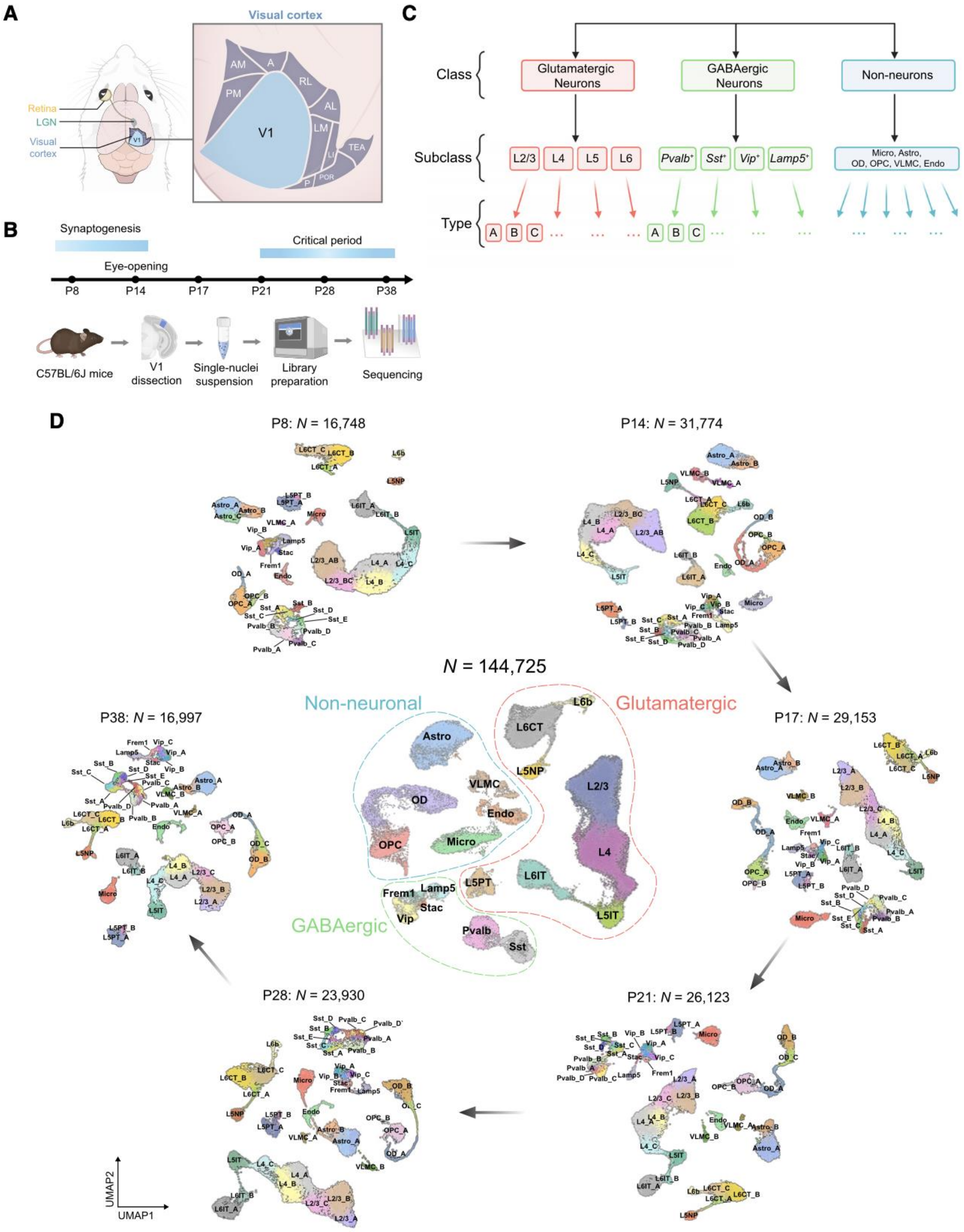

(*Figure 3.1 legend on next page*)

Figure 3.1. snRNA-seq profiling of V1 during postnatal development. (**A**) Schematic of the mouse visual system. Primary visual cortex (V1). Surrounding higher visual areas: A, anterior; AL, anterolateral; AM, anteromedial; LI, laterointermediate; LM, lateromedial; P, posterior; PM, posteromedial; POR, postrhinal; RL, rostrolateral; TEA, temporal anterior areas. (**B**) Experimental workflow of snRNA-seq profiling of V1 at six postnatal ages. (**C**) Cellular taxonomy of V1. (**D**) Uniform manifold approximation (UMAP) visualization of V1 transcriptomic diversity during postnatal development. Dots correspond to cells, and distances between them reflect degrees of transcriptomic similarity. The central panel shows cells from all six ages colored by subclass identity (**Table S3.1**). Peripheral panels show cells from different ages, colored by type identity determined via clustering. Data from each age and class were analyzed separately and then merged for visualization purposes.

The relative proportions of most neuronal subclasses were stable over time (**Figures 3.2C** and **S3.1L**), although proportions of non-neuronal subclasses varied (**Figure S3.1M).** This suggests that the neuronal subclass composition of V1 is established before P8, our earliest time point. We also identified subclass-specific markers (**Figures 3.2B**, **S3.2A-E**, and **Table S3.3**). This included *Ccbe1* (collagen and calcium-binding EGF domain-containing protein 1), which is specific for L2/3 glutamatergic neurons throughout development (**Figures 3.2D** and **S3.2A-C**).

Next, we performed dimensionality reduction and clustering for each class at each age separately. We henceforth refer to transcriptomically distinct clusters as types. The eight glutamatergic subclasses separated into 14-16 types, the six GABAergic subclasses separated into 14-15 types, and the six non-neuronal subclasses separated into 9-11 types depending upon age (**Figure 3.1D**) (**Methods**). Post-hoc differential expression analysis identified robust cell type-specific markers at each age (**Figures S3.3A-C**, **Table S3.4**).

Transcriptomic identities of L2/3 and 4 neuron types are established after eye opening

While the number of cell types within each class was similar at each age, it was not immediately clear how types identified at different ages were related to each other. Using transcriptomic similarity as a proxy for temporal relationships, we tracked the postnatal maturation of types within each class using a supervised classification framework (**Methods**). We observed striking subclass-specific differences in the maturation of glutamatergic neuron types (**Figure 3.2E**). L5, and to a slightly lesser extent L6, neuron types tightly corresponded throughout the time course, indicating that these types are established prior to eye-opening, and maintained. Conversely, upper-layer neuron types (L2/3 and L4) exhibited poor correspondences, suggesting gradual specification. Within L2/3, two neuron types at P8 and P14 matured into three types after eye-opening. By contrast, differences in the maturational patterns of GABAergic and non-neuronal subclasses were less pronounced (**Figures S3.2F-I, Methods**).

These subclass-specific differences in the timing of glutamatergic neuron type development are supported by five quantitative observations: 1) L5/6 types at different ages could be related in a 1:1 fashion with each other while L2/3/4 types could not be. These differences were based on the Adjusted Rand index (ARI), a measure of transcriptomic correspondence between two sets of clusters (**Figure 3.2F**). Furthermore, the clustering results for L2/3 and L4 were more sensitive ($P<0.0001$, one-way ANOVA) to changes in the resolution parameter than for L5 and L6 (**Figure 3.2G**); 2) The transcriptomic separation among L2/3 and L4 types was lower than that among L5 and L6 types, GABAergic types, and non-neuronal types at all ages (**Figures S3.2J-L**); 3) Differentially expressed genes that distinguished L2/3 and L4 neuron types varied with age, whereas those that defined L5 and L6 neuron types were stable (**Figures S3.3D-G**); 4) In a statistical test to identify temporally differentially expressed (tDE) genes in each layer (see **Methods**), L2/3 and 4 contained twice as many tDE genes as L5 and 6 (**Figure S3.3H**); and 5) The relative frequency of L2/3 and L4 types varied over time (see below). By contrast, the relative proportions of the ten L5 and L6 types, the smallest of which was present at an overall frequency of 1%, were stable throughout the time course. Together, these results suggest that within glutamatergic neurons of V1, transcriptomic specification of types within upper-layer subclasses (L2/3 and L4) occurs later than types in lower-layer subclasses (L5 and L6).

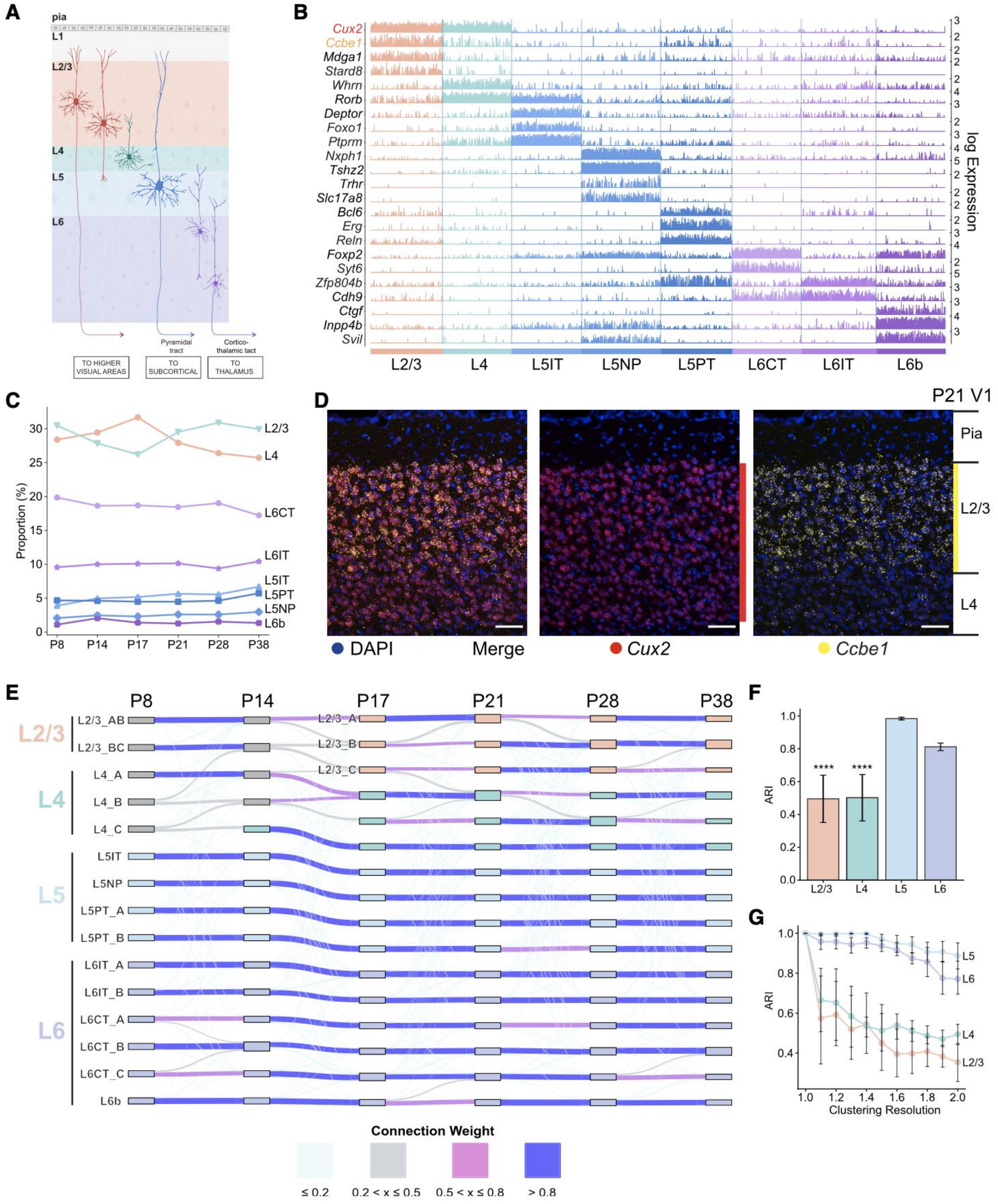

(*Figure 3.2 legend on next page*)

Figure 3.2. Transcriptomic diversity of V1 glutamatergic neurons during postnatal development. (**A**) Schematic of glutamatergic neurons in V1 arranged in layers L1-L6. (**B**) Tracks plot showing subclass-specific markers (rows) in glutamatergic neurons (columns), grouped by subclass (e.g., L2/3). 1000 randomly selected cells from each subclass were used for plotting. Scale on the y-axis (right), normalized, log-transformed transcript counts in each cell. *Ccbe1*, a L2/3 marker, and *Cux2*, a L2/3/4 marker, are highlighted. (**C**) The proportions of glutamatergic subclasses are stable with age despite significant variation in the number of cells profiled (**Table S3.2**). (**D**) Coronal section through V1 analyzed by fluorescent *in situ* hybridization (FISH) at P21. *Ccbe1* is selective for L2/3 glutamatergic neurons. *Cux2* is expressed in L2/3 and L4 glutamatergic neurons and in inhibitory neurons and non-neuronal cells (see **Figure S3.2B** for other ages). Scale, 50 µm. (**E**) Transcriptomic similarity identifies temporal associations among V1 glutamatergic neuron types across ages. Sankey diagram computed using a supervised classification approach. Nodes, individual V1 glutamatergic neuron types at each age (as in **Figure 3.1D**); edges, colored based on transcriptomic correspondence. (**F**) Adjusted Rand Index (ARI) values quantifying temporal correspondence of glutamatergic types between each pair of consecutive ages based on transcriptomic similarity. Individual bars denote layers. ARI ranges from 0 (no correspondence) to 1 (perfect correspondence). Bar heights, mean ARI computed across pairs of consecutive ages; error bars, standard deviation; ***, $P<0.0001$ (one-way ANOVA) for L2/3 and L4 against L5 and L6. (**G**) Types in L2/3 and L4, but not L5 and L6, are sensitive to changes in clustering resolution. Glutamatergic neurons at each age are re-clustered at different values of the resolution parameter (x-axis), and the results are compared with the base case corresponding to resolution = 1 (**Methods**). Line plots, mean ARI values for each layer (colors); error bars, standard deviation across ages.

L2/3 neuron types are spatially segregated

We classified L2/3 glutamatergic neurons into three types (A, B, and C) beginning at P17, the first time point assessed after the onset of vision at P14 (**Figure 3.3A**). These were visualized in tissue using *in situ* hybridization for marker genes *Cdh13*, *Trpc6*, and *Chrm2* for types L2/3_A, L2/3_B, and L2/3_C, respectively (**Figures 3.3B-D**). Within the L2/3 glutamatergic neuron subclass, these transcripts are specific for the aforementioned glutamatergic types. They are, however, expressed in other subclasses as well. Cells expressing the three transcripts were organized into sublayers that became more pronounced with age: L2/3_A close to the pia, L2/3_C bordering L4, and L2/3_B in between (**Figures 3.3D, E**). At the boundaries of these sublayers, cells co-expressed more than one type-specific marker, indicating a lack of discrete, sharp boundaries, and mirroring the continuous transcriptomic arrangement observed *in silico* (see below).

Prior to the onset of vision (P8 and P14), however, only two transcriptomic types were resolved. We denote these AB and BC. AB and BC were organized as two sublayers based on their differential expression of *Cdh13* and *Chrm2* (**Figures 3.3C** and **S3.4A-E**), with cells at the border co-expressing the two markers. In contrast, the B marker *Trpc6* was weakly expressed in cells scattered throughout L2/3 at these early stages (**Figures 3.3B-C, E-H,** and **S3.4D, E**). There is a striking difference in the distribution of *Cdh13* between P8 and P38. At P8, *Cdh13* extends to deep sublayers of L2/3, whereas by P38, expression is restricted to a narrow strip of cells at the top of L2/3. By contrast, *Chrm2* expression extends slightly more towards upper sublayers at P38. Multiple A-, B-, and C-specific markers were not expressed before P14 and only appeared at later stages (**Figure S3.3D**). Thus, we infer that the L2/3 glutamatergic types A, B, and C arise from AB and BC types following the onset of vision (**Figure 3.2E** and **Methods**).

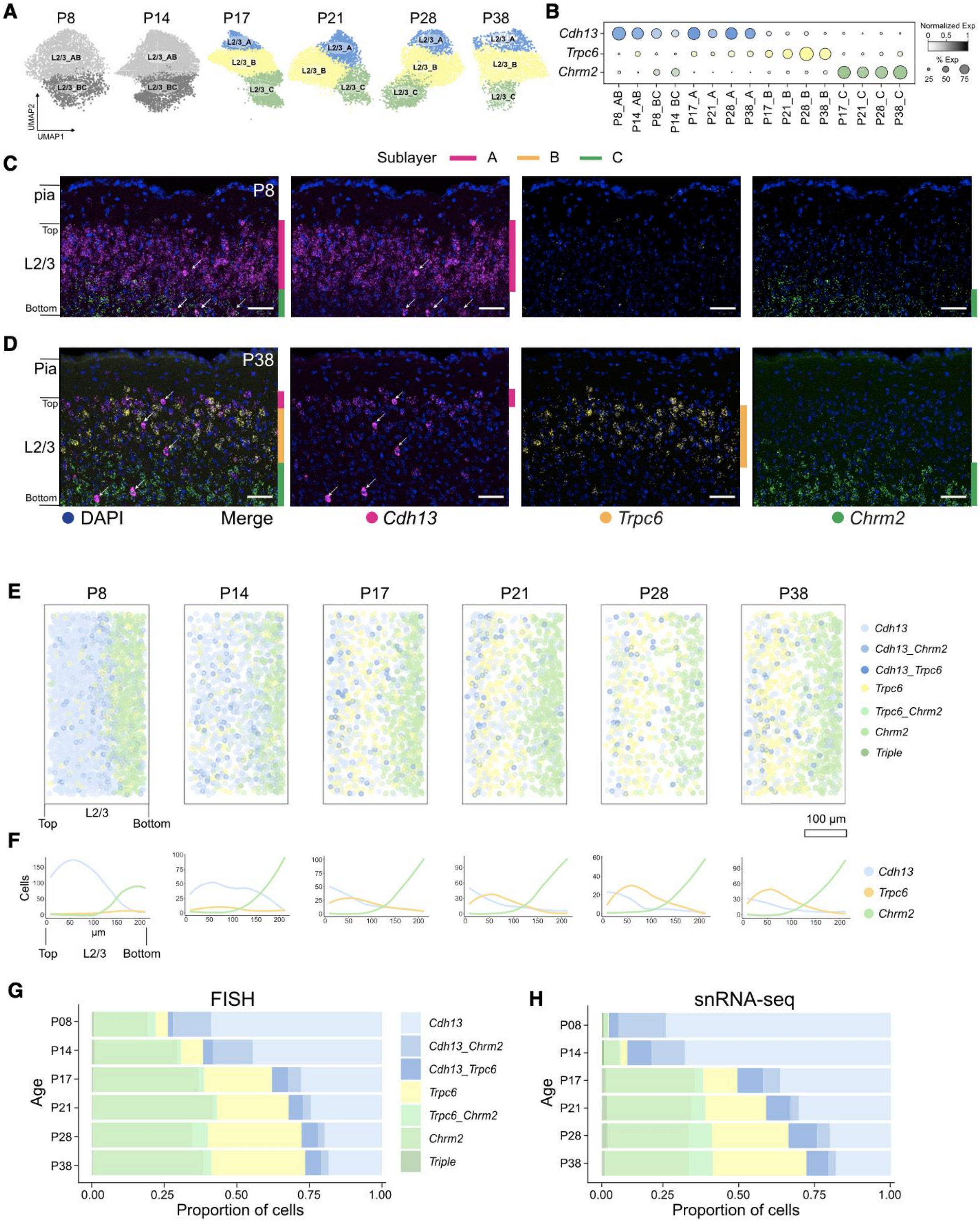

(*Figure 3.3 legend on next page*)

Figure 3.3. Anatomical and transcriptomic maturation of L2/3 glutamatergic neuron types. (**A**) UMAP plots of L2/3 glutamatergic neuron types across ages. (**B**) Dot plot showing expression patterns of L2/3 type-specific genes (rows and colors) across L2/3 neuron types arranged by age (columns). (**C**) FISH images showing type markers *Cdh13*, *Trpc6*, and *Chrm2* within L2/3 at P8. Vertical colored bars, sublayers expressing the indicated markers; arrows, large cells expressing *Cdh13* are not excitatory neurons; they are a subset of inhibitory and non-neuronal cells. Scale bars, 50 mm. (**D**) Same as (**C**), at P38. (**E**) Pseudo-colored representation of *Cdh13*, *Trpc6*, and *Chrm2* expression in L2/3 cells at six ages. Cells are colored based on expression levels of one or more of these markers. Each panel is an overlay of five or six images of V1 from three mice. Pial to ventricular axis is oriented horizontally from left to right within each panel. Total number of cells analyzed: P8, 2324; P14, 1142; P17, 1036; P21, 1038; P28, 653; and P38, 1034. Scale bars, 100 mm. (**E**) and (**F**) are rotated relative to (C) and (D). ''Top'' and ''bottom'' are indicated. (**F**) Line tracings quantifying the number of cells per bin at each position along the pial to ventricular axis corresponding to (E). 0 on the x axis, region of L2/3 closest to pia. 14 bins were used over the depth of L2/3. (**G**) Relative proportions of cells within each expression group defined in (E) quantified using FISH data. (**H**) Same as (**G**) using snRNA-seq data.

Vision is necessary for establishing and maintaining L2/3 neuron type identity

The emergence of three L2/3 neuron types following eye-opening prompted us to explore the role of vision in defining cell types. It is well established that vision is required for the development of cortical circuitry during the critical period for ocular dominance plasticity (P21-P38) (Espinosa and Stryker, 2012; Gordon and Stryker, 1996). We used snRNA-seq to profile V1 in animals that were dark-reared from P21 to P28 and P21 to P38. For brevity, these experiments are referred to as P28DR and P38DR, respectively (DR = dark rearing). We also profiled animals that were exposed to 8 hours of ambient light after dark-rearing from P21-P28 to assess the impact of visual stimulation following prolonged deprivation (**Figure 3.4A**). We refer to this experiment as P28DL (DL = dark-light). In total, we recovered 77,150 high-quality nuclei across these three experiments and identified classes, subclasses, and types using the same computational pipeline applied to the normally reared (NR) samples (**Figure 3.4B** and **Methods**).

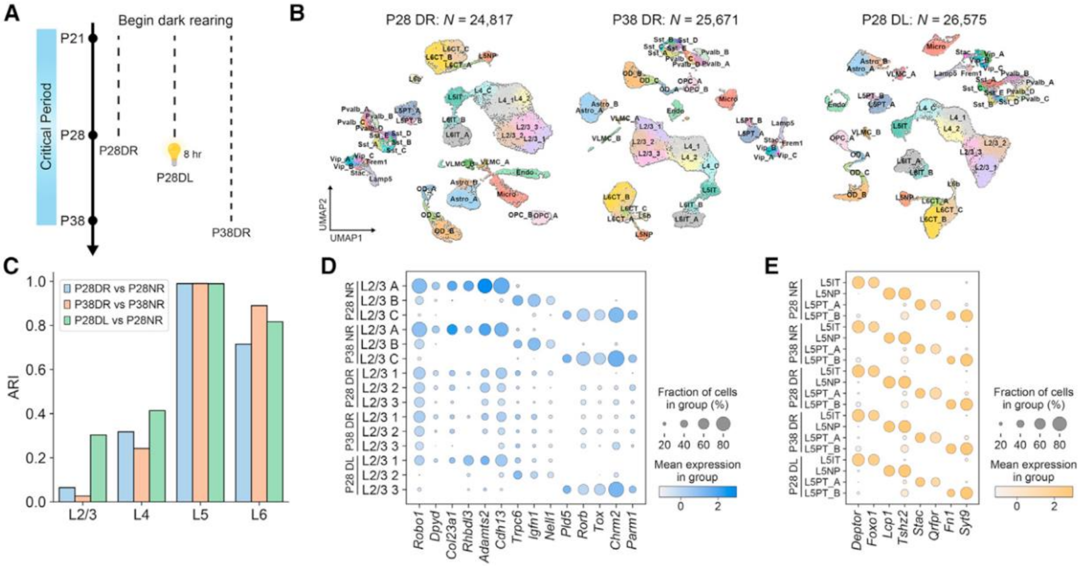

(*Figure 3.4 continued on next page*)

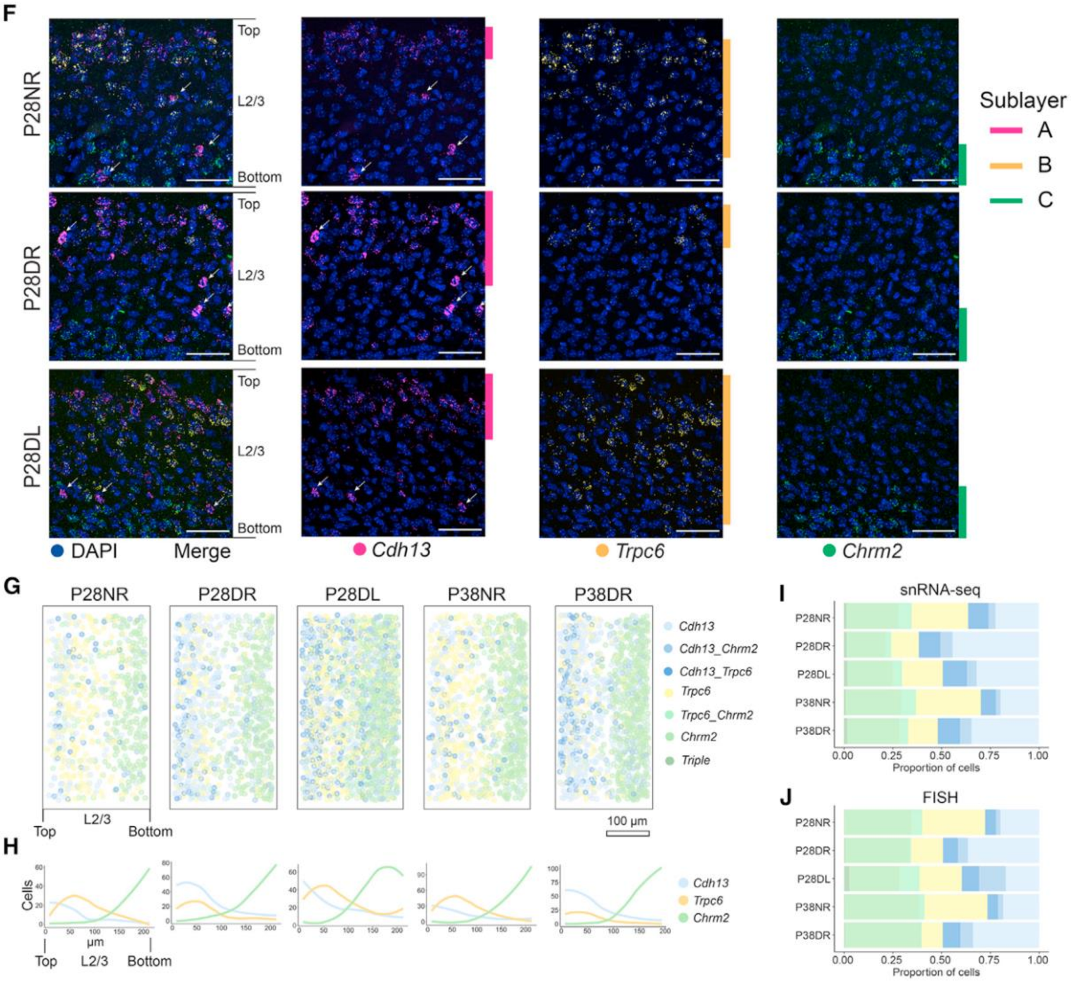

Figure 3.4. Visual experience is required to maintain L2/3 glutamatergic neuron types. (**A**) Schematic of experiments. Data collected from three rearing conditions: dark reared between P21–P28 (P28DR) and P21–P38 (P38DR) and between P21–P28 followed by 8 h (P28DL). (**B**) UMAP plots of transcriptomic diversity in P28DR, P38DR, and P28DL. Clusters that match 1:1 to normally reared (NR) types in Figure 1D are labeled. This was not possible for all L2/3 and two L4 clusters, which correspond poorly to NR types. We, therefore, provisionally labeled these clusters L2/3_1, L2/3_2, L2/3_3, L4_1, and L4_2. (**C**) Adjusted Rand Index (ARI) quantifying transcriptomic similarity within each layer (x axis) between glutamatergic clusters observed in dark-reared mice and types observed in normally reared (NR) mice. Colors correspond to comparisons as indicated. (**D**) Expression of L2/3 type markers (columns) in NR, DR, and DL types and clusters (rows) at P28 and P38. (**E**) Same as (D) for L5. DR and DL clusters are labeled based on their tight transcriptomic correspondence with NR types (Figures S5F and S5G). (**F**) FISH images showing expression of L2/3 markers in NR, DR, and DL at P28. Arrows, inhibitory neurons expressing *Cdh13*. The level of *Cdh13* is modestly repressed by vision. Scale bars, 50 mm. (**G**) Pseudo-colored representation of *Cdh13, Trpc6, and Chrm2* expression in NR, DR, and DL mice at P28 and P38. Each plot is an overlay of 5–6 images of V1 from three mice. The pial to ventricular axis is oriented horizontally from left to right within each panel. Total number of cells analyzed: P28NR, 653; P28DR, 989; P28DL, 1,732; P38NR, 1,034; and P38DR, 1,177. (**H**) Cells per bin at each position along the pial to ventricular axis corresponding to (G). 0 on the x axis, region of L2/3 closest to pia. 14 bins were used over the depth of L2/3. (**I**) Proportions of L2/3 cells within each expression group defined in (G) quantified using snRNA-seq data. (**J**) Same as (I) using FISH data.

We performed three computational analyses to probe the effect of visual deprivation (DR and DL) on the transcriptomic patterns observed in normally reared (NR) mice. First, we compared the overall transcriptional profiles of cell types across the three conditions. We found that dark rearing disrupted the type identities of L2/3 and L4, but not L5 and L6, glutamatergic neurons (**Figures 3.4C** and **S3.5F**). Furthermore, dark rearing neither altered the gene expression patterns that defined subclasses nor those defining GABAergic and non-neuronal cell types (**Figures S3.5A-C**). Second, the cell type markers identified in NR mice were disrupted by dark rearing in L2/3, and slightly in L4, but not L5 and 6 (**Figures 3.4D-E** and **S3.5D-E**). Third, we probed the effect of visual deprivation on type-specific genes within each layer. While the signatures within all four layers were different when comparing DR to NR, the effect was most dramatic for L2/3 (**Figure S3.6H**). Thus, vision selectively influences transcriptomic profiles of upper-layer glutamatergic cell types.

The effect of dark rearing was particularly striking in L2/3. The L2/3 clusters observed in dark-reared mice poorly resembled the three types in normally reared animals, and the expression patterns of cell type-specific marker genes were disrupted (**Figure 3.4C, D**). By contrast to the three sublayers highlighted by *Cdh13, Trpc6,* and *Chrm2* expression in L2/3 in normally reared mice, only two sublayers were observed in dark-reared mice. Notably, there was a sharp decrease in *Trpc6*-expressing cells (**Figure 3.4F-J**), consistent with snRNA-seq data (**Figure 3.4D**). There was also an increase in the number of *Cdh13*-expressing cells and the domain of expression extended into deeper layers. This was not simply a loss of one cell type, however, but a global disruption of gene expression patterns throughout L2/3 (see below, **Figure 3.6**). The two-layered pattern was more prominent in dark-reared animals at P38 compared to P28 (**Figures 3.4G-I** and **S3.5H-I**). Thus, in the absence of vision, the expression patterns of these markers were similar to those prior to the onset of vision (see panels P8 and P14 in **Figure 3.3E**).

The loss of cell type identity in animals deprived of light during the first half of the critical period was partially reversible. L2/3 transcriptomic clusters in mice exposed to 8 hours of ambient light after dark rearing between P21-P28 showed a marked recovery of gene expression patterns observed in normally reared animals (**Figures 3.4C-D** and **S3.5G**, **S3.6H**). In addition, the layered arrangement of *Cdh13*-, *Trpc6*- and *Chrm2*-expressing cells in these animals was also shifted towards that observed in normally reared animals (**Figures 3.4F-J** and **S3.5H-I**). These results demonstrate that vision is needed to maintain the transcriptomic and spatial identities of L2/3 cell types.

As the spatial expression of cell type markers in the absence of vision and at eye opening were similar, we set out to assess whether vision was not only necessary to maintain cell types, but also required for their establishment. To test this, we dark-reared mice from P8 to P17 (**Figure 3.5A**) and assessed the expression patterns of *Cdh13*, *Trpc6*, and *Chrm2* in tissue sections. These mice had two, instead of three, sublayers within L2/3, similar to P8 and P14 normally reared animals (**Figures 3.5B-D**). These changes included a dramatic reduction in *Trpc6*-expressing cells and an increase in *Cdh13* expression, which was accompanied by an expansion in its expression domain towards the middle sublayer in mice with no visual experience (**Figure 3.5E**). This was not a general effect on glutamatergic cell types, as the relative proportions of L5 neuron types were insensitive to changes in visual experience (**Figure S3.4G-H**). In summary, these results show that vision acts selectively in L2/3 to establish and maintain cell types.

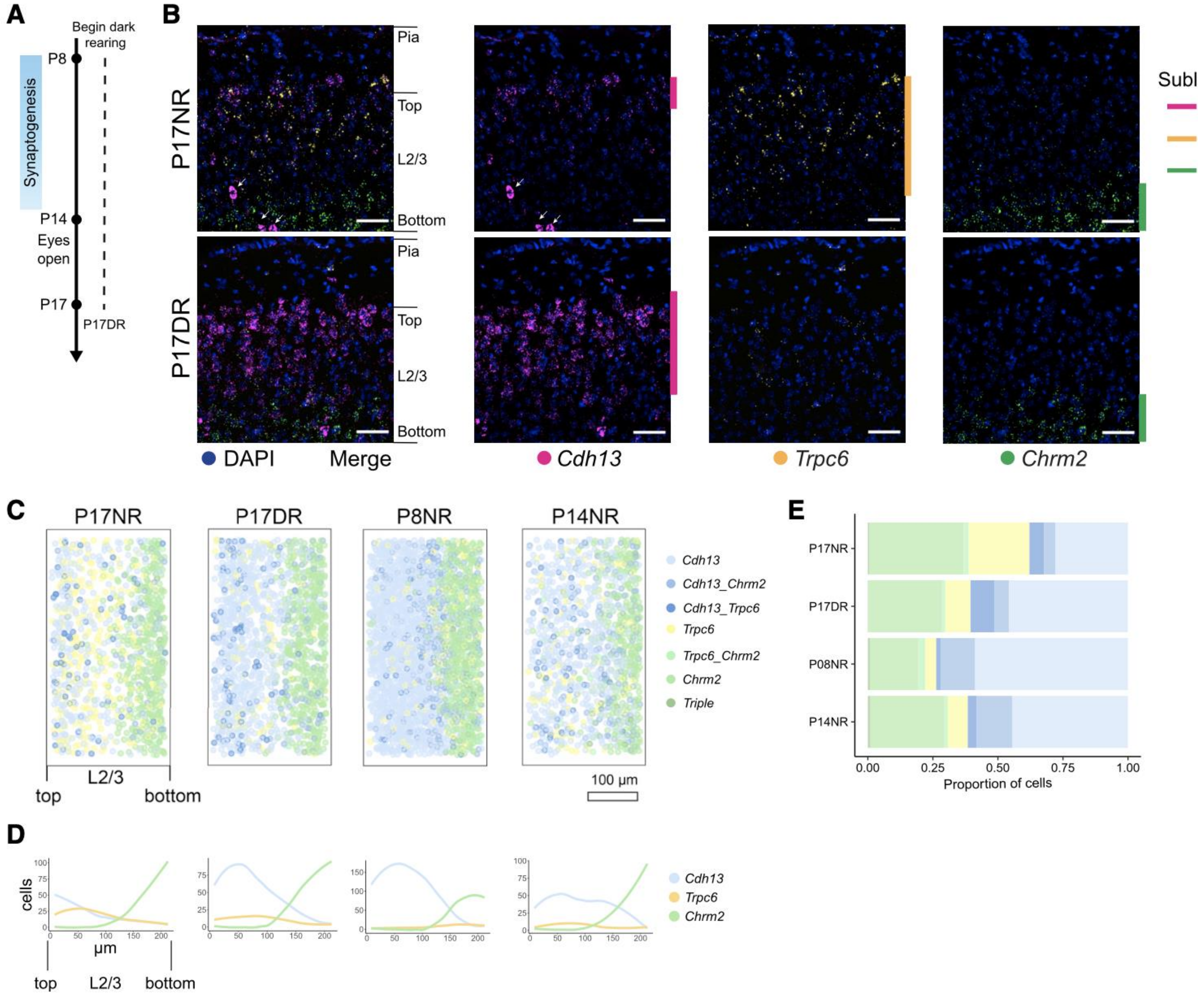

Figure 3.5. Vision is required to establish L2/3 glutamatergic neuron types. (**A**) Schematic of experiments. (**B**) FISH images of L2/3 markers in normally reared (NR) and dark-reared (DR) mice at P17. Arrows, inhibitory neurons expressing *Cdh13*. Scale bars, 50 mm. (**C**) Pseudo-colored representation of *Cdh13*, *Trpc6*, and *Chrm2* expression in L2/3 cells. Each plot is an overlay of six images of V1 from three mice. Cells quantified: P17NR, 1,036; P17DR, 1,411. (**D**) Line tracings quantifying cells per bin at each position along the pial to ventricular axis corresponding to (C). 0 on the x axis, L2/3 region closest to pia. 14 bins were used over the depth of L2/3. (**E**) Proportions of cells in each expression group defined in (C) quantified using FISH data.

Continuous variation of L2/3 neuron types and gene expression gradients are shaped by vision

The sublayers corresponding to types A, B, and C in L2/3 were partially overlapping, mirroring the continuous arrangement of their transcriptomes (see **Figures 3.3A, E**). Consistent with this continuous arrangement, more than 70% of the 285 differentially expressed genes among the L2/3 types in normally reared mice exhibited graded, rather than digital, differences (**Figures 3.6A** and **S3.6A-H)**. In dark-reared mice, these genes were no longer expressed in a graded fashion between the L2/3 clusters, although their overall (i.e., bulk) expression levels, for all but a few genes, were unaltered (**Figures S3.6C**). These gradients were partially recovered by brief restoration of normal visual experience to dark reared animals during the critical period (**Figure 3.6A**). Thus, vision selectively regulates gene expression in a sublayer-specific fashion, contributing to the continuous variation of L2/3 cell types.

We hypothesized that graded genes which are temporally regulated and expressed in a vision-dependent manner could be associated with functional changes in L2/3 during the critical period. Several genes fit this description, including cell surface molecules (CSMs) and transcription factors (TFs) (**Figures 3.6B, C** and **S3.6I, J**). Among these were cell surface and secreted proteins previously shown to be involved in the development of neural circuits, including proteins regulating cell recognition (e.g., *Kirrel3*, *Sdk2*) and synaptic adhesion (e.g., *Tenm1* and *Cbln2*) (**Figures 3.6B, C**).

To identify candidate cell surface proteins from this set that may contribute to vision-dependent changes in circuitry during the critical period, we selected genes that satisfied three criteria across all L2/3 glutamatergic types: 1) Selective upregulation during the critical period; 2) Downregulation in DR animals; and 3) Upregulation in DR animals in response to eight hours of ambient light at P28 (i.e., P28DL mice). Five genes (*Igsf9b*, *Epha10, Cdh4*, *Sdk2*, and *Sema4a*) satisfied all three criteria (**Figures 3.6E-F**) and all five encode cell surface proteins implicated in regulating neuronal wiring, raising the possibility that they contribute to experience-dependent circuit development in L2/3. As the expression levels and dynamics of *Igsf9b* were the most robust of this group, we explored its function during the critical period.

Igsf9b knock-out alters inhibitory synapses in L2/3

IGSF9B is a homophilic cell adhesion molecule of the immunoglobulin superfamily that promotes Neuroligin2 (Nlgn2)-dependent inhibitory synapse formation (Lu et al., 2017; Woo et al., 2013) (**Figure 3.6D**). This protein is of particular interest because inhibition plays an important role in regulating V1 circuitry during the critical period (Reh et al., 2020). We assessed the spatial distribution of *Igsf9b* transcripts in L2/3 at different times in development using FISH **(Figure 3.6G**) and *in silico* by regarding the transcriptomic positions of L2/3 neurons in gene expression space as "pseudo" spatial coordinates (**Figure 3.6H; Methods**). *Igsf9b* levels were low prior to eye opening and increased during the critical period in a graded manner favoring increased expression deeper into L2/3. Sensory activity further modulated the expression level and lamination of *Igsf9b*. Dark-rearing during the critical period decreased *Igsf9b* expression and slightly disrupted its graded expression in L2/3 neurons (**Figures 3.6F**, **I, J** and **Figure S3.6K**). These effects were reversed and *Igsf9b* expression levels were upregulated when dark-reared animals were exposed to ambient light for 8 hrs. Given the graded expression of *Igsf9b* across sublaminae increasing from upper to lower layers, it was particularly intriguing that a second gene encoding another Ig superfamily protein*,* Mdga1, a negative regulator of Nlgn2 (**Figure 3.6D**), was expressed in a graded and opposite spatial pattern to *Igsf9b* (**Figure 3.6G, H; Figure S3.6F**). Together, the spatiotemporal dynamics of *Igsf9b* and *Mdga1* expression after eye opening form a gradient of inhibitory synapse potential along the pial-ventricular axis of L2/3, with lower sublayers exhibiting increased inhibition.

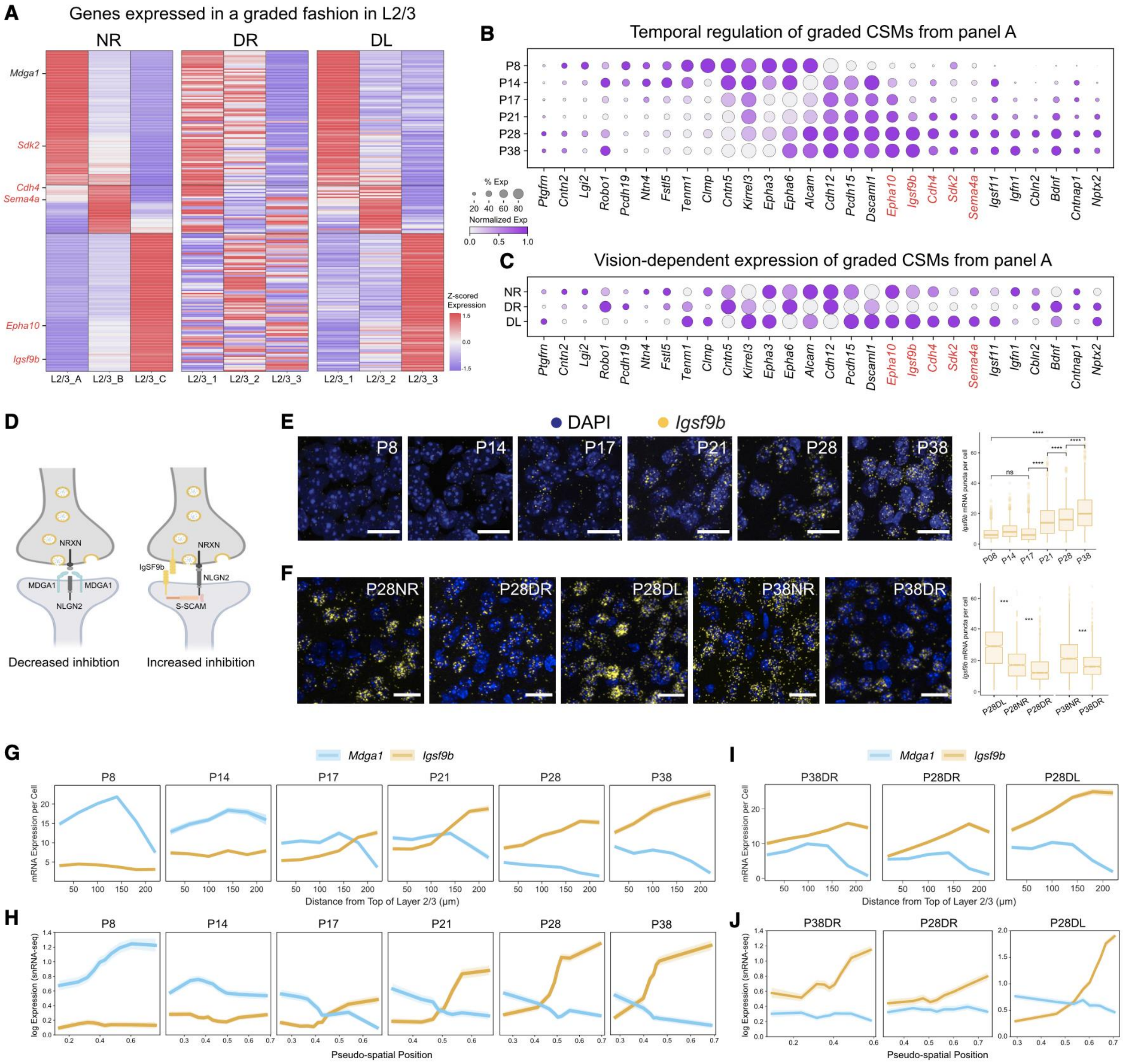

(Figure 3.6 legend on next page)

Figure 3.6. Continuous variation of L2/3 neuron types and vision-dependent gene gradients implicated in wiring. (**A**) Heatmap of L2/3 type-specific genes with graded expression in normally-reared mice (NR). This is disrupted in dark-reared mice (DR) and partially recovered by exposing DR mice to light for 8 hrs (DL). For the full set of L2/3 type-specific genes grouped by expression pattern, see **Figure S3.6A**. Genes satisfying criteria in panels B and C (see text) are indicated in red lettering. Two of the three L4 cell types also exhibit graded expression differences (see **Figure S3.6L-M**). (**B**) Temporal regulation of cell surface molecules (CSMs) in panel A. Red print, genes upregulated during the classical critical period (P21-P38), downregulated in DR, and upregulated in DL. (**C**) Same illustration as panel B across the conditions P28NR, P28DR, and P28DL. (**D**) Schematic of MDGA1 and IGSF9B interactions with NLGN2 at synapses. MDGA1 prevents NLGN2 interaction with NRXN presynaptically. IGSF9B binds homophilically and interacts with S-SCAM postsynaptically as does NLGN2. (**E**) FISH images of *Igsf9b* mRNA over time in V1. Three animals per time point, six images per animal. Scale, 20 µm. (*Right*) Box plot quantifying expression. Wilcoxon Rank Sum Test, **** $P < 0.0001$. Cells quantified: P8,1191; P14,1011; P17, 1389; P21, 1729; P28, 1277; and P38, 1588. (**F**) FISH images showing that dark rearing decreases *Igsf9b* expression in L2/3, and eight hours of light restores expression. Scale, 50 µm. (*Right*) Box plot quantifying expression. Three animals imaged per age and condition combination. Cells quantified: P28NR, 1290 cells; P28DL, 1506 cells; P28DR, 1521 cells; P38NR, 1629 cells; and P38DR, 1885. Quantified at 40X. Wilcoxon Rank Sum Test, *** $P < 0.001$. (**G**) FISH quantification of average *Mdga1* and *Igsf9b* expression (y-axis) in glutamatergic cells as a function of distance from the top of L2/3 (x-axis). Shaded ribbons represent standard error of the mean. Cells quantified: P8, 2204; P14, 928; P17, 1037; P21, 1183; P28, 719; and P38, 942. Data from three or four animals at each age. (**H**) Reconstruction of *Mdga1* and *Igsf9b* expression levels averaged across cells based on their inferred L2/3 pseudo-spatial locations in gene expression space (see **Methods**). Shaded ribbons, standard deviation. (**I**) Same as panel G for P38DR, P28DR, and P28DL. Cell numbers: P38DR, 719; P28DR, 1061; and P28DL, 1053 cells. Data collected from three animals at each time point. (**J**)Same as panel H for P38DR, P28DR, and P28DL. Note difference in scale for P28DL to capture the extent of increase in *Igfs9b* expression.

To explore the role of *Igsf9b* in the development of inhibitory synapses in L2/3, we examined the expression of five markers of inhibitory synapses in wild-type (WT) and *Igsf9b* knock-out (KO) mice. These markers included three postsynaptic proteins (Gamma-aminobutyric acid Type A receptor subunit alpha 1 (GABRA1), Neurolign2 (NLGN2), and Gephryin (GPHN)) and two presynaptic proteins (the presynaptic vesicular GABA transporter (VGAT) and the enzyme glutamic acid decarboxylase (GAD65)) (**Figure S3.7A**). Expression levels of the postsynaptic markers GABRA1 and NGLN2 were significantly decreased in P37 KO mice relative to WT littermates (**Figure S3.7B**), although GPHN remained unchanged (not shown). By contrast, there was an increase in the levels of presynaptic markers GAD65 and VGAT (**Figure S3.7B**); this increase may reflect a homeostatic response to the changes reflected in the decrease in postsynaptic markers. Consistent with our finding that expression of *Igsf9b* in L2/3 increases with depth, these phenotypes were more pronounced toward the bottom of L2/3 (**Figure S3.7D-G**; see **Figure 3.6G, H**). By contrast, excitatory synapse markers were unaffected in KO mice (**Figure S3.7C**). Thus, loss of *Igsf9b* specifically affects inhibitory synapses in a graded fashion along the L2/3 pial-ventricular axis.

Igsf9b regulates vision-dependent maturation of binocular circuitry

A defining feature of the critical period in V1 is the vision-dependent maturation of binocular neurons, which are required for depth perception, also known as stereopsis (La Chioma et al., 2019). To mediate stereopsis, these neurons must selectively respond to the same kind of visual information from both eyes (binocular matching). Although binocular neurons can be detected shortly after eye opening, they exhibit poor matching at early stages. Visual experience during the critical period (P21-P36) changes the population of binocular cells; binocular cells that are poorly tuned are rendered monocular and new well-tuned binocular neurons arise from well-tuned monocular neurons through recruitment of matched inputs from the other eye (Tan et al., 2021; Tan et al., 2020).

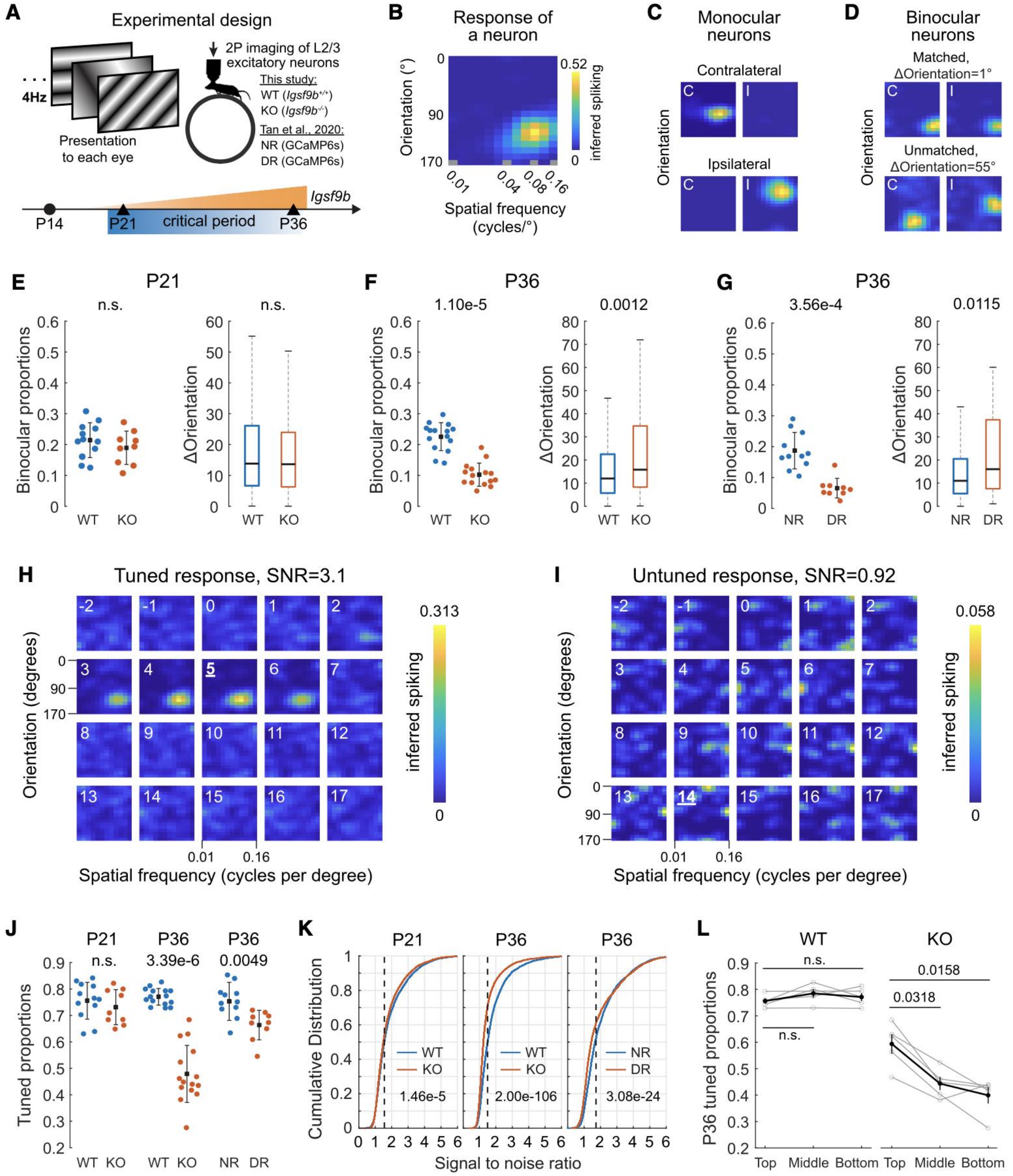

(Figure 3.7 legend on next page)

Figure 3.7. Igsf9B is required for vision-dependent maturation of binocular neurons in V1B L2/3. (**A**) Experimental setup for functional analysis . (*Top*) Schematic of 2-photon (2P) Ca^{2+} imaging using different sinusoidal gratings sequentially presented at 4 Hz. Visual stimuli were presented to each eye separately. The head-fixed mouse was awake on a running wheel. Mice used in this study are WT (*Igsf9B*$^{+/+}$) and KO (*Igsf9B*$^{-/-}$) expressing AAV encoded jGCaMP7f. Panels G, J, K include our unpublished results from NR and DR (dark reared from P22-P36) transgenic mice carrying GCaMP6s expressed in excitatory neurons (from Tan et al., 2020). (*Bottom*) WT and KO mice were imaged at P21 and P36, the onset and closure of the classical critical period, respectively. Orange, *Igsf9*b *m*RNA levels in L2/3 as a function of time. (**B**) Tuning kernel showing response of a single neuron (see **Figure S3.7L**) to the contralateral eye. The colors represent response strength (color bar, right) as a function of stimulus orientations (Y-axis) and spatial frequency (log scale; X-axis). (**C**) Response to contralateral (C) and ipsilateral eye (I) of monocular cells. Kernels for each neuron were normalized to the peak inferred spiking. (**D**) As in C, but for matched (*top*) and unmatched (*bottom*) binocular neurons. ΔOrientation, the difference in orientation preference between the two eyes. (**E**) (*Left*) proportions of binocular neurons in WT and KO mice at P21. Each point is from a single imaging plane. Mean and standard deviation, black dots and lines. Mann-Whitney U test. (*Right*) ΔOrientation of binocular neurons in WT (4 mice, 761 cells) and KO (3 mice, 619 cells) mice at P21. Black horizontal line, median; box, quartiles with whiskers extending to 2.698σ. Mann-Whitney U test. Note the absence of phenotype in binocular neurons at P21. (**F**) As in E but for binocular neurons at P36. WT, 5 mice, 602 cells; KO, 5 mice, 269 cells. (**G**) As in F but for binocular neurons in NR (4 mice, 339 cells) and DR (3 mice, 78 cells) mice. P36 phenotypes in KO and DR mice were similar. The difference in proportion between the WT (panel F) and NR (panel G) likely reflects differences in genetic background or experimental design (i.e., viral versus transgenic expression of GCaMP or differences between GCaMP6s and jGCaMP7f). (**H**) Example of a tuned cell from a WT mouse at P21. Inferred spiking as a function of imaging frames for a neuron with a tuned response. Numbers at the top left indicate imaging frames relative to stimulus onset. For this neuron, the SNR is 3.1, and peak response occurred 5 imaging frames or 323 ms after onset of its optimal stimuli, consistent with the kinetics of jGCaMP7f. (**I**) As in H but for an untuned cell in the same mouse at P21. (**J**) Proportions of tuned neurons in WT and KO mice at P21 and P36, and in NR and DR mice at P36. Each point is from a single imaging plane. Mean and standard deviation, black dots and lines. Mann-Whitney U test. (**K**) (*Left*) Cumulative distribution of SNR to either eye of all imaged neurons at P21 in WT (4 mice, 3436 neurons) or KO (3 mice, 3457 neurons) mice. Dashed vertical line marks the SNR threshold for visually evoked responses (see **Methods**). *P*-value from two-sample Kolmogorov-Smirnov test is shown in the plot. (*Middle*) As in the left, but for mice at P36 in WT (5 mice, 2698 neurons) and KO (5 mice, 2699 neurons). (*Right*) As in the middle, but for neurons in NR (4 mice, 1905 neurons) and DR (3 mice, 1188 neurons) mice. Neuronal responses to each eye were measured separately. (**L**) Proportions of tuned neurons as a function of depth in V1B L2/3 in WT and KO mice at P36. Top, middle, and bottom indicate the three imaging planes covering the corresponding sub-laminae within L2/3 in each mouse. Each gray line represents a mouse. Mean and standard error of the mean were shown as black dots and vertical lines. Mann-Whitney U test with Bonferroni correction.

We examined whether *Igsf9b* is required for the normal development of binocular responses in L2/3 using *in vivo* 2-photon calcium imaging in binocular V1 (**Figure S3.7H, I**). This region of V1 comprises not only neurons responsive to both eyes (i.e., binocular cells), but also monocular neurons responsive to stimuli presented to the ipsilateral or contralateral eye only. We measured responses of thousands of excitatory neurons to stimulation of each eye at P21 and P36 in normally reared WT and *Igsf9b* KO mice (**Figure 3.7A**; see **Methods**). These results were also compared to those from GCaMP6s transgenic mice that were normally reared (NR) or dark-reared (DR) during the critical period (Tan et al., 2020) (**Figure 3.7A**). Neuronal responses were measured at three depths, spanning the top (type A), middle (type B), and bottom (type C) sublayers of L2/3, corresponding to the regions of low, intermediate, and high *Igsf9b* expression, respectively (**Figure 3.7B-D, Figure S3.7J-L;** see **Methods**). At P21, the proportion of binocular neurons and their orientation matching in KO mice were indistinguishable from those in WT (**Figure 3.7E**). This is consistent with the low expression of *Igsf9b* in L2/3 before P21 (**Figure 3.7A**, see **Figure 3.6**). At

P36, after closure of the critical period—when *Igsf9b* expression would normally have increased—only about half the normal number of binocular neurons were observed in KO mice, and these few neurons displayed poor binocular matching (**Figure 3.7F**). This phenotype resembles that observed in DR mice (**Figure 3.7G**).

We also noted a marked decrease in the proportion of tuned cells in KO mice. Untuned cells were active, but by contrast to tuned cells, they were not responsive to specific visual stimuli in a time-locked fashion (**Figure 3.7H, I**). While visual deprivation decreased the proportion of visually responsive neurons from 75% (NR) to 66% (DR), *Igsf9b* KO decreased the proportion of responsive neurons to 47% by P36 (**Figure 3.7J**). This reduction in proportion of tuned neurons in KO mice from P21 to P36 correlated with a marked reduction in the signal to noise ratios (SNRs) of neuronal responses at critical period closure (**Figure 3.7K,** left and middle panels). The extent of SNR impairment in KO was more severe than in DR mice (**Figure 3.7K,** compare middle and right panels). Notably, the severity of reduction of tuned neurons in KO increased with depth (**Figure 3.7L**), mirroring the graded expression of *Igsf9b* in L2/3 types A, B, and C along the pial-ventricular axis in normally reared WT mice (see **Figure 3.6**). Taken together, these findings establish that *Igsf9b* regulates the vision-dependent maturation of L2/3 excitatory neurons in a graded fashion along L2/3 pial-ventricular axis.

Discussion

Critical periods define windows of postnatal development where neural circuitry is particularly sensitive to experience. Here we sought to gain insight into how experience influences circuitry during this period at the level of cell types in mouse V1.

A postnatal developmental atlas of mouse V1

To study vision-dependent cortical development at the level of cell types, we generated a developmental atlas of mouse V1 comprising over 220,000 nuclear transcriptomes spanning six postnatal ages and three light-rearing conditions. Several features of this dataset enabled us to identify robust and reproducible biological signals. First, we identified a similar number of transcriptomic clusters at all six ages, which were collected and processed separately. For all clusters, transcriptomic identities and relative proportions were comparable between independent samples, consistent with these being bona fide cell types. Second, computational inference of transcriptomic maturation showed that the GABAergic, deep-layer glutamatergic, and non-neuronal cell types were present prior to eye opening and remained largely unchanged through the critical period, whether animals were reared in a normal dark/light cycle or in the dark. Third, these stable cell types served as important "negative controls" that enabled us to identify the minority of cell types among the upper layer glutamatergic neurons that were specified following eye opening, and whose transcriptomic identities were profoundly influenced by vision. Fourth, we identified cell type markers that enabled us to uncover the arrangement of L2/3 cell types in sublayers **(**see **Figures 3.3B-D)**. And finally, the developmental atlas served as a foundation to investigate vision-dependent functional maturation of V1 at the resolution of cell types and molecules.

The establishment and maintenance of L2/3 neuron types require vision

In this study, we define a cell type based on a core transcriptomic signature that distinguishes it from other types. When the signature becomes invariant during development, we consider the cell type to be specified. For L2/3 and 4 cell types, these signatures are established following eye-opening, whereas for the remaining cell types, they are present from P8. These signatures allow us to assess cell type-specific gene regulation under sensory deprivation. While activity-dependent gene expression changes occur in every layer, the changes are more extensive in L2/3 and 4, where cell type identity is disrupted. This is not the case for deeper layers (L5 and 6).

It is striking that the acquisition of transcriptomic cell type identity in L2/3 excitatory neurons follows a time course similar to their functional maturation. We previously showed that there are few binocular neurons in L2/3 at eye opening. Their numbers increase over the next several days in a vision-dependent process (Tan et al., 2021). During the critical period, these binocular neurons, most of which are poorly tuned, are rendered monocular. In parallel, new binocular neurons are formed from the conversion of other well-tuned monocular neurons which gained matched responses to the other eye (Tan et al., 2020). It is through this exchange of neurons that well-tuned and matched binocular neurons emerge to give rise to mature binocular circuitry. This process relies on vision during the critical period. Activity may drive cell type changes that, in turn, instruct changes in circuit organization, or alternatively, transcriptomic programs could be regulated by circuit activity. Further experiments will be necessary to distinguish between these and other mechanisms. Experience-dependent regulation of upper-layer cortical cell types may be a general principle underlying cortical development during critical periods.

Continuous variation in L2/3 identity and sublayer arrangement

Although unsupervised clustering defined three predominant glutamatergic neuronal types in L2/3, the gene expression differences between them were graded, giving rise to continuous variation in transcriptomic identity (**Figures 3.6A** and **S3.6A-B**). This continuous variation *in silico* was seen as a spatially graded, sublayered arrangement in L2/3 via FISH. This is not a general feature of glutamatergic cell type specification, as glutamatergic cell type identity in L5, for example, is neither graded nor dependent upon vision. Continuous variation of cell type identity has been reported in other regions of the mammalian brain (Cembrowski et al., 2016; Cembrowski and Menon, 2018; O'Leary et al., 2020; Yao et al., 2021b).

That the molecular heterogeneity in L2/3 reflects functional differences is supported by a recent retrograde labeling analysis of adult V1, which identified transcriptional signatures of L2/3 glutamatergic neurons that project to the anterolateral (AL) and posteromedial (PM) higher visual areas (HVAs) (Kim et al., 2020; Kim et al., 2018). PM- and AL-projecting neurons localize in the upper and lower regions of L2/3 and express the markers *Cntn5/Grm1* and *Astn2/Kcnh5*, respectively **(Figure S3.6D).** In our data, these markers are expressed in a graded and opposite fashion along the pial-ventricular axis, suggesting that PM- and AL-projecting L2/3 neurons localize to the upper (type A) and lower (type C) sublayers, respectively (**Figure S3.6E**).

L2/3 neurons form numerous "local" circuits that process diverse visual information, but these are yet to be defined at the cell type level (Harris and Mrsic-Flogel, 2013). While a given excitatory neuron may participate in multiple circuits, there is evidence for synaptic specificity (Kim et al., 2018). It is tempting to speculate that this functional segregation may, in part, be due to graded molecular differences between neurons uncovered in our transcriptomic analysis. These graded differences may also exist along mediolateral and anteroposterior axes to further subdivide V1 into functional circuits.

Experience-dependent cell type specification in L2/3

One of our main findings is that vision specifies L2/3 cell types in V1 and that these cell types are arranged in a sublayered fashion. Recent studies have reported the sublayered organization of cell types in L2/3 of the mouse motor cortex, in addition to the visual cortex (Berg et al., 2021; Gouwens et al., 2019; Munoz-Castaneda et al., 2021; Network, 2021; Scala et al., 2020; Zhang et al., 2021), suggesting an analogous experience-dependent mechanism may be involved in patterning this region. Emerging transcriptomic, morphological, and physiological evidence of similar cell type continuums arranged in sublayers in L2/3 of the human cortex (Berg et al., 2021) raise the exciting possibility that experience-dependent cell-type specification may be a general principle of mammalian cortical development.

Igsf9b is a vision-dependent regulator of cortical circuitry

Patterns of experience-dependent activity may promote the expression of recognition molecules that regulate wiring. Indeed, different patterns of experience-independent activity have been shown to regulate the expression of cell-type specific wiring genes in the mouse olfactory system (Nakashima et al., 2019). Our identification of vision-regulated recognition molecules expressed in L2/3 neurons and genetic studies on *Igsf9b* provide support for the view that experience-dependent processes may also contribute to cell-type specific wiring (**Figures 3.7** and **S3.7**).

Analyses of V1 in mice that lack *Igsf9b* revealed changes in inhibitory, but not excitatory, synaptic markers. More significantly, *Igsf9b*$^{-/-}$ mice showed a significant decrease in the proportion of binocular neurons and the proportion of tuned neurons. In the case of the latter phenotype, the severity of the defect increased in deeper sublayers, where in wild type animals, *Igsf9b* expression is higher. A similar impact on the tuning of glutamatergic neurons, more broadly within L2/3, was observed in optogenetic experiments in which perisomatic PV inhibitory neuron activity was suppressed (Zhu et al., 2015). Thus, IGSF9B may modulate PV inhibitory input onto L2/3 excitatory neurons during the critical period. These findings are consistent with previous studies demonstrating a role for IGSF9B in regulating inhibitory synapses.

Limitations of the study

Our data clearly establish that many genes are expressed in a graded fashion along the pial-ventricular axis of L2/3. The simplest interpretation of this finding is that individual cells at different depths express varying ratios of these genes, which would be consistent with the single-cell sequencing data. However, to directly test this hypothesis, future studies should quantify the expression of multiple genes simultaneously in the same cell as a function of the cell's position using spatial transcriptomics methods (Ortiz et al., 2021).

Our single-cell sequencing, FISH, and genetic data support a model in which IGSF9B acts within L2/3 excitatory neurons in a graded fashion to regulate function. This observation mirrors the graded distribution of *Igsf9b* expression along the pial-ventricular axis in L2/3. However, as our deletion of *Igsf9b* was systemic, the precise molecular and cellular mechanisms underlying the phenotype are unclear. Future experiments in this regard would include inducible, cell-type specific knockouts of *Igsf9b* in L2/3 excitatory neurons, as well as other neuronal populations, with the goal of examining the maturation of L2/3 receptive tuning properties during the critical period. As IGSF9B physically interacts with Negr1 (Wojtowicz et al., 2020), a heterophilic ligand expressed on inhibitory neurons, genetic experiments will be necessary to assess the role of Negr1 in regulating the maturation of L2/3 neurons and to discriminate between a role for IGSF9B-mediated heterophilic versus homophilic interactions in circuit maturation. In a larger context, detailed biochemical, histological, and physiological analyses will be necessary to establish the relationship between the genetic requirement for IGSF9B for the functional maturation of L2/3 neurons and the development of inhibitory synapses.

Concluding Remarks

In summary, our results raise the exciting possibility that experience-dependent cell type specification is a general phenomenon in mammalian brain development. Understanding how the interplay between circuit function, cell type specification, and experience sculpts circuitry will rely on integrating multiple levels of analysis from molecules to behavior.

Material and Methods

Data and code availability

- All raw and processed snRNA-seq datasets reported in this study are publicly available via NCBI's Gene Expression Omnibus (GEO) Accession Number GSE190940. Processed h5ad files are available at https://github.com/shekharlab/mouseVC. Visualization of the atlas is available at https://singlecell.broadinstitute.org/single_cell (Study ID: SCP1664). The imaging data has been deposited at https://figshare.com/articles/dataset/Vision-dependent_specification_of_cell_types_and_function_in_the_developing_cortex/16992544.
- Computational scripts detailing snRNA-seq analysis reported in this paper are available at https://github.com/shekharlab/mouseVC. All custom software for imaging analysis will be made available upon request.

Experimental model and subject details

Mice

Mouse breeding and husbandry procedures were carried out in accordance with UCLA's animal care and use committee protocol number 2009-031-31A, at University of California, Los Angeles. Mice were given food and water *ad libitum* and lived in a 12-hr day/night cycle with up to four adult animals per cage. Only virgin male C57BL/6J wild-type mice were used for single nuclei sequencing and FISH experiments in this study.

For genetic analysis of *Igsf9b*, mice used in immunohistochemistry and 2-photon imaging experiments were naive subjects with no prior history of participation in research studies. All live imaging was performed on mice expressing jGCaMP7f in V1B neurons. GCaMP expression was induced by AAV pGP-AAV-syn-jGCaMP7f-WPRE intracortically injected into Igsf9b WT and KO mice. WT (*Igsf9b*$^{+/+}$) and KO (*Igsf9b*$^{-/-}$) mice were bred from *Igsf9b*$^{+/-}$ mice graciously gifted by the Krueger-Burg lab. These mice were originally obtained by their lab from Lexicon Pharmaceuticals (Thee Woodlands, TX, U.S.A.; Omnibank clon 281214, generated through insertion of the Omnibank gene trap vector 48 into Igsf9b gene in Sv129 ES cells). The commercial version of this mouse has since sold to Taconic Biosciences (1 Discovery Drivee, Suite 304, Rensselaer, NY 12144) (https://www.taconic.com/knockout-mouse/igsf9b-trapped). The mice were backcrossed onto C57BL/6J background for at least 6 generations by the Krueger-Burg lab and confirmed to be null KO in Babaev et al 2018 (https://doi.org/10.1038/s41467-018-07762-1). Genotyping was performed on P6-P9 pups, and genotypes of pups were identified by PCR that was outsourced to Transnetyx (transnetyx.com). Plots for NR and DR mice in Figure 3.7G, J and K were from unpublished results in Tan et al., 2020. A total of 14 mice, both male (9) and female (5) were used in 2-photon imaging. P21 WT: 3 males and 1 female. P21 KO: 1 male and 2 females. P36 WT: 4 males and 1 female (1 female overlaps with P21 WT). P36 KO: 1 male and 4 females (2 females overlap with P21 KO).

Visual deprivation experiments

Mice that were dark-reared were done so in a box covered from inside and outside with black rubberized fabric (ThorLabs Cat# BK5) for 7-17 days (P21-P28 or P21-P38) or 9 days (P8-P17) before being euthanized. The dark box was only opened with red light on in the room (mice are more than 10-fold less sensitive to red light). Mice that were dark-light reared were first dark reared for 7 days from P21 to P28 in the dark, and then transferred back to the mouse room to receive 8 hours of ambient light prior to euthanasia. Normally reared mice were housed in a 12 hr light-ON, 12 hr light-OFF cycle. Tissue was collected during a range of 4-8 hours into the light-ON phase. DR mice were dark reared for a period of 7 (P28 DR) and 17 (P38 DR) days with no light. Tissue was collected immediately after retrieving the mice from the dark box. For the dark-light rearing (P28 DL), mice were placed in the light for 8 hours during the light phase in the mouse room after coming out of the dark box.

V1 dissection to obtain single nuclei

Normally-reared mice were dissected at P8, P14, P17, P21, P28, and P38. Isoflurane was used for anesthetization and mice were euthanized by cervical dislocation. Dark-reared mice were dissected at P28 and P38. Dark-light reared mice were dissected at P28 after exposure to 8 hr ambient light. For each age or condition group, 30 mice were dissected: 15 for each biological replicate of single-nucleus(sn) RNA-sequencing. Mice were anesthetized in an isoflurane chamber, decapitated, and the brain was immediately removed and submerged in Hibernate A (BrainBits Cat# HACA). While the dissection was aimed to target V1b, the region enriched for binocular neurons, due to the small size of this region, the dissection invariably captured neighboring V1 tissue. Therefore, we refer to the tissue as V1. Extracted brains were placed on a metal mold and the slice containing V1 was isolated by inserting one blade 0.5 mm posterior to the lambdoid suture and a second blade 1.5 mm further anterior (2 spaces on the mold). This slice was removed and lowered to Hibernate A in a 60cc petri dish, which was placed on a ruler under a dissecting microscope. The midline was aligned with the ruler and the first cut was bilaterally 3.3 mm out from the midline. The second cut was 0.7 mm medial to the first cut. The cortex was peeled off the underlying white matter. The V1 piece with a total of 1 mm cortex depth by 1.5 mm thickness was transferred to a dish containing 600 µl of RNAlater (Thermo Fisher Cat# AM7020) and kept on ice until dissections were complete. Dissected tissues were then kept in RNAlater at 4°C overnight and transferred to -20°C the next day. Tissue was stored this way for up to 1 month prior to being processed for snRNA-seq.

Droplet-based single-nucleus(sn) RNA-sequencing

For each biological replicate, dissected V1 regions from 15 mice were removed from RNAlater, weighed, then chopped with a small blade on a cleaned slide on top of a cooling cube. Tissue was then transferred to a dounce homogenizer chilled to 4°C and denounced slowly 30 times with a tight pestle in 1 ml of homogenization buffer containing 250mM Sucrose, 150mM KCl, 30mM $MgCl_2$, 60mM Tris pH 8, 1 µM DTT, 0.5x protease inhibitor (Sigma-Aldrich Cat# 11697498001), 0.2 U/µl RNase inhibitor, and 0.1%TritonX. All solutions were made with RNase-free H_2O. Each sample was filtered through a 40 µm cell strainer and then centrifuged at 1000g for 10 minutes at 4°C. The pellet was resuspended in the homogenization buffer and an equal volume of 50% iodixanol was added to the resuspended pellet to create 25% iodixanol and nuclei mix. This mix was layered upon 29% iodixanol and spun at 13,500g for 20 minutes at 4°C. The supernatant was removed and the pellet was washed in a buffer containing 0.2 U/µl RNAse inhibitor, PBS (137 mM NaCl, 2.7 mM KCl, 8 mM Na_2HPO_4, and 2 mM KH_2PO_4, pH 7.4), 1% bovine serum albumin, and then filtered over a 40 µm filter and centrifuged at 500g for 10 minutes at 4°C. The pellet was resuspended and filtered with two more 40 µm filters, cells counted on a hemocytometer and then diluted to 700-1200 nuclei/mm^3. Nuclei were re-counted on a 10X automated cell counter. Nuclei were further diluted to the optimal concentration to target capturing 8000 cells per channel.

Nuclei from each biological replicate were split into two and run separately on two channels of 10X v3, targeting 8,000 cells per channel. We refer to these as library replicates. For each experiment, we performed two biological replicates towards a total of four library replicates. The two biological replicates were processed on different days. Sequencing was performed using the Illumina NovaSeq™ 6000 Sequencing System (S2) to a depth of ~30,000 reads per cell. All library preparation and sequencing were performed at the UCLA's Technology Center for Genomics & Bioinformatics (TCBG) core.

Single-molecule fluorescent in situ hybridization (smFISH)

C57/BL6J mice were anesthetized in isoflurane at ages ranging from P8 to P38 and then perfused transcardially with heparinized PBS followed by 4% paraformaldehyde (PFA) diluted in PBS and adjusted to pH 7.4. Following perfusion, the brains were collected and postfixed for 24h at 4°C in 4% PFA, and then cryoprotected sequentially in 10%, 20%, and 30% sucrose in PBS solution until the brain sank. Brains were then frozen in OCT using a methylbutane and dry ice bath and stored at -80°C until time of sectioning. Brains were cut into 15 µm thick coronal sections at -22/-20°C using a cryostat (Leica CM 1950) and single sections were collected in a charged microscope slide in ascending order from the frontal to the occipital region starting in V1. For localization of the visual cortex V1 and binocular zone of V1, coordinates from (Franklin, 2012) were used. Sections were stored at -80°C until further processing. For all FISH experiments, coronal sections were selected to be from a similar anatomical region within V1 when comparing conditions or ages.

Multiplex FISH was performed following ACD Biology's Multiplex RNAscope v2 assay (Advanced Cell Diagnostics, cat# 323110). Briefly, thawed sections were baked at 60°C, post-fixed for 1 hr at 4°C in 4% PFA, and then dehydrated in sequential ethanol treatments followed by H_2O_2 permeabilization and target retrieval. Protease III treatment was used, then application of probes and sequential amplification and fluorophore development fluorophores (Akoya Biosciences cat# FP1487001KT, FP1488001K, FP1497001KT). Slides were counterstained with 1 ug/ml 4,6-diamidino-2-pheenylindole (DAPI, Sigma cat #D9542) and mounted with Prolong Gold (Thermo Fisher Scientific cat# P36930). RNAscope probes used include: *Igsf9b* (cat# 832171-C3), *Mdga1* (cat#546411, 546411-C2), *Nlgn2* (cat# 406681). Cdh13 (cat # 443251-C3), *Chrm2* (cat # 495311-C2), *Deptor* (cat #481561 - C3), *Gad1* (cat3 400951-C2), *Slc17a7* (cat# 416631-C2, 416631, 416631-C3), *Trpc6* (cat# 442951), *Tshz2* (cat# 431061-C1). Each time point or condition had three to four biological replicates comprising brain sections from different mice. NR mice at P8, P14, P17, P21, P28, and P38, DR mice at P17, P28, and P38, and DL mice at P28 were used.

Immunolabeling for synaptic markers

Immunolabeling for VGLUT1 and GAD65 on brains at all time points shown was performed on perfusion-fixed brains that underwent the same preparation as for smFISH. Brains were sectioned to 15 µm sections. Sections were then incubated for 24 hr with anti-VGLUT1 (guinea pig polyclonal Millipore Sigma Cat# AB5905) and anti-GAD65 (mouse monoclonal Millipore Sigma Cat#MAB3521R) diluted 1:500 in blocking solution (10% NGS in 0.3% PBST), washed 3x times in PBS, and then incubated for 2 hr with goat anti-mouse 488 (Invitrogen Cat# A11029) and goat anti-guinea pig 568 (Invitrogen Cat#A11075) both diluted 1:500 in blocking solution.

Immunolabeling for synaptic markers in IGSF9B KO vs WT experiments were performed on perfusion-fixed brains sectioned to 40 µm and preserved in aliquots of antifreeze (42.8g Sucrose Fisher Cat # S25590B, 0.33g of MgCl2.6H2O Sigma Cat#M2670, 312.5g (250 mL) glycerol Sigma Cat#G7757, 25mL 10X PBS, total to 500 mL w/ ddH2O). On the day of the experiment, tissues were washed 4 times at 15 minutes per wash from antifreeze using 0.3% PBST, blocked with 10% goat serum in PBST, incubated with primary antibody at 4C for 2 nights (~44 hours). Samples were washed 4 times, 15 minutes each in 1X PBS, then secondary antibody diluted in blocking solution was added for 2 hr at room temperature. Samples were washed 4 times at 10minutes per wash in 1X PBS then stained with 1:10k DAPI for 15 minutes, washed for 10 min in PBS, and then mounted with Prolong Gold. Primary antibodies used include: anti-VGLUT1 (guinea pig polyclonal Millipore Sigma Cat# AB5905), anti-VGLUT2 (Guinea pig polyclonal Synaptic Systems Cat#135404, anti-GAD65 (mouse monoclonal Millipore Sigma Cat#MAB3521R), anti-NLGN2 (guinea pig polyclonal Synaptic Systems Cat#129205), anti-GABRA1 (rabbit polyclonal Synaptic Systems Cat#224203), anti-GABRG2 (guinea pig polyclonal Synaptic Systems Cat#224004 (anti-GPHN (mouse monoclonal Synaptic Systems Cat#147011), anti-VGAT (rabbit polyclonal Synaptic Systems Cat#131002), anti-PSD95 (rabbit polyclonal Invitrogen Cat#VH307495), anti-SSCAM (rabbit polyclonal Sigma Aldrich Cat#2441).

Secondary antibodies used include goat anti-guinea pig 566 (Invitrogen Cat#A11075), goat anti-guinea pig 647 (Life Technologies Cat#A21450), goat anti-mouse 488 (Invitrogen Cat#A11029), goat anti-guinea pig 568 (Invitrogen Cat#A11075), goat anti-rabbit 488 (Life Technologies Cat#A11008), goat anti-mouse 568 (Invitrogen Cat#A11031), goat anti-rabbit 647 (Invitrogen Cat#A21244), goat anti-rabbit 568 (Invitrogen Cat#A11011).

Confocal imaging

All histology images were acquired on a Zeiss LSM 880 confocal microscope with Zen digital imaging software. *In situ* hybridization images were acquired using 20x and 40x magnification objectives with 0.8 NA and 1.2 NA, respectively. Each image frame was 1024 pixels x 1024 pixels. For 20X and 40X images, this corresponded to a 425.1 µm x 425.1 µm and 212.5 µm x 212.5 µm coverage area per frame, respectively. Vertically tiled 20X images were acquired covering all cortical layers, as well as 40X horizontal tiled images to cover L2/3 only. Z-stacks were taken to cover the entire 15 µm section. *Mdga1* and *Ccbe1,* both L2/3-markers, were used as markers to assess the cortical depth covered by each 40X image. For each 40X frame starting at layer 2, one frame covered the depth of L2/3 based on *Mdga1* and *Ccbe1* signals.

For immunolabeling experiments of synaptic markers, images were taken using a confocal microscope with high NA 63X magnification objective (1.4 NA), imaged on both hemispheres of the brain in L2/3 of V1 based on anatomical landmarks. Each z-stack comprising 15 optical sections spanned the first 5 µm of each section imaged with step interval of 0.3648 µm. For thick (40 µm) immunohistochemical sections, two 5 µm thick z-stacks under 63X objective were vertically tiled to cover the entire L2/3 of V1. Each individual imaging frame is 1024x1024 in pixel with 134.95 µm x 134.95 µm area coverage; two tiled images result in a final area coverage of 134.95 µm x 269.9 µm.

Imaging quantification

3D z-stacked images were z-projected on FIJI version 2.1.0/1.53c. The entire z-stack covering the slide was projected into a 2D image with maximum intensity. 20X images were tiled using DAPI and *Slc17a7* channels (when available) as guides through linear blending to capture the entire cortical thickness. 40X and 63X images were processed as is. Maximum-projected images were entered into CellProfiler using a custom pipeline modified from the original SABER-FISH pipeline (Kishi et al., 2019). Modifications were made to detect up to four imaging channels (McQuin et al., 2018). CellProfiler was used to perform nuclear and cell segmentation, as well as puncta counting. Nuclear segmentation was done by using DAPI and cellular segmentation was done by taking a fixed radius of 5 pixels around the nucleus. For downstream computation, nuclear segmentation results were used. Segmented images had nuclear boundaries as well as individual puncta married in an overlay color with original image items in gray. All segmented images were inspected to ensure no aberration in segmentation or puncta calling.

After segmentation and puncta calling, data were analyzed in R using custom scripts to compare nuclear mRNA counts (i.e., number of puncta) between time points and conditions. For cell type experiments, cells were sorted into types based on mRNA counts of marker genes. Briefly, cells were ranked based on their mRNA counts of each gene and visualized as a scatter plot of counts vs. rank. The knee of this plot was located (Arneson et al., 2018). The mRNA count value at the knee was chosen as the cutoff for cell type assignment. Quantification of protein puncta in immunolabeling experiments also used Cell Profiler by adapting the same pipeline developed to count mRNA puncta. Protein puncta were quantified per image and normalized by the number of nuclei segmented in that image (**Figure S3.7B-F**). In **Figure S3.7G**, the unique peri-nuclear somatic distribution of NLGN2 enabled its quantification using a 20-pixel boundary around the nucleus and counting the puncta that fell in that boundary. This allowed for quantifying NLGN2 protein puncta per cell.

Surgery and AAV injection

All epifluorescence and two-photon imaging experiments were performed through chronically implanted cranial windows. Mice aged P10-11 (for P21 imaging) or P25-26 (for P36 imaging) were administered with carprofen analgesia prior to surgery, anesthetized with isoflurane (5% for induction; 0.75–1.5% during surgery), mounted on a stereotaxic surgical stage via ear bars and a mouth bar. Their body temperature was maintained at 37°C via a heating pad. The scalp and connective tissue were removed, and the exposed skull was allowed to dry. Then a thin layer of Vetbond was used to cover the exposed skull and wound margins. Once dry, a thin layer of dental acrylic was applied around the wound margins, avoiding the region of skull overlying V1. A metal head bar was affixed with dental acrylic caudally to V1. A 3mm circular piece of skull overlying binocular V1 on the left hemisphere was removed after using high-speed dental drill to thin the bone along the circumference of this circle. Care was taken to ensure that the dura was not damaged at any time during drilling or removal of the skull.

Local AAV injection into binocular V1 took place after the skull was removed. Exposed brain was submerged in normal saline during injection. AAV was diluted in 1xPBS that contains 2.5% mannitol (w/v) to a final titer of $6.7 \sim 7.5 \times 10^{12}$ genomes per ml. Mannitol was used to increase the viral spread (Mastakov et al., 2001). For both age groups, virus was injected at least 10 days before imaging. Virus injection was done using a glass micropipette (tip diameter: 19-25 μm) and Nanoject III (Drummond Scientific Company) attached on Scientifica PatchStar Micromanipulator (Scientifica) controlled with LinLab2 (Scientifica). Injection site was at 3 mm lateral from the midline and 1 mm rostral from lambda. Injections occurred at three depths: 470, 340 and 210 μm below the pial surface. At each depth, 65 cycles of injection were done, with each cycle injecting 5 nL at 5 nL/s speed, with 10 second intervals between cycles. Thus, 325 nL of AAV was injected at each depth, and 975 nL was injected into V1B in total. After virus injection, a sterile 2.5 mm diameter cover glass was placed directly on the exposed dura and sealed to the surrounding skull with Vetbond. The remainder of the exposed skull and the margins of the cover glass were sealed with dental acrylic. Mice were then recovered on a heating pad. When alert, they were placed back in their home cage. Carprofen was administered daily for 3 days post-surgery. Mice were left to recover for at least 10 days prior to imaging. Mice injected at P10-11 would also be imaged at P36 if their cranial windows remained clear.

Mapping of binocular area of the primary visual cortex

The precise location of the binocular region in V1 on the left hemisphere for each mouse was identified using low magnification, epifluorescence imaging of jGCaMP7f signals. For all mice, visual areas were mapped the day before imaging. Briefly, jGCaMP7f was excited using a 470nm light-emitting diode. A 27-inch LCD monitor (ASUS, refreshed at 60 Hz) was positioned such that the binocular visual field fell in the center of the monitor. The screen size was 112 deg in azimuth and 63 deg in elevation and the monitor was placed 20 cm from the eyes. A contrast reversing checkerboard (checker size 10x10 degree) bar windowed by a 1D Gaussian were presented along the horizontal or vertical axis to both eyes (**Figure S3.7H**). The checkerboard bar drifted normal to its orientation and swept the full screen width in 10 sec. Both directions of motion were used to obtain an absolute phase map along the two axes. Eight cycles were recorded for each of the four cardinal directions. Images were acquired at 10 frames per second with a PCO edge 4.2 sCMOS camera using a 35mm fixed focal length lens (Edmund optics, 35mm/F1.65, #85362, 3mm field of view). The camera focused on the pial surface. The visual areas were obtained from retinotopic maps of azimuth and elevation. The binocular area of the primary cortex was defined as the region of primary visual cortex adjacent to the higher visual area LM (**Figure S3.7I**).

Two-photon calcium imaging

Two-photon imaging was targeted to the binocular area of V1 using a resonant/galvo scanning two-photon microscope (Neurolabware, Los Angeles, CA) controlled by Scanbox image acquisition software (Los Angeles, CA). A Coherent Discovery TPC laser (Santa Clara, CA) running at 920 nm focused through a 16x water-immersion objective lens (Nikon, 0.8 numerical aperture) was used to excite jGCaMP7f. The objective was set at an angle of 10-11 degrees from the plumb line to reduce the slope of the imaging planes. Image sequences (512x796 pixels, 490x630 µm) were captured at 15.5 Hz at a depth of 120 to 320µm below the pial surface on alert, head-fixed mice that were free to run on a 3D-printed running wheel (14cm diameter). A rotary encoder was used to record the rotations of this running wheel. Three planes that were well separated in depth and covered the top, middle and bottom of L2/3 were imaged per mouse (**Figure S3.7J**). To measure responses of neurons to each eye separately, an opaque patch was placed immediately in front of one eye when recording neuronal responses to visual stimuli presented to the other eye.

Visual stimulation during 2-photon imaging

On the same screen that was used for visual area mapping, a set of sinusoidal gratings with 18 orientations (equal intervals of 10 degrees from 0 to 170 degrees), 12 spatial frequencies (equal steps on a logarithmic scale from 0.0079 to 0.1549 cycles per degree) and 8 spatial phases were generated in real-time by a Processing sketch using OpenGL shaders (see https://processing.org). These static gratings were presented at 4 Hz in full screen in pseudo-random sequence with 100% contrast (**Figure 3.7A**). Imaging sessions were 15 min long (3600 stimuli in total), thus each combination of orientation and spatial frequency appeared 16 or 17 times. Transistor-transistor logic signals were used to synchronize visual stimulation and imaging data. The stimulus computer generated these signals, and these were sampled by the microscope electronics and time-stamped by the acquisition computer to indicate the frame and line number being scanned at the time of the TTL.

Analysis of two-photon imaging data

Image processing

Movies for either eye from the same plane were processed together using a standard pipeline consisting of movie concatenation, motion correction, cell segmentation and ROI signal extraction using Suite2p (https://suite2p.readthedocs.io/). ROIs determined for each experiment were inspected and confirmed visually (**Figure S3.7K**). Neuronal spiking was estimated via non-negative temporal deconvolution of the extracted ROI fluorescence signal using Vanilla algorithm (**Figure S3.7L**) (Berens et al., 2018). Subsequently, fluorescent signals and estimated spiking for each cell were split into separate files corresponding to the individual imaging session for each eye. Each imaging plane was processed independently.

Calculation of response properties

Identification of visually responsive neurons using SNR

Signal to noise ratio (SNR) was used to identify neurons with significant visual responses (tuned neurons). SNR for each neuron was calculated based on the optimal delay of the neuron. Optimal delay was defined as the imaging frame after stimulus onset at which the neuron's inferred spiking reached maximum. To calculate SNR, signal was the mean of standard deviations of spiking to all visual stimuli around the optimal delay (4-6 frames, thus ~0.323 sec, after stimulus onset; see **Figure7H**), and noise was this value at frames well before or after stimulus onset (frames –2 to 0, and 13 to 17). Neurons whose optimal delays occurred outside of the time-locked stimulus response window of 3 to 7 frames after stimulus onset (padded by ±1 frame around the 4-6 frame range used above) were spontaneously active but visually unresponsive. They were untuned neurons and had SNR values close to 1 (**Figure 3.7I**). The SNR values of these untuned neurons were normally distributed (mean = 1.0±0.03) over a narrow range. Untuned neurons with optimal delays naturally occurring in the 3-7 frame time window can be distinguished from visually responsive neurons by SNR. This SNR threshold was defined at 3 standard deviations above the mean SNR of the above-mentioned normal distribution (See the vertical dashed lines in **Figure 3.7K**). SNR values were calculated separately for responses to the ipsilateral or contralateral eye. A neuron is monocular if its SNR for one eye, but not the other, was above the threshold (**Figure 3.7C**). A neuron is binocular if its SNR for either eye was above the threshold (**Figure 3.7D**). A neuron is untuned if its SNR for neither eye was above the threshold.

Tuning kernel for orientation and spatial frequency

The estimation of the tuning kernel was performed by fitting a linear model between the response and the stimulus. Cross-correlation maps were used to show each neuron's inferred spiking level to each visual stimulus (orientation and spatial frequency) and were computed by averaging responses over spatial phases. The final tuning kernel of a neuron was defined as the correlation map at the optimal delay (**Figure 3.7B**).

Orientation preference

We used vertical slices of the tuning kernel through the peak response and calculated the center of mass of this distribution as orientation preference. Orientation preference calculation:

$$Orientation = \frac{arctan\left(\sum_n O_n e^{i2\pi\theta_n/180}\right)}{2}$$

O_n is a 1x18 array, in which a level of estimated spiking (O_1 to O_{18}) occurs at orientations θ_n (0 to 170 degrees, spaced every 10 degrees). Orientation is calculated in radians and then converted to degrees.

ΔOrientation for binocular neurons

For a binocular neuron, Ori_{contra} is the neuron's orientation preference to contralateral eye and Ori_{ipsi} is the orientation preference to ipsilateral eye. *ΔOrientation* was calculated as

$$\Delta Orientation = \left|Ori_{contra} - Ori_{ipsi}\right|$$

If the value of *ΔOrientation* is above 90 (e.g., |170-10|=160), then the actual value for the difference of orientation preferences to two eyes is 180- *ΔOrientation* (180-160=20).

Quantification and Statistical Analysis for 2-photon imaging

A power analysis was not performed a-priori to determine sample size. All statistical analyses were performed in MATLAB (https://www.mathworks.com/), using non-parametric tests with significance levels set at $\alpha < 0.05$. Bonferroni corrections for multiple comparisons were applied when necessary. Mann-Whitney U-tests (Wilcoxon rank sum test) or two-sample Kolmogorov-Smirnov tests were used to test differences between two independent populations.

Computational analysis of single-nucleus transcriptomics data

Alignment and quantification of gene expression

Fastq files with raw reads were processed using Cell Ranger v3.1.0 (10X Genomics) with default parameters. The reference genome and transcriptome used was GRCm38.92 based on Ensembl 92, which was converted to a pre-mRNA reference package by following Cell Ranger guidelines. Each single-nucleus library was processed using the same settings to yield a gene expression matrix (GEM) of mRNA counts across genes (columns) and single nuclei (rows). Each row ID was tagged with the sample name for later batch correction and meta-analysis. We henceforth refer to each nuclear transcriptome as a "cell."

Initial pre-processing of normally reared samples to define classes, subclasses, and types

This section outlines the initial transcriptomic analysis of data from normally reared samples. Unless otherwise noted, all analyses were performed in Python using the SCANPY package (Wolf et al., 2018). The complete computational workflow is illustrated in **Figure S3.1D**.

1. Raw GEMs from 23 snRNA-seq libraries were combined: 6 ages, 2 biological replicates per age and 2 library replicates per biological replicate except for P38, where one of the technical replicates failed quality metrics at the earliest stage of processing. This resulted in a GEM containing 184,936 cells and 53,801 genes.

2. We then generated scatter plots of the number of transcript molecules in each cell (n_counts), the percent of transcripts derived from mitochondrially encoded genes (percent_mito), and the number of expressed genes (n_genes) to identify outlier cells. Cells that satisfied the following conditions were retained: 700 < n_genes < 6500, percent_mito < 1%, and n_counts < 40,000. Only genes detected in more than 8 cells were retained for further analysis. This resulted in a GEM of 167,384 cells and 30,869 genes.
3. Cells were normalized for library size differences. Transcript counts in each cell were rescaled to sum to 10,000 followed by log-transformation. For clustering and visualization, we followed steps described previously (Peng et al., 2019). Briefly, we identified highly variable genes (HVGs), z-scored expression values for each gene, and computed a reduced dimensional representation of the data using principal component analysis (PCA). The top 40 principal components (PCs) were used to compute a nearest-neighbor graph on the cells. The graph was then clustered using the Leiden algorithm (Traag et al., 2019) and embedded in 2D via the Uniform Manifold Approximation and Projection (UMAP) algorithm (Becht et al., 2018).

Additional filtering and class assignment

The analysis above yielded 42 clusters (**Figures S3.1E-F**). Canonical marker genes for cortical classes and subclasses were used to annotate these clusters (**Figure S3.1G, Table S3.1**). We then used Scrublet (Wolock et al., 2019) to identify doublets (**Figure S3.1H**). Clusters that expressed markers of two or more classes or contained more than 50% doublets were labeled “Ambiguous” (**Figure S3.1I**). Removal of ambiguous clusters and doublets in the dataset resulted in a GEM containing 147,236 cells by 30,868 genes.

For further analysis, this matrix was subset by cell class (glutamatergic neurons, GABAergic neurons, and non-neuronal cells) and age (P8, P14, P17, P21, P28 and P38) into 18 separate GEMs (**Figure S3.1D**).

Identification of cell types within each class by age

Each of the 18 GEMs were separately clustered using the procedure described above with one modification. Following PCA, we used Harmony (Korsunsky et al., 2019) to perform batch correction. The nearest-neighbor graph was computed using the top 40 batch-corrected PCs.

Each GEM was then iteratively clustered. We began by clustering cells using the Leiden algorithm, with the resolution parameter fixed at its default value of 1. As before, UMAP was used to visualize the clusters in 2D. Through manual inspection, small clusters with poor quality metrics or ambiguous expression signatures were discarded, likely representing trace contaminants that escaped detection in the earlier steps. The remaining clusters were annotated by subclass based on canonical expression markers (**Table S3.1, Figure 3.1D**). Next, we performed a differential expression (DE) analysis between each cluster and other clusters in its subclass. If a cluster did not display unique expression of one or more genes, it was merged with the nearest neighboring cluster in the UMAP embedding as a step to mitigate over-clustering. This DE and merging process was repeated until each cluster had at least one unique molecular signature (**Figures S3.3A-C**). We refer to the final set of clusters as types.

Workflow for supervised classification analyses

To assess transcriptomic correspondence of clusters across ages or between rearing conditions, we used XGBoost, a gradient boosted decision tree-based classification algorithm (Chen and Guestrin, 2016). In a typical workflow, we trained an XGBoost (version 1.3.3) classifier to learn subclass or type labels within a "reference" dataset, and used it to classify cells from another, "test" dataset. The correspondences between cluster IDs and classifier-assigned labels for the test dataset are used to map subclasses or types between datasets. The classification workflow is described in general terms below and applied to various scenarios in subsequent sections.

Let R denote the reference dataset containing N_R cells grouped into r clusters. Let T denote the test dataset containing N_T cells grouped into t clusters. Here, each cell is a normalized and log-transformed gene expression vector $\boldsymbol{u} \in R$ or $\boldsymbol{v} \in T$. The length of $\boldsymbol{u}$ or $\boldsymbol{v}$ equals the number of genes. Based on clustering results, each cell in R or T is assigned a single cluster label, denoted cluster($\boldsymbol{u}$) or cluster($\boldsymbol{v}$). cluster($\boldsymbol{u}$) may be a type or subclass identity, depending on context.

The main steps are as follows:

1. We trained multi-class XGBoost classifiers C_R^0 and C_R^T on R and T independently using all 30,868 genes as features. In each case, the dataset was split into training and validation subsets. For training we randomly sampled 70% of the cells in each cluster, up to a maximum of 700 cells per cluster. The remaining "held-out" cells were used for evaluating classifier performance. Clusters with fewer than 100 cells in the training set were upsampled via bootstrapping to 100 cells in order to improve classifier accuracy for the smaller clusters. Classifiers achieved a 99% accuracy or higher on the validation set. XGBoost parameters were fixed at the following values:
    1. 'Objective': 'multi:softprob'
    2. 'eval_metric': 'mlogloss'
    3. 'Num_class': r (or t)
    4. 'eta': 0.2
    5. 'Max_depth': 6
    6. 'Subsample': 0.6
2. When applied to a test vector $\boldsymbol{c}$, the classifier C_R^0 or C_R^T returns a vector $p = (p_1, p_2, \ldots)$ of length r or t, respectively. Here, p_i represents the probability value of predicted cluster membership within R or T, respectively. These values are used to compute the "softmax" assignment of $\boldsymbol{c}$, such that cluster($\boldsymbol{c}$) = $arg\ max_i\ p_i$ if $arg\ max_i\ p_i$ is greater than $1.2*(1/r)$ or $1.2*(1/t)$. Otherwise $\boldsymbol{c}$ is classified as 'Unassigned'.
3. Post training, we identified the set of top 500 genes based on average information gain for each C_R^0 and C_R^T. These gene sets are denoted G_R and G_T.
4. Using the common genes $G = G_R \cap G_T$, we trained another classifier C_R on 70% of the cells in R, following the procedure outlined in 1. As before, the performance of C_R was evaluated on the remaining 30% of the data.
5. Finally, we trained a classifier C_R on 100% of the cells in R. C_R was then applied to each cell $\boldsymbol{v} \in T$ to generate predicted labels cluster($\boldsymbol{v}$).

Comparing transcriptomic signatures of developmental V1 to adult V1/ALM subclasses (Tasic et al., 2018)

We used the aforementioned classification workflow to evaluate the correspondence between V1 subclasses in this work (**Figure 3.1D**) and those reported in a recent study of the adult V1 and motor cortex (ALM) (Tasic et al., 2018). We trained a classifier on the V1/ALM subclasses and used it to assign an adult label to each V1 cell collected in this study. A confusion matrix was used to visualize the correspondence between developmental V1 subclasses and V1/ALM subclasses at adulthood (**Figure S3.1J**). This correspondence served as a proxy to evaluate the overall conservation of subclass-specific transcriptomic signatures across developmental stages (developing vs. adult), RNA source (single-nucleus vs. single-cell), platform (3' droplet-based vs. full-length plate-based), and region (V1 vs. V1/ALM).

Inferring temporal association between V1 types using supervised classification

Relating types across time

The supervised classification workflow was used to relate cell types identified at each pair of consecutive ages within each class (5 x 3 = 15 independent analyses). In each case, the classifier was trained on the older age dataset and applied to each cell in the younger age dataset. Thus, each cortical cell at the younger age possessed two type labels, one identified via clustering of cells at that age and the other based on a classier trained at the next age. Assessing the correspondence between these labels enabled us to link cell types between consecutive ages (e.g., P8-P14, P14-P17 and so on) and track their maturation across development

Quantification and visualization of cluster correspondence

The correspondences between types throughout development were visualized using Sankey flow diagrams (**Figures 3.2E**, **S3.2F-G**). In the case of glutamatergic neurons, for example, inspecting the Sankey flow diagrams revealed that L2/3 and 4 types mapped more diffusely across time than L5 and 6 types, suggesting subclass specific differences in maturation. We quantified such subclass-specific differences using three methods,

(1) We computed the adjusted rand index (ARI) between the cluster labels and classifier-assigned labels. The ARI ranges from 0 and 1, with extremes corresponding to random association and perfect (i.e., 1:1) mapping, respectively. Negative values are possible for the ARI but were not observed in our data. The ARI was computed using the function sklearn.metrics.adjusted_rand_score(). ARI values were computed for each pair of consecutive ages (e.g., P8 and P14) within each subclass (e.g., L2/3). ARI differences between glutamatergic subclasses were visualized as bar plots (**Figure 3.2F**). The analysis was repeated for GABAergic and non-neuronal cells (**Figure S3.2H-I**).

(2) We computed for each type the F1 score, which is a measure of a classifier's effectiveness at associating cells within a type to their correct type label. Its value ranges from 0 to 1, with extremes corresponding to no association and perfect

association between transcriptome and type label, respectively. The F1 score was computed for each type at each time point using the function sklearn.metrics.f1_score(). Values were grouped by subclass to visualize differences (**Figures S3.2J-L**). This analysis showed that in addition to exhibiting poor temporal correspondence, L2/3 and L4 types were also less transcriptomically distinct than L5 and L6 types at any given time point (**Figure S3.2J)**. Subclasses within GABAergic and non-neuronal cells did not exhibit such striking differences (**Figures S3.2K-L).**

(3) We assessed the sensitivity of each subclass' clustering results to the clustering resolution parameter of the Leiden algorithm, which controls the number of output clusters. The clustering resolution was increased from 1 to 2. We computed the ARI between the clusters identified at each value of the resolution parameter and the baseline clusters computed at a resolution value of 1. The ARI was computed for the clusters within each subclass at each time point separately. L2/3 and L4 clustering was more sensitive to changes in the resolution parameter than the clustering in L5 and L6 (**Figure 3.2G**).

Analysis of visual deprivation experiments

Separation of major cell classes

In visual deprivation experiments, snRNA-seq profiles were collected from cortical samples of mice dark-reared from P21-P28 (P28DR), dark-reared from P21-P38, (P38DR) and dark-reared from P21-P28 followed by 8 hours of ambient light stimulation. Overall, 12 GEMs from these three experiments were combined and preprocessed (4 libraries per experiment) using the steps described above for normally reared samples. The numbers of cells prior to pre-processing were 43,234, 36,373 and 31,815 for P28DR, P38DR and P28DL respectively. The final numbers of high-quality cells reported were 24,817, 25,671, and 26,575, respectively.

Comparing DR and DL clusters to NR types using supervised classification

To examine cell type correspondence between visual deprivation and normally reared experiments, we used supervised classification as described above. Classifiers were trained on P28NR and P38NR types, and cells from P28DL, P28DR, and P38DR were mapped to the corresponding NR age. The resulting confusion matrices were visualized as dot plots, and the ARI was computed for types within each subclass (**Figure S3.5**).

Differential gene expression analysis

Differential expression (DE) was performed in multiple settings to identify genes enriched in specific classes, subclasses, types, or rearing conditions. We used the scanpy.tl.rank_genes_groups() function and Wilcoxon rank-sum test in the scanpy package for statistical comparisons (Wolf et al., 2018). While searching for genes enriched in a particular group of interest, only those expressed in >20% of cells in the tested group were considered.

The results of the DE analyses were used in the following contexts: 1) To assess the quality of cell populations identified in the initial analysis, where each cluster in **Figure S3.1F** was compared to the rest. Clusters that did not express a unique signature or those that express markers known to be mutually exclusive were removed; 2) To identify subclass markers (**Figure 3.2B**, **Figure S3.2D-E**). This was accomplished by comparing each subclass against the rest; 3) To identify type-specific markers within each subclass (**Figure S3.3A-C**). Here, each type was compared to other types of the same subclass; and 4) To identify gene expression changes as a result of visual deprivation. We performed DE between NR and DR (both ways) subclasses (**Figure 3.6A**, **Figure S3.6A**).

Identification of genes showing graded expression among L2/3 types

We compared each L2/3 type to the other two (e.g., A vs B and C) to identify 287 type-specific genes at fold change > 2 and p-value < 10^{-10} (Wilcoxon test). The expression levels of these genes were z-scored, and we used *k*-means clustering to identify *k*=7 groups based on their pattern of expression among the three types (**Figure S3.6A**). The optimal number of groups was identified using the elbow method. Five of the seven groups, containing 217 genes, showed graded expression differences that could be classified into one of the following patterns based on visual inspection: A > B > C (77 genes), A < B > C (36 genes), C > A > B (9 genes), C > B > A (85 genes) and A > C > B (10 genes). The remaining X genes were expressed in a digital fashion that fell into one of two groups: C > B = A (35 genes) and A > B = C (35 genes). Thus, approximately 75% of the DE genes among L2/3 types are expressed in a graded fashion.

Pseudo-spatial inference of gene expression in L2/3

FISH experiments targeting the three L2/3 glutamatergic type markers revealed that type A resides at the top (near the pia), type B in the middle, and type C at the bottom of L2/3, bordering L4 (**Figure 3.3**). Surprisingly, this relative positioning of A, B, and C types was mirrored in the UMAP embedding. We therefore hypothesized that the UMAP coordinates of a neuron may serve as a proxy for the approximate relative position of its soma in the tissue and used this to calculate the expected spatial expression profiles of genes in each dataset.

In a given scenario, we marked the “A” and “C” cells furthest from each other on the UMAP space as the “root” and the “leaf” and assumed that these represent the top and bottom of L2/3 respectively. We used diffusion pseudo-time (DPT) (Haghverdi et al., 2015; Wolf et al., 2019) to order all L2/3 cells relative to the root cell. DPT and similar methods have been used previously to order cells based on their developmental state (i.e., pseudo-time); we have used it in this context to infer “pseudo-spatial” position based on the observed correspondence described above. Pseudo-spatial positions for cells were close to 0 at the top, where type A begins, and gradually increased through types B and C, reaching the maximum normalized value of 1 at the end of L2/3 in UMAP space. We performed this pseudo-spatial analysis for L2/3 neurons in each of the six normally reared samples.

For the DR and DL datasets, where the spatial organization and transcriptomic profiles are disrupted, a root cell was randomly selected from the beginning of L2/3 in UMAP space (e.g., a cell from the edge of cluster “L2/3_1” was chosen for P28DR) (**Figure 3.4B**). Finally, to visualize the expression of gradient genes as a function of pseudo-spatial position (**Figure 3.6F, H**), we averaged the expressions along bins of pseudo-spatial location that contained as many cells as ~10% of a given dataset.

Identification of temporally regulated genes

This analysis was repeated separately for each of L2/3, L4, L5, and L6. Of the 30,868 genes in the data, we considered only those expressed in more than 20% of the cells in at least one of the six time points. This resulted in 6339, 5746, 6096, and 5428 genes for further analysis in L2/3, L4, L5, and L6, respectively. We first computed the average expression strength of every gene at each of the six time points. Here, the average expression strength $E_{g,t}$ of gene g at age t is defined as follows,

$$E_{g,t} = F_{g,t}X_{g,t}$$

where $F_{g,t}$ is the fraction of cells at age t that express gene g and $X_{g,t}$ is the mean transcript counts of g among cells with non-zero expression. We only considered genes that satisfied the following condition,

$$\frac{\max\left(E_{g,t}\right) - \min\left(E_{g,t}\right)}{\max\left(E_{g,t}\right)} \geq 0.3$$

resulting in 2594, 2410, 2190, and 2192 genes for further analysis in L2/3, L4, L5, and L6, respectively. Next, to identify genes that showed significant temporal variation, we z-scored each E_g vector and randomly shuffled the temporal identities of the cells. We then recomputed a randomized analog of $E_{g,t}$, which we call $\widehat{E_{g,t}}$. We then defined for each gene g a deviation score between the actual and randomized expression vectors,

$$\alpha_g = \frac{\sum_t^{\mathrm{T}}\left(E_{g,t}-\widehat{E_{g,t}}\right)^2}{\sqrt{\sum_t^{\mathrm{T}} E_{g,t}^2 \sum_t^{\mathrm{T}} \widehat{E_{g,t}^2}}}$$

Here, $T = 6$ is the number of time points and the denominator acts as a normalizing factor; we observed a bias towards highly expressed genes in its absence. High values of α_g indicate that the observed temporal pattern of expression is significantly different from the randomized pattern. We picked 855 genes for further analysis that had $\alpha_g > 0.2$. This threshold was chosen by computing an empirical null distribution for α_g using two randomizations $E_{g,t}^1$and $\widehat{E_{g,t}^2}$. The 99.9th percentile value of $P_{null}\left(\alpha_g\right)$ was 0.05, making $\alpha_g = 0.2$ a conservative threshold. Finally, we counted the number of temporally differentially expressed (tDE) genes identified in each layer (**Figure S3.3H**)

Separation of cell classes and subclasses using Seurat

In addition to clustering each time separately in SCANPY, Seurat (version 3.1, (Satija et al., 2015) was used to cluster data from all times and conditions together. This analysis was done to evaluate class and subclass level clustering, and to provide a framework to broadly check gene expression for FISH experiments in all subclasses at all times collectively. Seurat clustering was performed using two methods with similar final results. In the log-normalization based method, data were log normalized and scaled to 10,000 transcripts per cell, with 2000 variable genes used. In the generalized linear model method "SCTransform" (Hafemeister and Satija, 2019), normalization was used with 3000 variable genes. In both methods cells with fewer than 1000 or over 6000 genes or >1% mitochondrial content were filtered out. PCA was performed and unsupervised clustering was applied to the top 80 PCs. Major cell type markers from (Tasic et al., 2016) and (Tasic et al., 2018) were used to assign class and subclass designations to clusters. Clusters having two or more major markers were discarded as "doublet/debris" clusters, and clusters that were solely composed of one or two replicates were also discarded as debris clusters. In both log-normalization and SCT clustering by Seurat, the P8 cortico-cortical projecting excitatory neurons clustered separately from similar subclass neurons of later time points. Thus, P8 was clustered separately, and cell IDs from P8-only clustering were used to re-label the corresponding P8 cells in the full dataset. Class and subclass level clustering results matched SCANPY-based results (**Figure S3.2J**).

Differential gene expression analysis using Seurat

The Seurat-based clustering results were primarily used to assess subclass-level differentially expressed genes. Gene signatures of each cell subclass at different time points were identified with the FindMarkers function, performing pairwise time or condition comparisons and by comparing one time point to the average of others (a second method only used normally reared datasets). Genes were considered if they were present in 10% of cells, 0.25 log fold enriched (1.28 fold-change or more), and had a Benjamini-Hochberg corrected $P<0.05$. Of these, genes that were 0.4 log fold enriched (1.5-fold change or more) were classified as enriched.

Quantification and statistical analysis

Information for statistical analysis for all experiments and computational analyses are provided in the figure legends. Detailed descriptions of these statistical approaches can be found in the **Methods**.

Supplementary Materials

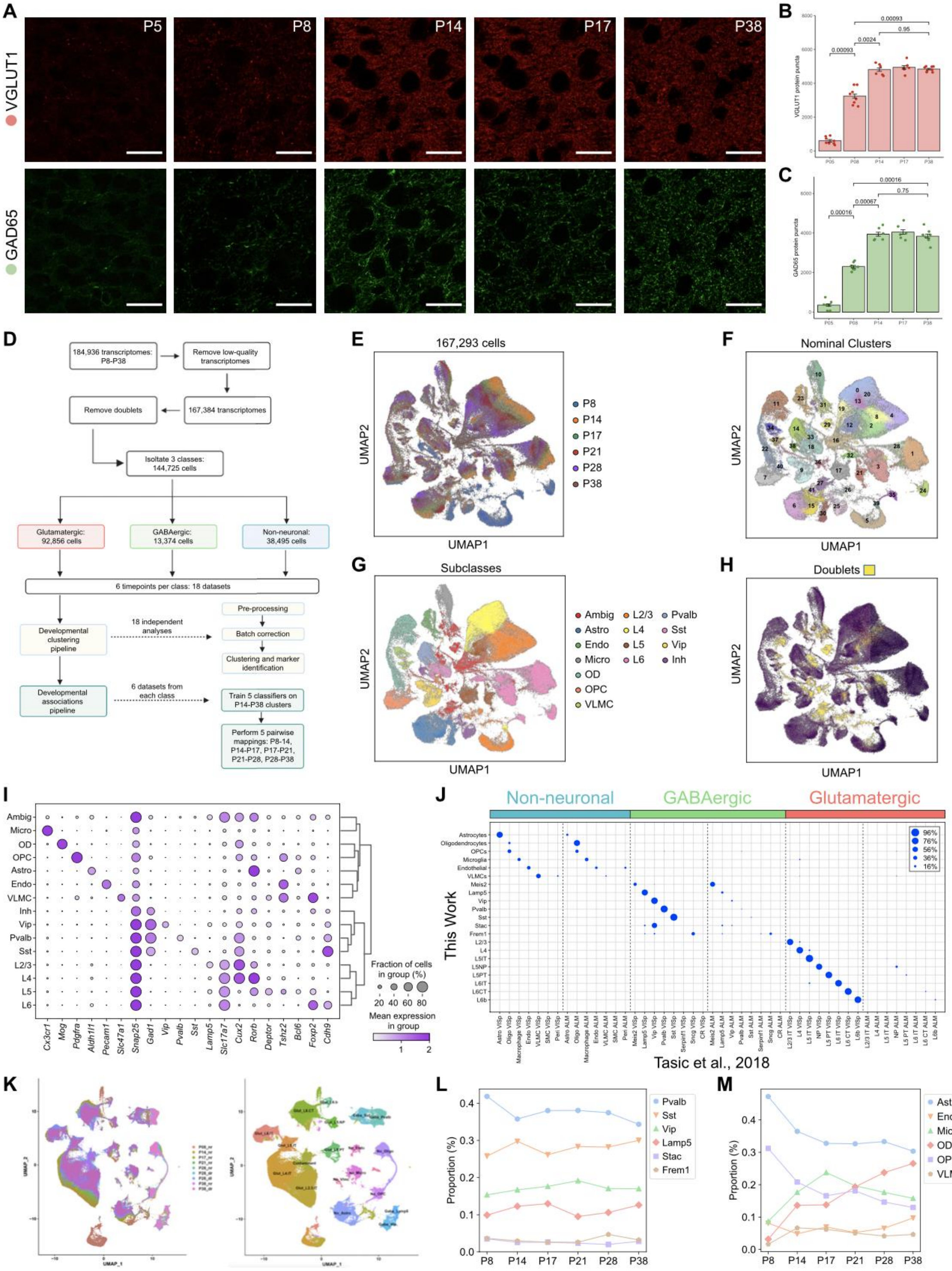

Figure S3.1. Expression of GABAergic and glutamatergic markers with age, snRNA-seq data pre-processing, and comparison to transcriptomic signatures of adult visual and motor cortices (Tasic et al., 2018), related to Figure 3.1

A. Immunohistochemical analysis of the expression of VGLUT1 (a glutamatergic marker) and GAD65 (a GABAergic marker) with age. Panels show a single confocal section of VGLUT1 (red) and GAD65 (green) during postnatal development in L2/3 of V1 in wild-type mice. Ages are indicated on the top right corner panels in the top row. Scale bar, 20 µm.
B. VGLUT1 protein puncta quantification over time, n = 3-4 mice per age, quantified by slide imaged. Horizontal bars show p-values corresponding to a comparison of the number of puncta between each pair of ages using the Wilcoxon rank-sum test. Bar heights denote mean value, error bars are ± SEM.
C. Same as B, for GAD65 protein puncta.
D. A graphical summary of the computational pipeline used to define cell classes, subclasses, and types at each age in normally reared (NR) mice and to analyze the maturation of types. A similar pipeline was used for analyzing the data obtained from dark-rearing (DR) and dark-light adaptation (DL) experiments described in **Figure 3.4**. See **Methods** for details.
E. Uniform Manifold Approximation (UMAP) visualization of V1 transcriptomes prior to removing doublets. Individual nuclei are colored by age.
F. Same as E, colored by transcriptomically defined clusters. This nominal clustering was used to identify and discard doublets and contaminants (**Methods**).
G. Same as E, with nuclei colored by their subclass identity. Clusters in F were assigned to subclasses based on known gene markers (**Table S3.1).**
H. Same as E, with computationally identified doublets highlighted in yellow. The doublets were identified using Scrublet, a nearest-neighbor classification framework that uses the data to simulate multiplets (Wolock et al., 2019). A post hoc analysis verified that the computationally identified doublets co-expressed markers from distinct classes and subclasses (**Table S3.1)** and were discarded prior to further analysis.
I. Dot plot showing marker genes (columns) that distinguish subclasses (rows) identified in panel G. The group labeled "Inh" is an admixture of inhibitory neuronal subclasses defined by *Lamp5, Stac,* and *Frem1* that were not separated at this stage. The size of each dot represents the fraction of cells in each subclass with non-zero expression and its color denotes the average normalized expression level.
J. Confusion matrix showing transcriptomic correspondence between subclasses identified in this study (rows) and subclasses (columns) reported in a scRNA-seq survey of the adult primary visual cortex (V1) and the anterior lateral motor cortex (ALM) (Tasic et al., 2018). The size of each dot represents the proportion of each row mapped to an adult cortex subclass based on an XGBoost classifier trained on the adult cortex. Each row of the matrix is normalized to sum to 100%. The specific pattern of mapping indicates that the transcriptomic correspondence at the level of classes and subclasses was robust despite differences in RNA source (nuclei vs. cells), age (P8-P38 vs. P70+), and sequencing methods (e.g., droplet-based and plate-based). Glutamatergic and GABAergic subclasses map specifically to their V1 counterparts, reflecting regional specificity. Non-neuronal cells, on the other hand, mapped promiscuously, suggesting shared transcriptional programs between V1 and ALM for this class.
K. UMAP visualization of subclass separation when the same dataset is analyzed using Seurat (**Methods**). (*Left*) colored by sample ID, (*right*) colored by subclass. X_0 denotes low quality cells that were discarded.
L. Line plots showing that the relative proportions of GABAergic neuronal subclasses remain stable with age despite significant variation in the number of nuclei collected (**Table S3.2**).
M. Line plots showing relative proportions vs. age for non-neuronal subclasses. Abbreviations: Astro, astrocyte; Endo, endothelial cell; Micro, microglia; OD, oligodendrocyte; OPC, oligodendrocyte precursor cells; VLMC, vascular and leptomeningeal cells.

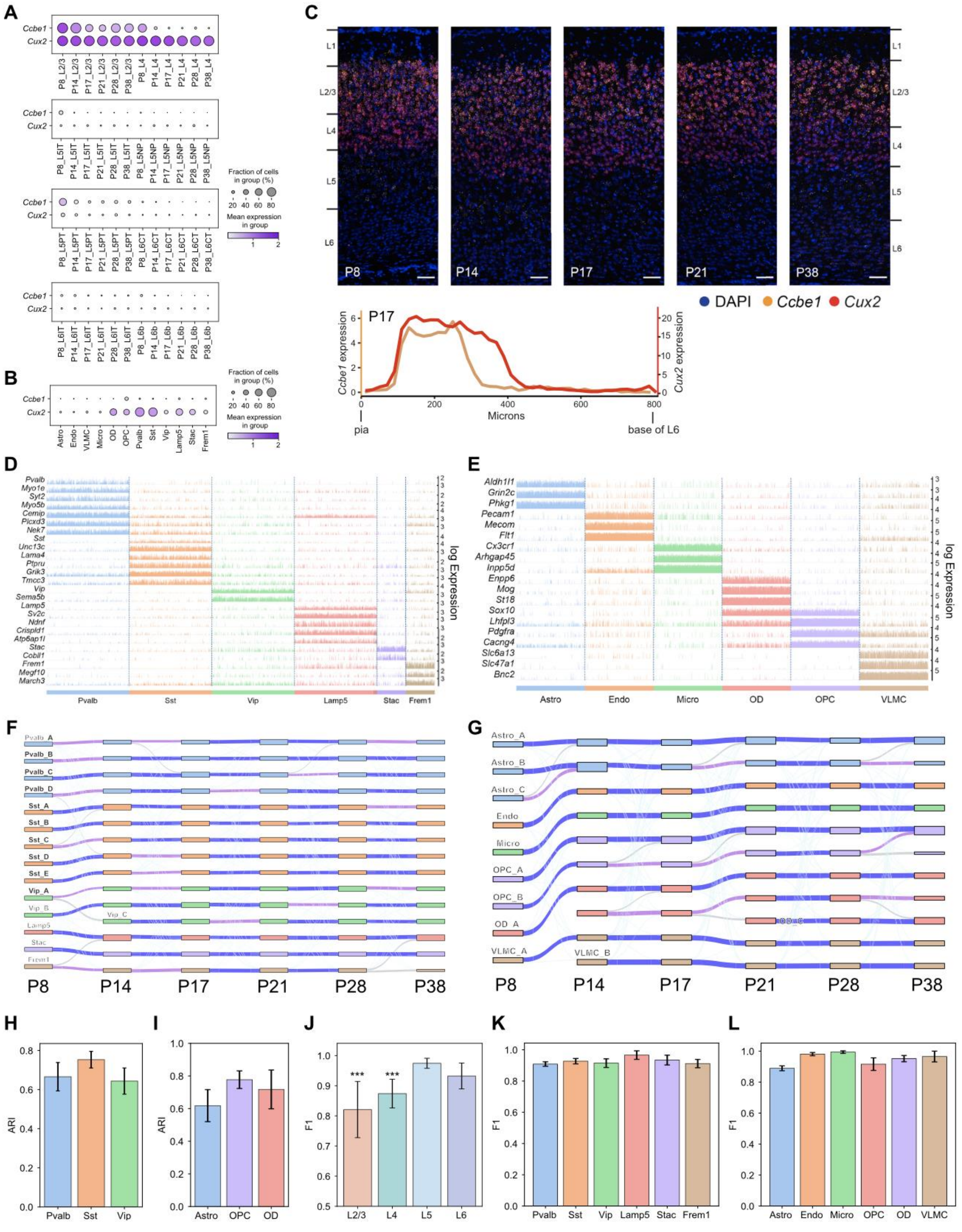

Figure S3.2. Additional data related to transcriptomic maturation of V1 cell types, related to Figure 3.2

A. *Ccbe1* is specific to L2/3 glutamatergic neurons (note transient expression in L4 and L5PT at P8), whereas *Cux2* is expressed in both L2/3 and L4 glutamatergic neurons throughout development.

B. *Cux2* is also expressed in GABAergic neurons and some non-neuronal subclasses, while *Ccbe1* is not. Thus, *Ccbe1* is a bona fide L2/3 glutamatergic neuron-specific marker.

C. (*Top*) FISH images from coronal sections show that *Cux2* is expressed in L2/3 and L4 while *Ccbe1* is selectively expressed in L2/3 glutamatergic neurons from P14 to P38. Scale bar, 100 µm. Note that at P8, *Ccbe1* and *Cux2* overlap in expression, which is consistent with snRNA-seq results (panel A). (*Bottom*) Quantification of *Ccbe1* and *Cux2* expression as a function of cortical depth at P17. Images are aligned prior to quantification, so pia begins at 0 µm and the base of the cortex is 800 µm from pia.

D. Tracks plot showing subclass-specific markers (rows) in inhibitory neurons (columns). For each gene, the scale on the y-axis (right) corresponds to normalized, log-transformed transcript counts detected in each cell. Columns are grouped and colored based by subclass (annotation bar, bottom). In addition to the well-known subclasses marked by *Pvalb*, *Sst* and *Vip,* we also identify subclasses of GABAergic neurons marked by the selective expression of *Lamp5*, *Stac* and *Frem1*. These subclasses were collapsed together in the group labeled "Inh" in **Figure S3.1I**.

E. Same as panel D for non-neuronal subclasses.

F. Sankey graph showing the transcriptomic maturation of V1 GABAergic types. Representation as in **Figure 3.2E**.

G. Same as F for non-neuronal types.

H. Adjusted Rand Index (ARI) values quantifying temporal specificity during maturation of inhibitory types within each subclass. ARI is a measure of similarity between two ways of grouping the data, with values ranging from 0 (no correspondence) to 1 (perfect correspondence). For each subclass at each age, ARI values are computed by comparing the cluster identity of cells with the identity assigned by a multiclass classifier trained on the subsequent age. Individual bars denote the three inhibitory subclasses containing more than 2 types each. Subclasses *Lamp5*, *Stac* and *Frem1* are not shown as these could not be satisfactorily subdivided into constituent types in this study. Bar heights, mean ARI computed across pairs of consecutive ages; error bars, standard deviation.

I. Same as panel H for non-neuronal subclasses. Subclasses Micro and Endo are not included as they each contain only one type.

J. F1 score values quantifying the degree of transcriptomic separation among types within each glutamatergic layer. Each bar represents the average F1 score calculated for types from each layer across all ages. $P^{***}<0.0001$ for comparison between L2/3 and L5/L6 and L4 and L5/6.

K. Same as panel J for GABAergic types.

L. Same as panel J for non-neuronal types.

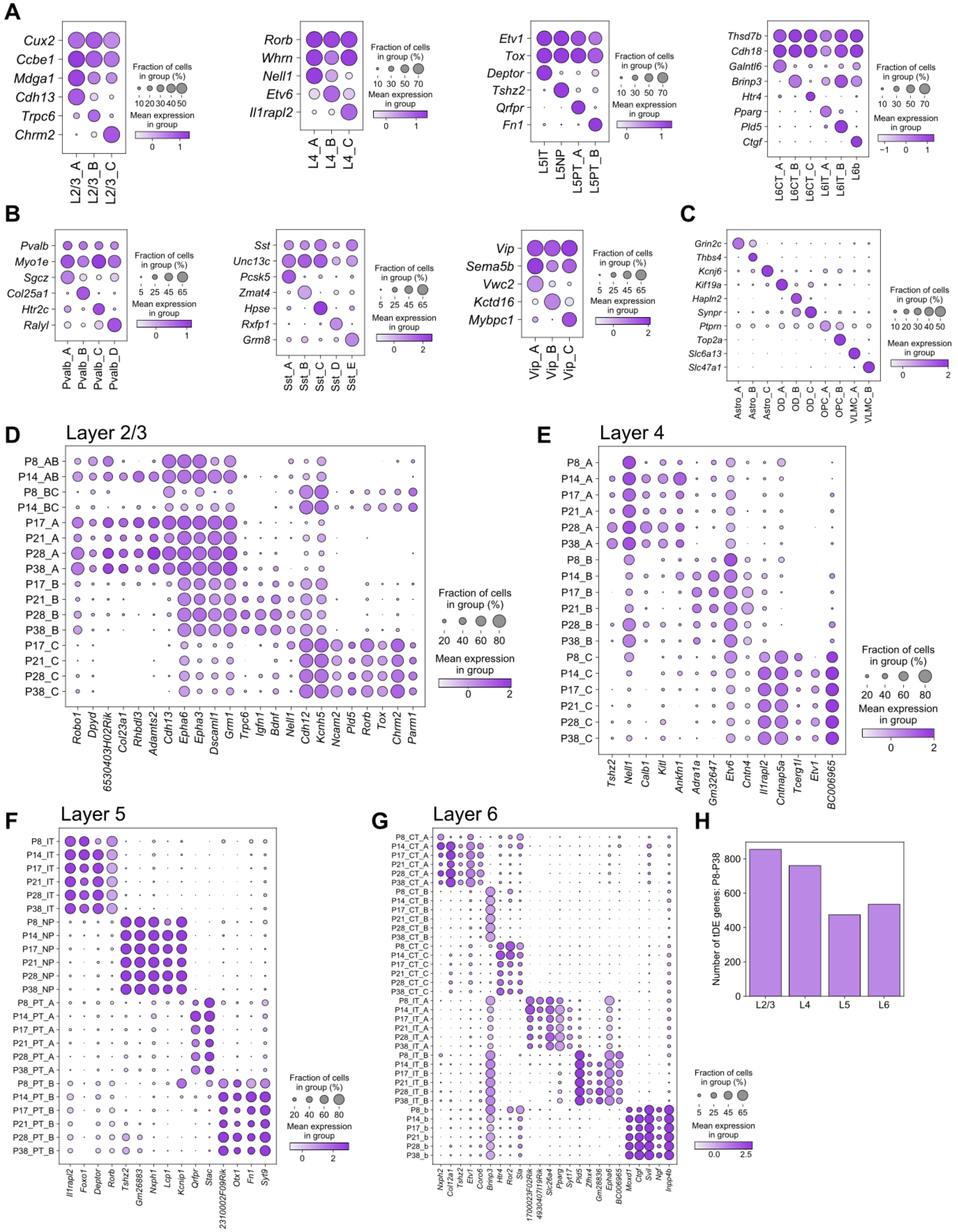

Figure S3.3. Cell type-specific markers for glutamatergic, GABAergic, and non-neuronal subclasses, related to Figure 3.2

A. Dot plot showing markers (rows) for glutamatergic types (columns) within each subclass (panels, left to right). Within each subclass panel, the top two genes (rows) represent markers shared by all types, while the remainder are type-specific markers. *Cux2* is also expressed in L4. By contrast, *Ccbe1* is specifically expressed in L2/3 excitatory neurons from P14-P38. It is, thus, a subclass-specific marker. Type-specific genes *Cdh13*, *Trpc6*, and *Chrm2* are specific to the A, B, and C type, respectively, within L2/3 but they could be expressed elsewhere in the developing V1. Expression levels are computed by pooling cells from all ages. Representation as in **Figure S3.1I**. Markers in all panels of this figure were identified using a Wilcoxon rank-sum differential expression test with the following thresholds: fold-change > 2 and FDR < 0.05.
B. Same as A, for GABAergic types within subclasses (panels, left to right).
C. Same as A, for non-neuronal types.
D. Dot plot showing that type-specific markers for L2/3 glutamatergic neurons vary with age. Also shown are markers for the precursor types AB and BC at P8 and P14, which are expressed in types A, B and C at later ages (P17-P38). The legend shown for this panel is the same for panels E-F. See **Figure 3.3A** and the corresponding text for a discussion of precursor types AB and BC.
E. Dot plot showing that type-specific markers for L4 glutamatergic neurons also vary with age.
F. Dot plot showing that type-specific markers for L5 glutamatergic neurons are stable with age
G. Dot plot showing that type-specific markers for L6 glutamatergic neurons are stable with age.
H. Bar plot showing the number of temporally differentially expressed (tDE) genes found in each layer. The elevated number of tDE genes in L2/3 and 4 is consistent with their late specification (see **Figure 3.2**). The selection criteria for tDE genes were identical for all layers (see **Methods**).

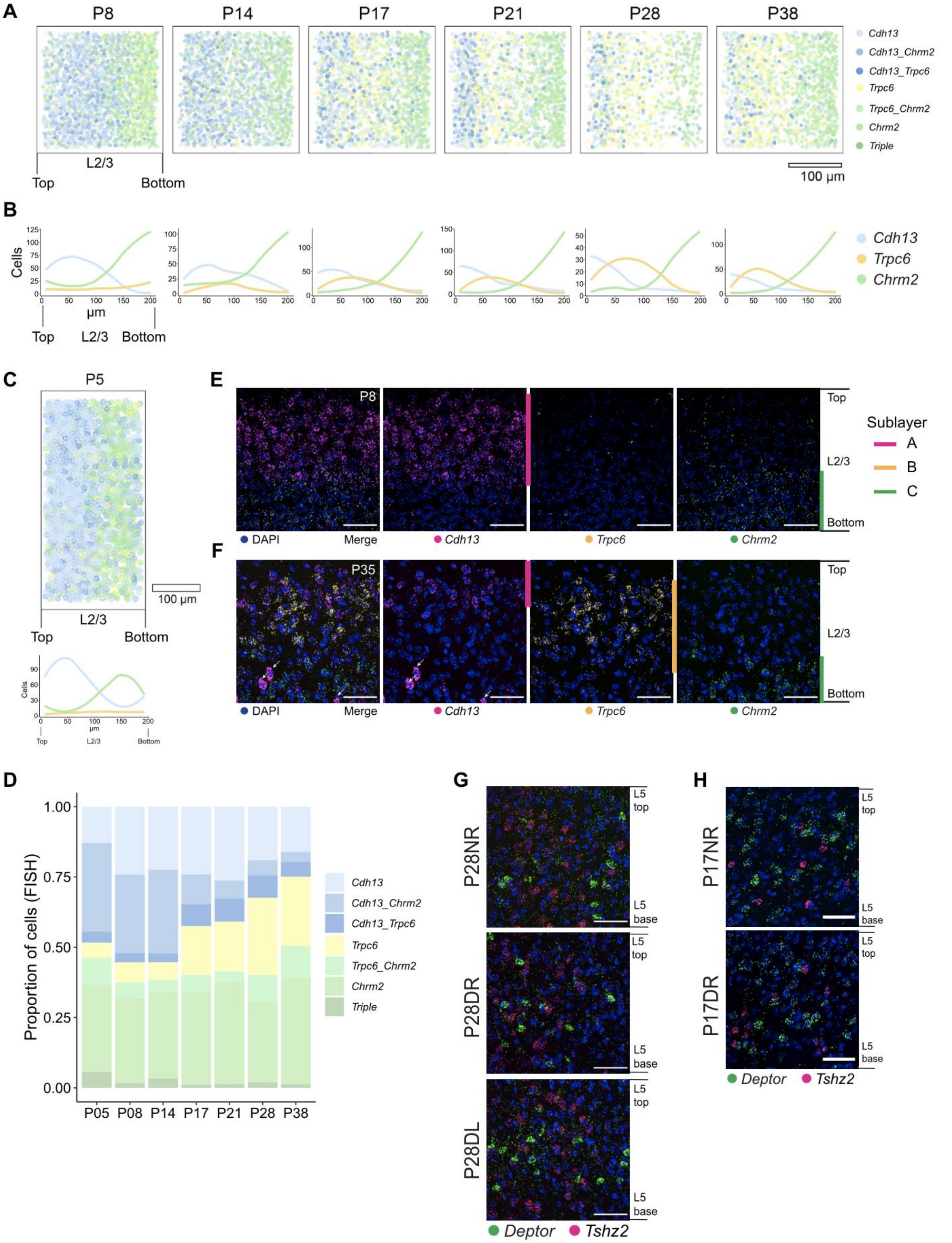

Figure S3.4. *In situ* analysis of L2/3 glutamatergic neuron types in normally reared mice, related to Figure 3.3

A. Pseudo-colored representation of imaged cells (**Methods**) within L2/3 expressing one or more of the type markers *Cdh13, Trpc6,* and *Chrm2* across the six ages. Each panel represents overlaid FISH images of 18

V1 regions from three mice imaged at 40X with the pial-ventricular axis oriented horizontally from left to right. Each imaging frame is 208 μm x 208 μm and is imaged starting at the top of L2/3 to the end of the imaging frame covering about the usual thickness of L2/3 in one frame. As pia could not be imaged within the same frame at 40X, alignment of overlaid images is less optimal compared to 20X images in the main figure. During quantification, this leads to an underrepresentation of *Cdh13*$^{+}$ cells at the top of the imaging frame in 40X compared to 20X images.

B. Line tracings quantifying number of cells per bin at each position along the pial to ventricular axis (x-axis) divided into 14 equally spaced bins, corresponding to panel A. 0 on the x axis is the region of L2/3 closest to pia.
C. Same as panels A and B, at P5.
D. Relative proportions of cells within each expression group defined in panel A as quantified by FISH. Total number of cells analyzed: P5, 2106; P8, 3734; P14, 2937; P17, 3102; P21, 2078; P28, 2078; and P38, 2775. Scale bar, 100 μm.
E. 40X FISH images of L2/3 at P8 labeled with the three type markers *Cdh13*, *Trpc6*, and *Chrm2* that become evident after P17. *Cdh13* and *Chrm2* are selectively expressed between the precursor types AB and BC at earlier ages. *Trpc6* is not expressed at this early stage. Pial to ventricular axis is oriented vertically from top to bottom. Scale bar, 50 μm.
F. 40X FISH images of L2/3 at P35 labeled with the three type markers *Cdh13*, *Trpc6*, and *Chrm2* showing sublayering along the pial to ventricular axis (top to bottom). Arrows denote inhibitory neurons expressing *Cdh13*. Scale bar, 50 μm. As in previous figures, the micrographs are rotated by 90 degrees compared to the quantification panels.
G. FISH images showing the expression of L5 type markers at P28NR, P28DR, and P28DL. *Deptor* is a marker for L5IT and *Tshz2* is a marker for L5NP. Scale bar, 50 μm.
H. Same as panel G at P17NR and P17DR. Scale bar, 50 μm.

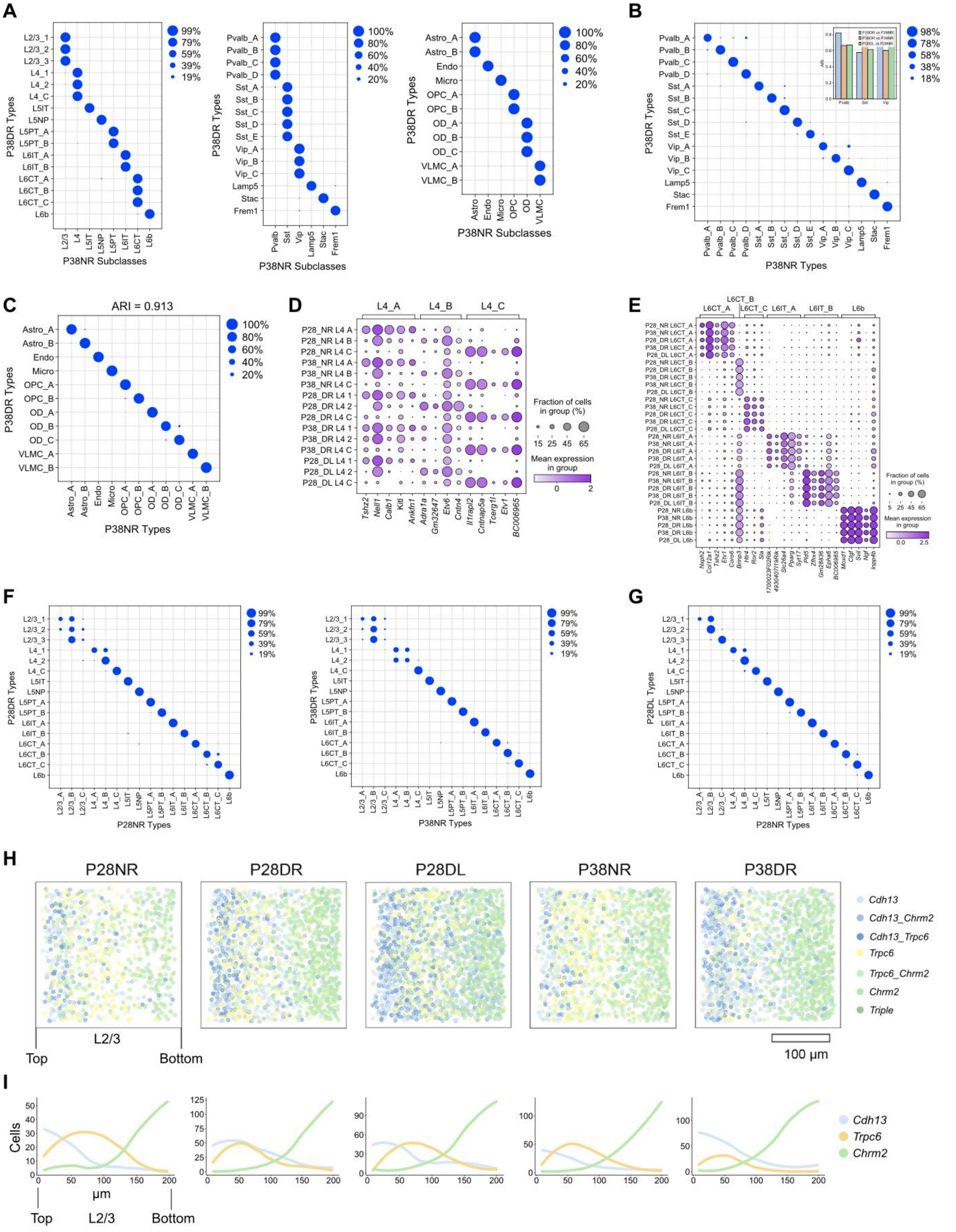

Figure S3.5. Transcriptomic changes in V1 cell type diversity in dark-rearing experiments, related to Figure 3.4

A. Confusion matrices from supervised classification analyses showing that transcriptomically-defined clusters in dark-reared (DR) mice (rows) map to the correct subclass in normally reared (NR) mice (columns). This shows that the transcriptome-wide signatures that define the major subclasses are not disrupted by visual deprivation. Panels correspond to glutamatergic (*left*), GABAergic (*middle*) and non-neuronal (*right*) subclasses at P38. Results are similar when comparing P28DR vs. P28NR or P28DL vs. P28NR (data not shown).

B. Confusion matrix from a supervised classification analysis showing that GABAergic clusters in P38DR mice (rows) transcriptomically correspond 1:1 to GABAergic types in P38NR mice (columns). Results are similar when comparing P28DR vs. P28NR and P28DL vs. P28NR (data not shown). Together these results show that the transcriptomic signatures that define types within GABAergic neurons are not disrupted by visual deprivation. Inset, bar plot of the adjusted rand index (ARI) showing high transcriptomic correspondence between P28DR, P38DR and P28DL types and NR types at the same age.

C. Same as panel B, showing the 1:1 transcriptomic correspondence of non-neuronal types between P38DR vs P38NR. ARI value is indicated on top. Results are similar for P28DR vs. P28NR and P28DL vs. P28NR (data not shown). Thus, the transcriptomic signatures that define non-neuronal types are not disrupted by visual deprivation.

D. Dot plot showing expression patterns of L4 type markers (columns) in NR types at P28 and P38, and DR and DL clusters at the same ages (rows). Markers are grouped by those specific for NR types L4_A, L4_B and L4_C (annotation bar, top).

E. Same as panel D for L6 types. L6 types in DR and DL experiments show a 1:1 correspondence with the NR types (panels D and E) and are therefore named accordingly. A similar 1:1 mapping is not possible for L2/3 and L4 clusters in DR and DL experiments because of the disruption of type-specific gene expression signatures.

F. Confusion matrices showing the transcriptomic correspondence between glutamatergic clusters in DR vs. types in NR at P28 (left) and P38 (right). With the exception of the three types in L2/3 and two types in L4, all the remaining types have a 1:1 match with a DR cluster. Thus, visual deprivation selectively impacts type-specification within L2/3 and L4 among glutamatergic types.

G. Confusion matrix showing the transcriptomic correspondence between glutamatergic clusters in DL vs. types in NR at P28. While the patterns are similar to panel D, L2/3 and L4 clusters show an increased correspondence, reflecting partial recovery of cell type specific signatures.

H. Pseudo-colored representation of imaged cells (**Methods**) within L2/3 expressing one or more of the type markers *Cdh13, Trpc6,* and *Chrm2* across five combinations of age and conditions, indicated on top. Each panel represents overlaid FISH images of 15-18 V1 regions from three mice imaged at 40X, with the pial-ventricular axis oriented horizontally from left to right. Each imaging frame is 208 μm x 208 μm and is imaged starting at the top of L2/3 to the end of the imaging frame covering about the usual thickness of L2/3 in one frame.

I. Line tracings quantifying number of cells per bin at each position along the pial to ventricular axis (x-axis), divided into 14 equally spaced bins, corresponding to panel H. 0 on the x-axis is the region of L2/3 closest to pia. Total number of cells analyzed in H, I: P28, 933; P28DR 1671; P28DL, 2148; P38NR, 1419; and P38DR, 1784.

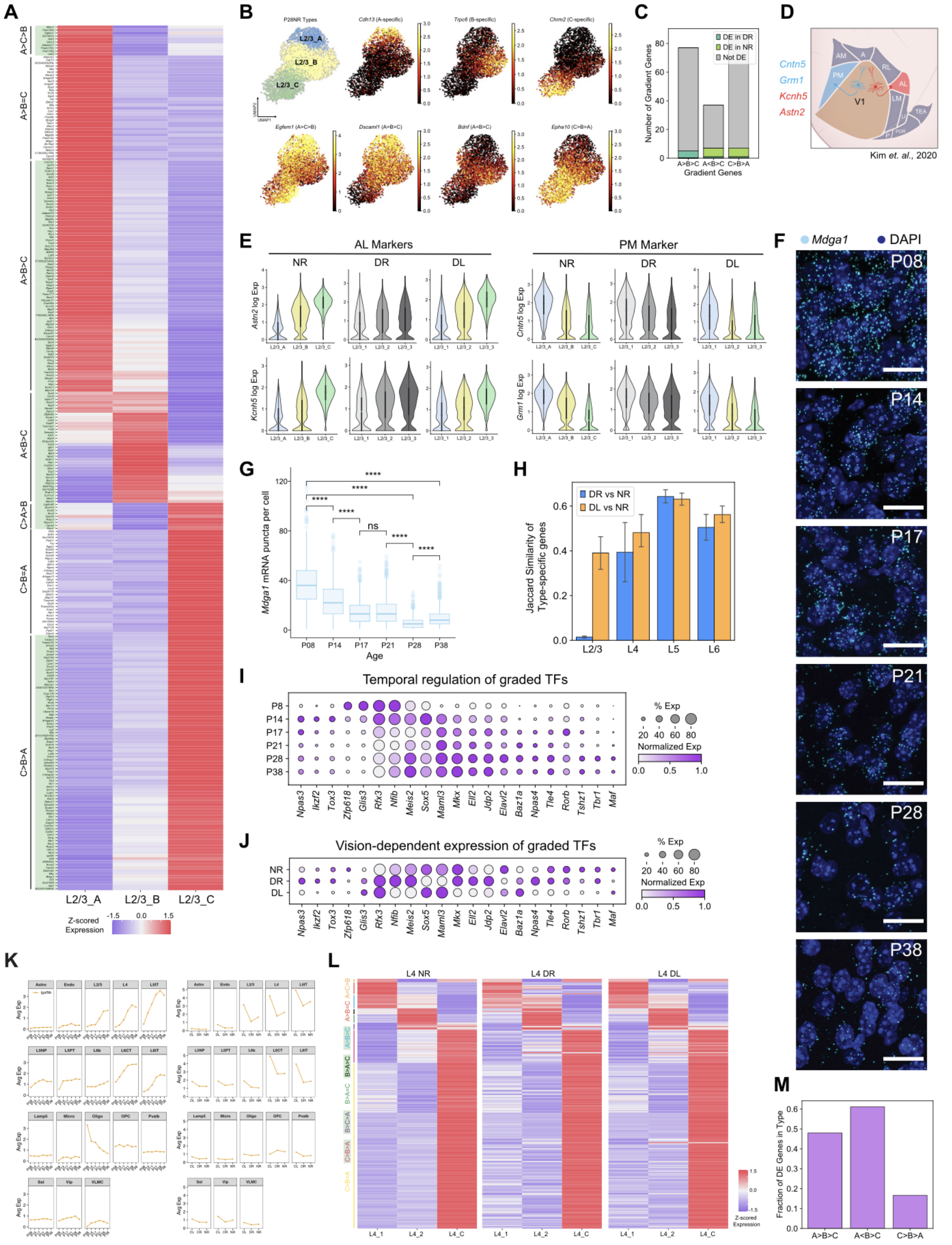

Figure S3.6. Graded gene expression among L2/3 types, and selective maturation of L2/3 types, related to Figure 3.6

A. Type-specific genes for L2/3 types A, B and C (columns) are predominantly expressed in a graded (i.e., not a digital) fashion among the types. Each type was compared to the other two, and only genes with a fold-change (FC) cutoff >2 were selected (FDR< 0.05 by Wilcoxon rank-sum test). Colors denote z-scored expression levels across the three types. Genes (rows) are grouped by expression patterns among the types (e.g., A>B>C). The analysis was performed at P28NR, and the pattern of expression is similar at P38NR (data not shown). Green shading highlights graded genes, which are shown in **Figure 3.6A**.

B. UMAP feature plots of L2/3 neurons at P28NR with cells colored based on their expression of selected DE genes from panel A. The leftmost panel on the top row shows the locations of the three types L2/3_A, L2/3_B, and L2/3_C. The remaining panels on the top row show three genes that are digitally expressed among the three L2/3 types. The bottom panels show four genes expressed in a graded fashion among the three L2/3 types.

C. Bar plot showing that only a small fraction of graded (shaded) genes from A are differentially expressed when L2/3 cells are compared in bulk between DR and NR mice at P28 (fold-change>2, *P-value* $< 10^{-10}$ by Wilcoxon rank-sum test). Thus, visual deprivation does not change the average expression levels of these genes but disrupts their graded patterning.

D. Schematic highlighting the anterolateral (AL) and posteromedial (PM) higher visual areas. Genes preferentially expressed by L2/3 neurons projecting to AL or PM are indicated. Colors identified by retrograde labeling experiments are listed (Kim et al., 2020).

E. Violin plots showing expression of markers enriched in AL (*left*) and PM (*right*) projecting neurons from Kim et al., 2020 in L2/3 cell types in NR mice vs. L2/3 cell clusters in DR and DL mice at P28. The graded expression in NR types is disrupted in DR clusters and partially recovered in DL clusters.

F. FISH images showing the expression of *Mdga1* mRNA over time in V1. Three animals per time point, six images per animal. Scale bar, 20 μm.

G. Box plot quantifying expression in panel F. Wilcoxon Rank Sum Test, **** p <0.0001. Number of cells quantified: P8,1191; P14,1011; P17, 1389; P21, 1729; P28, 1277; and P38, 1588.

H. Bar plot showing the dependence of visual experience (DR and DL) on cell type specific genes within each layer. Each bar represents the Jaccard similarity of type-specific genes between different experience conditions. This was computed for each type within a layer separately and the mean and standard deviation are shown. While the gene expression signatures within all four layers are different for mice with different visual experience conditions, the effect is most dramatic for L2/3 (see L2/3 DR vs NR). In addition, DL significantly recovers the similarity of L2/3 signatures to those found in NR.

I. Dot plot showing the temporal regulation of transcription factors (TFs) found in **Figure 3.6A**. Expression levels shown for L2/3 neurons.

J. Same illustration as panel I across the conditions P28NR, P28DR, and P28DL.

K. (*Left*) Line plot showing that the temporal regulation of *Igsf9b* expression is confined to glutamatergic subclasses with the exception of oligodendrocytes. (*Right*) Line plot showing the regulation of *Igsf9b* expression across rearing conditions at P28.

L. Assessment of L4 type markers to identify graded gene expression patterns. Each type was compared to the other two, and only genes with a fold-change (FC) cutoff >2 were selected (FDR< 0.05 by Wilcoxon rank-sum test). Colors denote z-scored expression levels across the three types. Genes (rows) are grouped and colored by expression patterns among the types (e.g., A>B>C). The analysis was performed at P28NR, and the pattern of expression is similar at P38NR (data not shown). Green shading highlights graded genes. As predicted by **Figure S3.5F**, the markers for L4_A and B are more disrupted by dark-rearing than those for L4_C. Gene names can be found in **Table S3.4**.

M. Bar plot showing the proportion of DE genes within each L4 type that are expressed in a graded fashion. The proportion of graded markers is higher for L4 types A and B (which neighbor L2/3) and is substantially lower for L4_C (which neighbors L5).

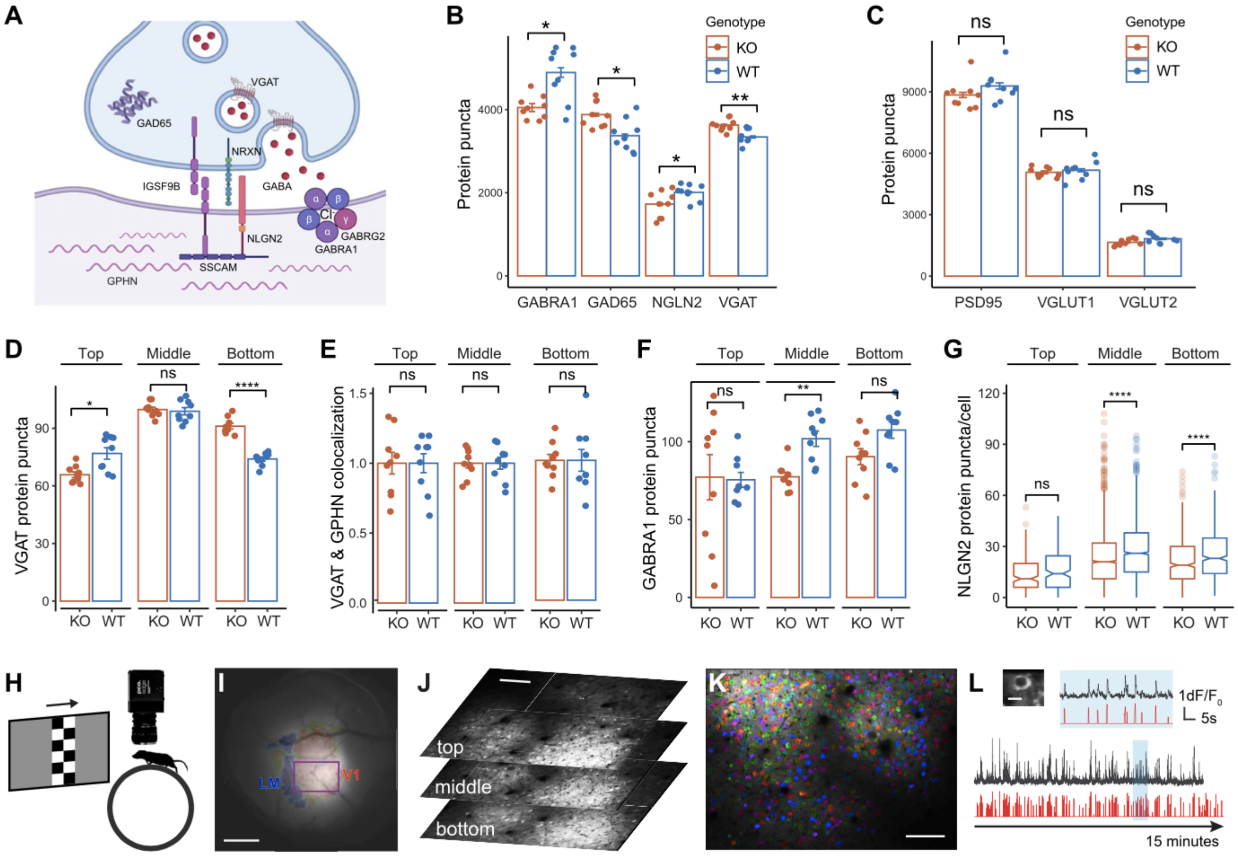

Figure S3.7. Immunohistological characterization of synaptic markers in *Igsf9b* KO, mapping V1b, and measuring receptive field tuning via 2-photon calcium imaging of awake mice, related to Figure 3.7

A. Schematic of molecules at an inhibitory synapse. GAD65, VGAT, and NRXN are presynaptic. IGSF9B is both pre- and post- synaptic and binds homophilically. The intracellular component of Igsf9b interacts with SSCAM in the postsynaptic compartment, which also interacts with the intracellular domain of NLGN2 and, thereby, may stabilize NRXN-NLGN interaction at the cell surface. GABA receptors are post-synaptic. They comprise 5 subunits including subunits GABRA1 and GABRG2.

B. Levels of GABRA1, GAD65, NLGN2, and VGAT protein in L2/3 of WT (n = 9) vs KO (n = 9) mice at P35-38. Y-axis shows total puncta counted within a 130 x 260 µm zone of L2/3 within V1 extending 260 µm from the top of L2/3 to the base of L2/3, and across by 130 µm. $*p < 0.05$. $**p < 0.005$ by Wilcoxon Rank Sum test. Exact P values: GABRA1, p = 0.0078; GAD65, p = 0.0056 VGAT, p = 0 .0028; NLGN2, p = 0.05.

C. No significant difference in expression of excitatory synapse markers in KO vs WT, 9 mice per group, measured in L2/3 of V1 as in **Figure 3.7B**.

D. VGAT protein as a function of L2/3 depth in KO (n = 9) vs WT (n = 9) mice. Top, p = 0.0078; Middle, p = 0.55; and bottom, p = 4.1x10^{-5}. Top, middle, and bottom regions of layer 2/3 are defined based on FISH results for type A, B, C markers. Top corresponds to the first 25 µm of L2/3 and bottom corresponds to the lower 50 µm with the middle being everything in between.

E. VGAT and GPHN colocalization as a function of L2/3 depth in KO (n = 9) vs WT (n = 9) mice.

F. GABRA1 as a function of L2/3 depth in KO (n = 9) vs WT (n = 9) mice, normalized by number of nuclei in the corresponding zone. Top region ns, Middle p = 0.00078, Bottom p = 0.063 (ns but trending).

G. NLGN2 protein puncta per cell, in WT (n = 9) vs KO (n = 9) mice at P35-39. Total quantified cells: 2945 from 9 mice in KO and 2786 cells from 9 mice in WT. Due to the perisomatic localization of Nlgn2, its level of expression was quantified on a cell by-cell basis by using a fixed 20-pixel ring around the nucleus as the cell border. **** $p < 0.00005$ by Wilcoxon Rank Sum test. Exact P values: Top ns. Middle p = 1.06 x 10^{-23}, Bottom p = 3.96x 10^{-5}.

H. Mapping visual cortical areas to localize the binocular region of V1 (V1b) using low-magnification epifluorescence imaging of jGCaMP7f evoked responses to checkerboard bars that were both drifting and flashing.
I. Example image of a cranial window highlighting V1b and its border with higher-order lateromedial (LM) area. The purple rectangle delineates the field of view used for 2-photon imaging. Scale bar, 0.5 mm.
J. Three planes of in vivo 2-photon calcium imaging of neurons within layer 2/3 in the field of view in panel I. The three imaging planes cover the top, middle and bottom sub-laminae in layer 2/3. Scale bar, 100 µm.
K. Overlay of motion-corrected average fluorescence image and segmentation of neurons for the middle plane in J. Scale bar, 100 µm.
L. Top left: a neuron expressing jGCaM7f in the bottom plane of panel J. Tuning kernel of this neuron was shown in **Figure 3.7B**. Scale bar, 10 µm. Bottom: the raw (black) and temporally deconvolved (red) jGCaMP7f signal from this neuron for 15 minutes of visual stimulation to the contralateral eye. The region in blue is expanded above horizontally to show more details of the signal.

Table S3.1. List of canonical markers used to identify neuronal and non-neuronal subclasses, related to Figures 3.1 and 3.2.

Table S3.2. Number of cells present in each of the 18 NR and 9 DR/DL datasets, related to Figures 3.1 and 3.4.

Table S3.3. Subclass-specific markers for each subclass in the study, related to Figure 3.1.

Table S3.4. Type-specific markers for each cell type in the study, related to Figure 3.1.

References

Ackman, J.B., Burbridge, T.J., and Crair, M.C. (2012). Retinal waves coordinate patterned activity throughout the developing visual system. Nature *490*, 219-225.

Arneson, D., Zhang, G., Ying, Z., Zhuang, Y., Byun, H.R., Ahn, I.S., Gomez-Pinilla, F., and Yang, X. (2018). Single cell molecular alterations reveal target cells and pathways of concussive brain injury. Nat Commun *9*, 3894.

Becht, E., McInnes, L., Healy, J., Dutertre, C.A., Kwok, I.W.H., Ng, L.G., Ginhoux, F., and Newell, E.W. (2018). Dimensionality reduction for visualizing single-cell data using UMAP. Nat Biotechnol.

Berg, J., Sorensen, S.A., Ting, J.T., Miller, J.A., Chartrand, T., Buchin, A., Bakken, T.E., Budzillo, A., Dee, N., Ding, S.L.*, et al.* (2021). Human neocortical expansion involves glutamatergic neuron diversification. Nature *598*, 151-158.

Cembrowski, M.S., Bachman, J.L., Wang, L., Sugino, K., Shields, B.C., and Spruston, N. (2016). Spatial Gene-Expression Gradients Underlie Prominent Heterogeneity of CA1 Pyramidal Neurons. Neuron *89*, 351-368.

Cembrowski, M.S., and Menon, V. (2018). Continuous Variation within Cell Types of the Nervous System. Trends Neurosci *41*, 337-348.

Chen, T., and Guestrin, C. (2016). XGBoost: A Scalable Tree Boosting System. arXiv *1603.02754v3*.

Espinosa, J.S., and Stryker, M.P. (2012). Development and plasticity of the primary visual cortex. Neuron *75*, 230-249.

Franklin, K.P., G (2012). Paxinos and Franklin's the Mouse Brain in Stereotaxic Coordinates, Compact, 4th edn (Elsevir).

Gordon, J.A., and Stryker, M.P. (1996). Experience-dependent plasticity of binocular responses in the primary visual cortex of the mouse. J Neurosci *16*, 3274-3286.

Gouwens, N.W., Sorensen, S.A., Berg, J., Lee, C., Jarsky, T., Ting, J., Sunkin, S.M., Feng, D., Anastassiou, C.A., Barkan, E.*, et al.* (2019). Classification of electrophysiological and morphological neuron types in the mouse visual cortex. Nat Neurosci *22*, 1182-1195.

Hafemeister, C., and Satija, R. (2019). Normalization and variance stabilization of single-cell RNA-seq data using regularized negative binomial regression. Genome Biol *20*, 296.

Haghverdi, L., Buettner, F., and Theis, F.J. (2015). Diffusion maps for high-dimensional single-cell analysis of differentiation data. Bioinformatics *31*, 2989-2998.

Harris, K.D., and Mrsic-Flogel, T.D. (2013). Cortical connectivity and sensory coding. Nature *503*, 51-58.

Hensch, T.K. (2004). Critical period regulation. Annu Rev Neurosci *27*, 549-579.

Hensch, T.K. (2005). Critical period plasticity in local cortical circuits. Nat Rev Neurosci *6*, 877-888.

Hinojosa, A.J., Deogracias, R., and Rico, B. (2018). The Microtubule Regulator NEK7 Coordinates the Wiring of Cortical Parvalbumin Interneurons. Cell Rep *24*, 1231-1242.

Hooks, B.M., and Chen, C. (2020). Circuitry Underlying Experience-Dependent Plasticity in the Mouse Visual System. Neuron *107*, 986-987.

Hrvatin, S., Hochbaum, D.R., Nagy, M.A., Cicconet, M., Robertson, K., Cheadle, L., Zilionis, R., Ratner, A., Borges-Monroy, R., Klein, A.M.*, et al.* (2018). Single-cell analysis of experience-dependent transcriptomic states in the mouse visual cortex. Nat Neurosci *21*, 120-129.

Katz, L.C., and Shatz, C.J. (1996). Synaptic activity and the construction of cortical circuits. Science *274*, 1133-1138.

Kim, E.J., Zhang, Z., Huang, L., Ito-Cole, T., Jacobs, M.W., Juavinett, A.L., Senturk, G., Hu, M., Ku, M., Ecker, J.R*., et al.* (2020). Extraction of Distinct Neuronal Cell Types from within a Genetically Continuous Population. Neuron *107*, 274-282 e276.

Kim, M.H., Znamenskiy, P., Iacaruso, M.F., and Mrsic-Flogel, T.D. (2018). Segregated Subnetworks of Intracortical Projection Neurons in Primary Visual Cortex. Neuron *100*, 1313-1321 e1316.

Kishi, J.Y., Lapan, S.W., Beliveau, B.J., West, E.R., Zhu, A., Sasaki, H.M., Saka, S.K., Wang, Y., Cepko, C.L., and Yin, P. (2019). SABER amplifies FISH: enhanced multiplexed imaging of RNA and DNA in cells and tissues. Nat Methods *16*, 533-544.

Ko, H., Cossell, L., Baragli, C., Antolik, J., Clopath, C., Hofer, S.B., and Mrsic-Flogel, T.D. (2013). The emergence of functional microcircuits in visual cortex. Nature *496*, 96-100.

Ko, H., Mrsic-Flogel, T.D., and Hofer, S.B. (2014). Emergence of feature-specific connectivity in cortical microcircuits in the absence of visual experience. J Neurosci *34*, 9812-9816.

Korsunsky, I., Millard, N., Fan, J., Slowikowski, K., Zhang, F., Wei, K., Baglaenko, Y., Brenner, M., Loh, P.R., and Raychaudhuri, S. (2019). Fast, sensitive and accurate integration of single-cell data with Harmony. Nat Methods *16*, 1289-1296.

La Chioma, A., Bonhoeffer, T., and Hubener, M. (2019). Area-Specific Mapping of Binocular Disparity across Mouse Visual Cortex. Curr Biol *29*, 2954-2960 e2955.

Li, M., Cui, Z., Niu, Y., Liu, B., Fan, W., Yu, D., and Deng, J. (2010). Synaptogenesis in the developing mouse visual cortex. Brain Res Bull *81*, 107-113.

Lu, W., Bromley-Coolidge, S., and Li, J. (2017). Regulation of GABAergic synapse development by postsynaptic membrane proteins. Brain Res Bull *129*, 30-42.

Lyckman, A.W., Horng, S., Leamey, C.A., Tropea, D., Watakabe, A., Van Wart, A., McCurry, C., Yamamori, T., and Sur, M. (2008). Gene expression patterns in visual cortex during the critical period: synaptic stabilization and reversal by visual deprivation. Proc Natl Acad Sci U S A *105*, 9409-9414.

Majdan, M., and Shatz, C.J. (2006). Effects of visual experience on activity-dependent gene regulation in cortex. Nat Neurosci *9*, 650-659.

Mardinly, A.R., Spiegel, I., Patrizi, A., Centofante, E., Bazinet, J.E., Tzeng, C.P., Mandel-Brehm, C., Harmin, D.A., Adesnik, H., Fagiolini, M*., et al.* (2016). Sensory experience regulates cortical inhibition by inducing IGF1 in VIP neurons. Nature *531*, 371-375.

McQuin, C., Goodman, A., Chernyshev, V., Kamentsky, L., Cimini, B.A., Karhohs, K.W., Doan, M., Ding, L., Rafelski, S.M., Thirstrup, D*., et al.* (2018). CellProfiler 3.0: Next-generation image processing for biology. PLoS Biol *16*, e2005970.

Meister, M., Wong, R.O., Baylor, D.A., and Shatz, C.J. (1991). Synchronous bursts of action potentials in ganglion cells of the developing mammalian retina. Science *252*, 939-943.

Motta, A., Berning, M., Boergens, K.M., Staffler, B., Beining, M., Loomba, S., Hennig, P., Wissler, H., and Helmstaedter, M. (2019). Dense connectomic reconstruction in layer 4 of the somatosensory cortex. Science *366*.

Munoz-Castaneda, R., Zingg, B., Matho, K.S., Chen, X., Wang, Q., Foster, N.N., Li, A., Narasimhan, A., Hirokawa, K.E., Huo, B*., et al.* (2021). Cellular anatomy of the mouse primary motor cortex. Nature *598*, 159-166.

Nakashima, A., Ihara, N., Shigeta, M., Kiyonari, H., Ikegaya, Y., and Takeuchi, H. (2019). Structured spike series specify gene expression patterns for olfactory circuit formation. Science *365*.

Network, B.I.C.C. (2021). A multimodal cell census and atlas of the mammalian primary motor cortex. Nature *598*, 86-102.

O'Leary, T.P., Sullivan, K.E., Wang, L., Clements, J., Lemire, A.L., and Cembrowski, M.S. (2020). Extensive and spatially variable within-cell-type heterogeneity across the basolateral amygdala. Elife *9*.

Ortiz, C., Carlen, M., and Meletis, K. (2021). Spatial Transcriptomics: Molecular Maps of the Mammalian Brain. Annu Rev Neurosci *44*, 547-562.

Peng, Y.R., Shekhar, K., Yan, W., Herrmann, D., Sappington, A., Bryman, G.S., van Zyl, T., Do, M.T.H., Regev, A., and Sanes, J.R. (2019). Molecular Classification and Comparative Taxonomics of Foveal and Peripheral Cells in Primate Retina. Cell *176*, 1222-1237 e1222.

Reh, R.K., Dias, B.G., Nelson, C.A., 3rd, Kaufer, D., Werker, J.F., Kolb, B., Levine, J.D., and Hensch, T.K. (2020). Critical period regulation across multiple timescales. Proc Natl Acad Sci U S A *117*, 23242-23251.

Sanes, J.R., and Zipursky, S.L. (2020). Synaptic Specificity, Recognition Molecules, and Assembly of Neural Circuits. Cell *181*, 536-556.

Satija, R., Farrell, J.A., Gennert, D., Schier, A.F., and Regev, A. (2015). Spatial reconstruction of single-cell gene expression data. Nat Biotechnol *33*, 495-502.

Scala, F., Kobak, D., Bernabucci, M., Bernaerts, Y., Cadwell, C.R., Castro, J.R., Hartmanis, L., Jiang, X., Laturnus, S., Miranda, E*., et al.* (2020). Phenotypic variation of transcriptomic cell types in mouse motor cortex. Nature.

Stuart, T., Butler, A., Hoffman, P., Hafemeister, C., Papalexi, E., Mauck, W.M., 3rd, Hao, Y., Stoeckius, M., Smibert, P., and Satija, R. (2019). Comprehensive Integration of Single-Cell Data. Cell *177*, 1888-1902 e1821.

Tan, L., Ringach, D.L., Zipursky, S.L., and Trachtenberg, J.T. (2021). Vision is required for the formation of binocular neurons prior to the classical critical period. Curr Biol.

Tan, L., Tring, E., Ringach, D.L., Zipursky, S.L., and Trachtenberg, J.T. (2020). Vision Changes the Cellular Composition of Binocular Circuitry during the Critical Period. Neuron *108*, 735-747 e736.

Tasic, B., Menon, V., Nguyen, T.N., Kim, T.K., Jarsky, T., Yao, Z., Levi, B., Gray, L.T., Sorensen, S.A., Dolbeare, T*., et al.* (2016). Adult mouse cortical cell taxonomy revealed by single cell transcriptomics. Nat Neurosci *19*, 335-346.

Tasic, B., Yao, Z., Graybuck, L.T., Smith, K.A., Nguyen, T.N., Bertagnolli, D., Goldy, J., Garren, E., Economo, M.N., Viswanathan, S*., et al.* (2018). Shared and distinct transcriptomic cell types across neocortical areas. Nature *563*, 72-78.

Traag, V.A., Waltman, L., and van Eck, N.J. (2019). From Louvain to Leiden: guaranteeing well-connected communities. Sci Rep *9*, 5233.

Tropea, D., Kreiman, G., Lyckman, A., Mukherjee, S., Yu, H., Horng, S., and Sur, M. (2006). Gene expression changes and molecular pathways mediating activity-dependent plasticity in visual cortex. Nat Neurosci *9*, 660-668.

Wang, B.S., Sarnaik, R., and Cang, J. (2010). Critical period plasticity matches binocular orientation preference in the visual cortex. Neuron *65*, 246-256.

Wiesel, T.N., and Hubel, D.H. (1963). Single-Cell Responses in Striate Cortex of Kittens Deprived of Vision in One Eye. J Neurophysiol *26*, 1003-1017.

Wojtowicz, W.M., Vielmetter, J., Fernandes, R.A., Siepe, D.H., Eastman, C.L., Chisholm, G.B., Cox, S., Klock, H., Anderson, P.W., Rue, S.M.*, et al.* (2020). A Human IgSF Cell-Surface Interactome Reveals a Complex Network of Protein-Protein Interactions. Cell *182*, 1027-1043 e1017.

Wolf, F.A., Angerer, P., and Theis, F.J. (2018). SCANPY: large-scale single-cell gene expression data analysis. Genome Biol *19*, 15.

Wolf, F.A., Hamey, F.K., Plass, M., Solana, J., Dahlin, J.S., Gottgens, B., Rajewsky, N., Simon, L., and Theis, F.J. (2019). PAGA: graph abstraction reconciles clustering with trajectory inference through a topology preserving map of single cells. Genome Biol *20*, 59.

Wolock, S.L., Lopez, R., and Klein, A.M. (2019). Scrublet: Computational Identification of Cell Doublets in Single-Cell Transcriptomic Data. Cell Syst *8*, 281-291 e289.

Woo, J., Kwon, S.K., Nam, J., Choi, S., Takahashi, H., Krueger, D., Park, J., Lee, Y., Bae, J.Y., Lee, D.*, et al.* (2013). The adhesion protein IgSF9b is coupled to neuroligin 2 via S-SCAM to promote inhibitory synapse development. J Cell Biol *201*, 929-944.

Xu, H.P., Furman, M., Mineur, Y.S., Chen, H., King, S.L., Zenisek, D., Zhou, Z.J., Butts, D.A., Tian, N., Picciotto, M.R.*, et al.* (2011). An instructive role for patterned spontaneous retinal activity in mouse visual map development. Neuron *70*, 1115-1127.

Yao, Z., Liu, H., Xie, F., Fischer, S., Adkins, R.S., Aldridge, A.I., Ament, S.A., Bartlett, A., Behrens, M.M., Van den Berge, K.*, et al.* (2021a). A transcriptomic and epigenomic cell atlas of the mouse primary motor cortex. Nature *598*, 103-110.

Yao, Z., Liu, H., Xie, F., Fischer, S., Booeshaghi, A.S., Adkins, R.S., Aldridge, A.I., Ament, S.A., Pinto-Duarte, A., Bartlett, A.*, et al.* (2020). An integrated transcriptomic and epigenomic atlas of mouse primary motor cortex cell types. BioRxiv.

Yao, Z., van Velthoven, C.T.J., Nguyen, T.N., Goldy, J., Sedeno-Cortes, A.E., Baftizadeh, F., Bertagnolli, D., Casper, T., Chiang, M., Crichton, K.*, et al.* (2021b). A taxonomy of transcriptomic cell types across the isocortex and hippocampal formation. Cell.

Yuste, R., Hawrylycz, M., Aalling, N., Aguilar-Valles, A., Arendt, D., Armananzas, R., Ascoli, G.A., Bielza, C., Bokharaie, V., Bergmann, T.B.*, et al.* (2020). A community-based transcriptomics classification and nomenclature of neocortical cell types. Nat Neurosci *23*, 1456-1468.

Zeng, H., and Sanes, J.R. (2017). Neuronal cell-type classification: challenges, opportunities and the path forward. Nat Rev Neurosci *18*, 530-546.

Zhang, M., Eichhorn, S.W., Zingg, B., Yao, Z., Cotter, K., Zeng, H., Dong, H., and Zhuang, X. (2021). Spatially resolved cell atlas of the mouse primary motor cortex by MERFISH. Nature *598*, 137-143.

Zhu, Y., Qiao, W., Liu, K., Zhong, H., and Yao, H. (2015). Control of response reliability by parvalbumin-expressing interneurons in visual cortex. Nat Commun *6*, 6802.

Chapter 4: Molecular states underlying neuronal cell type development and plasticity in the whisker cortex

This chapter is adapted from the following work:

Salwan Butrus*, Hannah R. Monday*, Christopher J. Yoo, Daniel E. Feldman#, and Karthik Shekhar#. Molecular states underlying neuronal cell type development and plasticity in the whisker cortex. *bioRxiv* (2024).

* Equal contribution
# Corresponding authors

S.B. and H.M. performed all snRNA-seq experiments H.R.M. performed all imaging experiments and analyses with assistance from C.J.Y. S.B. performed all computational analyses.

Abstract

Mouse whisker somatosensory cortex (wS1) is a major model system to study the experience-dependent plasticity of cortical neuron physiology, morphology, and sensory coding. However, the role of sensory experience in regulating neuronal cell type development and gene expression in wS1 remains poorly understood. We assembled and annotated a transcriptomic atlas of wS1 during postnatal development comprising 45 molecularly distinct neuronal types that can be grouped into eight excitatory and four inhibitory neuron subclasses. Using this atlas, we examined the influence of whisker experience from postnatal day (P) 12, the onset of active whisking, to P22, on the maturation of molecularly distinct cell types. During this developmental period, when whisker experience was normal, ~250 genes were regulated in a neuronal subclass-specific fashion. At the resolution of neuronal types, we found that only the composition of layer (L) 2/3 glutamatergic neuronal types, but not other neuronal types, changed substantially between P12 and P22. These compositional changes resemble those observed previously in the primary visual cortex (V1), and the temporal gene expression changes were also highly conserved between the two regions. In contrast to V1, however, cell type maturation in wS1 is not substantially dependent on sensory experience, as 10-day full-face whisker deprivation did not influence the transcriptomic identity and composition of L2/3 neuronal types. A one-day competitive whisker deprivation protocol also did not affect cell type identity but induced moderate changes in plasticity-related gene expression. Thus, developmental maturation of cell types is similar in V1 and wS1, but sensory deprivation minimally affects cell type development in wS1.

Introduction

Neural circuits and function in the neocortex develop in a two-step sequence. Intrinsic genetic programs specify diverse cell types and organize them into an embryonic connectivity map. Subsequently, sensory experience extensively refines this circuitry through activity-dependent mechanisms (Kandel, Eric R and Schwartz, James H and Jessell, Thomas M, 2000). The brain peaks in such experience-dependent plasticity during developmental stages known as critical periods (CPs) (Hubel et al., 1977; Lenneberg, 1967). These experience-dependent changes modulate individual neuronal features such as morphology and synaptic connectivity and alter network properties, including sensory coding and population activity dynamics (Espinosa and Stryker, 2012; Feldman and Brecht, 2005; Hensch, 2005). While sensory experience during critical periods influences the development of some neural cell populations, how these effects differ among the thousands of cell types that populate the mammalian cortex remains poorly explored (Yao et al., 2023, 2021; Zhang et al., 2023).

Recent work in mouse primary visual cortex (V1) suggested that the maturation of glutamatergic neuronal types within the upper cortical layers (L2/3/4), but not lower-layer glutamatergic neurons or inhibitory neuronal types, is vision-dependent (Cheng et al., 2022; Xie et al., 2023). In response to visual deprivation, the transcriptomic profiles, spatial gene expression patterns, and functional tuning of L2/3 glutamatergic neurons were altered. Whether such selective influence of experience on cell type maturation is generally conserved across neocortical areas has not been studied. Given well-described deficits in experience-dependent forms of plasticity in neurodevelopmental disorders like autism, understanding the influence of experience in normal brain development is particularly important.

To address this gap, we studied the transcriptomic maturation of cell types in the mouse whisker primary somatosensory cortex (wS1; **Figure 5.1A**) during normal postnatal development and during deprived whisker sensory experience. wS1 processes tactile (touch) information from the facial whiskers. This is possible because wS1 contains a somatotopic map of the whisker pad so that sensory manipulation (plucking or activation) of specific whiskers drives plasticity in the cortical columns corresponding to those whiskers. The somatotopic organization provides strong technical advantages for investigating mechanisms of plasticity and has made wS1 a workhorse for studying morphological and physiological experience-dependent plasticity (Erzurumlu and Gaspar, 2012; Feldman and Brecht, 2005; Fox and Wong, 2005). Cortical circuit development and critical periods are also well described in wS1 (**Figure 5.1B**). Thalamocortical axons arrive in L4 at postnatal day (P) 1-2, segregate into whisker-specific clusters at P3, and drive patterning of postsynaptic L4 neurons into modules (termed barrels) in L4. Barrel pattern development is partly driven by neural activity during this early period (P0-3). After this age, the anatomical barrel pattern remains stable, but alterations in whisker use drive physiological plasticity in wS1 that is maximal during two overlapping critical periods (CP1 and CP2). CP1 and CP2 initiate at the onset of active whisking (at P12) and coincide with peak synaptogenesis in wS1. From P12-14, whisker deprivation (WD) disrupts receptive field structure (Maravall et al., 2004; Stern et al., 2001) and spine motility (Lendvai et al., 2000) in L2/3 pyramidal (PYR) cells (CP1). From P12-16, removing all but one whisker strengthens L4-L2/3 and L2/3-L2/3 synapses to enhance the representation of the spared whisker (CP2) (Wen and Barth, 2011). Brief 1-day whisker deprivation (WD) also drives physiological plasticity in parvalbumin-positive (PV) interneurons in L2/3, which acts to homeostatically preserve whisker-evoked firing rates in PYR cells, a form of plasticity that is robust at P21 (Gainey et al., 2018). It is unknown whether these physiological changes are associated with changes in gene expression.

To study the relative contribution of intrinsic development and whisker experience to the establishment of wS1 cell types during early postnatal development, we combined single-nucleus RNA-sequencing (snRNA-seq), computational analyses, sensory perturbations, and fluorescence *in situ* hybridization (FISH) (**Figure 5.1C**). We first constructed transcriptomic atlases of wS1 at P12 and P22, which span from the onset of active whisking through CP1 and CP2. Within each atlas, single-nucleus transcriptomes were classified into a hierarchy comprising neuronal classes, subclasses, and types (**Figure 5.1D**). A comparison of gene expression between P12 and P22 identified 250 genes that were predominantly up- or down-regulated temporally in a subclass-specific fashion. We used FISH to validate some of the observed temporally regulated genes. These changes overlapped significantly with developmental changes observed in V1 during a similar period among corresponding neuronal groups (Cheng et al., 2022), suggesting that postnatal maturation programs may be conserved across cortical regions. At the resolution of neuronal cell types, we found the composition of lower-layer glutamatergic and GABAergic neuronal types to be highly concordant between P12 and P22. Similar to V1, only glutamatergic neuronal types in L2/3 underwent a significant compositional shift, suggesting they mature postnatally. Surprisingly, full-face whisker deprivation from P12 to P22 had minimal effect on gene expression programs and the development of cell type composition. This contrasts with V1, where dark-rearing imparted significant gene expression and compositional changes in L2/3 (Cheng et al., 2022; Xie et al., 2023). Brief (1-d) whisker deprivation of a subset of whiskers in adolescent (P21) mice, a manipulation known to drive competitive whisker map plasticity, led to whisker column-specific changes in the expression of immediate-early genes (IEGs) in L2/3, demonstrating plasticity-related regulation of gene expression. Altogether, our results suggest that wS1 and V1 develop similar cell types with a similar developmental timeline and exhibit activity-dependent gene expression changes but with very different effects of postnatal sensory experience on cell type development.

Results

A single-nucleus transcriptomic atlas of the developing mouse whisker cortex

To begin, we used droplet-based snRNA-seq to establish a reference atlas of wS1 neurons at P22 in mice with normal whisker experience. By P22, all established CPs are complete (**Figures 5.1B,C**). Next, to evaluate the influence of natural development and whisker experience on neuronal transcriptomic profiles, we used the same experimental approach to profile wS1 in three scenarios to compare with the reference atlas (**Figure 5.1B**). First, to identify temporally regulated genes and study cell type maturation from the onset of active whisking, we profiled wS1 from whisker-intact mice at P12, which coincides with peak synaptogenesis and the onset of CP1. We performed two additional experiments to study the role of whisker deprivation in regulating cell type-specific gene expression in wS1. In one experiment, we bilaterally deprived mice by plucking all whiskers from P12 to P22 to determine if WD from the onset of active whisking affects the composition of cell types and/or their gene expression programs. In the second, we plucked the B- and D-row whiskers for 1 day, from P21 to P22. This sensory manipulation induces plasticity of excitatory and inhibitory circuits within deprived whisker columns (Gainey et al., 2018; Li et al., 2014). The goal of this experiment was to test whether a brief WD caused cell type-specific transcriptomic changes that could explain this physiological plasticity.

Data from each experiment consisted of 2-4 snRNA-seq biological replicates, each derived from cells collected from 2-3 mice (**Methods**). The resulting gene expression matrices were filtered to remove low-quality cells and cell-doublets (Wolock et al., 2019), cells from non-neuronal populations, cells with a high proportion of mitochondrial transcripts (>1%), and cells that mapped poorly to other cortical datasets (**Methods**). In total, we obtained 81,462 high-quality nuclear transcriptomes corresponding to neurons across the four conditions profiled (**Figures 5.1C, S1A-C**). We then used standard dimensionality reduction and clustering approaches to hierarchically taxonomize wS1 neurons into 2 classes, 12 subclasses, and 53 molecularly distinct neuronal types. Annotations were performed by leveraging known markers, natural clustering, and supervised mapping to established cortical datasets (**Figures 5.1D-E, Methods)**. The relative frequencies of the neuronal subclasses, which spanned two orders of magnitude, were highly consistent across the experimental conditions (**Figure 5.1F**).

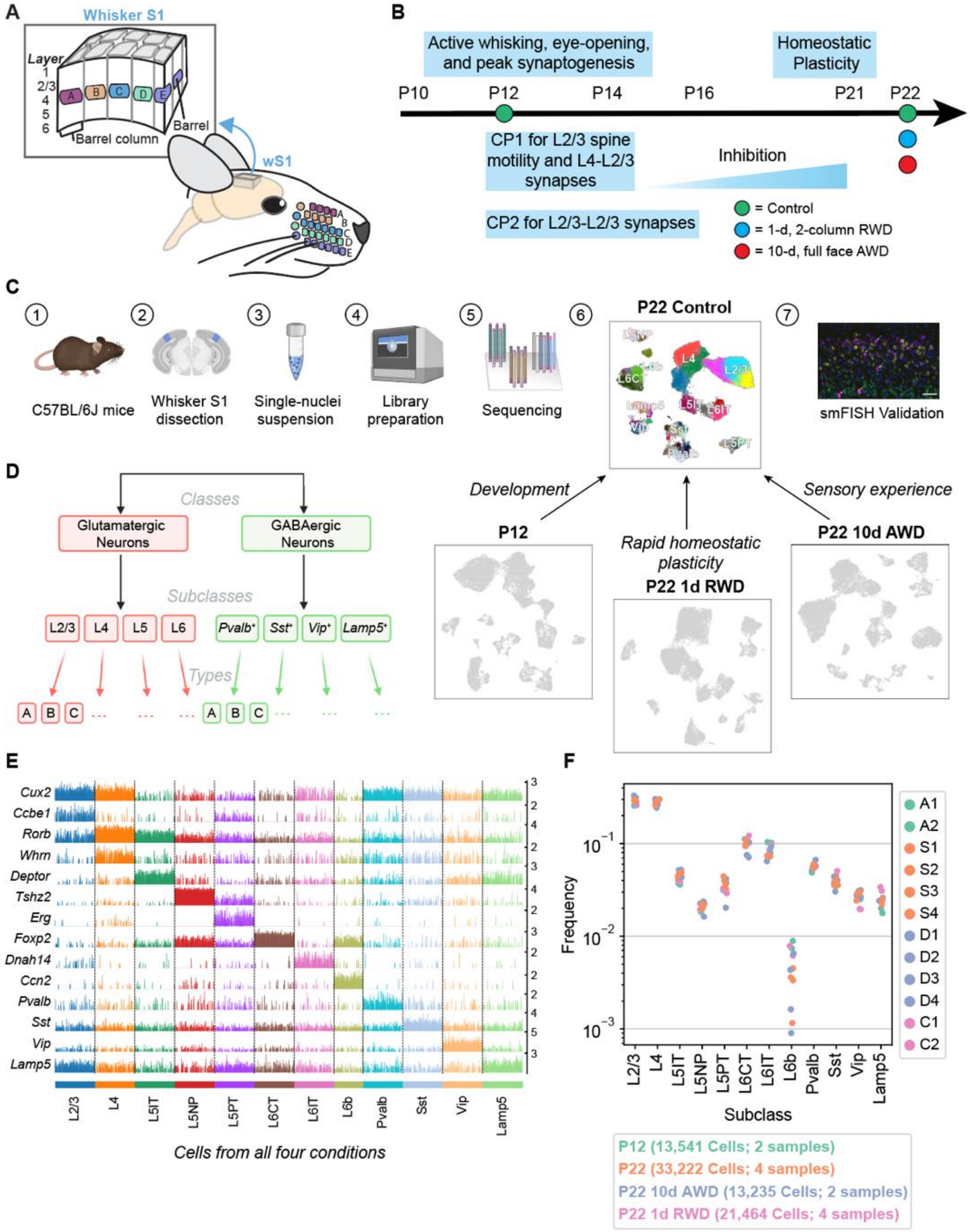

Figure 5.1. snRNA-seq atlas of the juvenile mouse primary whisker somatosensory cortex (wS1). (**A**) Schematic of the mouse whisker somatosensory system, including the facial whisker pad and the whisker somatosensory cortex (wS1). wS1 contains a somatotopic map of the whisker pad in which individual whiskers are represented by neural activity within barrel columns of the cortex. (**B**) Experimental design and developmental timeline for snRNA-seq profiling of one reference (control) dataset at P22 and three experimental conditions: an earlier time during development (P12) and following two different whisker deprivation paradigms at P22. RWD, row-whisker deprivation. AWD, all-whisker deprivation. (**C**) General experimental and computational workflow for snRNA-seq profiling and subsequent confirmatory studies. (**D**) Representation of cortical neuron diversity explored in this study highlighting the three taxonomic levels: classes, subclasses, and types. (**E**) Tracksplot showing marker genes (rows) for each neuronal subclass (columns). Data was aggregated from 81,456 nuclei across all four conditions and each subclass was subsampled to the size of the smallest subclass for plotting purposes. (**F**) Relative frequencies of neuronal subclasses are highly consistent across biological replicates and experimental conditions. The highest variance is seen for L6b glutamatergic neurons, whose frequency ranges from 0.1% to 1% of all neurons.

Developmental gene expression changes are subclass-specific

Next, we sought to characterize the patterns of developmental gene expression changes across the neuronal subclasses. We computed two scores for each gene: a subclass variability (SV) score, based on its maximum expression fold change among the subclasses, and a temporal differential expression (tDE) score, based on its maximum fold change between P12 and P22 among the subclasses. A total of ~4000 genes, each expressed in >40% of cells in at least one time point and at least one subclass, were included in this analysis (**Table S5.1**). Based on their scores (fold-change (FC) >2 along each axis), genes were stratified into four quadrants Q1-Q4 (**Figure 5.2A**, **Methods**). Glutamatergic and GABAergic subclasses showed a similar proportion of genes (~70-80%) with low SV and tDE scores (Q3 in **Figure 5.2B**). However, compared to GABAergic subclasses, glutamatergic subclasses were >3x more enriched (5.3% vs 1.5%) in genes with high subclass-variability and high tDE (Q1) and 1.5x more enriched (4.5% vs 3%) in genes with low subclass-variability and high tDE (Q2). Together, these results indicate that glutamatergic neurons undergo greater transcriptional changes during this period of postnatal maturation.

To understand the functional significance of Q1-Q4 for glutamatergic neurons, we computed the enrichment of curated lists of genes such as transcription factors (TFs), cell adhesion molecules (CAMs), ion channels (ICs), and housekeeping genes (HK) in glutamatergic subclasses using a Fisher's exact test (**Figure 5.2C, Methods**). Housekeeping genes generally had low scores on both scales and were therefore enriched in Q3, consistent with their constitutive and non-specific expression. TFs were not significantly enriched in any quadrant, which is in line with their broad roles in regulating transcription throughout development across all subclasses (Jain et al., 2022; Sousa and Flames, 2022). We found that CAMs, many of which are involved in regulating circuit formation (Sanes and Zipursky, 2020), were enriched strongly in Q1 and, to a lesser degree, in Q4. This is consistent with their previously reported cell type-specific and dynamic expression patterns during circuit formation in other organisms, suggesting that this is a conserved feature of neurons during key phases of wiring (Jain et al., 2022; Jain and Zipursky, 2023; Kurmangaliyev et al., 2020; Özel et al., 2021). ICs were also enriched in Q1 and Q4, which aligns with changes in the physiological properties of neurons during this developmental period. Consistent with these trends, a Gene ontology (GO) analysis focusing on "biological process" revealed enriched categories such as "cell adhesion" and "axon guidance" for Q1 genes. In contrast, Q3 was enriched for general cellular processes such as "protein/mRNA transport" and "chromatin reorganization" (**Figure 5.2D, Figure S5.1D**). Q2 was enriched in "synaptic translation" terms, reflecting a global developmental effort to synthesize proteins, and it also had ~60% of its enriched GO terms (8/13) overlapping with those of Q3 (**Figure S5.1D, S5.2A**). Q4 had a few terms overlapping with Q1 and many overlapping with Q3 (**Figure S5.2A**). Among its top terms were "ion transport", "cell-cell adhesion", and "protein phosphorylation" (**Figure S5.1D**). Together, these results suggest that Q1 is a subclass-specific program related to circuit development, Q2 is a global developmental program, Q3 is a static "housekeeping" program, and Q4 is a subclass-specific program associated with neuronal identity. These trends were qualitatively similar in GABAergic subclasses except with fewer Q1 and Q2 genes (**Figures 5.2B, S5.2B**).

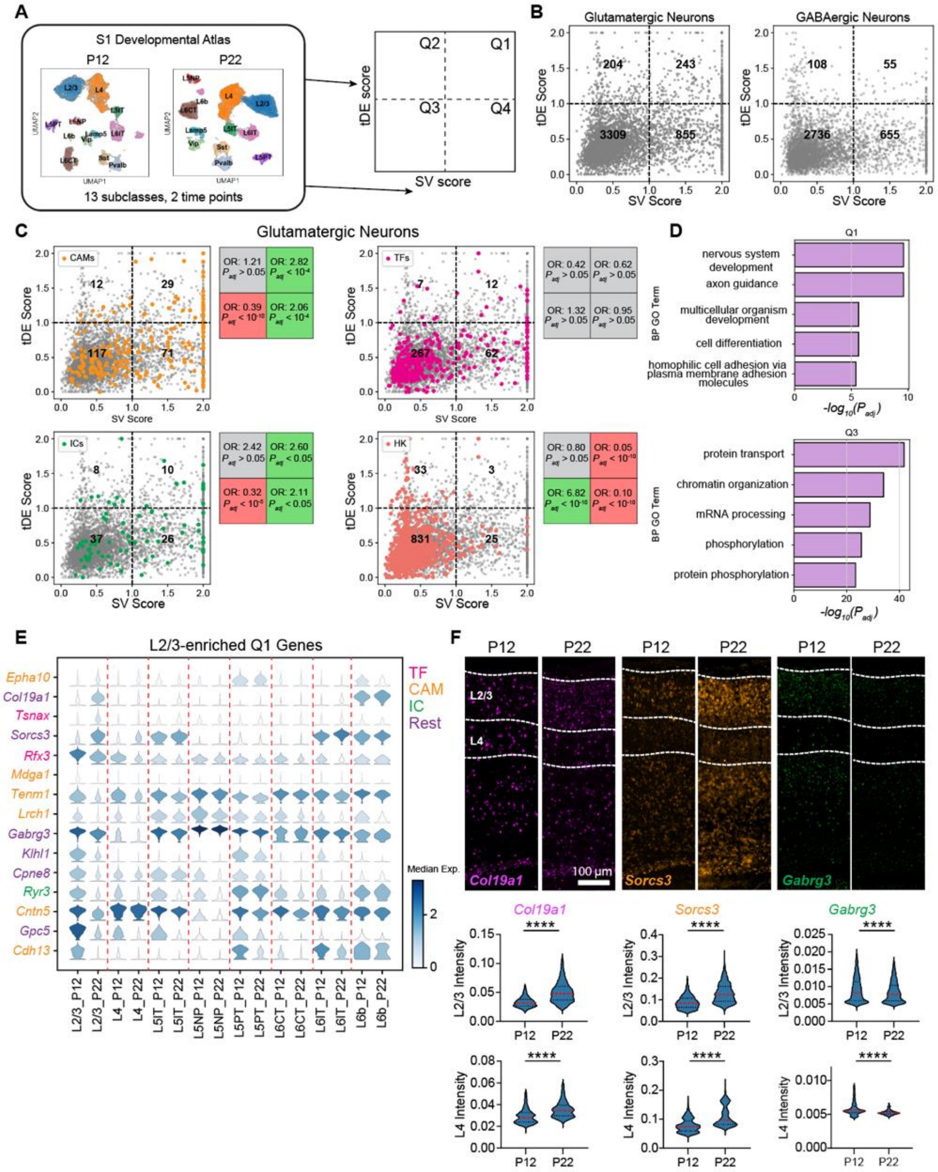

Figure 5.2. Gene expression changes between P12 and P22 are enriched in neurodevelopmental processes. (**A**) Overview of analyses to classify genes based on subclass variability and temporal differential expression. (**B**) Scatter plot of subclass variability (SV) scores and temporal differential expression (tDE) scores of genes in glutamatergic (*left*) and GABAergic neurons (*right*). Scores along each axis are capped at the value of 2. (**C**) Same as B for glutamatergic neurons with four gene categories highlighted. Subpanels (clockwise, starting from top left) correspond to cell adhesion molecules (CAMs), transcription factors (TFs), housekeeping genes (HKs), and ion channels (ICs). Boxes on the right of each panel list the odds ratio (OR) and adjusted p-value (P_{adj}) for the enrichment of the corresponding gene category in each quadrant (Fisher's exact test). Grey values indicate neither enrichment nor depletion, while red and green indicate depletion and enrichment, respectively (see **Methods** for details). (**D**) Q1 is enriched in gene ontology (GO) programs associated with neurodevelopment, while Q3 is enriched in general housekeeping processes. (**E**) Stacked violin plot of example genes (rows) from Q1 with the highest tDE score in L2/3. Columns correspond to subclasses at P12 and P22, violins represent the expression distribution, and color represents median expression. Genes are colored according to the functional categories as in panel C. (**F**) FISH for tDE genes. Representative images (*top*) from an 'across-row' (see Methods) section in wS1. Cortical layers 2/3 and 4 are indicated on the sections. Quantification (*bottom*) of mean intensity in nuclei revealed strong temporal regulation of gene expression in L2/3 consistent with what was measured with snRNA-seq (see **Figure 5.2E**). Mann-Whitney test, ****p< 0.0001. L2/3_*Col19a1*: n = 4133, 3268 nuclei, L4_*Col19a1*: n = 1904, 1665 nuclei, L2/3_*Sorcs3*: n = 4414, 3394, L4_*Sorcs3*: n = 2221, 1876, L2/3_*Gabrg3*: n = 4340, 3210, L4_*Gabrg3*: n = 1808, 1564. Three mice per condition, two slices per mouse.

Next, we examined the degree to which temporally regulated genes were shared among subclasses. We isolated each subclass and identified significantly up/down-regulated genes (fold-change > 2 between P12 and P22, FDR < 0.05 Wilcoxon rank-sum test) (**Table S5.2**). Of the ~421 genes identified, >60% were up/downregulated in a subclass-specific fashion (**Figures S5.2C-D**). These temporally regulated genes are a subset of the Q1-Q2 genes from **Figure 5.2B.** The subclass-specific genes were enriched in Q1, and the shared genes were restricted to Q2 **(Figures S5.2E,F).** Additionally, we detected ~1.5x more downregulated than upregulated genes (**Figure S5.2D**). A similar pattern has been observed in multiple studies of fly brain development, where repression of gene expression is a dominant developmental driving force ("Dedifferentiation of Neurons Precedes Tumor Formation in lola Mutants - PMC," n.d.; Rives-Quinto et al., 2020; Santiago et al., 2021).

Figure 5.2E shows some examples of temporally regulated genes enriched in L2/3 glutamatergic neurons, including CAMs, TFs, ICs, and other genes. To confirm the temporal and subclass-specific expression patterns seen with snRNA-seq, we performed multiplexed fluorescence *in situ* hybridization (FISH) using the RNAscope assay (**Figure 5.2F**). First, we verified the RNAscope assay was working as intended using proprietary positive and negative control probes. As expected, the positive control probes showed specific and widespread expression in the brain, and the negative control probes revealed no detectable signal (**Figure S5.3E-F)**. Next, we selected three temporally regulated genes enriched in L2/3 from **Figure 5.2E** (*Col19a1*, *Sorcs3*, and *Gabrg3*), and probed their expression at P12 and P22 in wS1 (**Figure 5.2F**). The pattern of temporal regulation of gene expression was consistent between snRNA-seq and FISH (**Figure 5.2E-F**), validating our findings of subclass-specific temporal regulation of gene expression in S1 during postnatal development.

Developmental changes in L2/3 cell type composition

We next analyzed the maturation of cell types between P12 and P22. Using a decision tree-based classifier (Chen and Guestrin, 2016) trained on the cell type transcriptional profiles at P22, we assigned P22 type labels to each P12 transcriptome (**Figures 5.3A, S5.3A-B; Methods**, **Table S5.3**). Based on transcriptomic similarity, each neuron at P12 could be unequivocally classified into one of the 45 cell types at P22. This mapping allowed us to compare each cell type between the two ages.

Despite spanning two orders of magnitude, cell type frequencies tightly corresponded between P12 and P22 within all four GABAergic subclasses and 7/8 glutamatergic subclasses (**Figure 5.3B-C**). This suggests that most wS1 cell types acquire a distinct and stable transcriptional signature prior to P12. The only exception was L2/3 glutamatergic neurons (**Figure 5.3C**). Similar to what was observed in V1 (Cheng et al., 2022), L2/3 glutamatergic neurons in wS1 can be clustered into three nominal types that we label L2/3_A, L2/3_B, and L2/3_C. The relative frequency of L2/3_C was similar between the two ages, but L2/3_A halved from P12 to P22, while L2/3_B doubled from P12 to P22 (**Figure 5.3C)**. Despite this prominent change in cell type composition, a principal component analysis (PCA) revealed that the transcriptomic programs underlying L2/3 heterogeneity were similar. The first two principal eigenvectors from PCA corresponded highly between P12 and P22 (**Figure 5.3D-E**). The correspondence was nearly 1:1 for the top two eigenvectors, but with a slight reduction in the correlation coefficient, likely due to the compositional shift of L2/3 neurons from P12 to P22. This temporal variation in cell type frequency coincided with i) a marked increase in the specificity of type A and C markers and ii) increased expression strength of B markers from P12 to P22 (**Figures 5.3F, S5.3C**). Consistent with the shift in cell type composition, >20% of L2/3 type-specific markers were temporally regulated, the highest among all subclasses (**Figure S5.3D**).

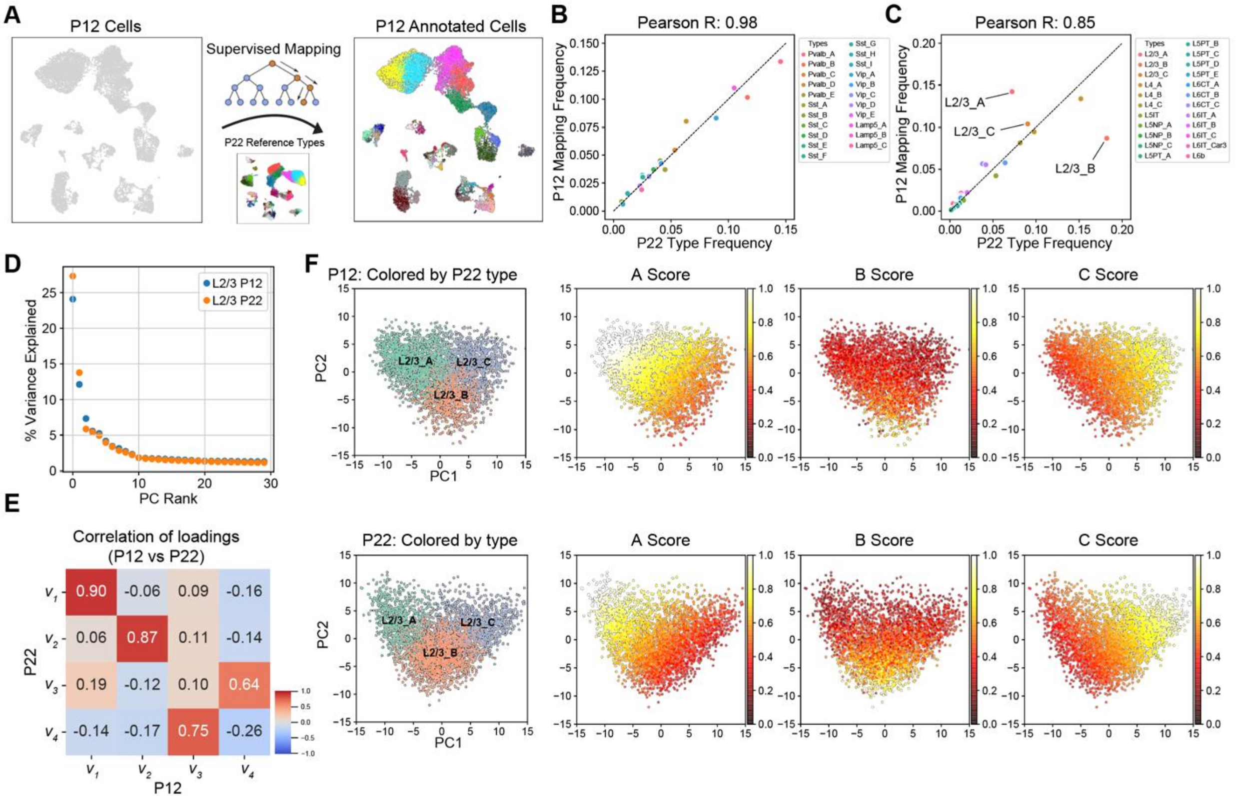

Figure 5.3. L2/3 pyramidal cell type composition is selectively regulated during development. (**A**) Schematic for transferring P22 cell type labels (reference data) to P12 cells to facilitate cell type-level comparisons. (**B**) Within GABAergic neurons (~20% of all neurons), all cell types have approximately the same relative frequency between P12 (y-axis) and P22 (x-axis). Pearson correlation coefficient between the relative frequencies is indicated on top. (**C**) Same as panel B, for glutamatergic neurons (~80% of all neurons). All glutamatergic cell types except for L2/3_A and L2/3_B have approximately the same relative frequency between P12 and P22. (**D**) Percent variance captured (y-axis) by each principal component (PC) within L2/3 neurons at P12 and P22 (colors). Note that PCA is performed independently on each dataset. For both ages, a spectral gap is observed after PC1 and PC2. (**E**) Pair-wise Pearson R values between the first four principal eigenvectors between P12 and P22. The first two principal eigenvectors corresponding to PC1 and PC2, which dominate the variance, map 1:1 between both ages with a high correlation. (**F**) Scatter plot of PC1 vs PC2 for L2/3 neurons at P12 (top row) and P22 (bottom row). With each row, the leftmost panel highlights cells by their type-identity (L2/3_A, L2/3_B, and L2/3_C). In the remaining panels within each row, cells are colored based on their aggregate expression levels of markers for each type (see **Methods**). Between P12 and P22, L2/3_A markers decrease in expression and increase in specificity, while L2/3_B markers increase in expression during development, driving cell type identity maturation.

Genes distinguishing L2/3 cell types and their temporal regulation

We sought to validate the cell type compositional shift described above by performing fluorescence *in situ* hybridization (FISH) in wS1. We targeted markers enriched in the three L2/3 types - *Cdh13* for L2/3_A, *Trpc6* for L2/3_B, and *Chrm2* for L2/3_C (**Figure 5.4A-B**). These three genes were reported earlier to mark L2/3 types in V1 (Cheng et al., 2022). FISH experiments showed that between P12 and P22, *Cdh13*+ L2/3_A cells decreased in frequency, *Trpc6*+ L2/3_B cells increased in frequency, and *Chrm2*+ L2/3_C were stable (**Figure 5.4C-D**). At P12, L2/3_A cells were concentrated at the L1/2 border, with a small population of L2/3_B cells and a large population of L2/3_C cells. At P22, there were very few L2/3_A cells at the L1/2 border, and the majority were concentrated in the middle of L2/3 (**Figure 5.4E**). Similar to what was observed in V1, we showed that *Cdh13*+ cells in the center of L2/3 are likely inhibitory neurons, as they do not co-express *Slc17a7* (vGlut1) (**Figure S5.5A)**. Between P12 to P22, the *Chrm2*+ L2/3_C cells maintain their frequency, whereas the *Trpc6*+ L2/3_B cells increase relative to *Cdh13*+ L2/3_A cells **(Figure 5.4E)**. In contrast to V1, where L2/3_A cells retain their L1/2 localization at ~P21 despite decreasing in frequency, in wS1, L2/3_A cells are reduced at the L1/2 border while *Trpc6*+ L2/3_B cells become more prevalent (**Figure 5.4E, Figure S5.5B-C**). As another validation of L2/3 compositional changes, we targeted *Adamts2* for L2/3_A, *Bdnf* for L2/3_B, and *Chrm2* for L2/3C (Cheng et al., 2022; Tasic et al., 2018). The expression of *Adamts2* and *Bdnf* showed the expected trend between P12 and P22 (**Figure S5.5D-E**), with *Adamts2*+ cells decreasing in abundance while *Bdnf*+ increased, agreeing with the snRNA-seq results (**Figure 5.4A**).

Additionally, **Figure S5.4** highlights the temporal regulation of several TFs, ICs, and CAMs differentially expressed among L2/3_A-C types. Note that genes enriched within a given type do not perfectly overlap and often bleed into the adjacent type, and this is related to the continuous nature of transcriptional variation within L2/3 (Cheng et al., 2022; Weiler et al., 2021; Xie et al., 2023). Some genes that retain expression patterns from P12 to P22 (e.g., *Meis2*, *Foxp1, Kcnh7, Dscaml1*) may be involved in the initial establishment and/or maintenance of cell type identity. Other genes (e.g., *Rfx3*, *Zbtb16*, *Scn9a*, *Ncam2*) are significantly temporally regulated and may be involved in the refinement of these cell type identities, including the maturation of their circuitry and physiology.

Taken together, our results suggest that for most neuronal cell types in wS1, transcriptomic distinctions and relative composition are established prior to P12 and persist through the period of early sensory experience. Even though there are significant gene expression changes related to growth and maturation (**Figure 5.2**), these changes do not impact cell type identity. The exceptions to this rule were L2/3 types whose composition and type-specific gene signatures are significantly altered between P12 and P22. This mirrors the scenario reported earlier in V1 (Cheng et al., 2022), raising the question of whether the two cortices also share global and subclass-specific gene expression programs related to maturation, which we now address.

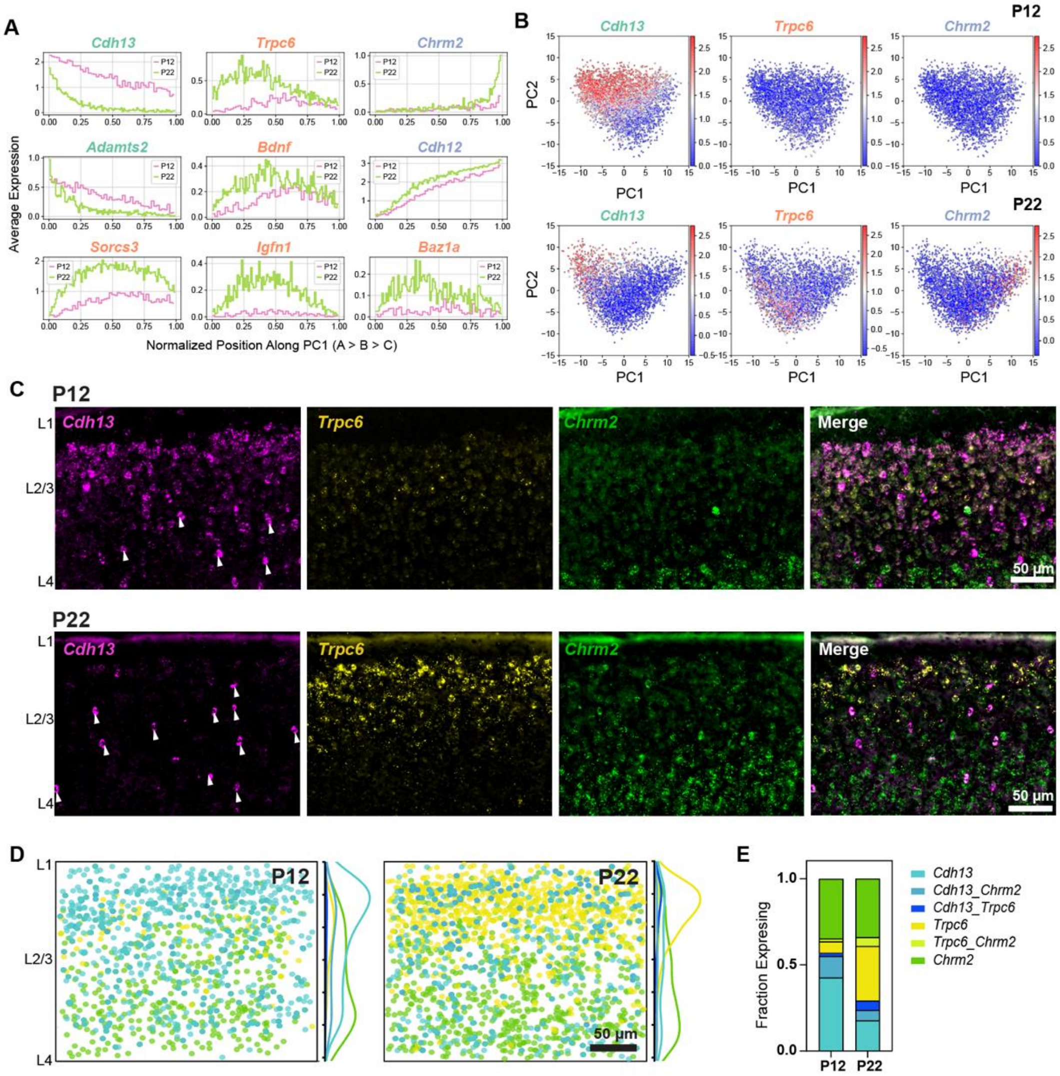

Figure 5.4. **Cell type-specific temporal gene expression changes in L2/3 glutamatergic neurons**. (**A**) Expression patterns of some L2/3 cell type-enriched genes along PC1 from **Figure 5.3F**. Genes are colored based on their type enrichment: A, green; B, orange; C, purple. Other genes are shown in **Figure S5.4**. (**B**) Same as **Figure 5.3F**, with cells colored by expression levels of *Cdh13* (left), *Trpc6* (middle), and *Chrm2* (right), which are targeted for FISH experiments in panels C-E. (**C**) Representative FISH images showing labeling of cell type markers *Cdh13, Trpc6,* and *Chrm2* at P12 and P22 within wS1 L2/3. Arrowheads indicate putative *Cdh13*-expressing interneurons (See **Figure S5.5A)**. (**D**) Summary plots based on overlay of all images of L2/3 visualizing expression of *Cdh13, Trpc6,* and *Chrm2* at P12 and P22. Circles represent individual excitatory cells within L2/3, colored based on their expression of one or more marker genes (color code as in panel E). To the right of each summary plot is the kernel density estimate for each type along the pial-ventricular axis. *Cdh13+* cells dominate in upper L2/3 at P12, whereas *Trpc6+* cells are more abundant at P22. N = 10-12 slices from 3 mice per time point. (**E**) Quantification of the fraction of excitatory (*Slc17a7+,* not shown) L2/3 cells expressing one or more markers *Cdh13*, *Trpc6*, and *Chrm2* at P12 and P22. N = 10-12 slices from 3 mice per time point.

Differences and similarities between wS1 and V1 in cell type development and gene expression changes

The results thus far have highlighted multiple similarities between wS1 and V1 maturation. For example, both regions share the same transcriptomic subclasses and markers, L2/3 is selectively regulated by development in both, and both contain equivalent L2/3 cell types and markers (Cheng et al., 2022). These similarities motivated a systematic comparison of developmental gene expression changes between wS1 and V1.

We identified tDE genes in V1 between P14 and P21, time points in the published data closest to those used in this study (**Table S5.4**). As in wS1, temporal gene regulation in V1 was predominantly subclass-specific (**Figures S5.6A-B**). Hypergeometric tests revealed that subclass-specific tDE genes were shared between wS1 and V1 for most subclasses (**Figure 5.5A**). For a few subclasses (e.g. inhibitory Sst, Vip and Lamp5 and excitatory L4 and L6b), there were too few tDE genes to conduct the analysis (**Figures S5.2C, S5.6A**). The shared subset of temporally regulated genes was enriched in GO terms related to neuronal development, including “GABAergic synapse”, “glutamatergic synapse”, “axon”, “nervous system development”, “axon guidance”, and other related programs (**Figures 5.5B, S5.6C**). Within L2/3, the overlapping genes were drawn from various functional categories, including CAMs, TFs, ICs, and NTRs (**Figure 5.5C**).

Moreover, wS1 and V1 share a striking correspondence in cell type composition. We trained classifiers on the V1 cell types at P14 and P21 and used them to transfer labels onto wS1 at P12 and P22, respectively. All 45 wS1 cell types mapped to the correct V1 subclass, and most cell types mapped 1:1 (**Figure S5.6D**). We also found that the relative cell type frequencies were highly concordant between the matched ages, indicating a high degree of overlap in cell type identity between the two cortical regions (**Figure 5.5D**). Together, this suggests that the two cortical regions share developmental programs at cell type resolution.

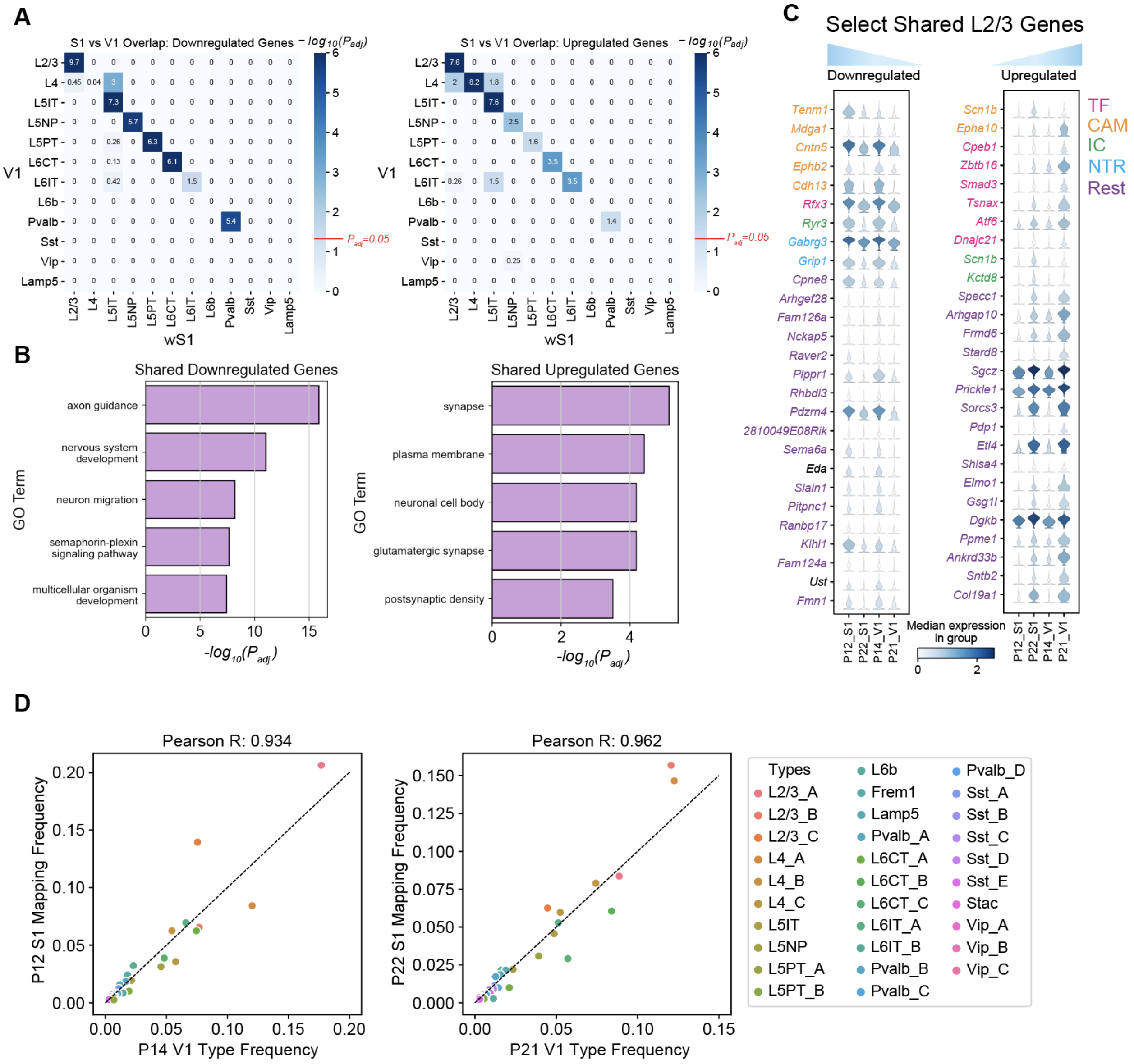

Figure 5.5. Comparative transcriptomic analysis of wS1 and V1. (**A**) Heatmap highlighting the overlap of tDE genes between all pairs of wS1 subclasses (P12 vs. P22; rows) and V1 subclasses (P14 vs. P21; columns). The left and right panels correspond to downregulated and upregulated genes. Values correspond to Bonferroni-corrected $-\log_{10}(P_{adj})$ values from a hypergeometric test of overlap of tDE genes. The background set for these tests was the set of all the genes regulated in any subclass. Except for L4, subclasses with fewer than 10 tDE genes (**Figures S5.2C, S5.6A**) showed little to no overlap. The value $P_{adj} = 0.05$ is highlighted on the scalebar (right). (**B**) Top 5 GO terms from shared downregulated and upregulated genes in V1 and wS1 in corresponding subclasses from panel A. See **Figure S5.6C** for a full list. (**C**) Examples of shared genes that are temporally downregulated (*left*) and upregulated (*right*) in L2/3 neurons between V1 and wS1. (**D**) Scatter plots showing highly similar relative frequencies between matched cell types (see **Figure S5.6D)** across V1 and wS1.

Full-face whisker deprivation by plucking does not alter cell type development

In mouse V1, 1-2 weeks of dark rearing during development selectively alters the transcriptomes of L2/3 cell types, revealing a requirement of visual experience for cell type development (Cheng et al., 2022; Xie et al., 2023). To test whether whisker deprivation has a similar effect on cell type development in wS1, we plucked all whiskers on the face from P12 to P22 and analyzed the resulting gene expression changes. We refer to this manipulation as 10-day all-whisker deprivation (10d AWD).

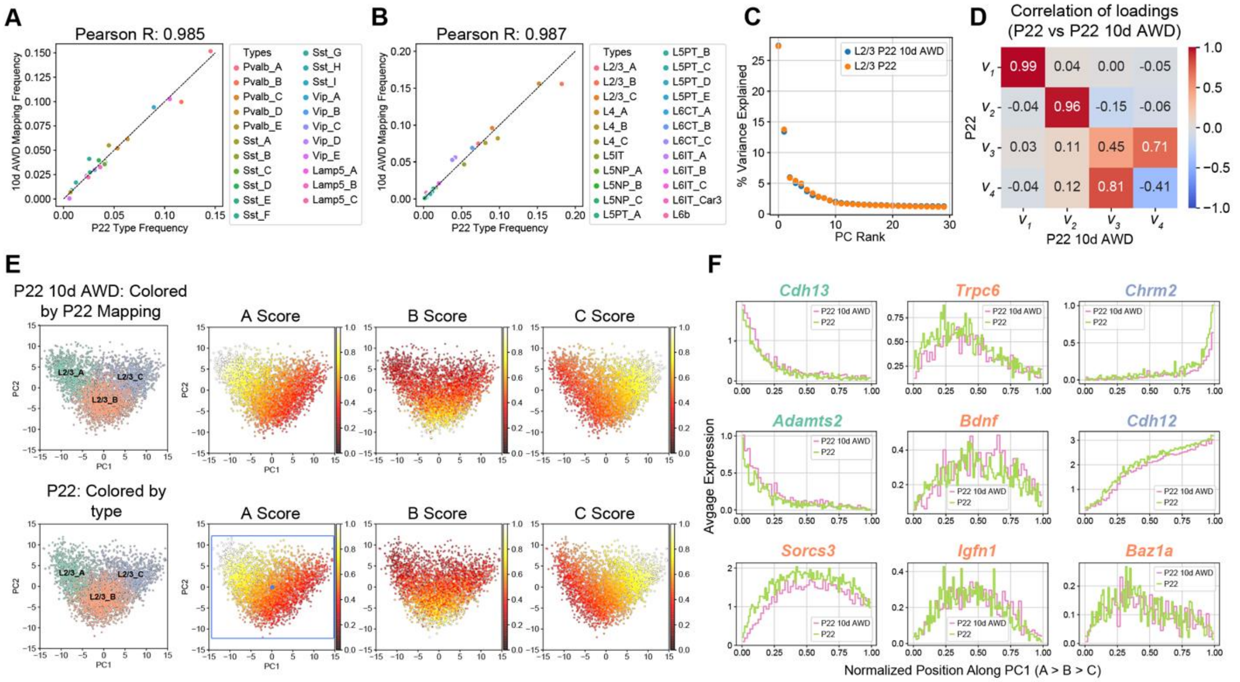

Figure 5.6. Full-face 10-day all-whisker deprivation (10d AWD) does not influence cell type maturation. (**A**) GABAergic cell types have approximately the same relative frequency in P22 10d AWD (y-axis) and normal P22 (x-axis). Note that cell type frequencies are normalized within all GABAergic neurons (~20% of all neurons). (**B**) Same as panel A for glutamatergic neurons (~80% of all neurons), highlighting similar cell type frequencies between P22 10d AWD (y-axis) and normal P22 (x-axis). (**C**) Similar to **Figure 5.3D**, showing that PC1 and PC2 are sufficient to describe transcriptional variance within L2/3 in the normal P22 and P22 10d AWD datasets. (**D**) Heatmap of Pearson correlation between the principal eigenvectors (as in **Figure 5.3E**) showing that the first two principal eigenvectors map 1:1 between the two datasets. (**E**) PC1 vs. PC2 scatter plot for L2/3 neurons at P22 10d AWD (top) and normal P22 (bottom), highlighting the location of types and the type-specific marker scores. Representation as in **Figure 5.3F**. Scores are similar between the two datasets (see also **Figure S5.7A**). (**F**) L2/3 markers genes, as in **Figure 5.4A**, are shown as a function of cells' position along PC1 comparing patterns between normal P22 and P22 10d AWD.

We repeated the analysis outlined in **Figures 5.3A-C,** training a classifier on the P22 cell types and using it to transfer P22 labels to 10d AWD transcriptomes. L2/3 composition and cell type frequency at P22 were minimally affected by 10d AWD (**Figures 5.6A-B**). Similar to the developmental analysis in **Figure 5.3,** we used PCA to study the influence on cell type composition in 10d AWD. For normal vs. 10d AWD P22, the top two principal eigenvectors, which captured >40% of the variance, exhibited a more robust 1:1 mapping compared to the case of the normal

P22 vs. normal P12 (**Figures 5.6C,D, 3E**), consistent with 10d AWD having a minimal effect on the overall expression levels and the correlation structure of gene expression. Furthermore, the expression patterns of L2/3 type markers along the first two principal components (PCs) were highly similar between normal and 10d AWD mice at P22 (**Figures 5.6E-F, S5.7A**).

Analysis of differentially expressed genes (DEGs) further confirmed that 10d AWD had a minimal influence on gene expression in all subclasses (**Table S5.5**). We found 51 DEGs, which is ~8x smaller than the number of temporally regulated DEGs between P12 and P22 (**Figures S5.7B-D**). For most of DEGs, regulation was subclass-specific, with *Lamp5+* interneurons exhibiting the largest number of changes. Altogether, we conclude that full-face whisker deprivation between P12 and P22 minimally impacts the maturation of cell types and subclass-specific transcriptional programs in wS1.

Brief row-based whisker deprivation upregulates column-specific activity-dependent gene expression programs in wS1

Previous work has shown that depriving a single row of whiskers for one day induces rapid plasticity in excitatory and inhibitory circuits in the columns corresponding to the deprived whiskers. This includes Hebbian and homeostatic synaptic plasticity and changes in the intrinsic excitability of neurons, with different mechanisms at play depending on the cell type and cortical layer (Gainey et al., 2018; Greenhill et al., 2015; House et al., 2011; Jacob et al., 2012; Li et al., 2014). However, the molecular factors behind these layer-specific changes in response to whisker deprivation in are still unknown.

We performed 1-day deprivation of the B and D whisker rows (1d RWD), a manipulation that induces competitive whisker map plasticity (Gainey et al., 2018), and assessed transcriptomic cell types and gene expression changes in S1 using snRNA-seq and FISH (**Figure 5.7A**). Cell type distributions were highly correlated between normal and 1d RWD datasets at P22 (**Figures S5.8A-B**). As in the normal and 10d AWD P22 datasets, variation within L2/3 neurons was captured well by the top two PCs (**Figure S5.8C**), which correlated 1:1 with the top two PCs of normal P22 data (**Figure S5.8D**). Furthermore, the expression patterns of L2/3 type markers along the first two principal components (PCs) were highly similar between normal and 1d RWD mice at P22 (**Figure S5.8E-G**). Altogether, this suggests that 1d RWD has a minimal influence on cell type identity in wS1, as expected for such a brief sensory manipulation.

It is well-established that sensory manipulation induces activity-dependent gene expression programs that result in long-lasting cellular adaptations essential for learning and maintaining circuit homeostasis (Bading, 2013; West and Greenberg, 2011). We hypothesized that 1d RWD may elicit an activity-dependent transcriptional response (**Figure 5.7A**). Within each neuronal subclass, we sought genes expressed in at least 20% of cells that were upregulated in 1d RWD mice (fold-change>2, FDR<0.05, Wilcoxon rank-sum test) (**Table S5.6**). We detected 59 such genes across all 12 subclasses. **Figure 5.7B** shows that the upregulated genes contain well-known "activity-dependent" genes such as *Npas4*, *Btg2*, *Junb*, and *Nr4a1* (West and Greenberg, 2011). Importantly, these genes were different from the few regulated by 10d WD (**Figure S5.7**), indicating their specificity to 1d RWD plasticity.

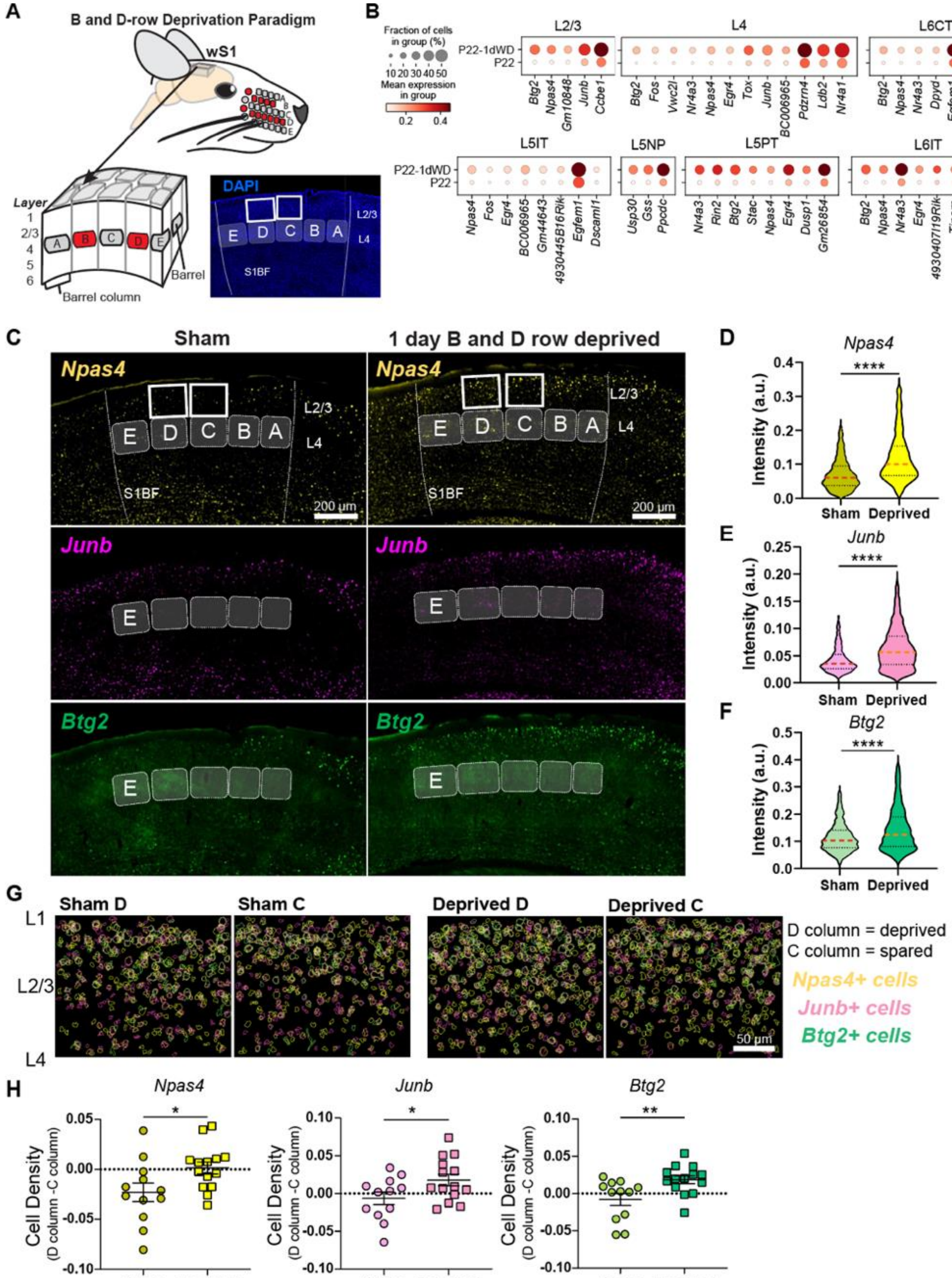

(*Figure 5.7 legend on next page*)

Figure 5.7. Brief row whisker deprivation (1d RWD) upregulates activity-dependent gene expression programs in deprived columns. (**A**) Schematic representation of the 1d row-whisker deprivation (RWD) manipulation and 'across-row' S1 section in which all barrel columns are identifiable. A representative image of DAPI labeling in 'across-row' S1 section. (**B**) Dotplots of genes upregulated by 1d RWD in glutamatergic subclasses (panels). Within each panel, rows indicate condition and columns indicate genes. The size of each circle corresponds to the % of cells with nonzero expression, and the color indicates average expression level. (**C**) Representative widefield images of wS1. Barrels and barrel fields are indicated with light grey rectangles and labeled. Boxes indicate the locations of ROIs used for analysis in **G.** (**D**) *Npas4* intensity inside *Slc17a7*+ L2/3 excitatory cells is increased after 1d RWD. Violin plots show median (dashed line) and quartiles (dotted lines). Mann-Whitney test, $p < 0.0001$ ****, n = 1571, 1337 cells respectively, from 3-4 mice per group. (**E**) *Junb* intensity inside *Slc17a7*+ L2/3 cells is increased after 1d RWD. Mann-Whitney test, $p < 0.0001$ ****, n = 1483, 1405 cells respectively, from 3-4 mice per group. (**F**) *Btg2* intensity inside *Slc17a7*+ L2/3 cells is increased after 1d RWD. Mann-Whitney test, $p < 0.0001$ ****, n = 1561, 1369 cells respectively, from 3-4 mice per group. (**G**) L2/3 C and D columns were compared to examine whether effects are specific to the deprived (D) column. Pseudocolored outlines of *Npas4, Junb, and Btg2* expressing cells. Each plot is an overlay of 5 images of L2/3 S1 from 3 mice. (**H**) Quantification of column-specific changes in 1d RWD upregulated genes measuring. Plotted values are the difference between the fraction of *Npas4/Junb/Btg2* expressing cells among all excitatory (*Slc17a7*+) cells in the L2/3 D column and the corresponding fraction in the L2/3 C column. Symbols represent slices from sham and 1d RWD mice. For each condition, mean and SEM (error bars) are shown. *Npas4*: Unpaired t-test, *p = 0.0321, n = 12,14 slices, 3-4 mice. *JunB*: Unpaired t-test, *p = 0.0427, n = 12,14 slices, 3-4 mice. *Btg2*: Mann-Whitney, **p = 0.0077, n = 12,14 slices, 3-4 mice.

We performed FISH experiments to confirm these gene expression changes and assess their laminar and columnar organization in the barrel field (**Figure 5.7C**). We used a plane of section that contains one whisker column in each of the five rows (A-E), enabling whisker row identity to be recognized since each whisker row maps to an array of cortical columns in the barrel field (Finnerty et al., 1999) (**Figure 5.7A**). We probed for three IEG candidates shown in **Figure 5.7C**--*Npas4*, *Btg2*, and *Junb*. These mRNAs were significantly increased in L2/3 of wS1 as measured by intensity per L2/3 cell (**Figure 5.7D-F**). To determine if the mRNAs were upregulated in a whisker column-specific manner, we separately analyzed the number of cells expressing each mRNA in excitatory L2/3 neurons in the deprived D vs. non-deprived C column of the same tissue section from sham and deprived mice (**Figures 5.7G,H**). We found that all mRNAs were upregulated in D compared to C in the whisker-deprived but not in sham controls, highlighting whisker column-specific gene regulation during competitive map plasticity (**Figure 5.7H**). Together, these results suggest that 1d RWD triggers rapid and selective induction of genes functionally associated with activity-dependent plasticity in a spatially localized pattern wherein mRNAs are more strongly upregulated in the deprived columns than in neighboring spared columns. Such gene expression patterns may constitute an early molecular mechanism of competitive map plasticity.

Discussion

A postnatal developmental atlas of mouse wS1

The somatosensory cortex is a canonical model to study experience-dependent and -independent development. Indeed, the principles of somatosensory organization and plasticity are similar between rodents and humans. Understanding the molecular programs underlying postnatal development of sensory cortex may be critical to understanding neurodevelopmental disorders such as autism that are associated with circuit dysfunction and impaired sensory processing. Prior studies have profiled the transcriptomic diversity of cell types in wS1 using scRNA-seq in adult mice (Yao et al., 2021) and bulk RNA-seq in adolescent mice (Kole et al., 2017a, 2017b; Yayon et al., 2023), but the gene expression changes that guide the emergence of cell type identity during early postnatal development in wS1 have not been explored.

We used snRNA-seq to study the postnatal development of transcriptomic cell types in wS1 from P12 to P22, the period of juvenile development immediately following the onset of whisking. Our mouse wS1 atlas comprises ~80,000 single-nucleus transcriptomes at two postnatal ages and across three rearing conditions. The overall taxonomy and frequency distribution of ~45 neuronal cell types were highly conserved across the time points and rearing conditions, allowing us to disambiguate broadly shared from cell type-specific changes during normal development and in response to whisker deprivation.

Proper assembly of cortical circuits involves precise control of gene expression in space and time. The comparison of expression profiles between P12 and P22 revealed hundreds of temporally regulated genes in wS1, over 60% of which were subclass-specific and enriched for functionally relevant processes associated with neuronal maturation, such as axon guidance and synapse maturation. Overall, glutamatergic neurons contained a higher proportion of temporally regulated genes than GABAergic neurons. A recent comparative transcriptomics study of V1 across human, macaque, and mouse showed that excitatory neurons are more evolutionarily divergent than inhibitory neurons ("Identification of visual cortex cell types and species differences using single-cell RNA sequencing | Nature Communications," n.d.), similar to the increased excitatory neuron developmental regulation we observed in wS1. The upstream mechanisms controlling the timing and subclass-specific expression of these genes and their potential roles in circuit formation and refinement are important areas for future research.

L2/3 cell types undergo significant changes during normal development

Of the 45 molecularly defined neuronal cell types, 42 were present at identical frequencies at P12 and P22, indicating that most wS1 neuron types are defined before P12. The only cell types that undergo significant changes in composition and cell type-specific gene expression between P12 and P22 are pyramidal cell subtypes in L2/3 (L2/3_A-C). The molecular identity and developmental changes of the three L2/3 cell types in wS1 mirror those observed in V1 (Cheng et al., 2022), where L2/3 cell types have been shown to possess unique binocular tuning properties and correlate with distinct projections to higher visual areas (HVAs)(Cheng et al., 2022; Kim et al., 2018). It is, therefore, reasonable to surmise that the three L2/3 cell types in wS1 may possess distinct functional properties and connectivity patterns. For example, *Cdh13* and *Cdh12* were expressed in different L2/3 neurons, with *Cdh13* enriched in type A and *Cdh12* in types B/C. A recent study demonstrated that *Cdh12+* and *Cdh13+* L5 pyramidal neurons in S1 are inhibited by CCK+ and PV+ interneurons, respectively (Jézéquel et al., 2023). Based on these trends, it is likely that L2/3_A cells are inhibited by PV+ neurons and L2/3_B/C cells are inhibited by CCK+ neurons. Another study identified that a group of mouse S1 L2/3 cells enriched in the *Baz1a* gene (likely the L2/3_B type) adapt to changes in whisker input via transient changes in IEG expression (Condylis et al., 2022). Thus, the delayed maturation of these L2/3 cell types may be linked to their experience-dependent plasticity in adulthood. Since the L2/3 cell types differ in laminar position, they may receive different thalamic inputs, with L2-situated cells (L2/3_A and B here) tending to receive less VPM axon innervation than L3-situated cells (L2/3_C)(Jouhanneau et al., 2014; Sermet et al., 2019), as well as different local inhibitory inputs (Audette et al., 2018).

A potential mechanism underlying the developmental flexibility of L2/3 neurons could be the presence of a transcriptomic gradient. In principal component space, we observed that L2/3 neurons form a triangle, with each of the three cell types occupying a vertex. Additionally, many markers were expressed in a gradient fashion, like the functional gradients observed for L2/3 neurons in V1 (Weiler et al., 2023). This suggests that wS1 L2/3 neurons exhibit an overall gradient pattern while also containing some specialist cell types, mirroring what has been observed in V1 and the intestine (Adler et al., 2019; Cheng et al., 2022; Xie et al., 2023). Occupying a flexible continuum could facilitate the drastic gene expression and compositional shifts observed in these neurons from P12 to P22.

Developmental transcriptomic conservation and divergence between V1 and wS1

Recent studies have shown a high degree of correspondence in neural diversity and cell type markers between cortical areas (Chen et al., 2024; Chou et al., 2013), and this was indeed the case between wS1 and V1. Our comparison of P12 to P22 in wS1 and P14 to P21 in V1 revealed similar developmental gene expression patterns. In most cases, there was significant overlap in the up- and down-regulated genes between matched neuronal subclasses between the two regions and little to no overlap across distinct subclasses. The notable exception was that L4 neurons did not share downregulated genes between the two regions (**Figure 5.6A**), which may be related to the fact that L4 contains spiny stellate cells in wS1 but not V1.

Despite this broad similarity, there was a laminar difference in the organization of L2/3 neuron subclasses between the two regions. Our data suggests that wS1 undergoes a similar remodeling of cell types from P12 to P22 as V1, with A-like cells decreasing and B-like cells increasing in number. However, unlike V1 where the L2/3_A-C cells segregate into sublaminae along the radial (pial-ventricular) axis at P21, we found that, in wS1, L2/3_A and L2/3_B somas are intermixed in superficial L2/3, but are spatially separated from the C somas, which reside in deep L2/3. The factors driving this difference between V1 and wS1 are unknown but may stem from broader differences in laminae across the sensory cortices (Chang et al., 2018).

The overall similarity in gene expression programs appears reasonable, given that V1 and wS1 share many aspects in the timing of their postnatal development. Thalamocortical axons begin innervating the cortical plate and reaching their targets in L4 around the same time in wS1 and V1 (Agmon et al., 1993; Ferrer and De Marco García, 2022). Callosal axons cross the midline around the same time in V1 and wS1 also and undergo activity-dependent rearrangement during postnatal week two. By the second postnatal week, sensory input increases in V1 and wS1 at the onset of activity whisking (P12) and eye-opening (P14). However, an important difference is that the maturation of wS1 is accelerated compared to V1. Sensory-evoked responses can be elicited even before birth with whisker stimulation, in contrast to V1 where these responses arise by the end of the first postnatal week. The classically defined critical periods for whisker deprivation-induced plasticity in wS1 close in postnatal weeks 1-2, while in V1 the classical critical period for ocular dominance plasticity doesn't end until P32 (Gordon and Stryker, 1996).

Despite the robust effects of whisker experience on wS1 circuit function, our results demonstrate that normal whisker experience from P12 to P22 is not required for the development of cell types in wS1. This contrasts with our previous observations in V1, where dark rearing led to significant changes in gene expression and composition of L2/3 cell types, resulting in altered spatial organization and functional tuning (Cheng et al., 2022; Xie et al., 2023). In wS1, 10d AWD did not impact gene expression or composition of L2/3 cell types. This result suggests that sensory experience may vary in importance for the maturation of cortical cell types across regions. In wS1, the proper formation and stabilization of neural circuits may rely more heavily on intrinsic programs, regardless of sensory input (Golshani et al., 2009).

Why might L2/3 cell type development be regulated by visual experience in V1, but not by 10d AWD whisker deprivation in wS1? One possibility is that the overall impact of sensory experience on cortical cell and circuit development is milder in wS1 than in V1. Consistent with this idea, ocular dominance shifts of V1 neurons driven by monocular deprivation are often stronger than whisker tuning shifts in wS1 driven by plucking a subset of whiskers (Margolis et al., 2012; Rose et al., 2016). During the critical period for ocular dominance plasticity in V1, visual experience shapes thalamocortical axons. It is required to maintain their structure, while in wS1, whisker sensory use does not alter thalamocortical or L4 topography after P4, and before that only nerve or follicle damage is sufficient to drive plasticity (Ferrer and De Marco García, 2022; Fox, 1992). The critical period for ocular dominance plasticity has a stark ending at P32 in mice (Gordon and Stryker, 1996), while S1 retains many forms of experience-dependent plasticity into adulthood (Feldman and Brecht, 2005), suggesting that wS1 plasticity may not be as tied to developmental mechanisms as in V1.

Alternatively, the lack of effect of whisker deprivation on wS1 cell type development may stem from differences in the efficiency of whisker vs. visual deprivation paradigms (Fox and Wong, 2005). Visual deprivation, such as dark rearing, completely removes sensory drive and statistical patterns of sensory input, leaving only retinal spontaneous activity, which has different properties. In contrast, whisker plucking does not fully eliminate external sensory input because direct contact with the skin of the mystacial pad, e.g. during grooming or cuddling, still provides some afferent activation. Thus, plucking is likely to eliminate less sensory input than dark rearing and, hence, may have a less pronounced impact on S1 gene expression.

Competitive whisker deprivation drives plasticity-related gene expression programs in L2/3

Despite the lack of requirement for whisker experience on cell type maturation, we found that brief whisker deprivation of only two rows of whiskers (1d RWD) upregulates activity-dependent gene expression programs in multiple wS1 cell types, including *Npas4, Btg2, Junb, and Nr4a1*, which are known to be involved in synaptic plasticity and circuit homeostasis (West and Greenberg, 2011). Typically, expression of these IEGs is thought to be driven by increased levels of activity, as occurs during environmental enrichment (P65-75 animals) in S1 (Kaliszewska and Kossut, 2015; Vallès et al., 2011) or dark rearing followed by light exposure in V1 (Xavier et al., 2024). A recent study in V1 showed that seven days of dark-rearing followed by 1-2 hours of light exposure induced IEG expression (Xavier et al., 2024). Interestingly, dark-rearing alone also increased the expression of several genes, particularly in L2/3 excitatory neurons (Xavier et al., 2024). Our finding that a subset of IEGs are upregulated in response to deprivation indicates that IEG induction may represent a general plasticity program broadly used to engage plasticity mechanisms rather than a specific consequence of elevated neural activity. Notably, these IEGs were expressed mainly in the L2/3_B cell population, highlighting the role of L2/3_B cells as a critical functionally distinct subpopulation in L2/3 (Condylis et al., 2022).

We found that the IEGs were upregulated in a column-specific fashion in wS1. Deprived columns showed strong upregulation of IEGs relative to neighboring spared columns. This deprivation paradigm triggers synaptic plasticity, a component of competitive map plasticity, wherein whisker-evoked responses to deprived whiskers weaken and shrink within the whisker map while responses to spared whiskers strengthen and expand (Feldman, 2009). Thus, the selective upregulation of IEGs in deprived columns may represent an early molecular step underlying competitive map plasticity. Together, the 1d RWD results indicate that whisker experience exerts only relatively subtle effects on the development of cell types, but has significant effects at the gene expression level within specific cell types.

Summary and limitations

This work contributes a single-nucleus transcriptomic resource for postnatal wS1 development under normal and deprived sensory experience. We delineated developmental changes in neuronal subclasses and types, and found that these were highly conserved between mouse V1 and wS1. However, whisker experience served a limited role in wS1 cell type development, which contrasts with the greater role of vision in V1 cell type development. Nevertheless, brief whisker deprivation induced significant changes in the expression of IEGs in a whisker column-specific fashion. Thus, while wS1 may rely less on experience and more on hardwired genetic programs than V1 to develop cell types, these cell types can undergo experience-dependent gene expression changes.

Throughout the study, we validated multiple scRNA-seq findings by performing FISH experiments targeting representative genes. Future studies could quantify the expression of many genes simultaneously in the same cell as a function of the cell's location, especially in the context of wS1 barrels, using spatial transcriptomics approaches to further test the hypotheses established in this work. The gene regulatory logic that translates experience-driven activity to cell-type specific transcriptome changes remains poorly explored. Further research aimed at dissecting patterns at the DNA level, such as chromatin organization and DNA methylation, could reveal the gene regulatory networks responsible for the transcriptomic patterns observed here. We also note that the paucity of changes in the transcriptome during 10d AWD or 1d RWD may be due to low sampling resolution in snRNA-seq, or because the underlying changes could be at the protein level. Finally, additional work could relate the cell type-specific IEG expression during 1d RWD reported here to changes in neuronal physiology, for example, by labeling specific cell types and surveying their properties using slice electrophysiology or by performing 2P imaging of labeled cell types *in vivo* during whisker sensory behavior.

Materials and methods

Computational Methods

Alignment and gene expression quantification

FASTQ files with raw reads were processed using Cell Ranger v7.0.1 (10X Genomics) with default parameters. We used the mm10 (GENCODE vM23/Ensembl 98) reference genome and transcriptome. Reads aligning to the entire gene body (exons, introns, and UTRs) are used to quantify expression levels. Each single-nucleus library was processed using the same settings to yield a gene expression matrix (GEM) of mRNA counts across genes (columns) and nuclei (rows). Each row ID was tagged with the sample metadata for later meta-analysis. We henceforth refer to each single-nucleus transcriptome as a ‘‘cell.’’

Initial pre-processing and quality control of snRNA-seq data

This section outlines the initial transcriptomic analysis of data from all samples. Unless otherwise noted, all analyses were performed in Python using the SCANPY package(Wolf et al., 2018) based on the following steps https://github.com/shekharlab/wS1dev:

1. Raw GEMs from 12 snRNA-seq libraries were combined: P12 control (A1, A2), P22 control (S1, S2, S3, S4), P22 1d RWD (D1, D2, D3, D4), and P22 10d AWD (C1,C2). This resulted in a GEM containing 199,524 cells and 32,285 genes.
2. We generated scatter plots of the number of transcript molecules in each cell (n_{counts}), the percent of transcripts derived from mitochondrially encoded genes (percent_mito), and the number of expressed genes (n_{genes}) to identify outlier cells. Cells that satisfied $n_{genes} < 7000$ and $n_{counts} < 40,000$, and $n_{counts} > 500$ were retained, and genes detected in fewer than 100 cells were removed from further analysis. This resulted in a GEM of 199,074 cells and 21,258 genes (**Figure S5.1A**). Cells were normalized for library size differences by rescaling the transcript counts in each cell to a total of 10,000, followed by log transformation.
3. For clustering and visualization, we followed steps described previously(Cheng et al., 2022). Briefly, we identified highly variable genes (HVGs), z-scored expression values for each HVG across cells, and used the z-scored data to compute a reduced dimensional representation based on principal component analysis (PCA). The top 40 principal components (PCs) were used to build a nearest-neighbor graph on the cells. We clustered this graph using the Leiden algorithm(Traag et al., 2019) and embedded it in 2D via the Uniform Manifold Approximation and Projection (UMAP) algorithm(Becht et al., 2019). We identified 39 preliminary clusters.
4. Four of the 39 preliminary clusters contained 20-40% mitochondrial transcripts, while the remaining clusters contained, on average, 5-10% mitochondrial transcripts. We removed these clusters from the data, resulting in 169,674 cells (**Figure S5.1A**). One cluster

belonged to samples S1/S2, another to A1/A2, another to C1/C2/S4, and the last one to S3/D3/D4.

5. With this filtered set of 169,674 cells, we re-ran the clustering pipeline described above to obtain a new set of clusters. To assess the quality of these clusters, we trained a multi-class classifier using XGBoost, a gradient boosted decision tree-based classification algorithm(Chen and Guestrin, 2016) on the subclasses from the primary visual cortex(Cheng et al., 2022) (V1). From the V1 study, we used all of the postnatal time points collected from normally reared animals. 28 out of the 39 preliminary clusters mapped strongly to one of the 20 V1 subclasses. However, 11 clusters mapped diffusely to the subclasses and/or mapped with low classifier confidence. Further inspection indicated that the poorly mapping clusters had higher doublet scores than tightly mapping clusters(Wolock et al., 2019), and their top markers were enriched in gene ontology (GO) terms related to "apoptosis" and "response to toxic substance". Removal of the 11 problematic clusters reduced the number of cells to 114,812. Next, we examined the V1 subclass composition of each remaining cluster and removed cells corresponding to any V1 subclass that accounted for <2% of the cluster. This further purified clusters, ultimately yielding 112,233 cells (**Figure S5.1A**).
6. Finally, we isolated each of the four experimental conditions (P12 control, P22 control, P22 1d RWD, and P22 10d AWD) and re-ran the clustering pipeline described above. Within each condition, we removed clusters containing cells that mapped to V1 subclasses in a non-specific manner. This yielded a final number of 111,299 cells that form the foundation of this paper (**Figure S5.1A**). Only the 81,462 neurons were used in all the analyses reported in this paper.

Temporal regulation and subclass specificity analysis

The gene quadrant analysis (**Figure 5.2)** was performed on the P12 and P22 control datasets separately for the glutamatergic and GABAergic neuronal classes. Within either class, we performed a Wilcoxon rank-sum test for each subclass against the rest of the subclasses to identify subclass-specific markers (fold-change (FC)>2, FDR<0.05, expressed in >40% of cells). For each pair of gene and subclass, we calculated fold changes separately at P12 and P22 and selected the maximum value as the subclass variability (SV) score. We next performed Wilcoxon rank-sum test between P12 and P22 for each subclass to identify temporally regulated genes (FC>2, FDR<0.05, expressed in >40% of cells). The maximum temporal FC value for each gene across all subclasses was assigned to be its tDE score. To define the quadrants, a threshold FC value of 2 was chosen, and we verified that values between 1.5 and 2.5 do not qualitatively impact the results shown in **Figures 5.2** and **S5.2**.

In **Figures 5.2B**,**C** of the main text, we assess the statistical enrichment of specific gene groups in each quadrant using a Fisher's Exact Test. For each quadrant, we calculated the odds ratio (OR) and p-value using Fisher's Exact Test to determine whether TFs, CAMs, ICs, or HKs were significantly over- or under-represented compared to the null expectation based on all genes. Given the multiple comparisons, we applied the Bonferroni correction to adjust the p-values, controlling for false positive rate. The results were visualized by categorizing the quadrants based on statistically significant under- or over-representation: quadrants were shaded grey if the adjusted p-value exceeded 0.05 (no enrichment), red if the adjusted p-value was less than 0.05 with OR <

1 (significant under-representation), and green if the adjusted p-value was less than 0.05 with OR > 1 (significant over-representation). This approach allowed us to identify statistically significant enrichment patterns, highlighting their potential regulatory roles in wS1 development. Finally, gene ontology (GO) enrichment analysis was performed on each quadrant's set of genes using the python package GOATOOLS (Klopfenstein et al., 2018). We used the default background set in GOATOOLS, which comprised all protein-coding genes.

Subclass-by-subclass differential gene expression analysis between each experimental condition and P22 control

We sought to identify gene expression differences at the subclass level between the P22 control dataset and the three experimental datasets, including P12, P22 10d AWD, and P22 1d RWD. Here, each subclass was isolated, and a Wilcoxon rank-sum test was performed for that subclass between P22 control and each of the three conditions. Of the genes expressed in >40% of cells in one of the two datasets, we selected those with FC>2 at false-discovery rate (FDR)<0.05. A python implementation of the R package UpSetPlot (Lex et al., 2014) was used to compute and visualize the number of genes regulated in a shared and subclass-specific fashion. For these differential gene expression tests, samples S3, D3, and D4 were excluded due to their relatively low number of transcript counts and expressed genes to not affect the results (**Figure S5.1B-C**). However, these samples were not excluded from any other analysis and consistently contained all neuronal subpopulations with no frequency discrepancies (**Figure 5.1F**).

Class, subclass, and cell type annotation of snRNA-seq data

We annotated cells in our dataset according to the taxonomy in **Figure 5.1D**. The two major neuronal classes were easily identified using glutamatergic marker *Slc17a7I* and GABAergic markers *Gad1* and *Gad2* in each condition separately. Additionally, we identified non-neuronal groups using known markers(Tasic et al., 2018). Non-neuronal cells were discarded at an early stage, and we focused on the two neuronal classes, which clustered distantly from each other in gene expression space. Clusters within each condition naturally separated according to subclasses that could be annotated based on established markers(Cheng et al., 2022). The class and subclass levels of the taxonomy are highly conserved across cortical regions and studies. However, as the cell type level tends to vary across regions, studies, and conditions, we annotated cell types in the P22 control dataset, and then transferred these labels onto the other conditions.

To annotate cell types in the P22 control dataset, we first trained a classifier on the cell types of the P21 V1 dataset(Cheng et al., 2022). We then applied the classifier to the P22 control dataset to assign each wS1 neuron a P21 V1 cell type label. Second, we isolated each subclass and used Leiden clustering(Traag et al., 2019), varying the resolution parameter from 0.25 to 2, with higher values providing more clusters. Third, we trained and validated a classifier for each clustering resolution, identifying the resolution at which cluster validation error (computed using held-out cells) increases significantly, indicating over-clustering. The general procedure to train and validate such classifiers is described in the following section. Another telltale sign for diagnosing over-clustering was when differential expression analysis yielded highly overlapping marker sets for their clusters. Ultimately, these steps nominated a range of optimal clustering resolutions, and we chose the final resolution at which the validation error was low (90%) and there was a high concordance with the V1 clustering. This resolution also yielded unique marker sets across the cell types.

Finally, we combined all subclasses for each of the two classes (glutamatergic and GABAergic neurons), and used a classification analysis to verify that we have not over-clustered the data. We trained a classifier on the P22 wS1 control data and mapped the P21 V1 data to it. Clusters from the P22 wS1 data were removed if they satisfied the following criteria simultaneously: 1) received no mapping from V1, 2) had a high doublet and/or mitochondrial score, and 3) were not learnable during training. This procedure filtered ~800 cells, approximately 2.5% of the P22 control data.

Classifier-based mapping of experimental conditions to P22 control data

To assess transcriptomic correspondence of clusters across ages (P12 vs. P22) or between rearing conditions (control vs. 1d RWD and 10d AWD), we used XGBoost, a gradient boosted decision tree-based classification algorithm(Chen and Guestrin, 2016). These analyses were performed to study the effects of development (P12), sensory experience (P22 10d WD), and rapid homeostatic plasticity (P22 1d WD) on cell type identity and composition. We also used this approach to compare the cell type compositional differences between V1 cell types and wS1 cell types. In a typical workflow, we trained an XGBoost (version 1.3.3) classifier to learn subclass or type labels within the P22 control "reference" dataset and applied this classifier to another "test" dataset. The correspondences between cluster IDs and classifier-assigned labels for the test dataset were used to map subclasses or types between datasets. The classification workflow is described in general terms below and applied to various scenarios throughout the study.

Let R denote the reference dataset containing N_R cells grouped into r clusters. Let T denote the test dataset containing N_T cells grouped into t clusters. Each cell is a normalized and log-transformed gene expression vector $\boldsymbol{u} \in R$ or $\boldsymbol{v} \in T$. The length of $\boldsymbol{u}$ or $\boldsymbol{v}$ equals the number of genes. Based on clustering results, each cell in R or T is assigned a single cluster label, denoted cluster($\boldsymbol{u}$) or cluster($\boldsymbol{v}$). cluster($\boldsymbol{u}$) may be a type or subclass identity, depending on context.

The main steps are as follows:

1. We trained a multi-class XGBoost classifier C_R^0 on R using the intersection of HVGs from R and T as features. The training dataset was split into training and validation subsets. For training, we randomly sampled 70% of the cells in each cluster, up to a maximum of 1000 cells per cluster. The remaining "held-out" cells were used for evaluating classifier performance. Clusters with fewer than 100 cells in the training set were upsampled via bootstrapping to 100 cells to improve classifier accuracy for the smaller clusters. Classifiers achieved >95% accuracy or higher on the validation set for most clusters, with some clusters yielding 85%-95% accuracy. XGBoost parameters were fixed at the following values:
    1. 'Objective': 'multi:softprob'
    2. 'eval_metric': 'mlogloss'
    3. 'Num_class': r
    4. 'eta': 0.2
    5. 'Max_depth': 6
    6. 'Subsample': 0.6

2. When applied to a test vector ***c***, the classifier C_R^0 returns a vector $p = (p_1, p_2, \ldots)$ of length r, respectively. Here, p_i represents the probability value of predicted cluster membership within R, respectively. These values are used to compute the "softmax" assignment of ***c***, such that cluster(***c***) = $\arg\max_i p_i$ if $\arg\max_i p_i > 1.2*(1/r)$. Otherwise ***c*** is classified as 'Unassigned'.
3. After determining that the initial classifier C_R^0 faithfully learns the reference clusters, we trained a classifier C_R on 100% of the cells in R. C_R was then applied to each cell $\boldsymbol{v} \in T$ to generate predicted labels cluster(***v***). In this study, T was P12, P22 10d AWD, P22 1d RWD, and V1 P21.

The cell type frequency distribution predicted for T was compared to the distribution of cell type labels in R using scatter plots. Each dot represented one of the clusters in R, and the axes represented the frequency of that cluster in each dataset.

Principal component analysis on L2/3 pyramidal neurons

The classification analyses revealed that L2/3 was the only subclass where cell type frequency differed significantly between P12 and P22 (**Figure 5.3B,C** in the main text). To explore this further, we performed principal component analysis on L2/3 cells only. Since we were interested in understanding L2/3 cell type identity and how it varies across conditions, we chose as the features the top markers for each type (Wilcoxon rank-sum test, FC>1.5, FDR<0.05, expressed in >20% of cells in type), resulting in a set of 489 genes. The same set of genes was used for the PCA of all conditions. Correlations between the principal eigenvectors across the conditions were computed by taking their dot product. This is equivalent to the correlation coefficient of the loadings. Note that, by construction, the principal eigenvectors are orthonormal within a sample. Finally, a score for each marker set was computed for each cell as the mean expression of all genes in the set in that cell.

Overlap of tDE genes between S1 and V1

To determine the degree to which tDE genes are shared between S1 and V1, we performed subclass-by-subclass differential gene expression on P14 and P21 V1 data, as they are the most closely matched to our P12 and P22 data(Cheng et al., 2022). We then performed a hypergeometric test for the overlap of tDE genes in either direction for each subclass. In each test for each subclass, four variables are set: N, the universal set comprising all of the genes downregulated/upregulated in every subclass, K, the number of tDE genes in V1, n, the number of tDE genes in wS1, and k, the intersections of K and n. The P value for each subclass was Bonferroni-corrected by multiplying by the number of subclasses tested.

Experimental Methods

Mice handling

All procedures were approved by the UC Berkeley Animal Care and Use Committee and were in accordance with NIH guidelines. C57Bl6J male mice were obtained from Charles River Laboratories. Mice were maintained on a 12 hr day/night cycle and housed with littermates and the mother in the UC Berkeley animal facility. For whisker deprivation, mice were anesthetized with isoflurane, and whiskers were carefully plucked under a dissecting microscope with forceps using slow and steady force to prevent removal of the whisker follicle. Sham mice were anesthetized for the same amount of time as deprived, but whiskers were only stroked briefly with forceps.

Droplet-based snRNA-seq

Mice were anesthetized with isofluorane, rapidly decapitated, and the brain was dissected out into ice-cold Hibernate A (BrainBits Cat# HACA). For each condition (P12, P22 control, P22 1d RWD, P22 10d AWD) 3 mice were used for each biological replicate of single-nucleus(sn) RNA-sequencing. Extracted brains were placed on a metal brain mold (Zivic Instruments,#5569) and the slice containing wS1 was isolated by inserting in the 11th space on the mold (~7.5 mm from the tip of the olfactory bulb, and a second blade 2 mm further anterior (4 spaces on the mold). This slice was removed and lowered to Hibernate A in a 60cc petri dish, placed on a ruler under a dissecting microscope. The midline was aligned with the ruler, and the first cut was bilaterally 2 mm out from the midline in a radial direction. The second cut was 2 mm medial to the first cut. The cortex was peeled off the underlying white matter. The wS1 piece was transferred into a RNAse-free cryovial, excess liquid was removed, and the tube was rapidly frozen on dry ice. Once all dissections were complete, the tissue was transferred from dry ice into a dewar of liquid nitrogen for storage before nuclei isolation.

Nuclei Isolation

Nuclei were isolated using the 10X Chromium nuclei isolation kit (10X Genomics,Cat#1000494). After isolation according to the chromium protocol, cells were counted on a hemocytometer in ethidium bromide and then diluted to 700-1200 nuclei/mm3. Nuclei from each biological replicate were split into two tubes and run separately on two channels of 10X v3, targeting 10,000 cells per channel. We refer to these as library replicates. For each experiment, we performed two or three biological replicates towards a total of four to six library replicates.

Fluorescence in situ hybridization (FISH)

C57BL/6 male mice (Charles River), from age P12 and P22, were anesthetized with isoflurane and transcardially perfused with 2% RNAse-free paraformaldehyde (PFA) in PBS (pH 7.4). Mouse brains were collected and immediately fixed in 4% RNAse-free PFA at 4ºC. After 24 hours, the brains were transferred to 30% sucrose in PBS and were allowed to sink 4ºC. Slices were cut from the left hemisphere in the 'across-row' plane. Brains were first mounted on a tissue guillotine with a 35º incline, rostral pointing upward. Brains were then cut at an angle 50º from the midsagittal plane. Using this plane, every S1 slice has one column from each whisker row A–E, and circuitry within columns remains largely intact (Allen et al., 2003; Finnerty et al., 1999). Slices were cut on a sliding microtome (Reichert Scientific Instruments 860) into 30 µm thick sections, collected into RNAse-free PBS, and onto charged microscope slides. Sections were air-dried overnight, then post-fixed in 4% RNAse-free PFA for 1 hour at 4ºC; this was followed by serial ethanol dehydration and dried before being promptly stored at -80ºC until further processing.

Multiplex fluorescence in situ hybridization followed the protocol for ACDBio's RNAscope Multiplex Fluorescent V2 Assay (Advanced Cell Diagnostics, cat# 323110). Thawed sections underwent H2O2 permeabilization, 5-minute target retrieval, and protease III treatment. RNAscope probes *Trpc6* (cat# 442951), *Chrm2* (cat# 495311-C2), *Cdh13* (cat# 443251-C3), *Slc17a7* (cat# 501101-C4), *Adamts2* (Cat# 806371-C3), *Bdnf* (Cat# 424821) *Btg2* (cat# 483001), *Npas4* (cat# 423431-C2), *Junb* (cat# 584761-C3), *Col19a1* (cat# 539701), *Sorcs3* (cat# 473421-C2), *Etv1* (cat# 557891-C3), and *Gabrg3* (cat# 514421-C4), were applied and amplified in sequence with TSA Vivid and Opal Polaris dyes (Advanced Cell Diagnostics, cat# 323271, 323272, 323273; Akoya Biosciences, cat# FP1501001KT). Cellular nuclei were counterstained with 1 µg/ml DAPI and mounted with Prolong Glass Antifade Mountant (Thermo Fisher Scientific, cat# P36982). All RNAscope runs were performed with both conditions side-by-side and controls, to reduce variability.

Imaging was performed using a Zeiss Axio Scan 7 slide scanner with Zen digital imaging software. Tilescan images were acquired of the entire wS1 including all cortical layers at 20X. All channels were acquired at the same exposure, gain and laser power settings for each condition. The relevant barrel columns were identified using DAPI staining in combination with the other markers and images were cropped to target L2/3 and barrel columns of interest in FIJI. All pre-processing steps were kept consistent between conditions. Cropped images were inputted into CellProfiler to detect 5 imaging channels. Nuclear segmentation was performed with DAPI channel and cellular segmentation was performed with the RNAscope probe *Slc17a7* (vGlut1), a marker for glutamatergic neurons. For analysis of temporally-regulated mRNAs, nuclear segmentation with DAPI was used as a region of interest (ROI) to measure mean intensity values for each mRNA in each nucleus. Layers were estimated using empirically measured distance from the pial surface. L2/3 was considered 50-250 µm deep, and L4 was 250-350 µm. For cell type analysis, thresholds were set to identify cells expressing markers above background. Threshold parameters for each channel were kept the same across conditions. To determine cell type identity and overlap, cell type markers were identified as objects. Objects that did not overlap with the cell segmentation marker *Slc17a7* were eliminated in order to isolate excitatory L2/3 cells. Lastly, object overlap across channels was computed. The coordinates of all identified objects from CellProfiler were used to generate scatterplots in Python with the Seaborn package. For immediate-early genes (IEG) analysis, cellular segmentation with *Slc17a7* was used as a region of interest (ROI) to measure intensity values for each mRNA in each excitatory L2/3 cell. Outliers were cleaned from the data in Graphpad Prism using the ROUT method(Motulsky and Brown, 2006). Outline plots were generated in CellProfiler(Carpenter et al., 2006), by relating cellular segmentation object results and IEG objects. Outlines for each image used in the analysis were overlaid by z-projecting in FIJI to generate summary outline figures. Plots and statistics were generated using Graphpad Prism 10. Normality tests were performed on all datasets. If datum were not normally distributed, nonparametric statistical tests were used. Each condition (P12, P22 control, P22 1d sham, P22 1d RWD) had 3-5 mice from which multiple brain sections were analyzed.

Data and code availability

All raw and processed snRNA-seq datasets reported in this study will be made publicly available via NCBI's Gene Expression Omnibus (GEO) Accession Number GSE276528. Processed h5ad files are available at https://github.com/shekharlab/wS1dev. These h5ad files contain all relevant metadata and log-normalized counts. Computational scripts detailing snRNA-seq analysis reported in this paper are available at https://github.com/shekharlab/wS1dev. All custom software for imaging analysis will be made available upon request. Any additional information required to reanalyze the data reported in this paper is available from the corresponding authors upon request.

Acknowledgments

Select images were made using BioRender. We thank Dr. Justin Choi from the QB3/Functional Genomics Lab (RRID:SCR_022170) for assistance with scRNA-seq. We also thank Drs. Melanie Oakes and Quy Nguyen from the UCI sequencing core for performing all sequencing for this study. The UCI Genomics Research and Technology Hub (GRT Hub) is partly supported by NIH grants to the Comprehensive Cancer Center (P30CA-062203) and the UCI Skin Biology Resource Based Center (P30AR075047) at the University of California, Irvine, as well as to the GRT Hub for instrumentation (1S10OD010794-01and 1S10OD021718-01). We are grateful to Drs. Juyoun Yoo and Saumya Jain from the UCLA Zipursky lab for feedback during the early stages of nuclei extraction protocol optimization. This work was funded by NIH grants 1F32 NS126310 (HRM), 1F31 F31NS131016 (SB), EY028625 (KS), R01 NS105333 (DF), as well as funds from the Society of Hellman Fellows (KS), the McKnight foundation (KS), and SFARI Investigator Award grant (DF).

Author Roles

S. B., Conceptualization, Data curation, Formal analysis, Investigation, Methodology, Validation, Visualization, Software, Writing – original draft, Writing – review & editing.

H.M., Conceptualization, Data curation, Formal analysis, Investigation, Methodology, Validation, Visualization, Writing – review & editing

C.Y., Investigation

D.F., Conceptualization, Methodology, Validation, Writing – review & editing, Resources, Funding Acquisition, Supervision

K.S., Conceptualization, Methodology, Validation, Writing – review & editing, Resources, Funding Acquisition, Supervision

S.B. and H.M. contributed equally to the study.

Supplementary Materials

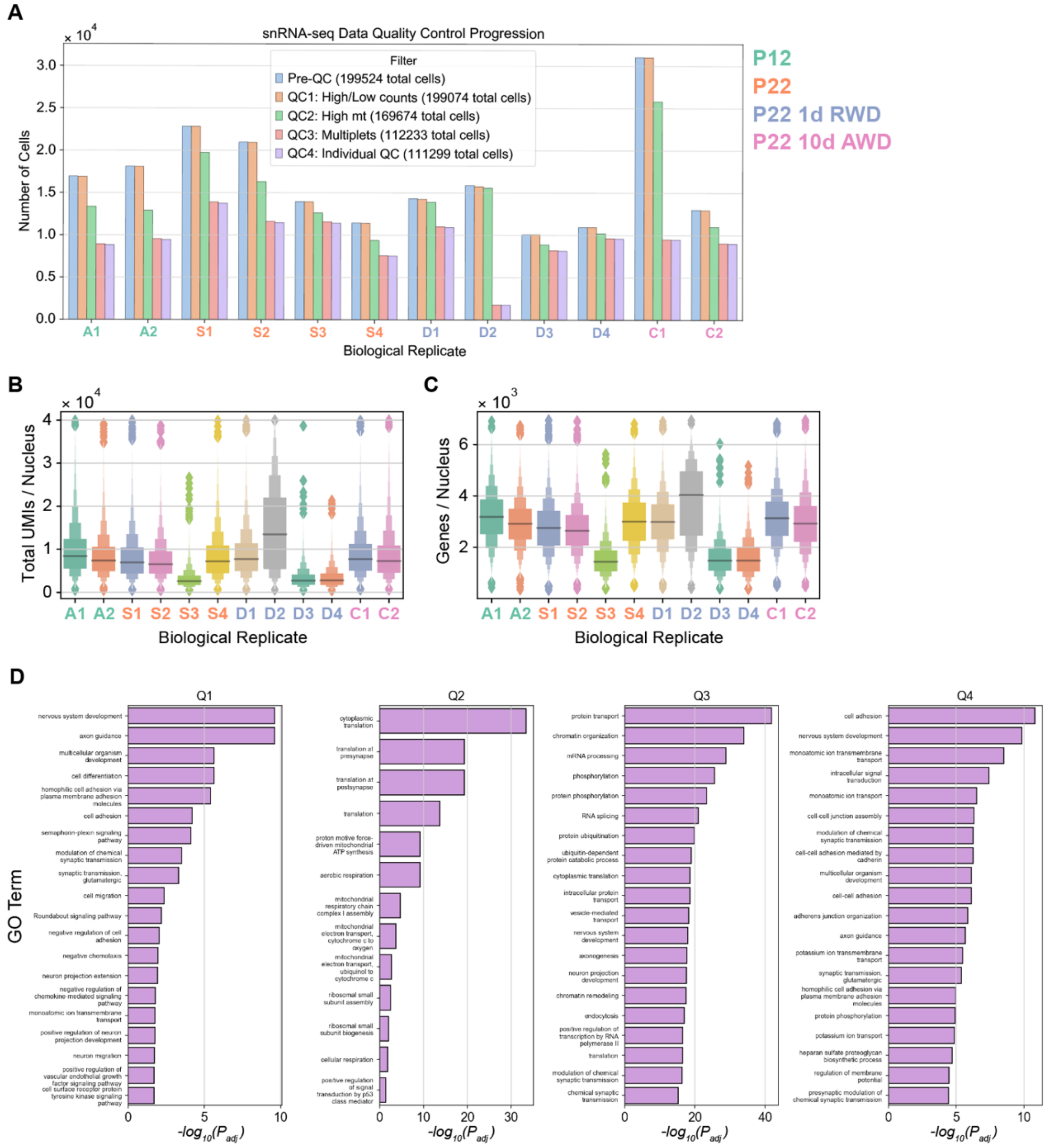

Figure S5.1. Data filtering steps, quality control, and gene ontology (GO) analysis of temporally regulated genes.

A. Bar plots showing the number of nuclei remaining in each biological replicate at the end of each filtering step (see **Methods** for details). Biological replicates (x-axis) are colored by their experimental condition (legend, right). "PreQC" represents the default number of nuclei the 10X CellRanger software provides. "QC4" represents the final set of nuclei used for downstream analyses.
B. Distribution of total RNA counts detected in each biological replicate from each condition.
C. Distribution of total number of genes detected in each biological replicate from each condition.
D. The top 20 "biological process" gene ontology terms for Q1-Q4 for glutamatergic subclasses as shown in **Figure 5.2D**.

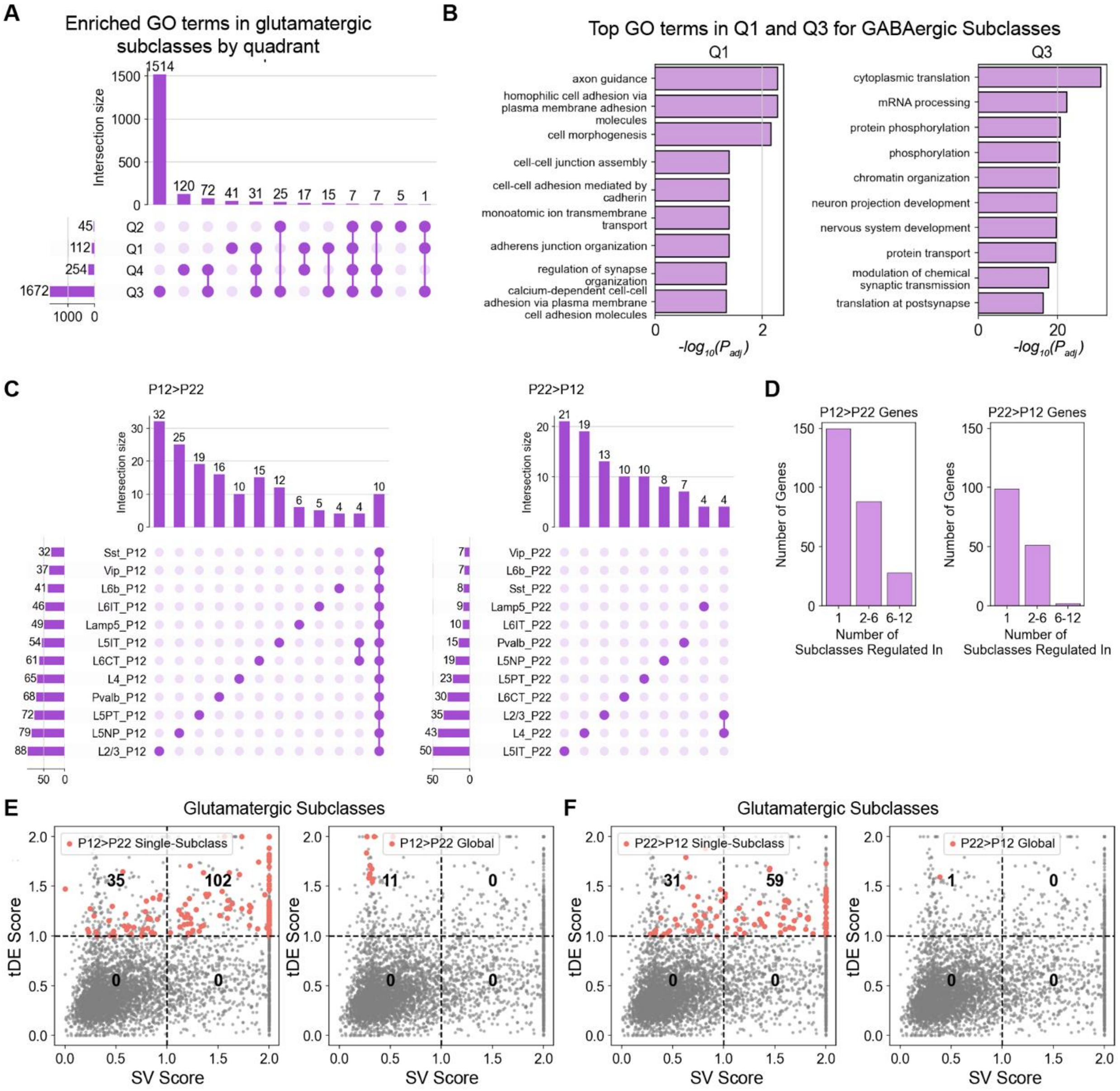

Figure S5.2. Developmental gene expression changes are subclass-specific.

A. UpSet plot (Lex et al., 2014) showing the overlap of GO terms associated with “biological process” (BP) across Q1-Q4 for glutamatergic neuronal subclasses. The lower panel indicates the set intersections corresponding to each column (e.g. the third column indicates the number of GO terms found in Q3 and Q4, but not in Q1 and Q2).
B. Top GO terms enriched in Q1 (*left*) and Q3 (*right*) for GABAergic neuronal subclasses.
C. UpSet plots showing that downregulated (*left*) and upregulated (*right*) tDE genes between P12 and P22 are primarily subclass-specific. Only set intersections containing at least four genes are shown. Note that, unlike panel A, the sets here correspond to groups of subclasses rather than groups of quadrants.
D. Bar plots summarizing that ~60% of genes are regulated in only one subclass and that the number of downregulated genes is ~1.6x that of upregulated genes.
E. Visualization of the subclass-specific and global P12>P22 genes from panel A in the quadrant analysis of **Figure 5.2B** for glutamatergic neurons.
F. Same as panel E for P22>P12 genes.

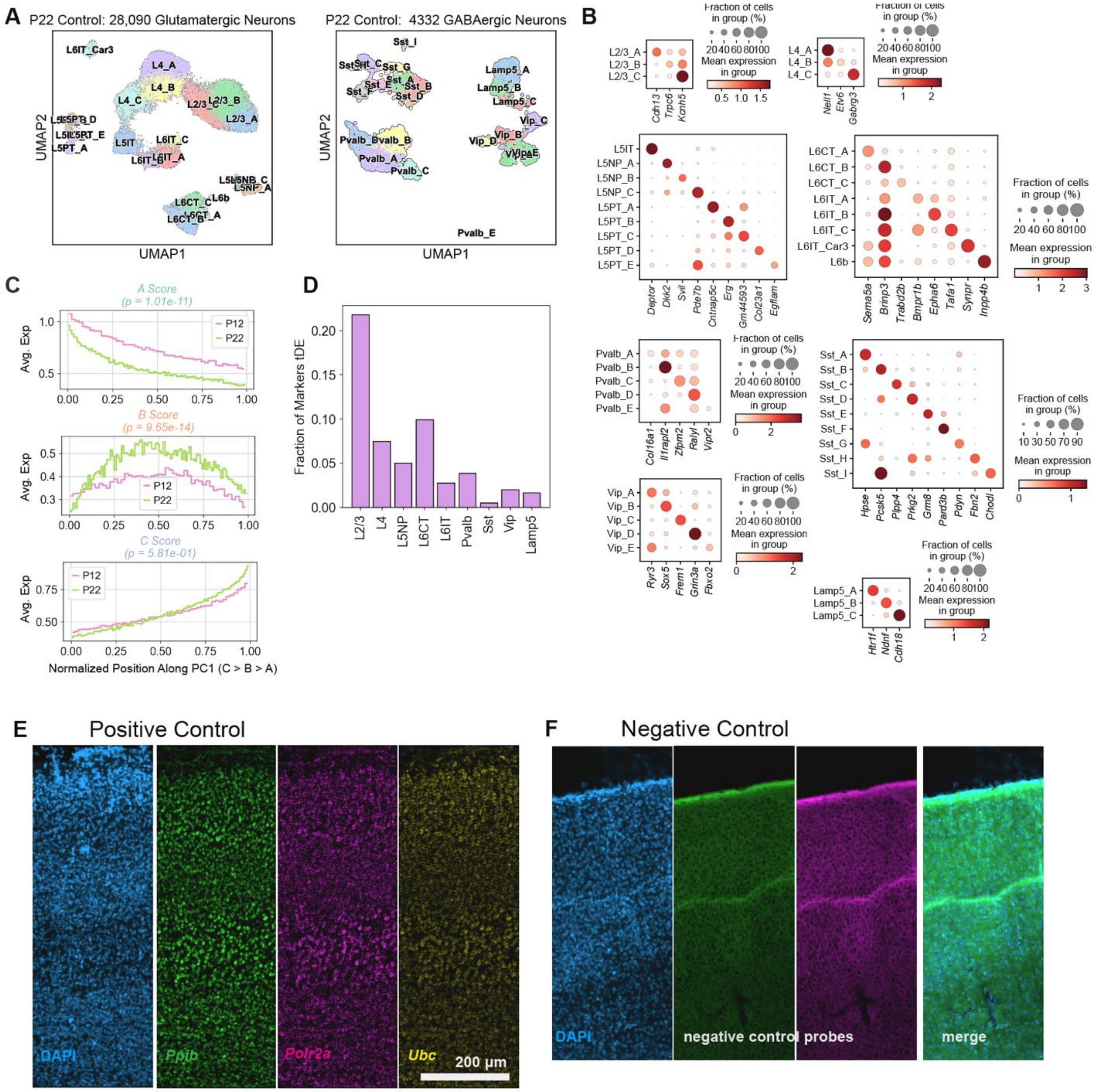

Figure S5.3. **Neuronal cell types at P22 and developmental changes.**

A. UMAP visualization of P22 wS1 cell types in glutamatergic (left) and GABAergic (right) neurons.
B. Dotplots showing top cell type markers within each subclass at P22. Within each dotplot panel, rows indicate cell types and columns indicate genes. The size of each circle corresponds to the % of cells with nonzero expression, and the color indicates average expression level.
C. Same as **Figure 5.4A**, but the y-axis now plots aggregate expression scores for_L2/3_A, L2/3_B, and L2/3_C along PC1. Curves correspond to P12 and P22. *P*-values are from a Kolmogorov–Smirnov test between the two ages.
D. Barplot showing that L2/3 has more markers that are tDE between P12 and P22 than the other subclasses.
E. Representative widefield images of RNAscope positive control showing expected labeling pattern.
F. Representative widefield images of RNAscope negative control using nontargeting probes showing no signal as expected.

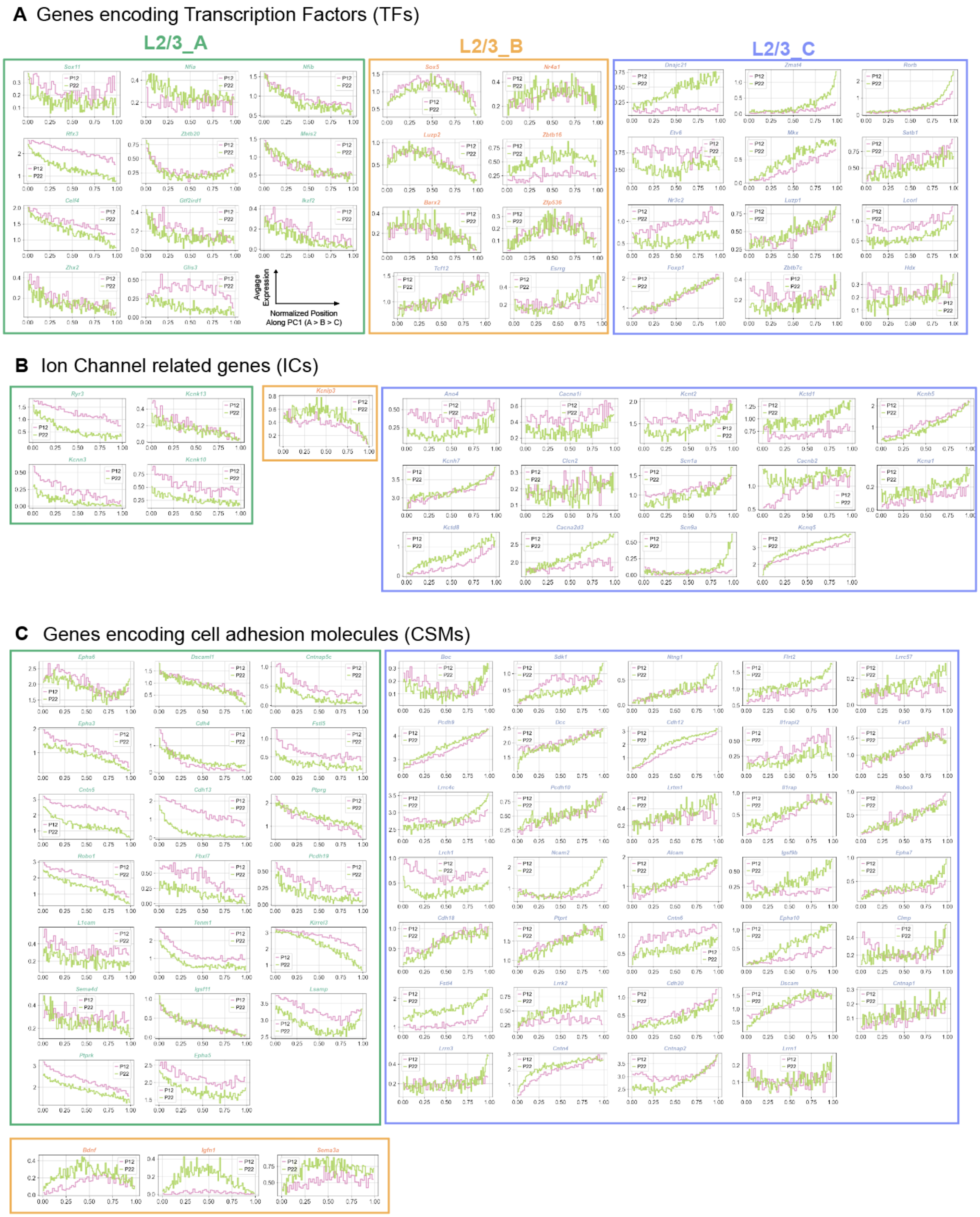

Figure S5.4. **Expression patterns at P12 and P22 along PC1 of L2/3 type-enriched genes related to transcription factors (TFs), cell adhesion molecules (CAMs), and ion channels (ICs).**

A. Expression patterns of type-enriched TFs at P12 and P22 in L2/3 cells ordered by PC1 value.
B. Same as A for ICs
C. Same as A for CAMs

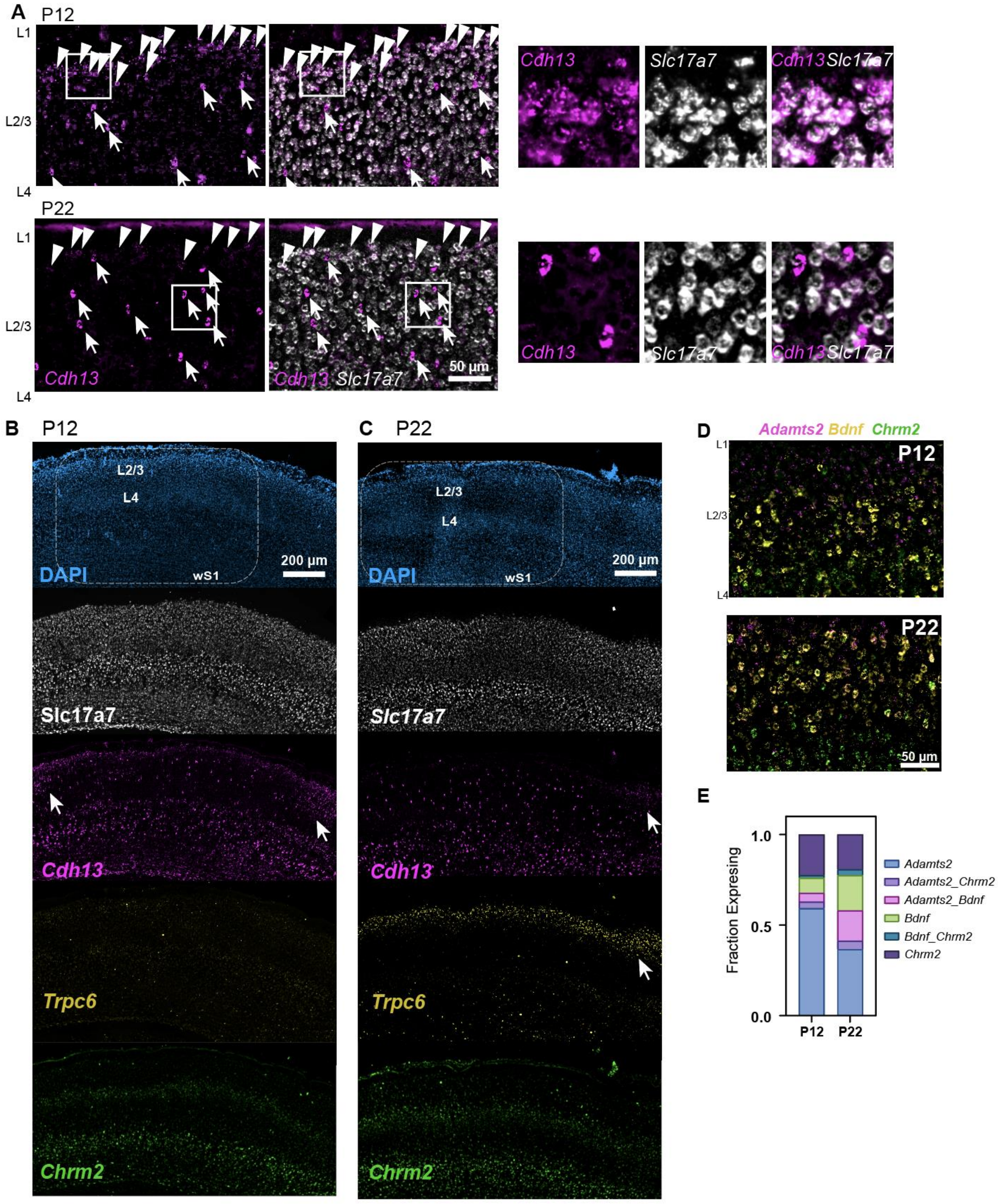

Figure S5.5. **Representative FISH images of L2/3 cell type markers.**

A. Representative images of *Cdh13* labeling at P12 (top row) and P22 (bottom row). Overlay with *Slc17a7* (vGlut1) shows that the majority of *Cdh13* expressing cells in the middle of L2/3 do not colocalize with

Slc17a7 (white arrows) whereas the *Cdh13+* cells along the Layer 1/2 border do coexpress *Slc17a7* (white arrowheads). (right) Inset from area inside white squares.

B. Widefield images of 'across-row' section (see Methods for details) with wS1 and surrounding cortical areas at P12. Arrows indicate cortical regions outside of wS1 where labeling becomes denser.

C. Widefield images of 'across-row' section with wS1 and surrounding cortical areas at P22. Arrows indicate cortical regions outside of S1 where labeling becomes denser.

D. Representative FISH images of wS1 L2/3 labeling cell type markers *Adamts2, Bdnf,* and *Chrm2* at P12 and P22.

E. Quantification of the fraction of excitatory (*Slc17a7+*, not shown) L2/3 cells expressing one or more of markers *Adamts2*, *Bdnf*, and *Chrm2* at P12 and P22. N = 3-4 slices from 2 mice per time point.

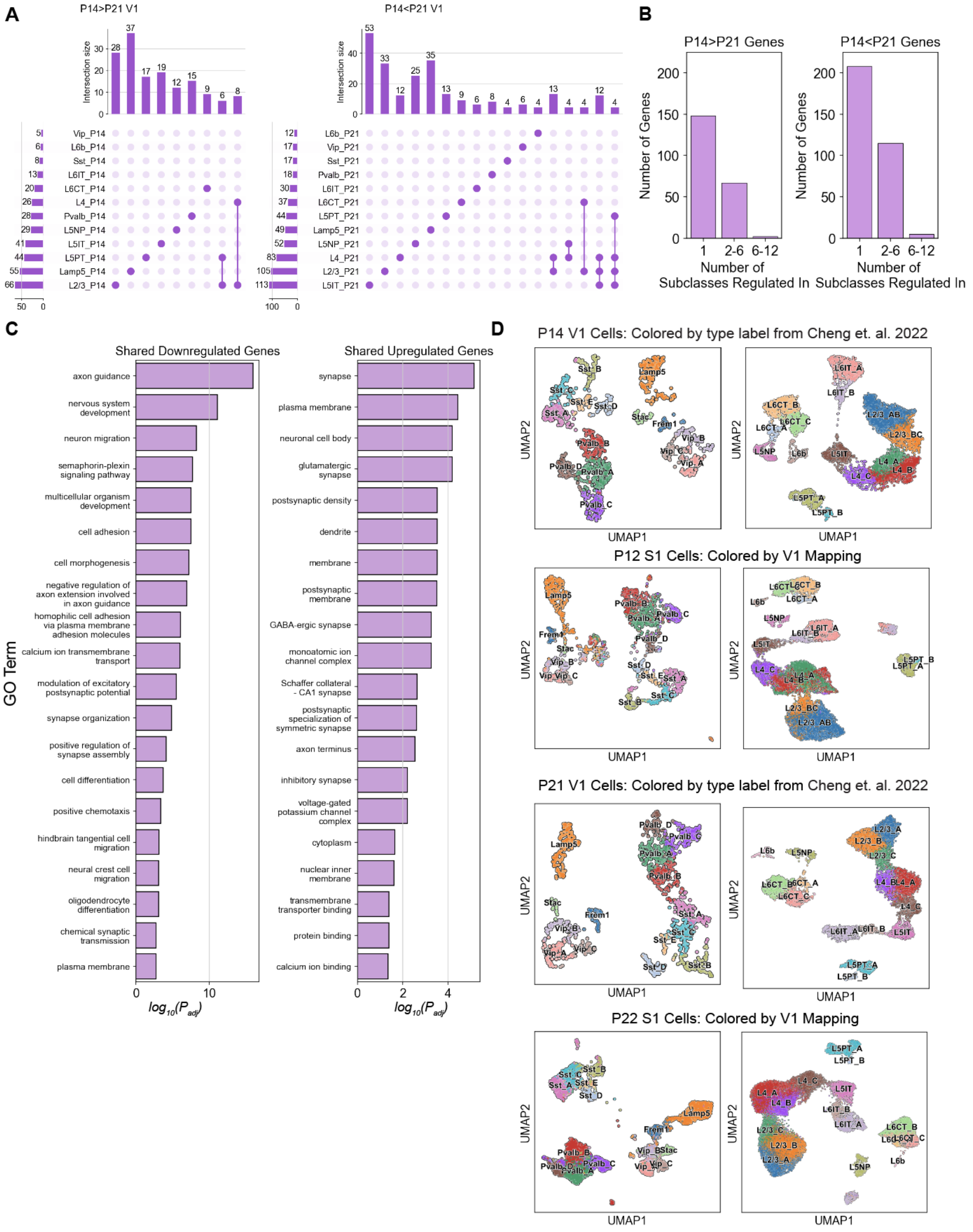

Figure S5.6. **Temporal gene expression changes in V1, GO enrichment for shared and region-specific genes, and mapping analysis.**

A. UpSet plot (as in **Figure S5.2C**) summarizing subclass-by-subclass tDE analysis of V1 data. Only combinations containing at least four genes are shown.
B. Barplots showing that as in the case of wS1 (**Figure S5.2D**), most downregulated (*left*) and upregulated (*right*) genes in V1 are subclass-specific.
C. Full list of GO terms enriched in shared downregulated (*left*) or upregulated (*right*) tDE genes between V1 and wS1.
D. UMAP plots of V1 (rows 1 and 3) and wS1 (rows 2 and 4) data colored by V1 labels. V1 neuron labels are based on the published clustering in Cheng et al. (Cheng et al., 2022), while wS1 neurons were labeled using a supervised mapping analysis (see **Methods**).

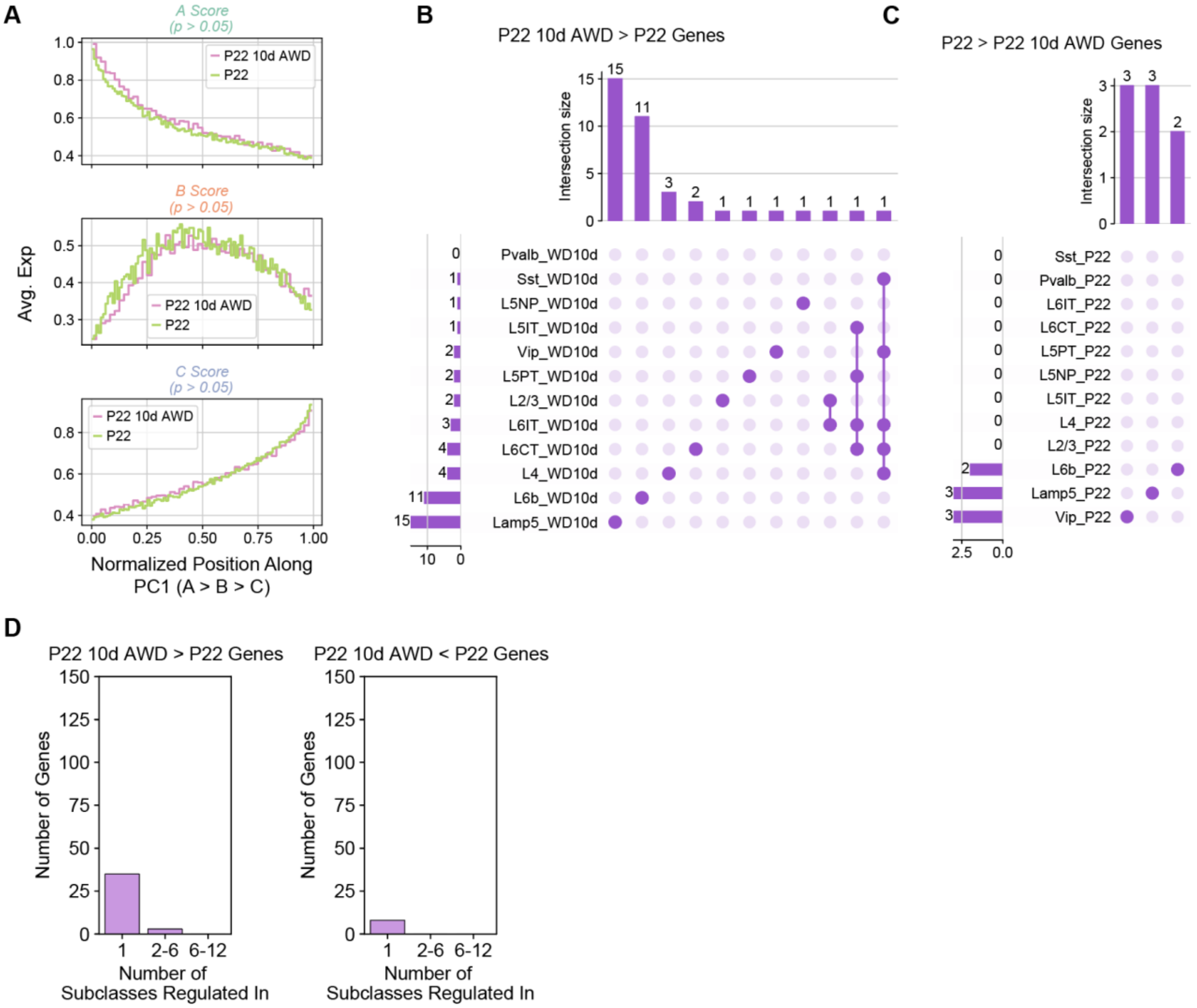

Figure S5.7. **Subclass-level gene expression changes between P22 10d AWD and P22 control.**

A. L2/3 type A, B, and C marker scores plotted as a function of a cell's position along PC1. *P* values are based on a Kolmogorov–Smirnov test comparing the two conditions.
B. UpSet plots showing that the few genes upregulated by 10d AWD are predominantly subclass-specific.
C. Same as B but for genes downregulated by 10d AWD.
D. Bar plots highlighting the small number of genes regulated by 10d AWD. Scale for y-axis is the same as for **Figure S5.2D** for comparison.

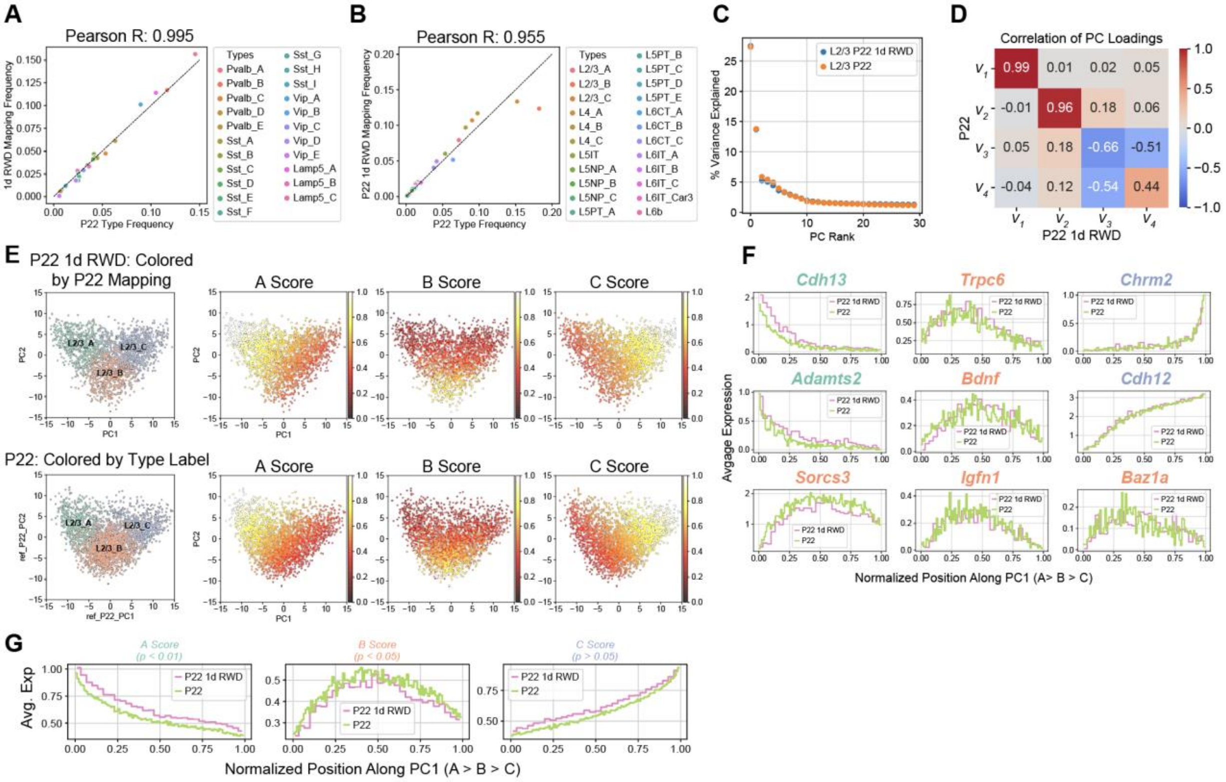

Figure S5.8. **1d RWD has little effect on L2/3 cell type identity.**

A. GABAergic cell types have approximately the same relative frequency at P22 1d RWD and P22 normal whisker experience. Representation as in **Figure 5.6A**.
B. Same as panel A, for glutamatergic cell types.
C. PC1 and PC2 are sufficient to describe transcriptional variance within L2/3 in the normal P22 and P22 10d AWD datasets
D. Similar to **Figure 5.6D,** comparing principal eigenvectors between the P22 1d RWD and normal P22 datasets. The first two principal eigenvectors map 1:1.
E. Similar to **Figure 5.6E** comparing the PC1 vs. PC2 distribution and type-specific scores between P22 1d RWD and normal P22 L2/3 datasets.
F. L2/3 markers genes, as in **Figure 5.4A**, are shown as a function of cells' position along PC1 comparing patterns between normal P22 and P22 1d RWD.
G. L2/3 type A, B, and C marker scores plotted as a function of a cell's position along PC1. *P* values are from a Kolmogorov–Smirnov test between the two conditions.

Table Legends

Table S5.1. tDE and SV scores for every tested gene in glutamatergic and GABAergic neurons.

Table S5.2. Subclass-by-subclass differential expression testing results between P12 and P22.

Table S5.3. Cell type markers from each subclass at P22.

Table S5.4. Subclass-by-subclass differential expression testing results between P14 and P21 V1 data.

Table S5.5. Subclass-by-subclass differential expression testing results between P22 10d AWD and P22

Table S5.6. Subclass-by-subclass differential expression testing results between P22 1d RWD and P22

References

Adler, M., Korem Kohanim, Y., Tendler, A., Mayo, A., Alon, U., 2019. Continuum of Gene-Expression Profiles Provides Spatial Division of Labor within a Differentiated Cell Type. Cell Syst 8, 43-52.e5. https://doi.org/10.1016/j.cels.2018.12.008

Agmon, A., Yang, L.T., O'Dowd, D.K., Jones, E.G., 1993. Organized growth of thalamocortical axons from the deep tier of terminations into layer IV of developing mouse barrel cortex. J Neurosci 13, 5365–5382. https://doi.org/10.1523/JNEUROSCI.13-12-05365.1993

Allen, C.B., Celikel, T., Feldman, D.E., 2003. Long-term depression induced by sensory deprivation during cortical map plasticity in vivo. Nat Neurosci 6, 291–299. https://doi.org/10.1038/nn1012

Audette, N.J., Urban-Ciecko, J., Matsushita, M., Barth, A.L., 2018. POm Thalamocortical Input Drives Layer-Specific Microcircuits in Somatosensory Cortex. Cereb Cortex 28, 1312–1328. https://doi.org/10.1093/cercor/bhx044

Bading, H., 2013. Nuclear calcium signalling in the regulation of brain function. Nat Rev Neurosci 14, 593–608. https://doi.org/10.1038/nrn3531

Becht, E., McInnes, L., Healy, J., Dutertre, C.-A., Kwok, I.W.H., Ng, L.G., Ginhoux, F., Newell, E.W., 2019. Dimensionality reduction for visualizing single-cell data using UMAP. Nat Biotechnol 37, 38–44. https://doi.org/10.1038/nbt.4314

Carpenter, A.E., Jones, T.R., Lamprecht, M.R., Clarke, C., Kang, I.H., Friman, O., Guertin, D.A., Chang, J.H., Lindquist, R.A., Moffat, J., Golland, P., Sabatini, D.M., 2006. CellProfiler: image analysis software for identifying and quantifying cell phenotypes. Genome Biology 7, R100. https://doi.org/10.1186/gb-2006-7-10-r100

Chang, M., Suzuki, N., Kawai, H.D., 2018. Laminar specific gene expression reveals differences in postnatal laminar maturation in mouse auditory, visual, and somatosensory cortex. J Comp Neurol 526, 2257–2284. https://doi.org/10.1002/cne.24481

Chen, T., Guestrin, C., 2016. XGBoost: A Scalable Tree Boosting System. Proceedings of the 22nd ACM SIGKDD International Conference on Knowledge Discovery and Data Mining 785–794. https://doi.org/10.1145/2939672.2939785

Chen, X., Fischer, S., Rue, M.C.P., Zhang, A., Mukherjee, D., Kanold, P.O., Gillis, J., Zador, A.M., 2024. Whole-cortex in situ sequencing reveals input-dependent area identity. Nature 1–10. https://doi.org/10.1038/s41586-024-07221-6

Cheng, S., Butrus, S., Tan, L., Xu, R., Sagireddy, S., Trachtenberg, J.T., Shekhar, K., Zipursky, S.L., 2022. Vision-dependent specification of cell types and function in the developing cortex. Cell 185, 311-327.e24. https://doi.org/10.1016/j.cell.2021.12.022

Chou, S.-J., Babot, Z., Leingärtner, A., Studer, M., Nakagawa, Y., O'Leary, D.D.M., 2013. Geniculocortical Input Drives Genetic Distinctions Between Primary and Higher-Order Visual Areas. Science 340, 1239–1242. https://doi.org/10.1126/science.1232806

Condylis, C., Ghanbari, A., Manjrekar, N., Bistrong, K., Yao, S., Yao, Z., Nguyen, T.N., Zeng, H., Tasic, B., Chen, J.L., 2022. Dense functional and molecular readout of a circuit hub in sensory cortex. Science 375, eabl5981. https://doi.org/10.1126/science.abl5981

Dedifferentiation of Neurons Precedes Tumor Formation in lola Mutants - PMC [WWW Document], n.d. URL https://www.ncbi.nlm.nih.gov/pmc/articles/PMC3978655/ (accessed 9.1.24).

Erzurumlu, R.S., Gaspar, P., 2012. Development and critical period plasticity of the barrel cortex. European Journal of Neuroscience 35, 1540–1553. https://doi.org/10.1111/j.1460-9568.2012.08075.x

Espinosa, J.S., Stryker, M.P., 2012. Development and plasticity of the primary visual cortex. Neuron 75, 230–249. https://doi.org/10.1016/j.neuron.2012.06.009

Feldman, D.E., 2009. Synaptic mechanisms for plasticity in neocortex. Annu Rev Neurosci 32, 33–55. https://doi.org/10.1146/annurev.neuro.051508.135516

Feldman, D.E., Brecht, M., 2005. Map plasticity in somatosensory cortex. Science 310, 810–815. https://doi.org/10.1126/science.1115807

Ferrer, C., De Marco García, N.V., 2022. The Role of Inhibitory Interneurons in Circuit Assembly and Refinement Across Sensory Cortices. Front Neural Circuits 16, 866999. https://doi.org/10.3389/fncir.2022.866999

Finnerty, G.T., Roberts, L.S., Connors, B.W., 1999. Sensory experience modifies the short-term dynamics of neocortical synapses. Nature 400, 367–371. https://doi.org/10.1038/22553

Fox, K., 1992. A critical period for experience-dependent synaptic plasticity in rat barrel cortex. J Neurosci 12, 1826–1838.

Fox, K., Wong, R.O.L., 2005. A Comparison of Experience-Dependent Plasticity in the Visual and Somatosensory Systems. Neuron 48, 465–477. https://doi.org/10.1016/j.neuron.2005.10.013

Gainey, M.A., Aman, J.W., Feldman, D.E., 2018. Rapid Disinhibition by Adjustment of PV Intrinsic Excitability during Whisker Map Plasticity in Mouse S1. J. Neurosci. 38, 4749–4761. https://doi.org/10.1523/JNEUROSCI.3628-17.2018

Golshani, P., Gonçalves, J.T., Khoshkhoo, S., Mostany, R., Smirnakis, S., Portera-Cailliau, C., 2009. Internally mediated developmental desynchronization of neocortical network activity. J Neurosci 29, 10890–10899. https://doi.org/10.1523/JNEUROSCI.2012-09.2009

Gordon, J.A., Stryker, M.P., 1996. Experience-dependent plasticity of binocular responses in the primary visual cortex of the mouse. J Neurosci 16, 3274–3286. https://doi.org/10.1523/JNEUROSCI.16-10-03274.1996

Greenhill, S.D., Ranson, A., Fox, K., 2015. Hebbian and Homeostatic Plasticity Mechanisms in Regular Spiking and Intrinsic Bursting Cells of Cortical Layer 5. Neuron 88, 539–552. https://doi.org/10.1016/j.neuron.2015.09.025

Hensch, T.K., 2005. Critical period plasticity in local cortical circuits. Nat Rev Neurosci 6, 877–888. https://doi.org/10.1038/nrn1787

House, D.R.C., Elstrott, J., Koh, E., Chung, J., Feldman, D.E., 2011. Parallel regulation of feedforward inhibition and excitation during whisker map plasticity. Neuron 72, 819–831. https://doi.org/10.1016/j.neuron.2011.09.008

Hubel, D.H., Wiesel, T.N., LeVay, S., 1977. Plasticity of ocular dominance columns in monkey striate cortex. Philos Trans R Soc Lond B Biol Sci 278, 377–409. https://doi.org/10.1098/rstb.1977.0050

Identification of visual cortex cell types and species differences using single-cell RNA sequencing | Nature Communications [WWW Document], n.d. URL https://www.nature.com/articles/s41467-022-34590-1#Abs1 (accessed 9.1.24).

Jacob, V., Petreanu, L., Wright, N., Svoboda, K., Fox, K., 2012. Regular spiking and intrinsic bursting pyramidal cells show orthogonal forms of experience-dependent plasticity in layer V of barrel cortex. Neuron 73, 391–404. https://doi.org/10.1016/j.neuron.2011.11.034

Jain, S., Lin, Y., Kurmangaliyev, Y.Z., Valdes-Aleman, J., LoCascio, S.A., Mirshahidi, P., Parrington, B., Zipursky, S.L., 2022. A global timing mechanism regulates cell-type-specific wiring programmes. Nature 603, 112–118. https://doi.org/10.1038/s41586-022-04418-5

Jain, S., Zipursky, S.L., 2023. Temporal control of neuronal wiring. Semin Cell Dev Biol 142, 81–90. https://doi.org/10.1016/j.semcdb.2022.05.012

Jézéquel, J., Condomitti, G., Kroon, T., Hamid, F., Sanalidou, S., Garces, T., Maeso, P., Balia, M., Rico, B., 2023. Cadherins orchestrate specific patterns of perisomatic inhibition onto distinct pyramidal cell populations. https://doi.org/10.1101/2023.09.28.559922

Jouhanneau, J.-S., Ferrarese, L., Estebanez, L., Audette, N.J., Brecht, M., Barth, A.L., Poulet, J.F.A., 2014. Cortical fosGFP expression reveals broad receptive field excitatory neurons targeted by POm. Neuron 84, 1065–1078. https://doi.org/10.1016/j.neuron.2014.10.014

Kaliszewska, A., Kossut, M., 2015. Npas4 expression in two experimental models of the barrel cortex plasticity. Neural Plast 2015, 175701. https://doi.org/10.1155/2015/175701

Kandel, Eric R and Schwartz, James H and Jessell, Thomas M, 2000. Principles of neural science. McGraw-hill New York.

Kim, M.-H., Znamenskiy, P., Iacaruso, M.F., Mrsic-Flogel, T.D., 2018. Segregated Subnetworks of Intracortical Projection Neurons in Primary Visual Cortex. Neuron 100, 1313-1321.e6. https://doi.org/10.1016/j.neuron.2018.10.023

Klopfenstein, D.V., Zhang, L., Pedersen, B.S., Ramírez, F., Warwick Vesztrocy, A., Naldi, A., Mungall, C.J., Yunes, J.M., Botvinnik, O., Weigel, M., Dampier, W., Dessimoz, C., Flick, P., Tang, H., 2018. GOATOOLS: A Python library for Gene Ontology analyses. Sci Rep 8, 10872. https://doi.org/10.1038/s41598-018-28948-z

Kole, K., Komuro, Y., Provaznik, J., Pistolic, J., Benes, V., Tiesinga, P., Celikel, T., 2017a. Transcriptional mapping of the primary somatosensory cortex upon sensory deprivation. GigaScience 6, gix081. https://doi.org/10.1093/gigascience/gix081

Kole, K., Lindeboom, R.G.H., Baltissen, M.P.A., Jansen, P.W.T.C., Vermeulen, M., Tiesinga, P., Celikel, T., 2017b. Proteomic landscape of the primary somatosensory cortex upon sensory deprivation. GigaScience 6, gix082. https://doi.org/10.1093/gigascience/gix082

Kurmangaliyev, Y.Z., Yoo, J., Valdes-Aleman, J., Sanfilippo, P., Zipursky, S.L., 2020. Transcriptional Programs of Circuit Assembly in the Drosophila Visual System. Neuron 108, 1045-1057.e6. https://doi.org/10.1016/j.neuron.2020.10.006

Lendvai, B., Stern, E.A., Chen, B., Svoboda, K., 2000. Experience-dependent plasticity of dendritic spines in the developing rat barrel cortex in vivo. Nature 404, 876–881. https://doi.org/10.1038/35009107

Lenneberg, E.H., 1967. Biological foundations of language. Wiley, New York.

Lex, A., Gehlenborg, N., Strobelt, H., Vuillemot, R., Pfister, H., 2014. UpSet: Visualization of Intersecting Sets. IEEE Transactions on Visualization and Computer Graphics 20, 1983–1992. https://doi.org/10.1109/TVCG.2014.2346248

Li, L., Gainey, M.A., Goldbeck, J.E., Feldman, D.E., 2014. Rapid homeostasis by disinhibition during whisker map plasticity. Proc Natl Acad Sci U S A 111, 1616–1621. https://doi.org/10.1073/pnas.1312455111

Maravall, M., Stern, E.A., Svoboda, K., 2004. Development of intrinsic properties and excitability of layer 2/3 pyramidal neurons during a critical period for sensory maps in rat barrel cortex. J Neurophysiol 92, 144–156. https://doi.org/10.1152/jn.00598.2003

Margolis, D.J., Lütcke, H., Schulz, K., Haiss, F., Weber, B., Kügler, S., Hasan, M.T., Helmchen, F., 2012. Reorganization of cortical population activity imaged throughout long-term sensory deprivation. Nat Neurosci 15, 1539–1546. https://doi.org/10.1038/nn.3240

Motulsky, H.J., Brown, R.E., 2006. Detecting outliers when fitting data with nonlinear regression – a new method based on robust nonlinear regression and the false discovery rate. BMC Bioinformatics 7, 123. https://doi.org/10.1186/1471-2105-7-123

Özel, M.N., Simon, F., Jafari, S., Holguera, I., Chen, Y.-C., Benhra, N., El-Danaf, R.N., Kapuralin, K., Malin, J.A., Konstantinides, N., Desplan, C., 2021. Neuronal diversity and convergence in a visual system developmental atlas. Nature 589, 88–95. https://doi.org/10.1038/s41586-020-2879-3

Rives-Quinto, N., Komori, H., Ostgaard, C.M., Janssens, D.H., Kondo, S., Dai, Q., Moore, A.W., Lee, C.-Y., 2020. Sequential activation of transcriptional repressors promotes progenitor commitment by silencing stem cell identity genes. eLife 9, e56187. https://doi.org/10.7554/eLife.56187

Rose, T., Jaepel, J., Hübener, M., Bonhoeffer, T., 2016. Cell-specific restoration of stimulus preference after monocular deprivation in the visual cortex. Science 352, 1319–1322. https://doi.org/10.1126/science.aad3358

Sanes, J.R., Zipursky, S.L., 2020. Synaptic Specificity, Recognition Molecules, and Assembly of Neural Circuits. Cell 181, 536–556. https://doi.org/10.1016/j.cell.2020.04.008

Santiago, I.J., Zhang, D., Saras, A., Pontillo, N., Xu, C., Chen, X., Weirauch, M.T., Mistry, M., Ginty, D.D., Pecot, M.Y., Peng, J., 2021. Drosophila Fezf functions as a transcriptional repressor to direct layer-specific synaptic connectivity in the fly visual system. Proc Natl Acad Sci U S A 118, e2025530118. https://doi.org/10.1073/pnas.2025530118

Sermet, B.S., Truschow, P., Feyerabend, M., Mayrhofer, J.M., Oram, T.B., Yizhar, O., Staiger, J.F., Petersen, C.C., 2019. Pathway-, layer- and cell-type-specific thalamic input to mouse barrel cortex. eLife 8, e52665. https://doi.org/10.7554/eLife.52665

Sousa, E., Flames, N., 2022. Transcriptional regulation of neuronal identity. Eur J Neurosci 55, 645–660. https://doi.org/10.1111/ejn.15551

Stern, E.A., Maravall, M., Svoboda, K., 2001. Rapid development and plasticity of layer 2/3 maps in rat barrel cortex in vivo. Neuron 31, 305–315. https://doi.org/10.1016/s0896-6273(01)00360-9

Tasic, B., Yao, Z., Graybuck, L.T., Smith, K.A., Nguyen, T.N., Bertagnolli, D., Goldy, J., Garren, E., Economo, M.N., Viswanathan, S., Penn, O., Bakken, T., Menon, V., Miller, J., Fong, O., Hirokawa, K.E., Lathia, K., Rimorin, C., Tieu, M., Larsen, R., Casper, T., Barkan, E., Kroll, M., Parry, S., Shapovalova, N.V., Hirschstein, D., Pendergraft, J., Sullivan, H.A., Kim, T.K., Szafer, A., Dee, N., Groblewski, P., Wickersham, I., Cetin, A., Harris, J.A., Levi, B.P., Sunkin, S.M., Madisen, L., Daigle, T.L., Looger, L., Bernard, A., Phillips, J., Lein, E., Hawrylycz, M., Svoboda, K., Jones, A.R., Koch, C., Zeng, H., 2018. Shared and distinct transcriptomic cell types across neocortical areas. Nature 563, 72–78. https://doi.org/10.1038/s41586-018-0654-5

Traag, V.A., Waltman, L., van Eck, N.J., 2019. From Louvain to Leiden: guaranteeing well-connected communities. Sci Rep 9, 5233. https://doi.org/10.1038/s41598-019-41695-z

Vallès, A., Boender, A.J., Gijsbers, S., Haast, R.A.M., Martens, G.J.M., de Weerd, P., 2011. Genomewide analysis of rat barrel cortex reveals time- and layer-specific mRNA expression changes related to experience-dependent plasticity. J Neurosci 31, 6140–6158. https://doi.org/10.1523/JNEUROSCI.6514-10.2011

Weiler, S., Guggiana Nilo, D., Bonhoeffer, T., Hübener, M., Rose, T., Scheuss, V., 2023. Functional and structural features of L2/3 pyramidal cells continuously covary with pial depth in mouse visual cortex. Cerebral Cortex 33, 3715–3733. https://doi.org/10.1093/cercor/bhac303

Weiler, S., Nilo, D.G., Bonhoeffer, T., Hübener, M., Rose, T., Scheuss, V., 2021. Functional and structural features of L2/3 pyramidal cells continuously covary with pial depth in mouse visual cortex. https://doi.org/10.1101/2021.10.13.464276

Wen, J.A., Barth, A.L., 2011. Input-specific critical periods for experience-dependent plasticity in layer 2/3 pyramidal neurons. J Neurosci 31, 4456–4465. https://doi.org/10.1523/JNEUROSCI.6042-10.2011

West, A.E., Greenberg, M.E., 2011. Neuronal Activity–Regulated Gene Transcription in Synapse Development and Cognitive Function. Cold Spring Harb Perspect Biol 3, a005744. https://doi.org/10.1101/cshperspect.a005744

Wolf, F.A., Angerer, P., Theis, F.J., 2018. SCANPY: large-scale single-cell gene expression data analysis. Genome Biology 19, 15. https://doi.org/10.1186/s13059-017-1382-0

Wolock, S.L., Lopez, R., Klein, A.M., 2019. Scrublet: Computational Identification of Cell Doublets in Single-Cell Transcriptomic Data. Cell Syst 8, 281-291.e9. https://doi.org/10.1016/j.cels.2018.11.005

Xavier, A.M., Lin, Q., Kang, C.J., Cheadle, L., 2024. A single-cell transcriptomic atlas of sensory-dependent gene expression in developing mouse visual cortex. https://doi.org/10.1101/2024.06.25.600673

Xie, F., Jain, S., Butrus, S., Shekhar, K., Zipursky, S.L., 2023. Vision sculpts a continuum of L2/3 cell types in the visual cortex during the critical period. bioRxiv 2023.12.18.572244. https://doi.org/10.1101/2023.12.18.572244

Yao, Z., van Velthoven, C.T.J., Kunst, M., Zhang, M., McMillen, D., Lee, C., Jung, W., Goldy, J., Abdelhak, A., Aitken, M., Baker, K., Baker, P., Barkan, E., Bertagnolli, D., Bhandiwad, A., Bielstein, C., Bishwakarma, P., Campos, J., Carey, D., Casper, T., Chakka, A.B., Chakrabarty, R., Chavan, S., Chen, M., Clark, M., Close, J., Crichton, K., Daniel, S., DiValentin, P., Dolbeare, T., Ellingwood, L., Fiabane, E., Fliss, T., Gee, J., Gerstenberger, J., Glandon, A., Gloe, J., Gould, J., Gray, J., Guilford, N., Guzman, J., Hirschstein, D., Ho, W., Hooper, M., Huang, M., Hupp, M., Jin, K., Kroll, M., Lathia, K., Leon, A., Li, S., Long, B., Madigan, Z., Malloy, J., Malone, J., Maltzer, Z., Martin, N., McCue, R., McGinty, R., Mei, N., Melchor, J., Meyerdierks, E., Mollenkopf, T., Moonsman, S., Nguyen, T.N., Otto, S., Pham, T., Rimorin, C., Ruiz, A., Sanchez, R., Sawyer, L., Shapovalova, N., Shepard, N., Slaughterbeck, C., Sulc, J., Tieu, M., Torkelson, A., Tung, H., Valera Cuevas, N., Vance, S., Wadhwani, K., Ward, K., Levi, B., Farrell, C., Young, R., Staats, B., Wang, M.-Q.M., Thompson, C.L., Mufti, S., Pagan, C.M., Kruse, L., Dee, N., Sunkin, S.M., Esposito, L., Hawrylycz, M.J., Waters, J., Ng, L., Smith, K., Tasic, B., Zhuang, X., Zeng, H., 2023. A high-resolution transcriptomic and spatial atlas of cell types in the whole mouse brain. Nature 624, 317–332. https://doi.org/10.1038/s41586-023-06812-z

Yao, Z., van Velthoven, C.T.J., Nguyen, T.N., Goldy, J., Sedeno-Cortes, A.E., Baftizadeh, F., Bertagnolli, D., Casper, T., Chiang, M., Crichton, K., Ding, S.-L., Fong, O., Garren, E., Glandon, A., Gouwens, N.W., Gray, J., Graybuck, L.T., Hawrylycz, M.J., Hirschstein, D., Kroll, M., Lathia, K., Lee, C., Levi, B., McMillen, D., Mok, S., Pham, T., Ren, Q., Rimorin, C., Shapovalova, N., Sulc, J., Sunkin, S.M., Tieu, M., Torkelson, A., Tung, H., Ward, K., Dee, N., Smith, K.A., Tasic, B., Zeng, H., 2021. A taxonomy of transcriptomic cell types across the isocortex and hippocampal formation. Cell 184, 3222-3241.e26. https://doi.org/10.1016/j.cell.2021.04.021

Yayon, N., Amsalem, O., Zorbaz, T., Yakov, O., Dubnov, S., Winek, K., Dudai, A., Adam, G., Schmidtner, A.K., Tessier-Lavigne, M., Renier, N., Habib, N., Segev, I., London, M., Soreq, H., 2023. High-throughput morphometric and transcriptomic profiling uncovers composition of naïve and sensory-deprived cortical cholinergic VIP/CHAT neurons. The EMBO Journal 42, e110565. https://doi.org/10.15252/embj.2021110565

Zhang, M., Pan, X., Jung, W., Halpern, A.R., Eichhorn, S.W., Lei, Z., Cohen, L., Smith, K.A., Tasic, B., Yao, Z., Zeng, H., Zhuang, X., 2023. Molecularly defined and spatially resolved cell atlas of the whole mouse brain. Nature 624, 343–354. https://doi.org/10.1038/s41586-023-06808-9

Chapter 5 Conclusions and Future Directions

The interaction between innate biological processes and external influences in shaping organisms has been contemplated for centuries. Recent technological advances in microscopy, electrophysiology, and genetics have deepened our understanding of experience-dependent plasticity (EDP) in the brain. However, the interaction between genetically programmed development and sensory experience was explored with methods that lacked the ability to fully consider the brain's massive diversity of cell types. Early research focused on measuring individual neurons with probes or populations of neurons with microscopy. The advent of next-generation sequencing marked a shift, allowing high-throughput profiling of cellular molecular content. This thesis introduces a new approach—examining EDP through the lens of cell types as a fundamental unit. It provides both experimental and computational frameworks to do so, supported by validated neuroscience findings. With a clearer understanding of how the mouse retina, visual cortex, and somatosensory cortex develop in experience-dependent and independent ways, the work in this thesis sets the foundation for future research that can build upon these findings.

The role of vision in the maturation of mouse retinal ganglion cell types

The development of neurons, their differentiation into distinct types, and their integration into information processing circuits all result from hard-wired genetically encoded programs that are modified by neural activity. Both genetic and activity-dependent modes of development rely on molecular mediators, but our knowledge of their identities is incomplete for the former and rudimentary at best for the latter. Mouse RGCs are well suited for addressing these open questions for several reasons: (i) their structure, function and development have been studied in detail; (2) they comprise a neuronal class that has been divided into several subclasses and numerous (~45) types, enabling analysis at multiple levels; and (3) methods are available for manipulating the sensory input they receive and thereby the patterns of activity they experience. Our method was scRNA-seq, which enables comprehensive classification of neuronal cell types, and their mapping across developmental stages and experimental conditions. By profiling RGCs at multiple developmental ages, we were able to map the changing transcriptional landscape of RGCs as they develop from embryonic stages to adulthood. By profiling adult RGCs that had been visually deprived in three different ways, we showed that vision is not required for full diversification of RGCs into subclasses and types but does affect cell type distinctness and patterns of gene expression in both global and type-specific ways. Our results can serve as a starting point for screening and assessing key molecular mediators of activity-independent and -dependent patterning of RGC development.

The fact that we find minimal influence of visual deprivation on RGC diversification may be in line with Hubel and Wiesel's findings in monkeys. In their seminal monocular deprivation experiments, they found that retinal ganglion cells in the deprived eye, as well as neurons in the lateral geniculate nucleus that receive input from the deprived eye, responded well to visual stimuli and had essentially normal receptive fields (Hubel et al., 1977). While vision-based activity may not be involved in cell type diversification, the role of spontaneous activity *via* retinal waves remains unknown. It is known that waves of spontaneous retinal activity propagate throughout the entire visual system before eye opening and carry patterned information, guiding activity-dependent development of complex intra- and inter-hemispheric circuits before image-forming vision begins (Ackman et al., 2012). Several mouse knockout approaches exist for disrupting waves at various time points in the first two weeks of development (Ford and Feller, 2012). It would be interesting to profile RGC cell types in these mouse models to gain a more complete understanding of how other sources of activity in the visual system such as spontaneous waves contribute to transcriptomic cell type diversification and maturation. Since retinal waves predominantly occur between P0 and P15, and this is the time when RGC diversification is nearing completion (Shekhar et al., 2022), a lack of waves could lead to an incomplete diversification of RGCs. Moreover, a less-characterized earlier stage of retinal waves occurs between embryonic (E16) day 16 and P0 (Voufo et al., 2023). If disrupting postnatal waves does not affect cell type diversification, it would be reasonable to study the influence of these embryonic retinal waves on RGC diversification.

While scRNA-seq has provided valuable insights into the transcriptional patterns underlying RGC diversification and maturation under different conditions, regulatory mechanisms driving these changes remain unknown. To bridge this gap, it is crucial to now perform upstream measurements, such as scATAC-seq, to explore the chromatin landscape that dictates gene expression patterns during RGC development. scATAC-seq allows us to map accessible chromatin regions, identifying active regulatory elements like enhancers and promoters that are likely driving the gene expression programs observed in the scRNA-seq data (Finkbeiner et al., 2022). Integrating the two modalities would help in elucidating how specific patterns of neural activity, including spontaneous retinal waves, influence chromatin accessibility and, consequently, gene expression during critical periods of RGC development. Moreover, comparing ATAC-seq profiles between normally developed RGCs and those from visually deprived or retinal wave-disrupted models could reveal key regulatory elements whose activity is modulated by different forms of neural activity. This would provide a more comprehensive understanding of the activity-dependent and independent mechanisms that shape RGC diversification and maturation, offering new targets for further functional studies. Incorporating these upstream measurements will enable us to uncover the underlying regulatory processes that guide these critical developmental changes. This shift in focus is essential for a more complete understanding of the molecular underpinnings of retinal ganglion cell development and their integration into visual processing circuits.

The interplay between natural development and visual experience in the maturation of cortical cell types

We studied the role of vision in the development of V1 cell types and their circuitry in mice by combining snRNA-seq, statistical inference, sensory perturbations, genetics, and *in vivo* functional imaging. We assembled a developmental transcriptomic atlas of postnatal mouse V1. Using this as a foundation, we discovered that: (1) vision is required for the establishment and maintenance of L2/3 glutamatergic types, but not other cell types in V1; (2) L2/3 glutamatergic cell types are organized as sublayers in V1 and form a transcriptomic continuum through the graded expression of ~200 genes; and (3) among these genes, *Igsf9b*, a vision-regulated cell adhesion molecule, is required in a graded fashion for the functional maturation of L2/3 glutamatergic neurons. Together, our study establishes a framework for future investigations of how experience regulates cell type development in the brain.

Our single-cell sequencing, FISH, and genetic data collectively point to a model where neuronal activity regulates IGSF9B functions within L2/3 excitatory neurons in a graded manner. This aligns with the observed graded expression pattern of *Igsf9b* along the pial-ventricular axis in L2/3. However, given that our *Igsf9b* deletion was systemic, the specific molecular and cellular mechanisms driving the observed phenotype remain to be fully characterized. Future investigations should involve inducible, cell-type-specific knockouts of *Igsf9b* in L2/3 excitatory neurons, as well as in other neuronal populations, to explore the maturation of L2/3 receptive tuning during the critical period. Considering that IGSF9B interacts with NEGR1, a heterophilic ligand expressed in inhibitory neurons (Wojtowicz et al., 2020), genetic studies will be needed to clarify the role of *Negr1* in L2/3 neuron development and to distinguish between the effects of IGSF9B-mediated heterophilic versus homophilic interactions in circuit formation. On a broader scale, comprehensive biochemical, histological, and physiological analyses are essential to determine how IGSF9B contributes to the functional maturation of L2/3 neurons and the development of inhibitory synapses.

Based on our findings, we can speculate that local circuitry within V1, inputs to and from higher visual areas, and inputs from other brain areas may, alone or in combination, sculpt cell type-specific transcriptomes and circuitry gradually and iteratively within different sublayers. These changes, in turn, would alter the circuit properties of neurons (e.g., their patterns of connections or synaptic function) leading to the establishment of multiple sublayer-specific networks of circuits with distinct functional properties. An initial step towards probing these hypotheses entails profiling the local connectivity of L2/3 neurons, especially during development and as a function of visual input. The knowledge we have established about the spatial and transcriptomic organization of L2/3 neuron types is an ideal launch point for these investigations. For example, one may apply emerging single-cell technologies that simultaneously measure the transcriptomic and connectomic profiles of single cells (Clark et al., 2021; Saunders et al., 2022; Yuan et al., 2024). By using these techniques to profile V1 during development and across rearing conditions, we can answer four key questions about the connectivity of L2/3 neurons. Do transcriptomically distinct cell types possess distinct wiring specificities to other cell types? Are the temporally-regulated cell-surface molecules identified in our study involved in this wiring? Are synaptic interactions of L2/3 cell types organized in a sublayered fashion in the recipient regions? Which interactions are sensitive to visual input? Establishing a molecular understanding of L2/3 connectivity by answering these questions is a prerequisite to understanding how vision sculpts the structure and function of circuits across the visual system.

Beyond local connectivity within V1, L2/3 pyramidal neurons project to 10 higher visual areas (HVAs) for object recognition, processing self-motion cues, and external object motion cues (Andermann et al., 2011; Glickfeld and Olsen, 2017). A study using axonal reconstructions from single neurons and RNA barcode-based mapping (MAPseq) showed that the anterolateral (AL), posteromedial (PM), and lateromedial (LM) areas receive the most projections out of the 10 HVAs (Han et al., 2018). A subsequent study, using retrograde viral tracing, focused on L2/3 neurons projecting to these three HVAs and found that PM-projecting neurons were confined to the pial pole of L2/3 while AL-projecting neurons bordered L4 (Kim et al., 2020). Our smFISH studies revealed that cell type L2/3_A was confined to the pial end of L2/3 while L2/3_C bordered L4, suggesting that L2/3_A projects to AL while L2/3_C projects to PM. Fortunately, the study reported gene markers for the AL- and PM-projecting neurons. When we tested the expression of these markers in our data, we found that AL and PM markers were selectively expressed in L2/3_A and C. These correlations we have established here between transcriptomically distinct cell types and HVA projection patterns warrant further investigation on several fronts. There are 10 HVAs in mouse V1 but we have only identified and tracked the development of three L2/3 pyramidal cell types using snRNA-seq. What explains this discrepancy? Do transcriptomically indistinguishable subsets within these three cell types project to different HVAs? Future work aimed at answering this question will need to inject multiple HVAs with a retrograde virus that then labels L2/3 neurons with a barcode that enables the mapping of gene expression profiles to projection targets. Subsequent studies can integrate other measurements, such as anatomy and physiology, with transcriptomics at different time points to determine the functionally-relevant number of cell types in L2/3 and how they develop. An initial hypothesis to test that would not require any experiments would be to compare the cell types in our study to the cell populations profiled with Patch-seq by the Allen Institute recently (Sorensen et al., 2023) to identify their morphological and physiological characteristics.

Traditional studies of experience-dependent plasticity in V1 analyzed changes in the receptive fields, ocular dominance, or functional characteristics of neurons in response to visual manipulations such as dark rearing or lid suturing. Our work utilizes single-cell transcriptomic profiles to assess the impact of visual deprivation. Thus, we investigate the sensitivity of a cell type's underlying gene expression program to sensory manipulation, which we propose as another facet of neuronal plasticity. While a critical period (CP) for ocular dominance plasticity (ODP) has been established for decades (Gordon and Stryker, 1996), we have yet to determine a critical period for the establishment of transcriptomic cell type identity. Our sensory manipulations were focused on the CP for ODP, which is not general to all brain circuits. Even within V1, the CPs for organization of neural connections differ among cortical layers and among features such as orientation and direction selectivity (Kandel, 2013). Moreover, multiple studies in the last two decades have raised the possibility that visual experience, in combination with spontaneous activity, shapes circuit development in V1 during a "precritical" period (Feller and Scanziani, 2005). The findings of a recent study strongly support this hypothesis by demonstrating that vision is required for the formation of binocular neurons shortly after eye-opening–up to a week prior to the onset of the classical CP (Tan et al., 2021). Given our discovery that cell type identity is sensitive to visual experience, it is important to establish a timeline for this type of plasticity. By dark-rearing mice from birth, exposing them to light for eight hours at P17, then performing snRNA-seq and smFISH, we can answer two key questions. To what degree will brief light exposure prior to the classical CP attenuate the effects of visual deprivation? Are the molecules and cell types involved the same or different from those observed in the P28DL experiment? Answers to these questions will elucidate the timescale for the plasticity of cell type identity in V1. Beyond these early postnatal stages, it would be important to understand if the effect of DR is temporally restricted to the CP discovered from these studies. For example, dark rearing experiments performed on adult mice (>P40) would reveal if dark rearing has no effect at those stages or if its effects are distinct from those observed at earlier stages.

The key finding of our study is that L2/3 pyramidal neurons undergo the most changes during postnatal development and are most sensitive to dark rearing compared to all other neuronal cell types. Several lines of future inquiry can help elucidate the underlying mechanism and teleology. The first line involves the fact that L2/3 neurons are born the latest during cortical neurogenesis compared to L4-L6 (Cooper, 2008). One way to test the link between late neurogenesis and prolonged plasticity in L2/3 neurons is by experimentally manipulating their birth timing. For example, using inducible genetic tools or in utero electroporation, the birth of L2/3 neurons could be delayed or advanced relative to their typical developmental schedule. By comparing the molecular, functional, and plasticity profiles of these neurons to normally timed counterparts, we could directly assess whether late neurogenesis is a key determinant of L2/3's prolonged plasticity and heightened sensitivity to sensory experience. Such experiments would provide mechanistic insights into how developmental timing shapes the unique properties of L2/3 neurons. The second line of inquiry involves the patterns of connectivity between layers. Research in mouse primary whisker somatosensory cortex (wS1) has shown that there are many more connections between L2/3 and 4 excitatory neurons than among L5 and L6 (Hooks and Chen, 2020). Perhaps the higher frequency of connections would require more time to establish and mature, providing one possible reason for the delayed maturation of superficial types. In addition, we know that L2/3 and L4 project from V1 in the intratelencephalic (IT) tract to other cortical regions, while L5 and L6 neurons project mostly back to the thalamus and pyramids (Shepherd and Yamawaki, 2021). Does the nature and complexity of visual processing tasks executed by L2/3 and L4 neurons make their development vision-dependent? Future research would map these projections in the context of the transcriptomic cell types we discovered to answer these questions.

The third line of inquiry could focus on L2/3 evolution. It is known that L2/3 pyramidal neurons have massively expanded during mammalian evolution: both in terms of relative numbers as well as cortico-cortical connectivity (Vanderhaeghen and Polleux, 2023). Furthermore, L2/3 neurons in primates exhibit delayed maturation compared to their rodent counterparts, a property known as neoteny. Could these reasons underlie the greater plasticity and experience-dependence of L2/3 cell types? An exciting project would be to compare V1 cell types from several species covering the last few hundred million years of evolution using single-cell multiomics. This would reveal how the cell types that populate L2/3 in extant mammals evolved and diversified from the common mammalian ancestor and what molecular factors underlie their expansion and neo-functionalization in primates. Such a project would be especially pertinent since a recent study of retinal ganglion cell (RGC) evolution across 17 species identified rodent orthologues of midget RGCs, which comprise more than 80% of RGCs in the human retina, subserve high-acuity vision, and were previously believed to be restricted to primates (Hahn et al., 2023). Projections of both primate and mouse orthologous types are overrepresented in the thalamus, which supplies V1. Molecular studies of V1 evolution would add to this work in the retina and enable us to build a more general theory of visual system evolution (Baden et al., 2020).

The neurons at the center of this study send excitatory signals, but previous studies have highlighted the importance of inhibitory inputs in adult neuronal plasticity (Davis et al., 2015; Lin et al., 2008; Reh et al., 2020). The transcriptomic changes we observed in L2/3 as a function of time and dark rearing must in some way be mediated by inhibitory neurons. We did not find evidence that gene expression in inhibitory neurons was affected by light deprivation, but it is possible that the proteomic, morphological, electrophysiological, or circuit properties of these neurons were modified in ways not detectable by snRNA-seq. Indeed, vision appears to be crucial for parvalbumin (PV) cells to receive excitatory input, while the connectivity of PV cells to pyramidal neurons might represent an intrinsic mechanism (Fang et al., 2021). Although PV cells fail to broaden their orientation tuning in dark-reared (DR) mice—likely due to impaired excitatory input from local neurons—the inhibitory currents recorded in pyramidal neurons continue to strengthen to adult levels even in the absence of visual experience. This suggests that the broadening of tuning is dependent on vision, potentially through vision-dependent factors expressed by PV cells that facilitate their innervation by local pyramidal neurons. For example, the molecular response of inhibitory neurons could be largely post-transcriptional, and would only be detected by performing proteomics or mRNA translation studies using ribosome profiling (VanInsberghe et al., 2021). This could especially be true since a different study found that PV cells exhibit minimal transcriptional changes in response to visual deprivation (Hrvatin et al., 2018). If the deficit observed in DR conditions is primarily due to altered innervation of PV cells by pyramidal neurons, that would explain the transcriptional changes being more pronounced in pyramidal neurons than interneurons.

Gene regulatory networks underlying the development of L2/3 pyramidal neurons in V1

Sensory experience refines an embryonic blueprint of the primary visual cortex (V1), enabling the maturation of functional circuits. Recently, we showed that the transcriptomic and functional identity of layer (L) 2/3 cell types in V1 arises postnatally in a vision-dependent fashion. However, the temporally coordinated interactions between transcription factors (TFs) and enhancers that underlie these transcriptional dynamics are unknown. In a currently ongoing study, we profiled chromatin accessibility and gene expression at single-nucleus resolution within V1 across several time points and light-rearing conditions. We then used computational approaches to infer gene regulatory networks (GRNs) associated with cell type development in V1. We discovered two orthogonal programs that regulate the maturation of a L2/3 continuum consisting of three archetypes. The first is the vision-independent *Rfx3+* program, peaking in activity before eye-opening, and the second is the vision-dependent *Npas4+* program, peaking in activity after eye-opening. Future work should focus on perturbing these programs *in vivo* to assess their roles in various V1 functions.

Our preliminary results show that type L2/3_A initially predominates in frequency (>50% of L2/3 cells). Between P12-P14, the L2/3_B type increases in frequency at the expense of L2/3_A cells. As neurons are postmitotic at this stage with no clear evidence of cell death, these frequency changes are likely due to a redistribution of L2/3_A cells acquiring L2/3_B-like gene expression patterns. By comparison, L2/3_C is relatively stable. The postnatal expansion of L2/3_B-like cells is common to both V1 and wS1, but the functional significance is not clear. Does L2/3_B represent a meaningful functional unit essential for animal behavior, or is it merely an epiphenomenon observed through snRNA-seq? We found that *Rfx3* is selectively expressed in L2/3_A neurons throughout development. The activity of its target regions and genes peaks between P10 and P14, and it predominantly regulates genes and regions that are L2/3_A-specific. One hypothesis motivated by these results is that knocking out *Rfx3* embryonically or during early postnatal development prevents the development of the L2/3_B type. In this scenario, L2/3_A cells may continue to predominate in frequency into later postnatal stages, affecting V1's functional development, including the functional tuning and projection patterns of L2/3 neurons (Kim et al., 2020; Tan et al., 2020). One could also perturb the vision-dependent program, involving TFs such as *Npas4*, *Fosb*, *Fosl2*, and *Fos*. This GRN switches on after eye-opening (P14) and is selective to L2/3_B neurons. The target genes and chromatin regions featured in this program are L2/3-B specific, and both were suppressed by dark-rearing. Therefore, while the intrinsic *Rfx3+* GRN is likely responsible for "preparing" L2/3 for the emergence of L2/3_B, these activity-dependent GRNs form the basis for this new cell state. Perturbing these vision-dependent GRNs would offer an alternative approach to creating a V1 without L2/3_B neurons, providing a way to test for the functional role of this cell type.

Another crucial factor in regulating gene expression during L2/3 pyramidal neuron development could be the protein MeCP2, which binds to methylated cytosine bases in DNA, often found in regions called CpG islands. MeCP2 is known to interpret and translate the epigenetic information encoded in DNA methylation patterns, influencing the structure of chromatin and thereby impacting gene expression (Gulmez Karaca et al., 2019). Disruptions in MeCP2 function are linked to neurodevelopmental disorders, most notably Rett syndrome, which is characterized by severe cognitive and physical impairments due to mutations in the MECP2 gene. A recent study showed that loss of MeCP2 disrupts sublayer-resolved gene programs in L2/3 of V1 (Moore et al., 2024). This disruption is striking similar to what we have observed in dark-reared animals. This result suggests that MeCP2 might be involved in fine-tuning the expression of genes critical for the development and function of L2/3 neurons. Future work should explore the temporal dynamics of MeCP2 binding in L2/3 neurons, particularly in relation to changes in chromatin accessibility observed in our ATAC-seq data. By integrating ChIP-seq data for MeCP2, we can investigate whether regions with high MeCP2 binding show decreased accessibility over time in specific L2/3 cell types, and how this correlates with the development of these cells. Additionally, we could examine the overlap of differentially methylated sites between MeCP2 knockout (KO) and wild-type (WT) neurons with our ATAC peaks to determine how MeCP2-mediated methylation influences gene regulatory networks in V1. Such studies would provide deeper insights into the epigenetic mechanisms underlying sensory experience-dependent development in the cortex.

The role of whisker experience in the maturation of cortical cell types in health and disease

To study experience-dependent wS1 development at the resolution of transcriptomic cell types, we generated an atlas of mouse wS1 containing over 80,000 nuclear transcriptomes spanning two postnatal ages and three rearing conditions. We found that developmental gene expression changes are highly subclass-specific and that L2/3 pyramidal neuron type identity changes dramatically during development. In comparative analyses, developmental gene expression and cell type changes were largely conserved between mouse V1 and wS1. However, whisker experience served a limited role in wS1 cell type development, which is in stark contrast to the strong role of vision in V1 cell type development. Nevertheless, brief whisker deprivation did induce activity-dependent gene expression in a whisker column-specific fashion. The dataset we generated and its associated findings present a variety of exciting avenues for future research

The publicly accessible dataset enables the pursuit of several research directions without the immediate need for experiments. First, future work could use CellChat (Jin et al., 2023) to explore how intercellular communication evolves across developmental stages, conditions, and cell types in this dataset. For example, applying CellChat to L2/3 neurons at P12 and P22 under both 1-day and 10-day deprivation conditions could reveal how specific ligand-receptor interactions are modulated by development and sensory experience. Comparing signaling networks between excitatory and inhibitory populations may highlight shifts in ligand-receptor dynamics during circuit maturation. Integrating results across these variables would ultimately offer a comprehensive model of how developmental timing and sensory experience shape cortical communication networks. Second, future directions could focus on determining whether the observed transcriptomic patterns in this dataset can be explained by underlying gene regulatory networks. Applying Single-Cell Regulatory Network Inference and Clustering (SCENIC) across different neuronal subclasses in both control and whisker deprivation conditions would allow for the comparison of inferred gene regulatory networks (GRNs) between these states (Van de Sande et al., 2020). SCENIC leverages co-expression of genes and transcription factors (TFs) to infer GRNs by integrating scRNA-seq data with TF motif discovery, searching for TF binding sites around co-expressed genes. This analysis could reveal regulatory dynamics driving observed changes and help generate hypotheses about DNA-level mechanisms. For instance, by analyzing L2/3 neurons at P12 and P22, we could infer regulons and visualize their activity to identify persistent and temporally regulated programs. Exploring whether P12 neurons are enriched for TFs related to type specification or comparing regulon expression across cell types and conditions would further clarify the developmental trajectory of these cells.

Our work employed smFISH to validate the cell type-specificity or temporal regulation of select genes nominated by scRNA-seq. To further test the hypotheses generated in this work, future studies should quantify the expression of many genes simultaneously in the same cell as a function of the cell's location, especially in the context of wS1 barrels, using spatial transcriptomics methods across multiple time points and rearing conditions. For example, recent work showed that the barrel cortex contains two distinct L2/3 pyramidal neuron subpopulations: a stable columnar framework of columnar whisker-tuned cells that may promote spatial perceptual stability and an intermixed, non-columnar surround with highly unstable tuning (Wang et al., 2022). It would be interesting to determine if these subpopulations are marked by distinct genes and if they follow similar developmental trajectories. Another study used spatial transcriptomics to identify gene expression patterns distinguishing L4 septal from spiny stellate neurons and their innervation by specific thalamic inputs during development (Young et al., 2023). In the future, by integrating spatial gene expression data with cellular physiology and connectivity patterns, such approaches can reveal how distinct transcriptomic landscapes correspond to specific functional subpopulations, and how these profiles are dynamically regulated by sensory experience.

Furthermore, transcriptomic measurements provide a window into "what" cells are doing (their state) at the time of tissue sampling but do not reveal "how" the cell arrived at that point. Future studies aimed at dissecting patterns at the DNA level, such as chromatin organization and DNA methylation, will reveal the gene regulatory networks responsible for the transcriptomic patterns observed herein. Finally, additional work must be undertaken to assess the findings of our study in the context of neuronal physiology and animal behavior. Experiments labeling specific cell types and surveying their properties using slice electrophysiology will provide a mapping between the types discovered here and their functions and how these change under different experimental conditions. Additionally, 2P imaging of labeled cell types coupled with a whisking-related task would pinpoint the role of these cell types in the context of animal behavior. Ultimately, these studies could bridge the gap between transcriptomic diversity and functional specialization in cortical circuits. One immediate hypothesis to test is whether the cell type-specific expression of *Cdh13* and *Cdh12* we observe in L2/3 pyramidal neurons contributes similarly to inhibitory microcircuit specificity as in L5 IT and ET neurons in wS1 (Jézéquel et al., 2023). A targeted study replicating the L5 analysis in L2/3 neurons could reveal analogous or distinct mechanisms of inhibitory connectivity, shedding light on the broader principles of synaptic organization across cortical layers.

Beyond studying wS1 during typical development, the disrupted organization of neural circuits in wS1 during critical periods (CPs) may underlie the manifestation of neurodevelopmental disorders such as autism (Chen et al., 2020; Llamosas et al., 2021; Michaelson et al., 2018; Zhang et al., 2014, 2021). A long-standing model of autism spectrum disorders (ASDs) is that a cortical increase in synaptic excitation-to-inhibition (E-I) ratio drives hyperexcitability that is hypothesized to potentiate the cognitive and behavioral symptoms of ASD (Nelson and Valakh, 2015; Rubenstein and Merzenich, 2003). A recent study profiled E-I ratio phenotypes in L2/3 neurons of wS1 in four mouse ASD models, including the Fragile X Syndrome *Fmr1* KO (Antoine et al., 2019). Rather than causing circuit hyperexcitability, they found that an increased E-I ratio is a compensatory mechanism that stabilizes synaptic depolarization and spiking excitability in all four models. Structural and physiological synaptic defects that lead to sensory abnormalities in mouse models of autism have been identified in S1 (Balasco et al., 2019; Robertson and Baron-Cohen, 2017). However, the gene expression changes in S1 cell types that underlie these phenotypes remain unknown. One hypothesis could be that ASD causes neurodevelopmental transcriptomic alterations that disrupt cell type plasticity in whisker S1. Discovering the cell types involved in this process would enable us to link molecular and behavioral phenotypes and improve our understanding of ASD pathophysiology. Future studies should combine snRNA-seq with whisker deprivation on *Fmr1* KO mice to uncover transcriptomic signatures underlying ASD's influence on cellular homeostasis and laminar circuitry.

References

Ackman, J.B., Burbridge, T.J., Crair, M.C., 2012. Retinal waves coordinate patterned activity throughout the developing visual system. Nature 490, 219–225. https://doi.org/10.1038/nature11529

Andermann, M.L., Kerlin, A.M., Roumis, D.K., Glickfeld, L.L., Reid, R.C., 2011. Functional Specialization of Mouse Higher Visual Cortical Areas. Neuron 72, 1025–1039. https://doi.org/10.1016/j.neuron.2011.11.013

Antoine, M.W., Langberg, T., Schnepel, P., Feldman, D.E., 2019. Increased Excitation-Inhibition Ratio Stabilizes Synapse and Circuit Excitability in Four Autism Mouse Models. Neuron 101, 648-661.e4. https://doi.org/10.1016/j.neuron.2018.12.026

Baden, T., Euler, T., Berens, P., 2020. Understanding the retinal basis of vision across species. Nat Rev Neurosci 21, 5–20. https://doi.org/10.1038/s41583-019-0242-1

Balasco, L., Provenzano, G., Bozzi, Y., 2019. Sensory Abnormalities in Autism Spectrum Disorders: A Focus on the Tactile Domain, From Genetic Mouse Models to the Clinic. Front Psychiatry 10, 1016. https://doi.org/10.3389/fpsyt.2019.01016

Chen, Q., Deister, C.A., Gao, X., Guo, B., Lynn-Jones, T., Chen, N., Wells, M.F., Liu, R., Goard, M.J., Dimidschstein, J., Feng, S., Shi, Y., Liao, W., Lu, Z., Fishell, G., Moore, C.I., Feng, G., 2020. Dysfunction of cortical GABAergic neurons leads to sensory hyper-reactivity in a Shank3 mouse model of ASD. Nat Neurosci 23, 520–532. https://doi.org/10.1038/s41593-020-0598-6

Clark, I.C., Gutiérrez-Vázquez, C., Wheeler, M.A., Li, Z., Rothhammer, V., Linnerbauer, M., Sanmarco, L.M., Guo, L., Blain, M., Zandee, S.E.J., Chao, C.-C., Batterman, K.V., Schwabenland, M., Lotfy, P., Tejeda-Velarde, A., Hewson, P., Manganeli Polonio, C., Shultis, M.W., Salem, Y., Tjon, E.C., Fonseca-Castro, P.H., Borucki, D.M., Alves de Lima, K., Plasencia, A., Abate, A.R., Rosene, D.L., Hodgetts, K.J., Prinz, M., Antel, J.P., Prat, A., Quintana, F.J., 2021. Barcoded viral tracing of single-cell interactions in central nervous system inflammation. Science 372, eabf1230. https://doi.org/10.1126/science.abf1230

Cooper, J.A., 2008. A mechanism for inside-out lamination in the neocortex. Trends Neurosci 31, 113–119. https://doi.org/10.1016/j.tins.2007.12.003

Davis, M.F., Figueroa Velez, D.X., Guevarra, R.P., Yang, M.C., Habeeb, M., Carathedathu, M.C., Gandhi, S.P., 2015. Inhibitory Neuron Transplantation into Adult Visual Cortex Creates a New Critical Period that Rescues Impaired Vision. Neuron 86, 1055–1066. https://doi.org/10.1016/j.neuron.2015.03.062

Fang, Q., Li, Y.-T., Peng, B., Li, Z., Zhang, L.I., Tao, H.W., 2021. Balanced Enhancements of Synaptic Excitation and Inhibition Underlie Developmental Maturation of Receptive Fields in the Mouse Visual Cortex. J Neurosci 41, 10065–10079. https://doi.org/10.1523/JNEUROSCI.0442-21.2021

Feller, M.B., Scanziani, M., 2005. A precritical period for plasticity in visual cortex. Curr Opin Neurobiol 15, 94–100. https://doi.org/10.1016/j.conb.2005.01.012

Finkbeiner, C., Ortuño-Lizarán, I., Sridhar, A., Hooper, M., Petter, S., Reh, T.A., 2022. Single-cell ATAC-seq of fetal human retina and stem-cell-derived retinal organoids shows changing chromatin landscapes during cell fate acquisition. Cell Rep 38, 110294. https://doi.org/10.1016/j.celrep.2021.110294

Ford, K.J., Feller, M.B., 2012. Assembly and disassembly of a retinal cholinergic network. Vis Neurosci 29, 61–71. https://doi.org/10.1017/S0952523811000216

Glickfeld, L.L., Olsen, S.R., 2017. Higher-Order Areas of the Mouse Visual Cortex. Annu Rev Vis Sci 3, 251–273. https://doi.org/10.1146/annurev-vision-102016-061331

Gordon, J.A., Stryker, M.P., 1996. Experience-dependent plasticity of binocular responses in the primary visual cortex of the mouse. J Neurosci 16, 3274–3286. https://doi.org/10.1523/JNEUROSCI.16-10-03274.1996

Gulmez Karaca, K., Brito, D.V.C., Oliveira, A.M.M., 2019. MeCP2: A Critical Regulator of Chromatin in Neurodevelopment and Adult Brain Function. Int J Mol Sci 20, 4577. https://doi.org/10.3390/ijms20184577

Hahn, J., Monavarfeshani, A., Qiao, M., Kao, A.H., Kölsch, Y., Kumar, A., Kunze, V.P., Rasys, A.M., Richardson, R., Wekselblatt, J.B., Baier, H., Lucas, R.J., Li, W., Meister, M., Trachtenberg, J.T., Yan, W., Peng, Y.-R., Sanes, J.R., Shekhar, K., 2023. Evolution of neuronal cell classes and types in the vertebrate retina. Nature 624, 415–424. https://doi.org/10.1038/s41586-023-06638-9

Han, Y., Kebschull, J.M., Campbell, R.A.A., Cowan, D., Imhof, F., Zador, A.M., Mrsic-Flogel, T.D., 2018. The logic of single-cell projections from visual cortex. Nature 556, 51–56. https://doi.org/10.1038/nature26159

Hooks, B.M., Chen, C., 2020. Circuitry Underlying Experience-Dependent Plasticity in the Mouse Visual System. Neuron 106, 21–36. https://doi.org/10.1016/j.neuron.2020.01.031

Hrvatin, S., Hochbaum, D.R., Nagy, M.A., Cicconet, M., Robertson, K., Cheadle, L., Zilionis, R., Ratner, A., Borges-Monroy, R., Klein, A.M., Sabatini, B.L., Greenberg, M.E., 2018. Single-cell analysis of experience-dependent transcriptomic states in the mouse visual cortex. Nat Neurosci 21, 120–129. https://doi.org/10.1038/s41593-017-0029-5

Hubel, D.H., Wiesel, T.N., LeVay, S., 1977. Plasticity of ocular dominance columns in monkey striate cortex. Philos Trans R Soc Lond B Biol Sci 278, 377–409. https://doi.org/10.1098/rstb.1977.0050

Jézéquel, J., Condomitti, G., Kroon, T., Hamid, F., Sanalidou, S., Garces, T., Maeso, P., Balia, M., Rico, B., 2023. Cadherins orchestrate specific patterns of perisomatic inhibition onto distinct pyramidal cell populations. https://doi.org/10.1101/2023.09.28.559922

Jin, S., Plikus, M.V., Nie, Q., 2023. CellChat for systematic analysis of cell-cell communication from single-cell and spatially resolved transcriptomics. https://doi.org/10.1101/2023.11.05.565674

Kandel, E.R., 2013. Principles of Neural Science, Fifth Edition. McGraw Hill Professional.

Kim, E.J., Zhang, Z., Huang, L., Ito-Cole, T., Jacobs, M.W., Juavinett, A.L., Senturk, G., Hu, M., Ku, M., Ecker, J.R., Callaway, E.M., 2020. Extraction of Distinct Neuronal Cell Types from within a Genetically Continuous Population. Neuron 107, 274-282.e6. https://doi.org/10.1016/j.neuron.2020.04.018

Lin, Y., Bloodgood, B.L., Hauser, J.L., Lapan, A.D., Koon, A.C., Kim, T.-K., Hu, L.S., Malik, A.N., Greenberg, M.E., 2008. Activity-dependent regulation of inhibitory synapse development by Npas4. Nature 455, 1198–1204. https://doi.org/10.1038/nature07319

Llamosas, N., Michaelson, S.D., Vaissiere, T., Rojas, C., Miller, C.A., Rumbaugh, G., 2021. Syngap1 regulates experience-dependent cortical ensemble plasticity by promoting in vivo excitatory synapse strengthening. Proc Natl Acad Sci U S A 118, e2100579118. https://doi.org/10.1073/pnas.2100579118

Michaelson, S.D., Ozkan, E.D., Aceti, M., Maity, S., Llamosas, N., Weldon, M., Mizrachi, E., Vaissiere, T., Gaffield, M.A., Christie, J.M., Holder, J.L., Miller, C.A., Rumbaugh, G., 2018. SYNGAP1 heterozygosity disrupts sensory processing by reducing touch-related activity within somatosensory cortex circuits. Nat Neurosci 21, 1–13. https://doi.org/10.1038/s41593-018-0268-0

Moore, J.R., Nemera, M.T., D'Souza, R.D., Hamagami, N., Clemens, A.W., Beard, D.C., Urman, A., Mendoza, V.R., Gabel, H.W., 2024. Non-CG DNA methylation and MeCP2 stabilize repeated tuning of long genes that distinguish closely related neuron types. https://doi.org/10.1101/2024.01.30.577861

Nelson, S.B., Valakh, V., 2015. Excitatory/Inhibitory balance and circuit homeostasis in Autism Spectrum Disorders. Neuron 87, 684–698. https://doi.org/10.1016/j.neuron.2015.07.033

Reh, R.K., Dias, B.G., Nelson, C.A., Kaufer, D., Werker, J.F., Kolb, B., Levine, J.D., Hensch, T.K., 2020. Critical period regulation across multiple timescales. Proceedings of the National Academy of Sciences 117, 23242–23251. https://doi.org/10.1073/pnas.1820836117

Robertson, C.E., Baron-Cohen, S., 2017. Sensory perception in autism. Nat Rev Neurosci 18, 671–684. https://doi.org/10.1038/nrn.2017.112

Rubenstein, J.L.R., Merzenich, M.M., 2003. Model of autism: increased ratio of excitation/inhibition in key neural systems. Genes Brain Behav 2, 255–267.

Saunders, A., Huang, K.W., Vondrak, C., Hughes, C., Smolyar, K., Sen, H., Philson, A.C., Nemesh, J., Wysoker, A., Kashin, S., Sabatini, B.L., McCarroll, S.A., 2022. Ascertaining cells' synaptic connections and RNA expression simultaneously with barcoded rabies virus libraries. Nat Commun 13, 6993. https://doi.org/10.1038/s41467-022-34334-1

Shekhar, K., Whitney, I.E., Butrus, S., Peng, Y.-R., Sanes, J.R., 2022. Diversification of multipotential postmitotic mouse retinal ganglion cell precursors into discrete types. eLife 11, e73809. https://doi.org/10.7554/eLife.73809
Shepherd, G.M.G., Yamawaki, N., 2021. Untangling the cortico-thalamo-cortical loop: cellular pieces of a knotty circuit puzzle. Nat Rev Neurosci 22, 389–406. https://doi.org/10.1038/s41583-021-00459-3
Sorensen, S.A., Gouwens, N.W., Wang, Y., Mallory, M., Budzillo, A., Dalley, R., Lee, B.R., Gliko, O., Kuo, H., Kuang, X., Mann, R., Ahmadinia, L., Alfiler, L., Baftizadeh, F., Baker, K.S., Bannick, S., Bertagnolli, D., Bickley, K., Bohn, P., Bomben, J., Boyer, G., Brouner, K., Cahoon, A., Chen, N., Chen, C., Chen, K., Chvilicek, M., Collman, F., Daigle, T.L., Dawes, T., Frates, R. de, Dee, N., DePartee, M., Egdorf, T., El-Hifnawi, L., Esposito, L., Farrell, C., Gala, R., Gamlin, C., Gary, A., Goldy, J., Gu, H., Hadley, K., Hawrylycz, M., Henry, A., Hill, D., Hirokawa, K.E., Huang, Z., Johnson, K., Juneau, Z., Kebede, S., Kim, L., Kruse, L., Lee, C., Leon, A., Lesnar, P., Li, A., Li, Y., Liang, E., Link, K., Maxwell, M., McGraw, M., McMillen, D.A., Mukora, A., Ng, Lindsay, Oldre, A., Park, D., Pom, C.A., Popovich, Z., Potekhina, L., Rajanbabu, R., Ransford, S., Reding, M., Ruiz, A., Sandman, D., Sevigny, J., Shulga, L., Siverts, L., Slaughterbeck, C., Smith, K.A., Stoecklin, M., Sulc, J., Sunkin, S.M., Tieu, M., Ting, J., Trinh, J., Vargas, S., Vumbaco, D., Walker, M., Wang, M., Wanner, A., Waters, J., Williams, G., Wilson, J.A., Xiong, W., Lein, E.S., Berg, J., Kalmbach, B.E., Yao, S., Gong, H., Luo, Q., Ng, Lydia, Sumbul, U., Jarsky, T., Yao, Z., Tasic, B., Zeng, H., 2023. Connecting single neuron transcriptomes to the projectome in mouse visual cortex. https://doi.org/10.1101/2023.11.25.568393
Tan, L., Ringach, D.L., Zipursky, S.L., Trachtenberg, J.T., 2021. Vision is required for the formation of binocular neurons prior to the classical critical period. Curr Biol 31, 4305-4313.e5. https://doi.org/10.1016/j.cub.2021.07.053
Tan, L., Tring, E., Ringach, D.L., Zipursky, S.L., Trachtenberg, J.T., 2020. Vision Changes the Cellular Composition of Binocular Circuitry during the Critical Period. Neuron 108, 735-747.e6. https://doi.org/10.1016/j.neuron.2020.09.022
Van de Sande, B., Flerin, C., Davie, K., De Waegeneer, M., Hulselmans, G., Aibar, S., Seurinck, R., Saelens, W., Cannoodt, R., Rouchon, Q., Verbeiren, T., De Maeyer, D., Reumers, J., Saeys, Y., Aerts, S., 2020. A scalable SCENIC workflow for single-cell gene regulatory network analysis. Nat Protoc 15, 2247–2276. https://doi.org/10.1038/s41596-020-0336-2
Vanderhaeghen, P., Polleux, F., 2023. Developmental mechanisms underlying the evolution of human cortical circuits. Nat Rev Neurosci 24, 213–232. https://doi.org/10.1038/s41583-023-00675-z
VanInsberghe, M., van den Berg, J., Andersson-Rolf, A., Clevers, H., van Oudenaarden, A., 2021. Single-cell Ribo-seq reveals cell cycle-dependent translational pausing. Nature 597, 561–565. https://doi.org/10.1038/s41586-021-03887-4
Voufo, C., Chen, A.Q., Smith, B.E., Yan, R., Feller, M.B., Tiriac, A., 2023. Circuit mechanisms underlying embryonic retinal waves. eLife 12, e81983. https://doi.org/10.7554/eLife.81983
Wang, H.C., LeMessurier, A.M., Feldman, D.E., 2022. Tuning instability of non-columnar neurons in the salt-and-pepper whisker map in somatosensory cortex. Nat Commun 13, 6611. https://doi.org/10.1038/s41467-022-34261-1
Young, T.R., Yamamoto, M., Kikuchi, S.S., Yoshida, A.C., Abe, T., Inoue, K., Johansen, J.P., Benucci, A., Yoshimura, Y., Shimogori, T., 2023. Thalamocortical control of cell-type specificity drives circuits for processing whisker-related information in mouse barrel cortex. Nat Commun 14, 6077. https://doi.org/10.1038/s41467-023-41749-x

Yuan, L., Chen, X., Zhan, H., Henry, G.L., Zador, A.M., 2024. Massive multiplexing of spatially resolved single neuron projections with axonal BARseq. Nat Commun 15, 8371. https://doi.org/10.1038/s41467-024-52756-x

Zhang, Y., Bonnan, A., Bony, G., Ferezou, I., Pietropaolo, S., Ginger, M., Sans, N., Rossier, J., Oostra, B., LeMasson, G., Frick, A., 2014. Dendritic channelopathies contribute to neocortical and sensory hyperexcitability in Fmr1−/y mice. Nat Neurosci 17, 1701–1709. https://doi.org/10.1038/nn.3864

Zhang, Z., Gibson, J.R., Huber, K.M., 2021. Experience-dependent weakening of callosal synaptic connections in the absence of postsynaptic FMRP. eLife 10, e71555. https://doi.org/10.7554/eLife.71555